

EISSN 1305-3612

DIR

Diagnostic and Interventional Radiology

TSR
1924
TURKISH SOCIETY
OF RADIOLOGY

dirjournal.org

VOLUME 30
ISSUE 1
JANUARY 2024

Editor in Chief

Mehmet Ruhi Onur, MD

Department of Radiology, Hacettepe University Faculty of Medicine, Ankara, Turkey

ORCID ID: 0000-0003-1732-7862

Section Editors and Scientific Editorial Board

Abdominal Imaging

İlkay S. İdilman, MD 

Department of Radiology, Hacettepe University Faculty of Medicine, Ankara, Turkey

ORCID ID: 0000-0002-1913-2404

Sonay Aydın, MD 

Department of Radiology, Erzincan Binali Yıldırım University Faculty of Medicine, Erzincan, Turkey

ORCID ID: 0000-0002-3812-6333

Artificial Intelligence and Informatics

Burak Koçak, MD 

Department of Radiology, University of Health Sciences, Başakşehir Çam and Sakura City Hospital, İstanbul, Turkey

ORCID ID: 0000-0002-7307-396X

Breast Imaging

Füsun Taşkın, MD 

Department of Radiology, Acıbadem University Faculty of Medicine, İstanbul, Turkey

ORCID ID: 0000-0001-7985-3660

Chest and Cardiovascular Imaging

Furkan Ufuk, MD 

Department of Radiology, Pamukkale University Faculty of Medicine, Denizli, Turkey

ORCID ID: 0000-0002-8614-5387

Hybrid Imaging and Nuclear Medicine

Evrin Bengi Türkbey, MD 

Radiology and Imaging Sciences, Clinical Center, National Institutes of Health Bethesda, Maryland, United States

ORCID ID: 0000-0002-5216-3528

Interventional Radiology

Barbaros Çil, MD, FCIIRSE 

Department of Radiology, Koç University School of Medicine, İstanbul, Turkey

ORCID ID: 0000-0003-1079-0088

Bahri Üstünsöz, MD 

Department of Radiology, LSUHSC (Louisiana State University Health Science Center) School of Medicine, New Orleans, United States

ORCID ID: 0000-0003-4308-6708

James Milburn, MD 

Department of Radiology, Ochsner Medical System, New Orleans, Louisiana, USA

ORCID ID: 0000-0003-3403-2628

Musculoskeletal Imaging

Zeynep Maraş Özdemir, MD 

Department of Radiology, İnönü University Faculty of Medicine, Malatya, Turkey

ORCID ID: 0000-0003-1085-8978

Neuroradiology

Gülgün Yılmaz Ovalı, MD 

Department of Radiology, Celal Bayar University Faculty of Medicine, Manisa, Turkey

ORCID ID: 0000-0001-8433-5622

Erkan Gökçe, MD 

Department of Radiology, Tokat Gaziosmanpaşa University Faculty of Medicine, Tokat, Turkey

ORCID ID: 0000-0003-3947-2972

Pediatric Radiology

Meltem Ceyhan Bilgici, MD 

Department of Radiology, 19 Mayıs University Faculty of Medicine, Samsun, Turkey

ORCID ID: 0000-0002-0133-0234

Evrin Özmen, MD 

Department of Radiology, Koç University Hospital, İstanbul, Turkey

ORCID ID: 0000-0003-3100-4197

Publication Coordinator

Şükrü Mehmet Ertürk, MD 

Department of Radiology, İstanbul University, İstanbul Faculty of Medicine, İstanbul, Turkey

ORCID ID: 0000-0003-4086-675X

Biostatistical Consultant

İlker Ercan, PhD 

Department of Biostatistics, Uludağ University School of Medicine, Bursa, Turkey

ORCID ID: 0000-0002-2382-290X

Publication Services

Galenos Publishing, İstanbul, TR

Past Editors

Editors in Chief

Mustafa Seçil, MD (2016-2023)

Nevzat Karabulut, MD (2011-2016)

Üstün Aydingöz, MD (2010-2011)

Okan Akhan, MD (2001-2010)

Ferhun Balkancı, MD (1999-2001)

Aytekin Besim, MD (1994-1999)*

* Dr. Aytekin Besim actually served as the General Coordinator. His work in this capacity, however, was in effect that of an Editor in Chief.

Editors

Ayşenur Cila, MD (2001-2002)

Suat Kemal Aytaç, MD (1997-2001)

Erhan Ilgıt, MD (1994-2001)

Okan Akhan, MD (1994-2001)

Ferhun Balkancı, MD (1994-2000)

Serdar Akyar, MD (1994-1997)

Section Editors

Section Editorship was established in 2002 at the tenure of Dr Okan Akhan, Editor in Chief.

Abdominal Imaging

Bengi Gürses, MD (2020-2023)

Mehmet Ruhi Onur, MD (2016-2023)

Bariş Türkbey, MD (2014-2020)

Mustafa N. Özmen, MD (2012-2018)

Murat Acar, MD (2015-2016)

Mustafa Seçil, MD (2011-2016)

Ahmet Tuncay Turgut, MD (2011)

Deniz Akata, MD (2007-2011)

Ayşe Erden, MD (2002-2011)

Okan Akhan, MD (2002-2010)

Hakan Özdemir, MD (2002-2010)

Artificial Intelligence and Informatics

Bariş Türkbey, MD (2020-2023)

Breast Imaging

Mustafa Erkin Arıbal, MD (2016-2023)

Sibel Kul (2015-2018)

Ayşenur Oktay, MD (2009-2014)

Ayşegül Özdemir, MD (2004-2009)

Cardiovascular Imaging

Uğur Bozlar, MD (2016-2023)

Muşturay Karçaaltıncaba, MD (2007-2010)

Mecit Kantarcı (2010-2016)

Chest Imaging

Nevzat Karabulut, MD (2010-2014)

Çetin Atasoy, MD (2007-2010)

Macit Arıyürek, MD (2002-2007)

Figen Demirkazık, MD, (2014-2018)

General Radiology

Ersin Öztürk, MD (2014-2017)

Utku Şenol, MD (2010-2013)

Oğuz Dicle, MD (2007-2010)

Interventional Radiology

Cüneyt Aytekin, MD (2016-2023)

Bora Peynircioğlu, MD (2012-2015)

Levent Oğuzkurt, MD (2011-2014)

Fatih Boyvat, MD (2007-2010)

İsmail Oran, MD (2015-2019)

Musculoskeletal Imaging

Hatice Tuba Sanal, MD (2016-2023)

Fatih Kantarcı, MD (2014-2016)

Ayşenur Oktay, MD (2011-2013)

Üstün Aydıngöz, MD (2002-2011)

Berna Dirim Mete (2016-2017)

Neuroradiology and Head & Neck Imaging

Kubilay Aydın, MD (2016-2023)

Nafi Aygün, MD (2016-2023)

Kader Karlı Oğuz, MD (2011-2015)

Süleyman Men, MD (2007-2013)

Muhteşem Ağıldere, MD (2002-2011)

Nuclear Medicine

A. Cahid Civelek, MD (2016-2023)

Oktay Sarı, MD (2015)

Akın Yıldız, MD (2011-2014)

Pediatric Radiology

Korgün Koral, MD (2016-2023)

Murat Kocaoğlu, MD (2016-2023)

Ensar Yekeler, MD (2014-2016)

Suat Fitöz, MD (2007-2013)

Diagnostic and Interventional Radiology (Diagn Interv Radiol) is a bimonthly periodical of the Turkish Society of Radiology and the content of the journal is available at <https://www.dirjournal.org/>. It is peer-reviewed and adheres to the highest ethical and editorial standards. The editors of the journal endorse the Editorial Policy Statements Approved by the Council of Science Editors Board of Directors (<https://cse.memberclicks.net/march-31--2000-draft-editorial-policies>). The journal is in compliance with the Recommendations for the Conduct, Reporting, Editing and Publication of Scholarly Work in Medical Journals published by the International Committee of Medical Journal Editors (updated May 2022, www.icmje.org).

First ten volumes of Diagnostic and Interventional Radiology have been published in Turkish under the name of Tanısal ve Girişimsel Radyoloji (Index Medicus® abbreviation: Tani Girişim Radyol), the current title's exact Turkish translation.

Diagnostic and Interventional Radiology is an open access publication, and the journal's publication model is based on Budapest Open Access Initiative (BOAI) declaration. All published content is available online, free of charge at <https://www.dirjournal.org/>. Authors retain the copyright of their published work in Diagnostic and Interventional Radiology. The journal's content is licensed under a Creative Commons Attribution-NonCommercial (CC BY-NC) 4.0 International License which permits third parties to share and adapt the content for non-commercial purposes by giving the appropriate credit to the original work.

Diagnostic and Interventional Radiology is indexed in Science Citation Index Expanded, Pubmed/MEDLINE, PubMed Central, Web of Science, DOAJ, TUBITAK ULAKBIM TR Index, HINARI, EMBASE, CINAHL, Scopus, Gale and CNKI.

Contact Information

Diagnostic and Interventional Radiology Turkish Society of Radiology

Hoşdere Cad., Güzelkent Sok., Çankaya Evleri, F/2, 06540

Ankara, Turkey

E-mail: info@dirjournal.org

Phone: +90 (312) 442 36 53 Fax: +90 (312) 442 36 54

Publisher Contact

Address: Molla Gürani Mah. Kaçamak Sk.

No: 21/1 34093 İstanbul, Turkey

Phone: +90 (530) 177 30 97

E-mail: info@galenos.com.tr/yayin@galenos.com.tr

Web: www.galenos.com.tr Publisher Certificate Number: 14521

Online Publication Date: January 2024

EISSN 1305-3612

International scientific journal published bimonthly.



Instructions to Authors

Diagnostic and Interventional Radiology (Diagn Interv Radiol) is a medium for disseminating scientific information based on research, clinical experience, and observations pertaining to diagnostic and interventional radiology. The journal is the double-blind peer-reviewed, bimonthly, open-access publication organ of the Turkish Society of Radiology and its publication language is English. Diagnostic and Interventional Radiology is currently indexed by Science Citation Index Expanded, PubMed MEDLINE, PubMed Central, TUBITAK ULAKBIM TR Index, HINARI, EMBASE, CINAHL, Scopus, Gale and CNKI.

The journal is a medium for original articles, reviews, pictorial essays, technical notes related to all fields of diagnostic and interventional radiology.

The editorial and publication process of the Diagnostic and Interventional Radiology are shaped in accordance with the guidelines of the International Committee of Medical Journal Editors (ICMJE), World Association of Medical Editors (WAME), Council of Science Editors (CSE), Committee on Publication Ethics (COPE), European Association of Science Editors (EASE), and National Information Standards Organization (NISO). The journal is in conformity with the Principles of Transparency and Best Practice in Scholarly Publishing.

Authorship

Each individual listed as an author should fulfill the authorship criteria recommended by the International Committee of Medical Journal Editors (ICMJE - www.icmje.org). To be listed as an author, an individual should have made substantial contributions to all four categories established by the ICMJE: (a) conception and design, or acquisition of data, or analysis and interpretation of data, (b) drafting the article or revising it critically for important intellectual content, (c) final approval of the version to be published, and (d) agreement to be accountable for all aspects of the work in ensuring that questions related to the accuracy or integrity of any part of the work are appropriately investigated and resolved. Individuals who contributed to the preparation of the manuscript but do not fulfill the authorship criteria should be acknowledged in an acknowledgements section, which should be included in the title page of the manuscript. If the editorial board suspects a case of "gift authorship", the submission will be rejected without further review.

Ethical standards

For studies involving human or animal participants, the authors should indicate whether the procedures followed were in accordance with the ethical standards of the responsible committee on human and animal experimentation (institutional or regional) and with the Helsinki Declaration). Application or approval number/year of the study should also be provided. The editorial board will act in accordance with COPE guidelines if an ethical misconduct is suspected.

It is the authors' responsibility to carefully protect the patients' anonymity and to verify that any experimental investigation with human subjects reported in the submission was performed with informed consent and following all the guidelines for experimental investigation with human subjects required by the institution(s) with which all the authors are affiliated with. For photographs that may reveal the identity of the patients, signed releases of the patient or of his/her legal representative should be enclosed.

Prospective human studies require both an ethics committee approval and informed consent by participants. Retrospective studies require an ethics committee approval with waiver of informed consent. Authors may be required to document such approval.

All submissions are screened by a similarity detection software (iThenticate by CrossCheck). Manuscripts with an overall similarity index of greater than 20%, or duplication rate at or higher than 5% with a single source are returned back to authors without further evaluation along with the similarity report.

In the event of alleged or suspected research misconduct, e.g., plagiarism, citation manipulation, and data falsification/fabrication, the Editorial Board will follow and act in accordance with COPE guidelines.

Withdrawal Policy

Articles may be withdrawn under certain circumstances.

The article will be withdrawn if it;

- violates professional ethical codes,
- is subject to a legal dispute,
- has multiple submissions,
- includes fake claims of authorship, plagiarism, misleading data, and false data that may pose a severe health risk.

The editorial board will follow the principles set by COPE (Committee on Publication Ethics) in case of an article withdrawal.

Manuscript Preparation

The manuscripts should be prepared in accordance with ICMJE-Recommendations for the Conduct, Reporting, Editing, and Publication of Scholarly Work in Medical Journals (updated in May 2022 - <https://www.icmje.org/recommendations/>).

Original Investigations and Reviews should be presented in accordance with the following guidelines: randomized study – CONSORT, observational study – STROBE, study on diagnostic accuracy – STARD, systematic reviews and meta-analysis PRISMA, nonrandomized behavioral and public health intervention studies – TREND.

Manuscripts are evaluated and published on the understanding that they are original contributions, and do not contain data that have been published elsewhere or are under consideration by another journal. Authors are required to make a full statement at the time of submission about all prior reports and submissions that might be considered duplicate or redundant publication, and mention any previously published abstracts for meeting presentations that contain partial or similar material in the cover letter. They must reference any similar previous publications in the manuscript.

Authors must obtain written permission from the copyright owner to reproduce previously published figures, tables, or any other material in both print and electronic formats and present it during submission. The original source should be cited within the references and below the reprinted material.

The manuscripts and all documents are recommended for scanning by language-checking applications such as Grammarly, Consistency Checker, etc.

Cover letter: A cover letter must be provided with all manuscripts. This letter may be used to emphasize the importance of the study. The authors should briefly state the existing knowledge relevant to the study and the contributions their study make to the existing knowledge. The correspondent author should also include a statement in the cover letter declaring that he/she accepts to undertake all the responsibility for authorship during the submission and review stages of the manuscript.

Title page: A separate title page should be submitted with all manuscripts and should include the title of the manuscript, name(s), affiliation(s), and major degree(s) of the author(s). The name, address, telephone (including the mobile phone number) and fax numbers and e-mail address of the corresponding author should be clearly listed. Grant information and other sources of support should also be included. Individuals who contributed to the preparation of the manuscript but do not fulfill the authorship criteria should also be acknowledged in the title page. Manuscripts should not be signed by more than 6 authors unless they are multicenter or multidisciplinary studies.

Main document

Abstract: All submissions (except for Letters to the Editor) should be accompanied by an abstract limited to 400 words. A structured abstract is only required with original articles and it should include the following subheadings: PURPOSE, METHODS, RESULTS, CONCLUSION, CLINICAL SIGNIFICANCE.

Main points: Each submission should be accompanied by 3 to 5 “main points”, which should emphasize the most striking results of the study and highlight the message that is intended to be conveyed to the readers. As these main points would be targeting radiology residents, experts and residents of other fields of medicine, as well as radiology experts, they should be kept as plain and simple as possible. These points should be constructed in a way that provides the readers with a general overview of the article and enables them to have a general idea about the article.

The main points should be listed between ‘Abstract’ and ‘Introduction’.

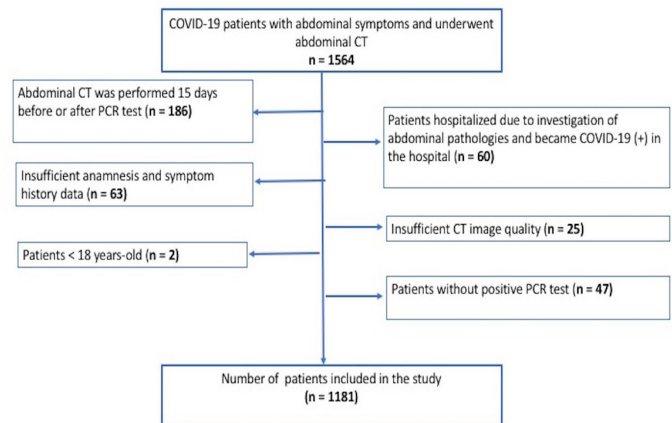
Example: Liu S, Xu X, Cheng Q, et al. Simple quantitative measurement based on DWI to objectively judge DWI-FLAIR mismatch in a canine stroke model. *Diagn Interv Radiol* 2015; 21:348–354.

- The relative diffusion-weighted imaging signal intensity (rDWI) of ischemic lesions might be helpful to identify the status of fluid attenuated inversion recovery (FLAIR) imaging in acute ischemic stroke.
- The relative apparent diffusion coefficient (rADC) value appears not useful to identify the status of FLAIR imaging in the acute period.
- Based on our embolic canine model, rDWI increased gradually in the acute period, while the rADC kept stable, which might explain why rDWI is helpful to identify the status of FLAIR imaging, while rADC is not.

Main text

Original Articles

Original articles should provide new information based on original research. The main text should be structured with Introduction, Methods, Results, and Discussion subheadings. The number of cited references should not exceed 50 and the main text should be limited to 4500 words. Number of tables included in an original article should be limited to 4 and the number of figures should be limited to 7 (or a total of 15 figure parts). The first figure of original articles (Figure 1) should be the flowchart of the study representing the criteria and number of patients from initial retrieval to the final study cohort. An example related to the relevant table is as follows:



Introduction

State briefly the nature and purpose of the work, quoting the relevant literature.

Methods

Include the details of clinical and technical procedures.

Research ethics standards compliance

All manuscripts dealing with human subjects must contain a statement indicating that the study was approved by the Institutional Review Board or a comparable formal research ethics review committee. If none is present at your institution, there should be a statement that the research was performed according to the Declaration of Helsinki principles (www.wma.net/e/policy/b3.htm). There should also be a statement about whether informed consent was obtained from research subjects.

Results

Present these clearly, concisely, and without comment. Statistical analysis results should also be provided in this section to support conclusions when available.

Discussion

Explain your results and relate them to those of other authors; define their significance for clinical practice. Limitations, drawbacks, or shortcomings of the study should also be stated in the discussion section before the conclusion paragraph. In the last paragraph, a strong conclusion should be written.

Review Articles

Review articles are scientific analyses of recent developments on a specific topic as reported in the literature. No new information is described, and no opinions or personal experiences are expressed. Reviews include only the highlights on a subject. Main text should be limited to 4000 words and the number of cited references should not exceed 75. Number of tables included in a review article should be limited to 4 and the number of figures should be limited to 15 (or a total of 30 figure parts).

Pictorial Essay

This is a continuing medical education exercise with the teaching message in the figures and their legends. Text should include a brief abstract; there may be as many as 30 figure parts. No new information is included. The value of the paper turns on the quality of the illustrations. Authors can submit dynamic images (e.g. video files) or include supplemental image files for online presentation that further illustrate the educational purpose of the essay. Maximums: Pages of text – 4 (1,500 words); References – 20; Figures – 15 or total of 30 images; No table Main text should be limited to 1500 words and the number of cited references should not exceed 15.

Technical Notes

Technical note is a brief description of a specific technique, procedure, modification of a technique, or new equipment of interest to radiologists. It should include a brief introduction followed by Technique section for case reports or Methods section for case series, and Discussion is limited to the specific message, including the uses of the technique, equipment, or software. Literature reviews and lengthy descriptions of cases are not appropriate.

Main text should be limited to 1500 words and the number of cited references should not exceed 8. Number of tables included in a technical note should be limited to 4 and the number of figures should be limited to 3 (or a total of 6 figure parts).

Letter to the Editor and Reply

Letters to the Editor and Replies should offer objective and constructive criticism of published articles within last 6 months. Letters may also discuss matters of general interest to radiologists and may include images. Material being submitted or published elsewhere should not be duplicated in letters.

Main text should be limited to 500 words and the number of cited references should not exceed 6. No tables should be included and the number of figures should be limited to 2 (or a total of 4 figure parts).

Recommendations for Manuscripts:

Type of manuscript	Word limit	Abstract word limit	Reference limit	Author limit	Table limit	Figure limit
Original Article	4500	400 (Structured)	50	6*	4	7 or total of 15 images
Review Article	4000	200	75	5	4	15 or total of 24 images
Pictorial Essay	1500	400	20	5	1	15 figures or total of 30 figure parts
Technical Note	1500	200	8	5	2	3 figures or total of 6 figure parts
Letter	500	N/A	6	4	No tables	2 figures or total of 4 figure parts

*Manuscripts should not be signed by more than 6 authors unless they are multicenter or multidisciplinary studies.

**Considering the specific condition of the manuscript, minor flexibilities may be applied for the recommendations upon the decision of Editor-in-Chief or the Section Editors.

References

Both in-text citations and the references must be prepared according to the AMA Manual of style.

While citing publications, preference should be given to the latest, most up-to-date publications. Authors are responsible for the accuracy of references. If an ahead-of-print publication is cited, the DOI number should be provided. Journal titles should be abbreviated in accordance with the journal abbreviations in Index Medicus/MEDLINE/PubMed. When there are six or fewer authors, all authors should be listed. If there are seven or more authors, the first three authors should be listed followed by “et al.” In the main text of the manuscript, references should be cited in superscript after punctuation. The reference styles for different types of publications are presented in the following examples.

Journal Article: Economopoulos KJ, Brockmeier SF. Rotator cuff tears in overhead athletes. *Clin Sports Med.* 2012;31(4):675-692.

Book Section: Fikremariam D, Serafini M. Multidisciplinary approach to pain management. In: Vadivelu N, Urman RD, Hines RL, eds. *Essentials of Pain Management.* New York, NY: Springer New York; 2011:17-28.

Books with a Single Author: Patterson JW. *Weedon's Skin Pathology.* 4th ed. Churchill Livingstone; 2016.

Editor(s) as Author: Etzel RA, Balk SJ, eds. *Pediatric Environmental Health.* American Academy of Pediatrics; 2011.

Conference Proceedings: Morales M, Zhou X. Health practices of immigrant women: indigenous knowledge in an urban environment. Paper presented at: 78th Association for Information Science and Technology Annual Meeting; November 6-10; 2015; St Louis, MO. Accessed March 15, 2016. <https://www.asist.org/files/meetings/am15/proceedings/openpage15.html>

Thesis: Maiti N. Association Between Behaviours, Health Characteristics and Injuries Among Adolescents in the United States. Dissertation. Palo Alto University; 2010.

Online Journal Articles: Tamburini S, Shen N, Chih Wu H, Clemente KC. The microbiome in early life: implications for health outcomes. *Nat Med.* Published online July 7, 2016. doi:10.1038/nm4142

Epub Ahead of Print Articles: Websites: International Society for Infectious Diseases. ProMed-mail. Accessed February 10, 2016. <http://www.promedmail.org>

Tables

Tables should be included in the main document and should be presented after the reference list. Tables should be numbered consecutively in the order they are referred to within the main text. A descriptive title should be provided for all tables and the titles should be placed above the tables. Abbreviations used in the tables should be defined below by footnotes (even if they are defined within the main text). Tables should be created using the “insert table” command of the word processing software and they should be arranged clearly to provide an easy reading. Data presented in the tables should not be a repetition of the data presented within the main text but should be supporting the main text.

Figures and figure legends

Figures, graphics, and photographs should be submitted as separate files (in TIFF or JPEG format) through the submission system. The files should not be embedded in a Word document or the main document. When there are figure subunits, the subunits should not be merged to form a single image.

Instructions to Authors

Each subunit should be submitted separately through the submission system. Images should not be labelled (a, b, c, etc.) to indicate figure subunits. Thick and thin arrows, arrowheads, stars, asterisks, abbreviations and similar marks can be used on the images to support figure legends. Like the rest of the submission, the figures too should be blind. Any information within the images that may indicate the institution or the patient should be removed.

Figure legends should be listed at the end of the main document.

General

All acronyms and abbreviations used in the manuscript should be defined at first use, both in the abstract and in the main text. The abbreviation should be provided in parenthesis following the definition.

Statistical analysis should be performed in accordance with guidelines on reporting statistics in medical journals (Altman DG, Gore SM, Gardner MJ, Pocock SJ. Statistical guidelines for contributors to medical journals. *Br Med J* 1983; 7: 1489–1493.). Information on the statistical analysis process of the study should be provided within the main text.

When a drug, product, hardware, or software mentioned within the main text product information, the name and producer of the product should be provided in parenthesis in the following format: "Discovery St PET/CT scanner (GE Healthcare)."

All references, tables, and figures should be referred to within the main text and they should be numbered consecutively in the order they are referred to within the main text.

Initial evaluation and peer review process

Manuscripts submitted to Diagnostic and Interventional Radiology will first go through a technical evaluation process where the editorial office staff will ensure that the manuscript is prepared and submitted in accordance with the journal's guidelines. Submissions that do not conform the journal's guidelines will be returned to the submitting author with technical correction requests.

All submissions are screened by a similarity detection software (iThenticate by CrossCheck), and those with an overall similarity index of greater than 20%, or duplication rate at or higher than 5% with a single source are returned back to authors without further evaluation along with the similarity report.

Manuscripts meeting the requirements mentioned in journal's guideline will go under the review process. The initial review will be performed by Editor-in-Chief and the Section Editor, which include the evaluation of the manuscript for its originality, importance of the findings, scientific merit, interest to readers and compliance with the policy of the journal in force. Manuscripts with insufficient priority for publication are not sent out for further review and rejected promptly at this level to allow the authors to submit their work elsewhere without delay.

Manuscripts that pass through the initial review are sent to peer review, which is performed in a blinded manner by least two external and independent reviewers. During the review process, all original articles are evaluated by at least one senior consultant of statistics for proper handling and consistency of data, and use of correct statistical method. The Section Editor and / or Editor-in-Chief are the final authority in the decision-making process for all submissions.

Revisions

When submitting a revised version of a paper, the author must submit a detailed "Response to reviewers" that states point by point how each issue raised by the reviewers has been covered and where it can be found (each reviewer's comment followed by the author's reply and line numbers where

the changes have been made) as well as an annotated copy, and a clear copy of the main document.

Revised manuscripts must be submitted within 30 days from the date of the decision letter. If the revised version of the manuscript is not submitted within the allocated time, the revision option will be automatically cancelled by the submission system. If the submitting author(s) believe that additional time is required, they should request an extension before the initial 30-day period is over.

Proofs and DOI Number

Accepted manuscripts are copy-edited for grammar, punctuation, and format by professional language editors. Following the copyediting process, the authors will be asked to review and approve the changes made during the process. Authors will be contacted for a second time after the layout process and will be asked to review and approve the PDF proof of their article for publication. Once the production process of a manuscript is completed it is published online on the journal's webpage as an ahead-of-print publication before it is included in its scheduled issue.

Publication Fee Policy

Diagnostic and Interventional Radiology (DIR) applies an Article Processing Charge (APCs) for only accepted articles. No fees are requested from the authors during submission and evaluation process. All manuscripts must be submitted via Manuscript Manager.

An APC fee of and local taxes will be applied depending on the article type (see Table 1)

Review	\$ 1250
Original Article	\$ 1000
Pictorial Essay	\$ 750
Technical Note	

Table 1. Article Types and Fees

The APCs will be accepted through the link that will be sent to the corresponding author of each article via the online article system. In the next step, the authors will be receiving a receipt of their payment.

*Please note that the Article Processing Charge (APC) will not affect neither the editorial and peer-review process nor the priority of the manuscripts by no means. All submissions will be evaluated by the Editorial Board and the external reviewers in terms of scientific quality and ethical standards.

Refund Policy:

Returning the article to the author; Diagnostic and Interventional Radiology (DIR) will refund the submission fees with a coupon code if the article is returned to the author. Using this code, authors can use the submission fees of different articles without making a new payment.

Article Retraction:

Infringements of publication/research ethics, such as multiple submissions, bogus claims of authorship, plagiarism, and fraudulent use of data could lead to article retraction.

A retraction statement titled "Retraction: [article title]" must be signed by the authors and/or the editor. The original article is marked as retracted but a PDF version remains available to readers, and the retraction statement is linked to the original published paper.

Contents

EDITORIAL

1 Editorial. Letter from the Editor-in-Chief: A New Year for *Diagnostic and Interventional Radiology*. Mehmet Ruhi Onur

ABDOMINAL IMAGING

3 Original Article. Manual and semi-automated computed tomography volumetry significantly overestimates the right liver lobe graft weight: a single-center study with adult living liver donors. Hakkı Çelik, Hüseyin Odaman, Canan Altay, Tarkan Ünek, Mücahit Özbilgin, Tufan Egeli, Cihan Ağalar, Ibrahim Kemal Astarçioğlu, Funda Barlık

ARTIFICIAL INTELLIGENCE AND INFORMATICS

9 Original Article. Prediction of osteoporosis using MRI and CT scans with unimodal and multimodal deep-learning models. Yasemin Küçükçiloğlu, Boran Şekeroğlu, Terin Adalı, Niyazi Şentürk

CARDIOVASCULAR IMAGING

21 Original Article. Coronary artery calcium score percentiles: data from a single center in Turkey. Gülsüm Kılıçkap, Halil Tekdemir, Kübra Bahadır, Numan İlteriş Çevik, Betül Akdal Dölek, Murat Vural

CHEST IMAGING

28 Letter to the Editor. Centrilobular ground-glass nodule pattern in acute myeloid leukemia patients receiving cytosine arabinoside chemotherapy: an important form of drug-induced lung disease. Ömer Önder, Selin Ardalı Düzgün, Gamze Durhan, Orhan Macit Arıyürek

EMERGENCY RADIOLOGY

30 Review Article. Earthquakes from a radiological perspective: what is demanded from the radiologists, and what can we do? A pictorial review. Sonay Aydin, Omer Kazci, Bunyamin Ece, Mecit Kantarci

INTERVENTIONAL RADIOLOGY

42 Pictorial Essay. Techniques for portal vein targeting during a transjugular intrahepatic portosystemic shunt. Dan Laney, Hector Ferral, Alexandra Fairchild, Bahri Üstünsöz

48 Review Article. Magnetic resonance imaging-guided radiofrequency ablation of breast cancer: a current state of the art review. Chuan Zhang, Jing Shi, Bing Li, Xiaoxuan Yu, Xu Feng, Hanfeng Yang

55 Original Article. Pre-emptive transjugular intrahepatic portosystemic shunt in pediatric cystic fibrosis-related liver disease and portal hypertension: prospective long-term results. Laurens Hermie, Stephanie Van Biervliet, Anne Hoorens, Lien Van Cauwenbergh, Eddy Robberecht, Luc Defreyne

65 Original Article. Short-term clinical outcomes of transarterial embolization for symptomatic hand osteoarthritis refractory to conservative treatment. Sieh-Yang Lee, Wei-Xiong Lim, Kuan-Ting Wu, Cheng-Ta Wu, Chung-Cheng Huang, Ching-Di Chang

NEURORADIOLOGY

72 Letter to the Editor. Unusual collaterals through interhemispheric connections in Moyamoya disease. Ömer Bağcılar, Bora Korkmazer, Osman Kızılkılıç, Civan Işlak

Dear Reviewers,

Thank you for your invaluable contributions as reviewers to Diagnostic and Interventional Radiology in 2023. Your expertise and insightful feedback have helped to maintain our journal's high standards and ensure the quality of the articles we publish. We appreciate your interest in our journal and wish you every success in your academic career.

Sincerely,

A. Cahid Civelek
Abeer Alhussaini
Abidin Kılınçer
Afak Durur Karakaya
Afonso César Polimanti
Ahmet Baki Yağcı
Ahmet Erdemir
Ahmet Kürşad Poyraz
Ahmet Sığırıcı
Ahmet Veysel Polat
Ahsun Riaz
Ali Balcı
Ali Murat Koç
Ali Özgen
ALİ Yusuf Öner
Aliya Qayyum
Alparslan Kurtul
Alpay Alkan
Alper Selver
Alperen Kayalı
Ambarish Bhat
Antonio Facciorusso
Antonio Rosario Pisani
Arda Kayhan
Arzu Arslan
Arzu Canan
Arzu Serpil Arslan
Asli Tanrıvermiş Sayıt
Atakan Tanacan
Atilla Hikmet Çilengir
Ayaz Aghayev
Aydan Avdan Aslan
Aydın Demircioğlu
Ayşe Kalyoncu Uçar
Ayşegül Akdoğan Gemici

Ayşegül Altunkeser
Ayşenur Oktay
Ayşe Keven
Aytül Hande Yardımcı
Bahri Üstünsöz
Baki Hekimoğlu
Barış Türkbey
Berat Acı
Beyza Doğanay Erdoğan
Bing Ji
Birkan Bozkurt
Boran Şekeroğlu
Bökebatur Ahmet Raşit Mendi
Brandon Fields
Brian Quinn
Bünyamin Ece
Burak Koçak
Burçak Çakır Pekoz
C. Chad Quarles
Canan Altay
Carlo A. Mallio
Cassius Iyad Ochoa Char
Chien-Han Lai
Chinmay Kulkarni
Choirul Anam
Cihat Cinar Basekim
Çağdaş Topel
Deng Liangna
Derya Bako
Derya Yakar
Dietrich Beitzke
Diğdem Kuru Öz
Dilek Sağlam
Dongying Zhang
Duygu Herek

Düzgün Can Şenbil
Ebru Düşünceli Atman
Ebru Ozan
Ece Ateş Kuş
Ekim Gümeler
Elena Belloni
Elif Bulut
Elizabeth Tai
Ely Felker
Emine Şebnem Durmaz
Emre Bozkurt
Emre Ünal
Eray Atlı
Ercan Ayaz
Ercan Karaarslan
Erdal Karavaş
Erik Robert Ranschaert
Erkan Gökçe
Erkan Yıldırım
Erkin Arıbal
Erol Tülümen
Evrin Özmen
Ezgi Güler
Fahrettin Küçükay
Fatih Alper
Fazil Gelal
Federico Fontana
Fei-Yun Wu
Ferdi Çay
Ferhat Can Pişkin
Firat Atak
Figen Palabıyık
Filippo Cademartiri
Francesco Tiralongo
Funda Dinç

Furkan Ufuk
Gabriele Piffaretti
Gamze Durhan
Giampiero Francica
Gianluca Milanese
Gizem Timoçin Yiğman
Gökçe Kaan Ataç
Gonca Eldem
Gonca Erbaş
Gonca Koç
Gökçen Çoban
Gökhan Gökbalp
Gregoire Boulouis
Gülstan Bahat
Güner Sönmez
Güven Kahrıman
Gülnur Erdem
H. Gobara
H. Nursun Özcan
Hadi Sasani
Haitao Jiang
Hakan Artaş
Hamza Özer
Hans-Jonas Meyer
Harjus Birk
Hasan Önner
Hasan Yerli
Hatice Öztürkmen Akay
Hatice Tuba Sanal
Haytham Shebel
Hector Ferral
Hernán Chaves
Hilal Sipahi
Hongbin Han
Houchun Harry Hu
Hüseyin Tuğsan Ballı
Irene Bargellini
Irmak Durur-Subasi
Işıl Basara Akın
İlkay Çamlıdağ
İlkay S. İdilman
İlker Ercan
İsmail Yıldırım

İsmail Oran
Javad Heshmati
Jia Fan
Jiaywei Tsauo
Jin Ho Hwang
Jinoo Kim
Joe Leyon
Jonghyouk Yun
José Hugo Luz
Jose Luis del Cura
Juan Carlos Perez Lozada
Juan Luis Alcazar
Kaan Esen
Kader K. Oğuz
Kaichuang Ye
Kamil Karaali
Kate Elmore
Katrien Gieraerts
Kemal Bugra Memis
Keng-Wei Liang
Kenneth Ouriel
Kerbi Alejandro Guevara-Noriega
Kerim Aslan
Kiret Dhindsa
Kiyeol Lee
Kubilay Aydin
Laurens J. L. de Cocker
Lebriz Uslu Beşli
Li Fan
Liza Lindenberg
Lukas Beyer
M. Alper Selver
Maoqiang Wang
María de la Luz Escobar
Mark Ahlman
Martin Weng Chin Hng
Masaaki Takeuchi
Masafumi Kidoh
Masako Kataoka
Masashi Tamura
Matthew D. Givens
Matthew J. Roberts
Matthew Seager

Mecit Kantarcı
Mehmet Fatih İncelikli
Mehmet Öztürk
Mehmet Ruhi Onur
Mehmet Sedat Durmaz
Melahat Kul
Melis Baykara Ulusan
Meltem Gülsün Akpınar
Menna Allah Mahmoud
Merter Keçeli
Mi-Jung Lee
Michael J. Lee
Michail E. Klontzas
Minobu Kamo
Mirjan Nadrljanski
Muhammet Arslan
Murat Baykara
Murat Beyhan
Murat Dokdok
Murat Fani Bozkurt
Murat Kocaoğlu
Mustafa Mahmut Barış
Mutlu Gülbay
Naganathan B. S. Mani
Nail Bulakbaşı
Naim Ceylan
Naima Amin
Nakarın İnmutto
Nam Yeol Yim
Nefise Çağla Tarhan
Nermin Tunçbilek
Nesrin Gündüz
Nguyen Minh Duc
Nieun Seo
Nil Tokgöz
Nimer Adeeb
Nuno Adubeiro
Nuray Haliloğlu
Nuri Karabay
Nursel Yurttutan
Ogün Bülbül
Oğuz Dicle
Oğuz Lafcı



Okan Dilek
Onur Buğdaycı
Onur Taydaş
Osman Ahmed
Osman Melih Topçuoğlu
Osman Öcal
Ömer Kaya
Ömer Nas
Özgür Tosun
Özüm Yüksel Buğdaycı
Parisa Kaviani
Philip Chan
Pierleone Lucatelli
Po-Ming Chow
Polat Gökteş
Qi Wanyin
Qiang Huang
R. Rajagopal
Rafael De Freitas
Ravza Yılmaz
Reinhard Kopp
Riccardo de Robertis
Richard H. Marshall
Rifeng Jiang
Roberto Cannella
Rohini Gupta Ghasi
Ruimeng Yang
Salih Özgöçmen
Salvatore Gitto
Sandeep Kandregula
Sanjay Rastogi
Sato Yozo
Sebastiano Piana

Selçuk Akkaya
Selen Bayraktaroğlu
Selin Ardalı Düzgün
Sena Tuncer Azamat
Serap Gültekin
Serçin Özkök
Serdar Aslan
Serkan Arıbal
Serpil Ağlamış
Shankar Kumar
Sherief Abd-Elsalam
Shintaro Ichikawa
Shiro Miyayama
Shorav Bhatnagar
Sibel Kul
Simone Grassini
Sinan Altun
Sinan Balcı
Sinan Deniz
Sirish A. Kishore
Som Biswas
Sophie I. Mavrogeni
Sriram Jaganathan
Stavros Spiliopoulos
Suat Fitoz
Süreyya Burcu Görkem
Şebnem Karasu
Şebnem Örgüç
Şehnaz Evrimler
T. Katsumori
Takhesi Nakaura
Tamar C. Brandler
Te-Chang Wu

Theodoros Tokas
Thierry de Baere
Thomas Frauenfelder
Tiago Bilhim
Tomohiro Matsumoto
Tugba Akinci DAntonoli
Tuğçe Ağırlar Trabzonlu
Tumay Bekçi
Uday Patel
Uğur Toprak
Ulysses S. Torres
Ung Bae Jeon
Ural Koç
Utku Şenol
Üstün Aydınöz
Veysel Atilla Ayyıldız
Vinko Vidjak
Warren Clements
Wen-Tao Kong
William C. Torreggiani
Xuetong Tao
Yan Epelboym
Yasemin Kayadibi
Yeliz Pekçevik
Yılmaz Önal
Ying-Shi Sun
Yunus Emre Şentürk
Yusuf Baytar
Yusuke Matsui
Yuxin Hu
Zehra Pınar Koç
Zeynep Maraş Özdemir
Zhongmin Wang



Copyright@Author(s) - Available online at dirjournal.org.
Content of this journal is licensed under a Creative Commons
Attribution-NonCommercial 4.0 International License.

Letter from the Editor-in-Chief: A New Year for *Diagnostic and Interventional Radiology*

Mehmet Ruhi Onur
Editor-in-Chief

Hacettepe University Faculty of Medicine,
Department of Radiology, Ankara, Turkey

At the beginning of the new year, it is a pleasure for me to give you information about *Diagnostic and Interventional Radiology* and share my thoughts about the future with our new issue. We published six issues and 110 articles in *Diagnostic and Interventional Radiology* last year. The acceptance rate of manuscripts to be published was 17.87%. The majority of published articles were original articles (76.36%). Our average evaluation period for manuscripts sent to referees was 27 days, and the average number of referees who evaluated the manuscripts was 3. The average waiting time for online publication of accepted articles was 14 days. It is a pleasure for me to announce that *Diagnostic and Interventional Radiology* has shortened the online publication waiting time of the accepted manuscripts, as I promised in last year.¹ I am grateful to the authors, reviewers, editors, and all our readers who contributed to the performance of our journal last year.

I would like to inform you about the changes we have made to the *Journal Diagnostic and Interventional Radiology* over the past year. First of all, we have established the preprint policy of our journal and our policy regarding articles created with the help of artificial intelligence in accordance with the guidelines of current scientific journal policymakers and published them on the designated section of our journal's website (<https://www.dirjournal.org/Peer-Review-and-Ethic>). Second, we have added the option "Reject and resubmit", which, in our journal, is not one of the options offered to authors to decide on an article. Third, we have also added the title "Clinical Significance" as the last heading in the abstract of newly submitted manuscripts to *Diagnostic and Interventional Radiology*. Fourth, we used our social media accounts more actively, increased the number of our followers, and followed more social media accounts. As a result, *Diagnostic and Interventional Radiology* had more interaction in the social media area of radiology. Some of the goals we intend to achieve next year include supporting the articles published in *Diagnostic and Interventional Radiology* with podcasts and making the articles more visible and interesting with graphical abstracts and infographics.

Impact factors should be considered as important objective and quantitative data when evaluating the performance of scientific journals. The current impact factor and ranking values of our journal were announced by international databases in June 2023, taking into account the end of 2022 data, and are as follows: Journal Citation Index impact factor (JIF): 2.1, last five-year JIF: 2.5, JIF quartile: Q3, JIF rank: 90/135, JIF percentile: 33.7%, Scopus CiteScore: 3.9 (Table 1). When these values are examined, there has been a decrease in the impact factor in *Diagnostic and Interventional Radiology* after the pandemic, as in almost all radiology

Table 1. Journal citation and index ranking results of Diagnostic and Interventional Radiology between 2018 and 2022

JCR year	JIF	JCI	JIF rank	JCI rank	JIF quartile	JCI quartile
2018	1.464	0.60	97/129	93/182	Q4	Q3
2019	1.871	0.59	85/134	98/184	Q3	Q3
2020	2.630	0.65	77/133	83/186	Q3	Q2
2021	3.346	0.69	70/136	85/206	Q3	Q2
2022	2.1	0.60	90/135	104/203	Q3	Q3

JCR, Journal Citation Reports; JIF, Journal Impact Factor; JCI, Journal Citation Indicator (category of radiology, nuclear medicine and medical imaging)



Publication date: 08.01.2023
DOI: 10.4274/dir.2024.242663

You may cite this article as: Onur MR. Letter from the Editor-in-Chief: A New Year for Diagnostic and Interventional Radiology. *Diagn Interv Radiol*. 2024;30(1):1-2.

journals. In the future, we aim to increase our impact factor score by publishing scientific articles that reflect current developments in the field of radiology. For this reason, I invite all our readers and authors to contribute to *Diagnostic and Interventional Radiology* with their research articles, review articles, technical notes, pictorial essays, commentaries,

and letters to the editor. As in previous years, our journal will maintain its respected place among scientific journals published in the field of radiology and continue to contribute to the radiology literature by keeping the article evaluation period at reasonable levels and by accelerating online publication of accepted manuscripts. I wish a happy and

healthy new year to all *Diagnostic and Interventional Radiology* readers, authors, reviewers, and editors.

Reference

1. Onur MR. Letter from the New Editor-in-Chief. *Diagn Interv Radiol*. 2023;29(2):203-204. [\[CrossRef\]](#)



Manual and semi-automated computed tomography volumetry significantly overestimates the right liver lobe graft weight: a single-center study with adult living liver donors

Hakkı Çelik¹
 Hüseyin Odaman¹
 Canan Altay¹
 Tarkan Ünek²
 Mücahit Özbilgin²
 Tufan Egeli²
 Cihan Ağalar²
 İbrahim Kemal Astarçioğlu²
 Funda Barlık¹

¹Dokuz Eylül University Faculty of Medicine,
Department of Radiology, İzmir, Turkey

²Dokuz Eylül University Faculty of Medicine,
Department of General Surgery, İzmir, Turkey

Corresponding author: Hakkı Çelik

E-mail: dr.celik90@gmail.com

Received 20 November 2022; revision requested 30
December 2022; last revision received 03 March 2023;
accepted 12 April 2023.



Epub: 08.05.2023

Publication date: 08.01.2023

DOI: 10.4274/dir.2023.221903

PURPOSE

Preoperative evaluation of donor liver volume is indispensable in living donor liver transplantation to ensure sufficient residual liver and graft-to-recipient weight ratio. This study aims to evaluate the accuracy of two computed tomography (CT) volumetry programs, an interactive manual and a semi-automated one, in the preoperative estimation of the right lobe graft weight.

METHODS

One hundred and nine right liver lobe living donors between January 2008 and January 2020 were enrolled in this retrospective study. Two radiologists measured the liver graft volumes independently using manual and semi-automated CT volumetry, and the interaction time was recorded. Actual graft weight (AGW) measured intraoperatively served as the reference standard. The paired samples t-test was used to compare the estimated graft weight (EGW) and the AGW. Inter-user and inter-method agreements were assessed with Bland–Altman plots.

RESULTS

Both manual and semi-automated CT volumetry significantly overestimated the graft weight (EGW manual: 893 ± 155 mL vs. AGW manual: 787 ± 128 g, $P < 0.001$, EGW semi-automated: 879 ± 143 mL vs. AGW semi-automated, $P < 0.001$). The junior radiologist measured higher volumes than the senior radiologist with either method ($P < 0.001$). The Bland–Altman analysis revealed mean difference and standard deviation for inter-method agreement of 7 ± 48 cc for the senior radiologist, and 34 ± 54 cc for the junior radiologist. The mean difference and standard deviation for inter-method agreement was 63 ± 59 cc in manual volumetry and 22 ± 38 cc in semi-automated volumetry. The mean interaction time was 27.3 ± 14.2 min for manual volumetry and 6.8 ± 1.4 min for semi-automated volumetry ($P < 0.001$).

CONCLUSION

Both manual and semi-automated CT volumetry significantly overestimated the right liver graft weight, while semi-automated volumetry significantly reduced the interaction time.

KEYWORDS

Liver, living donor liver transplantation, manual CT volumetry, semi-automated CT volumetry, transplantation

owing to technical improvements and the standardization of the operation, living donor liver transplantation (LDLT) has become as effective as cadaveric liver transplantation. The right hepatic lobe, which includes segments V, VI, VII, and VIII according to the Couinaud classification, is routinely used for adult-to-adult LDLT.¹ An acceptable graft-to-recipient weight ratio (GRWR) and donor safety with sufficient remnant are the most important concerns in LDLT. Inadequate liver volume is among the most common causes of imaging-based donor exclusion.² A residual liver of at least 30% of the initial volume should be

You may cite this article as: Çelik H, Odaman H, Altay C, et al. Manual and semi-automated computed tomography volumetry significantly overestimates the right liver lobe graft weight: a single-center study with adult living liver donors. *Diagn Interv Radiol.* 2024;30(1):3-8.

left for the safety of the donor, while a minimum of 40% of standard liver volume (SLV) or GRWR ≥ 0.8 is required for the recipient.^{3,4} Hence, a precise preoperative volumetric evaluation of the living donor liver is of great importance.^{3,5} Although conventional manual segmentation is the gold standard, its use is limited due to the lengthy and tedious process.⁶ Automated and semi-automated software developed for liver volume calculation has made volumetric evaluation less time-consuming.⁷ Estimated graft volume (EGV) measured by computed tomography (CT) volumetry programs in many studies revealed admissible accuracy in estimating the actual graft weight (AGW), although they still need validation in clinical use.^{6,8-10} The aim of this study is to analyze the difference between the estimated and actual right liver lobe graft weights to determine the accuracy of manual and semi-automated CT volumetry programs used in the authors' center.

Methods

Preoperative donor evaluation

Living liver donor evaluation included medical and psychiatric/social assessment, biochemistry and serology tests, and imaging studies. Eligible donors underwent imaging studies, including chest X-ray, abdominal ultrasound, and magnetic resonance imaging, to exclude any unknown disease. Living donors needed to be first, second, third, or fourth-degree relatives of the recipient. Spouses and others were approved by the Dokuz Eylül University Non-invasive Research Ethics Committee (decision/protocol number: 2019/11-11; date of the approval: 24.04.2019), and informed written consent was obtained from all donors. Other eligibility criteria for living donors included an age of 18–65 years, negative serology for hepatitis

B and C, normal renal hepatic and hematological functions, and ABO blood group compatibility.

All living donors who underwent the right hemihepatectomy procedure between January 2008 and January 2020 were retrieved from the hospital database. Patients who underwent contrast-enhanced multi-phase CT angiography of the abdomen during donor candidacy selection for LDLT were included, and 11 patients without preoperative CT were excluded. Figure 1 summarizes the patient accrual.

Computed tomography imaging

CT examinations were performed with a 64-slice spiral CT (Philips Brilliance 64, Philips Healthcare, Netherlands) using a triple-phase CT protocol. Initially, a non-contrast scan was performed to exclude severe hepatic steatosis as it was associated with a poor graft

outcome.¹¹ The hepatic arterial and portal venous phases were assessed for the identification of anatomical variations that might be surgically significant, while all three phases were evaluated for the detection and characterization of hepatic lesions. One hundred mL of iodinated contrast medium (Omnipaque 350, GE Healthcare, Shanghai, China) was administered intravenously at a flow rate of 3–5 mL/sec using an automatic injector, followed by a bolus of 50 mL of saline at the same rate. CT scans included the area from the right dome of the diaphragm to the lower pole of the kidneys. Table 1 summarizes the CT triple-phase liver protocol.

Computed tomography volumetry

Volume measurements of the right liver lobes were performed by two radiologists (a senior radiologist with 13 years of experience and a junior radiologist with 3 years of experience).

Table 1. Computed tomography protocol used in potential living liver donors

Phase	Tube voltage (kV)	Tube current (mAs)	Rotation time (sec)	Pitch	Collimation	Slice thickness (mm)	Slice increment	Delay (sec)
Non-enhanced	120	220	0.75	1.178	64 × 0.625	2	1	NA
Hepatic arterial	120	250	0.5	0.91	64 × 0.625	0.9	0.45	15–25
Portal venous	120	250	0.75	1.178	64 × 0.625	2	1	40–60

NA, non-applicable.

Main points

- Both manual and semi-automated computed tomography (CT) volumetry significantly overestimated the right liver graft weight.
- Semi-automated volumetry provided a strong agreement with manual volumetry with experienced users while significantly shortening the user time.
- Less experienced users tended to measure higher graft volumes with both CT volumetry methods.
- A higher graft-to-recipient weight can be applied to prevent small-for-size syndrome when evaluating the liver graft with CT volumetry.

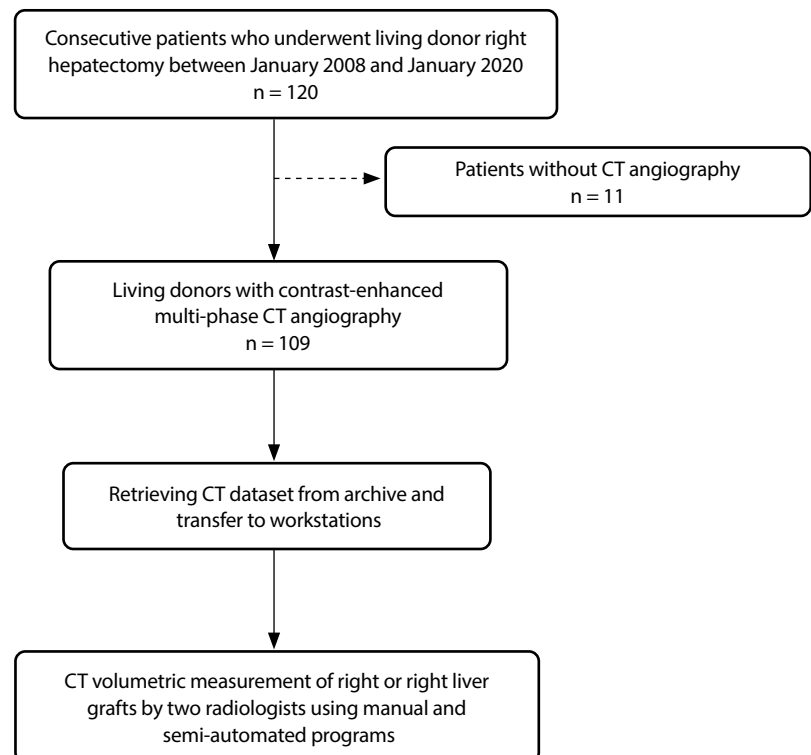


Figure 1. Flowchart summarizing patient accrual. CT, computed tomography.

rience in CT volumetry of the liver) using axial portal venous phase images. The archived CT data set was transferred to the relevant workstations for CT volumetry analysis.

First, the radiologists measured the right liver lobe volumes using the interactive manual program (Advanced Vascular Analysis, Philips Healthcare). Users selected one of three different volume sizes (low, medium, and high; 400, 1.500, and 4.000 voxels, respectively), then moved the pointer to paint the entire liver area on the transverse CT image. The users painted every 5–20 slices, depending on the parenchymal homogeneity and the volume size chosen. When the users painted an area outside the liver contours, that part could be removed using a spheric eraser tool with three diameter options: small, medium, and large, 5, 10, and 30 voxels, respectively. Consistent with the current standard approach,¹² volumetric measurements included intrahepatic vessels but excluded large vessels. A transection line was drawn along the middle hepatic vein (MHV) to determine the right and left liver lobe volumes. To measure the volume of the right liver lobe, users removed painted parenchyma to the left of the MHV and the MHV itself with the eraser tool. This removal could also be done on the three-dimensional volumetric image. The resulting volume of the right liver lobe was displayed in cubic centimeters (cc) (Figure 2).

The semi-automated software (CT Liver Analysis, Philips Healthcare) used in this study was developed for liver segmentation only. As a first step, the liver was identified on axial CT images and the total liver volume was automatically determined. Liver borders could be corrected manually if necessary. The vessels were then automatically detected and grouped as portal, hepatic, or unclassified vessels and included in the total liver volume. The users delineated the transection plane by setting two points (the vena cava inferior and the MHV) to measure the volumes of the right and left liver lobes semi-automatically (Figure 3).

The time needed to complete each CT volumetric measurement was recorded for each user. The time required to load the digital imaging and communications in medicine images on the workstation was not included in the user time.

Intraoperative data acquisition

Soon after the resection, the graft was flushed with histidine-tryptophan-ketoglutarate (HTK) solution (Dr. Franz Köhler Che-

mie GmbH, Alsbach-Hähnlein, Germany) containing 2.000 units of unfractionated heparin through the open ends of the main branches of the main hepatic artery and the portal vein, until the outflow from the hepatic veins was completely cleared. After flushing, the graft weight was measured using an electronic laboratory scale on the back table. The intraoperative graft weights were also considered actual graft volumes, as the mean density of the healthy liver tissue was assumed to be 1.00 g/mL.¹³

Statistical analysis

Descriptive analysis of the quantitative data was expressed as means and standard

deviations. The paired samples t-test was used to compare the mean of the graft volumes calculated by the two radiologists using manual and semi-automated CT volumetry programs. A Bland–Altman analysis was used to evaluate the level of agreement between the observers and between the CT volumetry programs. The preoperatively calculated right lobe graft volume was converted to a graft weight with a conversion ratio of one (1 mL = 1 g).¹³ A *P* value of < 0.05 was considered significant. Statistical analysis was performed with SPSS version 18.0 (SPSS Inc. Released 2009. PASW Statistics for Windows, version 18.0. Chicago: SPSS Inc.) and

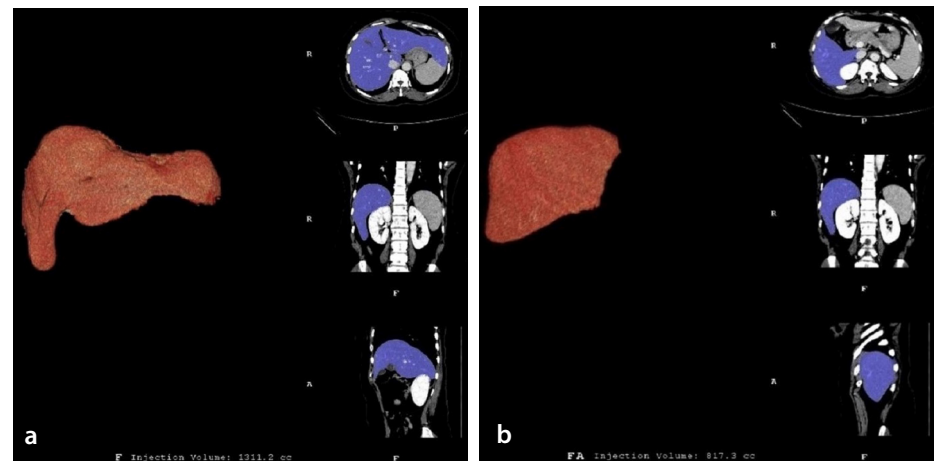


Figure 2. Interactive manual computed tomography (CT) volumetry (Volume Tracing in Advanced Vessel Analysis, Philips Healthcare). Three-dimensional rendered images representing the painted liver parenchyma on CT images: whole liver (a) and right liver lobe (b).

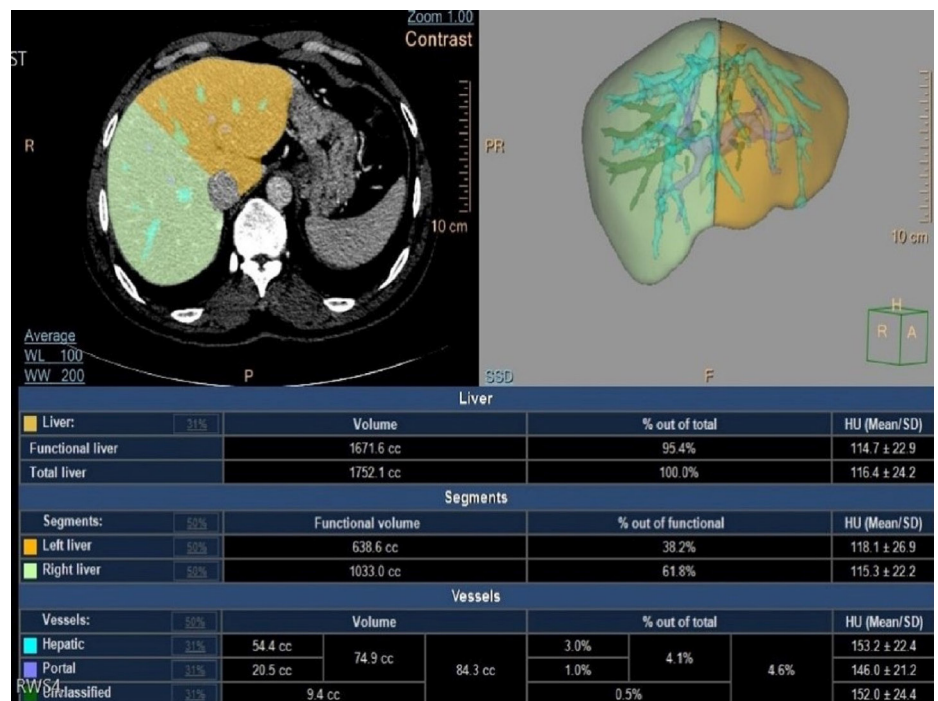


Figure 3. Semi-automated computed tomography (CT) volumetry (CT Liver Analysis, Philips Healthcare). The liver was automatically identified on CT images, and total liver volume was obtained. The volumes of each liver lobe were calculated semi-automatically after placing the landmark points on the middle hepatic vein and the inferior vena cava.

Results

Of the 109 liver donors included in this study, 37/109 (34%) were female, and 72/109 (66%) were male, with a mean age of 31.4 ± 11.3 years (range 18–50). Table 2 presents the baseline demographics of the living liver donors.

Both manual and semi-automated CT volumetry significantly overestimated the AGWs ($P < 0.001$ for both methods). There was no significant difference between the interactive manual and the semi-automated volumetric measurements of the senior radiologist, however, the junior radiologist measured higher volumes using the manual program ($P < 0.001$). The Bland–Altman graphs showed that the 95% limits of agreement between the CT volumetry programs ranged from -79 to 65 cc with a mean difference of 7 ± 48 cc for the senior radiologist and -48 to $+116$ cc with a mean difference of 34 ± 54 cc for the junior radiologist (Figure 4). The junior radiologist calculated significantly higher volumes with both CT volumetry methods than the senior radiologist ($P < 0.001$ for both methods). The Bland–Altman plots revealed that the inter-observer variation tended to be greater in interactive manual volumetry. The 95% limits of agreement between the observers ranged from -54 to 179 cc with a mean difference of 63 ± 59 cc in manual volumetry and -20 to 64 cc with a mean difference of 22 ± 38 cc in semi-automated volumetry (Figure 5). The mean difference between the AGW and the EGV was 13.5% in the manual program and 11.7% in the semi-automated program. Table 3 summarizes the mean values of all measured volumes and the AGWs.

The required mean time to determine the volume of the right liver lobe with the manual method was 27.3 ± 14.2 min/case and 6.8 ± 1.4 min/case for the semi-automated volumetry ($P < 0.001$). There was no significant difference between the user times in both CT volumetry programs.

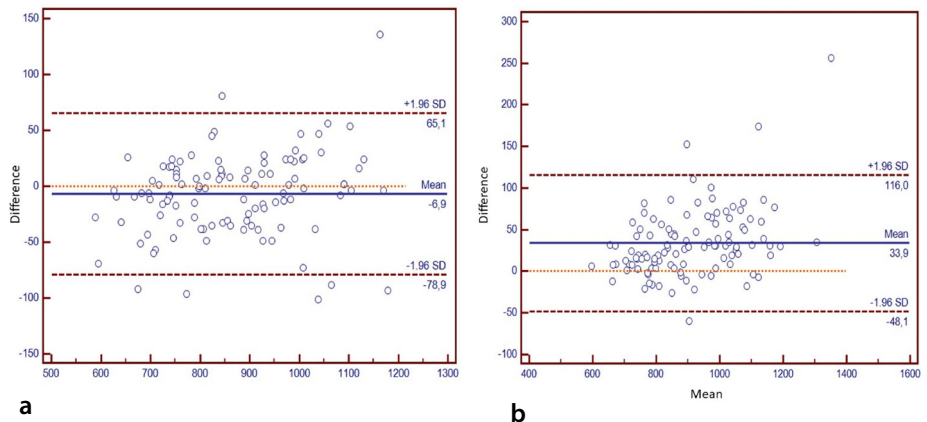


Figure 4. The Bland–Altman plots of the volume difference between the semi-automated software and the manual volumetry: senior radiologist (a) and junior radiologist (b). The mean difference was demonstrated with a solid line and 95% limits of agreement with dashed lines.

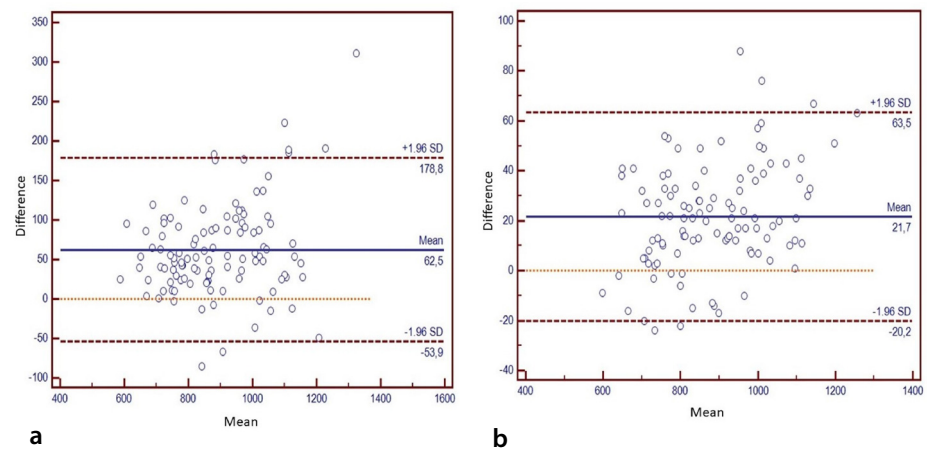


Figure 5. The Bland–Altman plots of the volume difference between the measurements of the junior radiologist and the senior radiologist: manual volumetry (a) and semi-automated volumetry (b). The mean difference was demonstrated with a solid line and 95% limits of agreement with dashed lines.

Table 2. Baseline demographics of living liver donors

Age (year)	31.4 ± 11.3
Sex	
Male	72 (66%)
Female	37 (34%)
Body mass index (kg/m²)	
Mean \pm standard deviation	26.7 ± 8.9
Smoking history*	26 (24%)

*Both current and former smokers.

Table 3. Liver graft volume measurements (mean \pm standard deviation)

	Junior radiologist	Senior radiologist	Mean value of two observers
Manual CT volumetry	924 ± 163 cc	861 ± 147 cc	893 ± 155 cc
Semi-automated CT volumetry	890 ± 146 cc	868 ± 139 cc	879 ± 143 cc
Actual graft weight			787 ± 128 gr

CT, computed tomography.

Discussion

Automated and interactive CT volumetry programs provide an acceptable measurement and decrease the time needed for volumetric evaluation. Nevertheless, these volumetry programs tend to reveal more discrepancies than conventional segmentation methods.^{6,14} Considering that optimal GRWR ≥ 0.8 is essential for a good prognosis in LDLT, an overestimated graft weight may create a risk of the small-for-size syndrome, particularly in cases with borderline GRWR.

The present study showed that right liver graft volumes measured using both interactive manual and semi-automated CT volumetry were significantly higher than the AGWs. Lemke et al.¹⁵ concluded that intraoperative graft weight could be accurately predicted by reducing the preoperatively measured graft weight with a rectification factor of 0.75. Niehues et al.¹⁶ found a 13% overestimation of *in vivo* volumes in an animal model. Another study revealed a 20.5% overestimation of the right liver lobe volumes using a non-commercial self-developed image post-processing software.¹⁰

There are various factors that may explain the overestimation of graft volumes by CT volumetry, although intraoperative blood loss is considered the main reason.¹⁷ Blood within the intrahepatic vasculature during imaging largely explains the overestimation of the graft volume compared to the actual blood-free liver graft measured after resection. Preoperative CT examination represents the “*in situ*” state in which the liver is exposed to physiological perfusion. However, the condition of the graft after resection during liver transplantation is not physiological. Fluids, such as blood, bile, and lymph, flow out of the vascular structures that have not yet been anastomosed with the recipient, and accordingly, the liver graft shrinks.^{10,18} As a consequence, a fair amount of intraoperative volume loss is inevitable in the graft after resection.¹⁰ In the present study, the right liver lobe grafts resected from the living donors were weighed in *ex vivo* conditions without blood after flushing with HTK solution. In a study, the preoperatively measured graft volume using CT volumetry was approximately 20% greater than the intraoperatively measured volume of the drained graft, while this difference was only 4% for the blood-filled graft.¹⁸ Hwang et al.¹⁷ revealed a rectification factor of 1.22 between the blood-free graft weight and the *in vivo* graft volume. Lemke

et al.¹⁵ revealed that the AGW could be calculated with sufficient accuracy by reducing the preoperatively estimated volume of the right hepatic lobe by a correction factor of 0.75. However, using a specified rectification factor may cause erroneous calculations as there may be inter-individual variations.

Transplant centers generally accept the mean density of healthy liver tissue as 1.00 g/mL and therefore assume that 1 g of liver tissue equals 1 cc of the liver in preoperative volumetry measurements.^{15,19} Based on this fact, it can be assumed that the volume of the right hepatic lobe is equal to the respective weight. In this study, the conversion factor between the preoperatively measured graft volumes in milliliters and the graft weight in grams was also accepted as “1”. However, Lemke et al.¹⁰ found that the physical density of the right liver lobe grafts was 1.1172 ± 0.1015 g/mL, ranging between 1.00 and 1.33 g/mL. Therefore, it should be kept in mind that there may be a negligible level of inter-individual differences in the physical densities of transplanted liver lobes.

A virtual resection line that is misidentified on CT images and does not match the actual surgical resection line may cause a mismatch between the EGV and the AGW.²⁰ Intraoperative resection planes may differ from the lines separating the Couinaud segments. The Couinaud classification divides the liver into eight segments in straight lines along the hepatic and portal veins, but these vessels are usually not straight. Intraoperative dehydration of the graft by the hyperosmolar HTK solution may be considered as another factor that may contribute to the overestimation of the preoperative graft volume.²¹

Accurate and rapid calculation of the liver volumes to be resected and left in the donor in the LDLT is extremely important in transplantation clinics. In the authors’ study, both the interactive manual and the semi-automated program significantly reduced the time required for volumetric evaluation compared with conventional segmentation methods, while the semi-automated software was even four times faster than the interactive manual method. In the current study, CT volumetric measurements were performed by two radiologists with different levels of experience. The authors found that the less experienced observer measured higher graft volumes using both methods, resulting in higher differences between the AGW and the EGV. However, the inter-observer difference was less in the semi-automated

volumetry compared with the manual volumetry. Similarly, in another study, the less experienced users measured higher volumes in both the manual and the semi-automated volumetry, and the inter-observer difference was less in the semi-automated volumetry.²² The fact that the experienced observers measured the liver graft volumes more accurately shows that there is still a need for new volumetry software that offers better inter-user agreement. Volume measurement should be performed by specialists who can accurately determine the hepatectomy plane to reduce potential errors and maximize the accuracy of volumetric estimates.

Excluding intrahepatic vascular volume can improve the performance of volumetry programs.²³ Additionally, by using equations developed from the data obtained in previous CT volumetry studies, anticipated intraoperative graft weight can be determined more accurately.^{23,24} In a study, the following formula was developed to calculate the SLV by measuring the thoracoabdominal circumference (TAC) of the body at the level of the liver dome, especially in patients with potentially small grafts: $SLV = (TAC \times 3.58) - (age \times 3.98) - (sex \times 109.74) - 934.59$.²³

This study has some limitations. In this study, the water displacement method could not be used for intraoperative volume measurement of the liver graft. Although intrahepatic vascular volume can be obtained in the semi-automated program, it was not excluded from the graft volumes to avoid a methodological difference between the volumetry programs. Intra-observer agreement was not investigated to assess the repeatability of these programs. Last, the semi-automated software has some extra features that were not tested in the current study but could be used in other future studies, such as preprocedural planning of radiofrequency ablation.

In conclusion, the authors’ study suggests that both manual and semi-automated CT volumetry significantly overestimates the AGW. Semi-automated CT volumetry significantly shortens the user time and provides strong agreement with the manual program if the user is sufficiently experienced. A higher GRWR can be applied to prevent small-for-size syndrome when evaluating the liver graft with these CT volumetry programs.

Conflict of interest disclosure

The authors declared no conflicts of interest.

References

1. Fan ST, Lo CM, Liu CL, Yong BH, Chan JK, Ng IO. Safety of donors in live donor liver transplantation using right lobe grafts. *Arch Surg*. 2000;135(3):336-340. [\[CrossRef\]](#)
2. Mussin N, Sumo M, Lee KW, et al. The correlation between preoperative volumetry and real graft weight: comparison of two volumetry programs. *Ann Surg Treat Res*. 2017;92(4):214-220. [\[CrossRef\]](#)
3. Hiroshige S, Shimada M, Harada N, et al. Accurate preoperative estimation of liver-graft volumetry using three-dimensional computed tomography. *Transplantation*. 2003;75(9):1561-1564. [\[CrossRef\]](#)
4. Lo CM, Fan ST, Liu CL, et al. Adult-to-adult living donor liver transplantation using extended right lobe grafts. *Ann Surg*. 1997;226(3):261-269; discussion 269-270. [\[CrossRef\]](#)
5. Radtke A, Sotiropoulos GC, Nadalin S, et al. Preoperative volume prediction in adult living donor liver transplantation: how much can we rely on it? *Am J Transplant*. 2007;7(3):672-679. [\[CrossRef\]](#)
6. Nakayama Y, Li Q, Katsuragawa S, et al. Automated hepatic volumetry for living related liver transplantation at multisection CT. *Radiology*. 2006;240(3):743-748. [\[CrossRef\]](#)
7. Suzuki K, Epstein ML, Kohlbrenner R, et al. Quantitative radiology: automated CT liver volumetry compared with interactive volumetry and manual volumetry. *AJR Am J Roentgenol*. 2011;197(4):W706-W712. [\[CrossRef\]](#)
8. Luciani A, Rusko L, Baranes L, et al. Automated liver volumetry in orthotopic liver transplantation using multiphase acquisitions on MDCT. *AJR Am J Roentgenol*. 2012;198(6):W568-W574. [\[CrossRef\]](#)
9. Gondolesi GE, Yoshizumi T, Bodian C, et al. Accurate method for clinical assessment of right lobe liver weight in adult living-related liver transplant. *Transplant Proc*. 2004;36(5):1429-1433. [\[CrossRef\]](#)
10. Lemke AJ, Brinkmann MJ, Schott T, et al. Living donor right liver lobes: preoperative CT volumetric measurement for calculation of intraoperative weight and volume. *Radiology*. 2006;240(3):736-742. [\[CrossRef\]](#)
11. Chu MJ, Dare AJ, Phillips AR, Bartlett AS. Donor hepatic steatosis and outcome after liver transplantation: a systematic review. *J Gastrointest Surg*. 2015;19(9):1713-1724. [\[CrossRef\]](#)
12. Hermoye L, Laamari-Azjal I, Cao Z, et al. Liver segmentation in living liver transplant donors: comparison of semiautomatic and manual methods. *Radiology*. 2005;234(1):171-178. [\[CrossRef\]](#)
13. Lemke AJ, Hosten N, Neumann K, et al. CT-volumetrie der leber vor transplantation [CT volumetry of the liver before transplantation]. *Rofo*. 1997;166(1):18-23. [\[CrossRef\]](#)
14. Gondolesi GE, Yoshizumi T, Bodian C, et al. Accurate method for clinical assessment of right lobe liver weight in adult living-related liver transplant. *Transplant Proc*. 2004;36(5):1429-1433. [\[CrossRef\]](#)
15. Lemke AJ, Brinkmann MJ, Pascher A, et al. Voraussagegenauigkeit der präoperativen CT-gestützten Gewichtsbestimmung des rechten Leberlappens bezüglich des intraoperativen Transplantatgewichts bei Leberlappen-Lebendspendern [Accuracy of the CT-estimated weight of the right hepatic lobe prior to living related liver donation (LRLD) for predicting the intraoperatively measured weight of the graft]. *Rofo*. 2003;175(9):1232-1238. [\[CrossRef\]](#)
16. Niehues SM, Unger JK, Malinowski M, Neymeyer J, Hamm B, Stockmann M. Liver volume measurement: reason of the difference between in vivo CT-volumetry and intraoperative ex vivo determination and how to cope it. *Eur J Med Res*. 2010;15(8):345-350. [\[CrossRef\]](#)
17. Hwang S, Lee SG, Kim KH, et al. Correlation of blood-free graft weight and volumetric graft volume by an analysis of blood content in living donor liver grafts. *Transplant Proc*. 2002;34(8):3293-3294. [\[CrossRef\]](#)
18. Frericks BB, Kiene T, Stamm G, Shin H, Galanski M. CT-basierte Lebervolumetrie im Tiermodell: Bedeutung für die klinische volumetrie im Rahmen der Leberlebendspende [CT-based liver volumetry in a porcine model: impact on clinical volumetry prior to living donated liver transplantation]. *Rofo*. 2004;176(2):252-257. [\[CrossRef\]](#)
19. Selle D, Preim B, Schenk A, Peitgen HO. Analysis of vasculature for liver surgical planning. *IEEE Trans Med Imaging*. 2002;21(11):1344-1357. [\[CrossRef\]](#)
20. Kwon HJ, Kim KW, Kim B, et al. Resection plane-dependent error in computed tomography volumetry of the right hepatic lobe in living liver donors. *Clin Mol Hepatol*. 2018;24(1):54-60. [\[CrossRef\]](#)
21. Mohapatra N, Gurumoorthy Subramanya Bharathy K, Kumar Sinha P, Vasantrao Sasturkar S, Patidar Y, Pamecha V. Three-dimensional volumetric assessment of graft volume in living donor liver transplantation: does it minimise errors of estimation? *J Clin Exp Hepatol*. 2020;10(1):1-8. [\[CrossRef\]](#)
22. Noschinski LE, Maiwald B, Voigt P, Wiltberger G, Kahn T, Stumpp P. Validating new software for semiautomated liver volumetry—better than manual measurement? *Rofo*. 2015;187(9):788-794. [\[CrossRef\]](#)
23. Shaw BI, Burdine LJ, Braun HJ, Ascher NL, Roberts JP. A Formula to calculate standard liver volume using thoracoabdominal circumference. *Transplant Direct*. 2017;3(12):e225. [\[CrossRef\]](#)
24. Yang X, Chu CW, Yang JD, et al. Estimation of right-lobe graft weight from computed tomographic volumetry for living donor liver transplantation. *Transplant Proc*. 2017;49(2):303-308. [\[CrossRef\]](#)



Prediction of osteoporosis using MRI and CT scans with unimodal and multimodal deep-learning models

Yasemin Küçükçiloğlu^{1,2}

Boran Şekeroğlu³

Terin Adalı^{2,4,5}

Niyazi Şentürk^{2,4}

¹Near East University Faculty of Medicine,
Department of Radiology, Nicosia, Cyprus

²Near East University, Center of Excellence, Tissue
Engineering and Biomaterials Research Center,
Nicosia, Cyprus

³Near East University, Applied Artificial Intelligence
Research Center, Nicosia, Cyprus

⁴Near East University Faculty of Engineering,
Department of Biomedical Engineering, Nicosia,
Cyprus

⁵Sabancı University, Nanotechnology Research and
Application Center, İstanbul, Turkey

PURPOSE

Osteoporosis is the systematic degeneration of the human skeleton, with consequences ranging from a reduced quality of life to mortality. Therefore, the prediction of osteoporosis reduces risks and supports patients in taking precautions. Deep-learning and specific models achieve highly accurate results using different imaging modalities. The primary purpose of this research was to develop unimodal and multimodal deep-learning-based diagnostic models to predict bone mineral loss of the lumbar vertebrae using magnetic resonance (MR) and computed tomography (CT) imaging.

METHODS

Patients who received both lumbar dual-energy X-ray absorptiometry (DEXA) and MRI (n = 120) or CT (n = 100) examinations were included in this study. Unimodal and multimodal convolutional neural networks (CNNs) with dual blocks were proposed to predict osteoporosis using lumbar vertebrae MR and CT examinations in separate and combined datasets. Bone mineral density values obtained by DEXA were used as reference data. The proposed models were compared with a CNN model and six benchmark pre-trained deep-learning models.

RESULTS

The proposed unimodal model obtained 96.54%, 98.84%, and 96.76% balanced accuracy for MRI, CT, and combined datasets, respectively, while the multimodal model achieved 98.90% balanced accuracy in 5-fold cross-validation experiments. Furthermore, the models obtained 95.68%–97.91% accuracy with a hold-out validation dataset. In addition, comparative experiments demonstrated that the proposed models yielded superior results by providing more effective feature extraction in dual blocks to predict osteoporosis.

CONCLUSION

This study demonstrated that osteoporosis was accurately predicted by the proposed models using both MR and CT images, and a multimodal approach improved the prediction of osteoporosis. With further research involving prospective studies with a larger number of patients, there may be an opportunity to implement these technologies into clinical practice.

KEYWORDS

Osteoporosis, dual-energy X-ray absorptiometry, lumbar vertebrae, deep learning, multimodal CNN

Corresponding author: Boran Şekeroğlu

E-mail: boran.sekeroglu@neu.edu.tr

Received 19 January 2023; revision requested 12
February 2023; last revision received 20 April 2023;
accepted 06 May 2023.



Epub: 13.06.2023

Publication date: 08.01.2023

DOI: 10.4274/dir.2023.232116

Osteoporosis is a systemic skeletal degenerative disease characterized by the deterioration of the microstructure of the bone tissue and low bone mineral density (BMD), with a consequential increase in bone fragility and susceptibility to fracture.¹ The major complication of osteoporosis is fragility fractures that lead to morbidity, mortality, and decreased quality of life. The prevalence of the disease is rising as the proportion of the elderly population increases.² It was expected that by 2020, in the United States, approximately 12.3 million individuals older than 50 would have osteoporosis.³ Tuzun et al.⁴ showed that

the prevalence of osteoporosis among Turkish citizens increases with age, with 3%-4% affected at the age of 50 and more than 30% affected by the age of 80. These numbers are predicted to have increased by 64% (870,000 men and 1,841,000 women) in 2035.⁴

Accordingly, screening for osteoporosis is clinically advisable for fracture prevention. There are several imaging techniques, including radiography, ultrasonography, low-dose computed tomography (CT), and dual-energy X-ray absorptiometry (DEXA), which, with its negligible dose of radiation, is considered the gold standard imaging technique for the diagnosis of osteoporosis.⁵ Recent research concluded that lumbar spine magnetic resonance imaging (MRI) and CT used for lower-back pain could be used to predict osteoporosis.⁶ MRI provide accurate information on tissue structure, and CT images allow researchers to observe the anatomical structure of the vertebrae.⁷ However, the advantages of using artificial intelligence (AI) in diagnosing osteoporosis have been rarely studied.⁸

AI techniques have gained significant ground in the field of computer vision, particularly in medical applications.^{9,10} As a result, the use of AI has become common in the public health sector and now significantly impacts every aspect of early prediction and

primary care.^{11,12} Since deep-learning models can detect, learn, and predict indistinct and fuzzy patterns, they provide fast, effective, and reliable outcomes for the considered problem domain.¹³ Furthermore, the synthesis and analysis of different images and data types have enabled AI and deep learning to make remarkable improvements in complex data environments in which the human capacity to identify high-dimensional relationships is limited in terms of processing a higher number of data and computational time.¹⁴ However, the modification of recent deep-learning models and the proposal of particular architectures by considering the basic characteristics of specific applications has led to the achievement of more accurate results.

Osteoporosis prediction, or identifying the presence of osteoporosis, is one of the primary aims of diagnostic imaging. Several types of AI research have been performed for this purpose,¹⁵ and different imaging modalities and metadata have been considered in these studies. Xu et al.¹⁶ considered micro-CT images for osteoporosis diagnosis. The classification followed several image pre-processing steps by support vector machine and k-nearest-neighbor algorithms. Lim et al.⁸ performed machine-learning analyses using DEXA features and abdominopelvic CT to predict osteoporosis prevalence. To classify osteoporosis, Yamamoto et al.¹⁷ trained five pre-trained convolutional neural network (CNN) models using hip radiographs and patient clinical covariates. Similarly, Jang et al.¹⁸ proposed a deep neural network to predict osteoporosis using hip radiography images. Liu et al.¹⁹ proposed a three-layered hierarchical model to distinguish osteoporosis and normal BMD using patients' clinical data. In that study, a logistic regression model achieved superior results by achieving receiver operating characteristics (ROC) area under the curve (AUC) scores of 0.818–0.962 for three layers.

All the abovementioned studies achieved reasonable and promising results. However, the use of MR and CT images in predicting osteoporosis with deep learning requires more investigation. In addition, the impact of the use of multimodal deep-learning models in diagnosing osteoporosis has not been studied adequately.

Based on this information, the current study aimed to accurately distinguish osteoporosis and normal BMD using different imaging modalities, including CT and MRI,

to support and assist radiologists in clinical diagnoses. For this purpose, we considered two primary datasets, including lumbar CT and MRIs of patients who received both lumbar DEXA and MRI examinations or CT scans. We proposed a dual-block CNN-based model with different filter sizes and pooling operations and performed several experiments on the considered datasets to achieve a high-accuracy diagnosis of osteoporosis. The efficacy of different modalities on osteoporosis prediction was analyzed by considering CT and MRI scans in separate, combined, and multimodal implementations in unimodal and multimodal experiments. The proposed unimodal and multimodal CNN models were compared with six pre-trained and traditional CNN models.

Methods

Dataset and study population

Study group

Lumbar DEXA examinations of 1,800 patients obtained between January 2018 and March 2021 from the Near East University Hospital's Radiology Department were evaluated retrospectively. A total of 1,554 patients with T-scores higher than -1 at levels L1–L4 and patients with severe scoliosis or lumbar deformity, spondyloarthritis, inflammatory diseases (tuberculosis, brucella, ankylosing spondylosis, etc.), tumoral lesions (leukemia, lymphoma, multiple myeloma, vertebral metastasis, etc.), or a history of lumbar stabilization surgery were excluded from the study. Spondyloarthritis can cause sclerosis at the vertebral plateau and osteophyte formations, which are bony spurs with high density. These lesions can cause higher BMD calculations and errors at DEXA examinations. More accurate data was aimed by excluding this patient group. A total of 246 patients with T-scores lower than -1 at levels L1–L4 were re-evaluated for the presence of recorded lumbar MRI or CT images obtained within six months.

The MRI study group consisted of 62 patients (2 males, 60 females), with ages ranging between 44 and 86 years [mean: 65, standard deviation (SD): ± 9.9]. A total of 535 T1-weighted sagittal MRI of these patients were included in the study. The study group for CT consisted of 50 patients (3 males, 47 females), with ages ranging between 46 and 83 years (mean: 68, SD: ± 8.7); 562 sagittal reformatted CT images of these patients were used in the study.

Main points

- This study considered two primary datasets that included magnetic resonance image (MRI) and computed tomography (CT) images and proposed specifically designed convolutional neural network (CNN) models for osteoporosis prediction. The proposed unimodal and multimodal CNN models included two parallelized blocks to extract and combine the loss of individual blocks based on the characteristics of lumbar scan images.
- The proposed unimodal CNN model outperformed the other models in predicting osteoporosis using MRI and CT images separately and obtained 96.54% and 98.84% balanced accuracy, respectively. Superior results were obtained using the proposed multimodal CNN model, and 98.90% balanced accuracy was achieved. Furthermore, a hold-out test set was used to test the models, and the proposed models outperformed the other considered models. Similarly, a superior result was obtained by the multimodal model (97.91%).
- The obtained results showed that the developed deep-learning models could produce accurate results in osteoporosis prediction using different imaging techniques.

Control group

Lumbar MRI and lumbar CT images of patients, aged 18 to 44, obtained between January 2018 and March 2021 in Near East University Hospital's Radiology Department were evaluated retrospectively. Postmenopausal female patients and male patients over 50 years of age, patients with severe scoliosis or deformity, spondyloarthritis, inflammatory diseases (tuberculosis, brucella, ankylosing spondylitis, etc.), tumoral lesions (leukemia, lymphoma, multiple myeloma, vertebral metastasis, etc.), or a history of lumbar stabilization surgery, glucocorticoid steroid use, or any disease that may cause secondary osteoporosis were excluded from the study. Furthermore, 526 sagittal T1-weighted MRI of 58 patients (26 males, 32 females, aged 20 to 44 years (mean: 32, SD: ± 8.3) and 534 sagittal reformatted CT images of 50 patients (30 males, 20 females, aged 18 to 44 years (mean: 28, SD: ± 7.6) were used in the study.

The BMDs of the patients were evaluated by DEXA (Lunar DPX, GE, Madison, USA), and MRI examinations were performed using a 1.5-T system (Magnetom Aera, Siemens Healthcare, Erlangen, Germany). The standard lumbar MRI protocol at Near East University Hospital's Radiology Department included sagittal T1- and T2-weighted sequences, sagittal short-tau inversion recovery sequences, and axial T2-weighted sequences. Sagittal T1-weighted images (repetition time: 400 ms, echo time: 7.7 ms, slice thickness: 3.5 mm, slice gap: 0.7 mm, matrix: 256×320 , field of view: 30 cm) were used in this study. The CT examinations were performed using a 256-detector multislice CT scanner (Somatom Definition Flash, Siemens Healthcare, Erlangen, Germany). Figures 1 and 2 present the data selection procedure of this study for MRI and CT examinations, respectively.

Written informed consent was obtained from all individual participants included in the study.

This study was performed in line with the principles of the Declaration of Helsinki. Approval was granted by the Ethics Committee of Near East University (30.09.2021/YDU/2021/95-1394).

Test set

It is not difficult to distinguish a young person's spine from that of an elderly person. To demonstrate that the dataset was not biased, a hold-out test set was extracted from

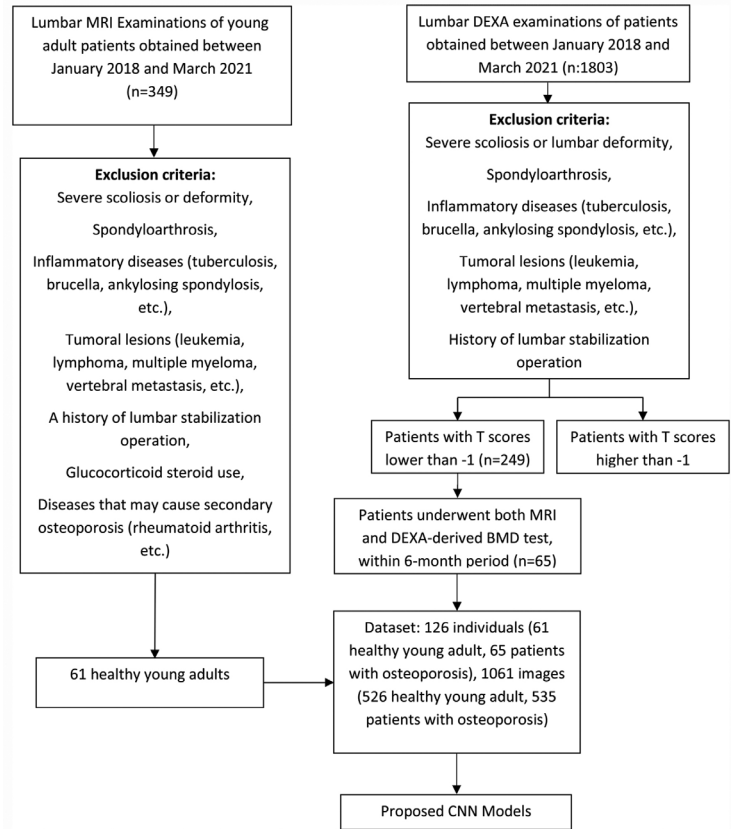


Figure 1. Data selection procedure of the study for magnetic resonance imaging examinations. MRI, magnetic resonance imaging; DEXA, dual-energy X-ray absorptiometry; CNN, convolutional neural network; BMD, bone mineral density.

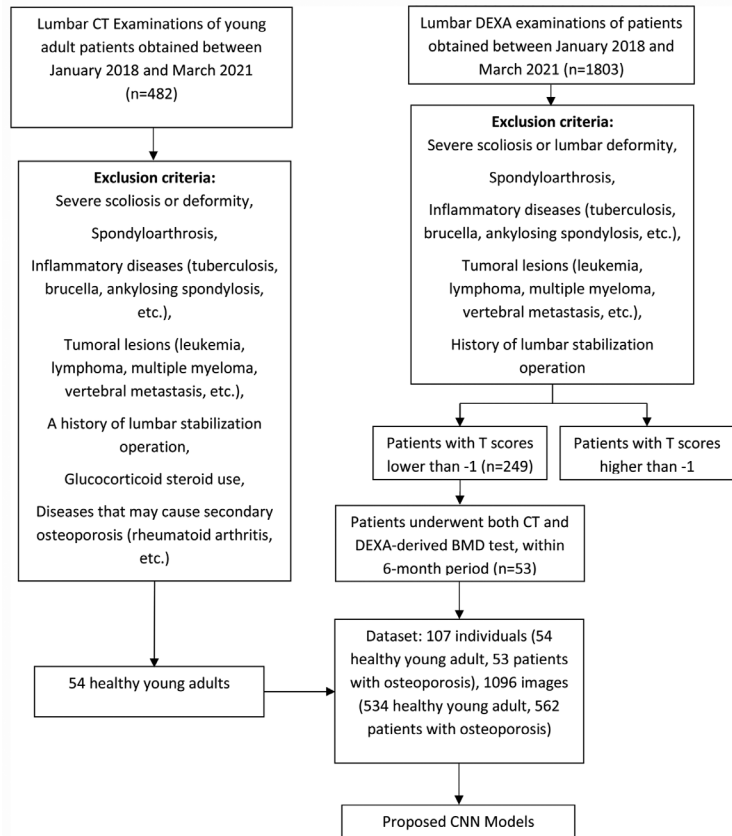


Figure 2. Data selection procedure of the study for computed tomography examinations. CT, computed tomography; DEXA, dual-energy X-ray absorptiometry; CNN, convolutional neural network; BMD, bone mineral density.

the dataset of the CT and MRI scans of the control and patient groups. Close age ranges were selected for both groups to observe the diagnostic abilities of all models and to check possible bias using the minimized age differences between the control and patient groups.

The control group of the set included 24 MRI (age: 39–44 years) and 34 CT scans (age: 40–44 years). The patient group of the set included 24 MRI (age: 44–46 years) and 34 CT scans (age: 46–48 years). Therefore, a total of 116 images were obtained (48 MRI/68 CT, 58 controls/58 patients).

The hold-out test set was not included in any part of the models' training, and additional experiments were performed. All models were trained using the rest of the images in the dataset, and the hold-out test set was used only for testing.

The distributional differences between the training and testing sets were analyzed in the patient and control groups. The skewness of distribution between the training and test groups is presented in Table 1. The skewness-of-distribution results showed that the training and test sets of the CT images were moderately skewed, while the MRI training and testing data had a fairly symmetrical distribution. These results suggest a minimal influence on the generalizability of our models.

Proposed model

A CNN is a deep-learning method that includes feature extraction and classification phases. Typical convolution layers consist of convolution operations using a number of predefined-sized kernels, an activation layer, and a pooling layer. In the classification phase, the extracted features are flattened and fed to the fully-connected layers for classification.

A 3×3 filter size effectively extracts low-level features of images with minimal noise; however, the connectivity of the features that provide significant distinguishable patterns according to the image characteristics might be lost by minimizing the filter size. On the other hand, bigger filters, such as 5×5 , extract more details on superimposed regions using convolutions by considering more spatial pixels of the input images.

The pooling process aims to reduce the number of features by choosing the most informative one among the extracted features to decrease the computational cost of a model; however, relevant features might be eliminated.

In this study, a CNN-based architecture using parallelized dual blocks was designed to extract and combine different levels of features in accordance with the properties of the considered dataset. The first block included two convolutional layers with 3×3 filters followed by a 2×2 max-pooling operation. Similarly, the second block included two convolutional layers; however, the filter sizes were set to 5×5 to consider more spatial pixels in a wider region to detect the connected features. This enabled the extraction of both low- and high-level features and edges of the lumbar vertebrae. In addition, the max-pooling operation was not applied to the convolution layers in the second block, and the feature map size was reduced by shifting the filters by two spatial pixels (stride: 2). Therefore, the features obtained by the commonly used convolutional layers with 3×3 filters and a max-pooling operation were added to the features obtained by block 2. This provided new combined features using the variational properties of different blocks. Commonly, 32 filters and the rectified linear unit activation function are considered within block 1 and block 2. Since block 1 of the proposed model focuses on high-level features, such as general shape and intensity values, block 2 was used to extract more significant intensity values and provide more informative low-level features. Each convolutional layer of blocks was followed by batch normalization to avoid over-fitting.

A final convolutional layer was added to the proposed model to apply 5×5 filters to the added features and extract their most informative characteristics. Furthermore, the number of filters was increased, and the pooling operation was not considered to feed a fully connected layer with a maximum number of features to provide better convergence. The proposed model consisted of two fully connected layers with 32 and 16 neurons.

There are several approaches to creating multimodal models. One approach uses different planes of a single imaging technique (i.e., the axial, sagittal, and coronal planes of CT scans) as different modalities to create multimodal models. Another approach

uses images acquired by different imaging devices in different modalities, such as using CT and MRI scans as separate modalities to implement a multimodal model. It is also possible to create multimodal models using images and text data as different modalities.^{7,20} The use of modalities can include information from the same data or independent data for a common task. In addition, the multimodality of the models might include a single model for different modalities or independent models for the fed data.^{21,22} As a result, the fusion of different modalities can be performed at the feature, classification, or decision level.²³ The fusion at the feature level includes the process of the different modality images, such as CT and MRI; it also unifies the extracted features and uses multimodal data representation to train a classifier. Conversely, the fusion of data at the classifier level uses the representation of independent features of different modalities in a concatenated feature set to train a multimodal model. Finally, fusing at the decision level trains an independent classifier for different modalities, and the outputs of each classifier are fused for the final decision.²³

The proposed model was implemented as unimodal and multimodal approaches with common properties. In this study, the multimodality of the model was created by using two imaging techniques, MRI and CT, as separate modalities with two identical unimodal architectures. The loss functions (categorical cross entropy) of general unimodal architectures (L1 and L2) were used to determine the final loss (L3) of the multimodal model. Therefore, the multimodal model provided the common convergence of the CT and MRI scans and allowed us to test the model using either both modalities or a single modality simultaneously. The formula of binary cross-entropy is given in equation (1):

$$L_x = BCE = -(y_x \log(p_x) + (1 - y_x) \log(1 - p_x)) \quad (1)$$

where x represents the CT or MRI modality, and y and p denote the target and predicted classes. The final loss of the model is calculated as given in equation (2):

$$L_r = L_c + L_{M'} \quad (2)$$

Table 1. Skewness of distribution between the training and test groups

Group	Skewness of distribution
CT control group	0.519
CT patient group	-0.745
MRI control group	-0.037
MRI patient group	-0.129

CT, computed tomography; MRI, magnetic resonance imaging.

where L_f , L_c , and L_m denote the final, CT, and MRI modality losses. The general architecture of the proposed model with both unimodal and multimodal phases is shown in Figure 3.

Experimental design

This section presents the experimental design, validation strategy, and the considered evaluation metrics in detail. The experiments were performed in four stages to observe the accuracy of osteoporosis diagnosis using different imaging modalities.

The first two experimental stages involved training the proposed unimodal model using MRI and CT images, respectively. Considering separated MRI and CT modalities provided to analyze the effect of different medical imaging systems on osteoporosis diagnosis. The third stage was performed using the combined dataset created by shuffling both the CT and MRI datasets using the unimodal model. Finally, the fourth stage was implemented using the proposed model as a multimodal approach; CT and MRI scans were fed separately to the model and trained together.

A patient-based experiment was also performed to test the predictive ability of the models. A total of 27 patients (6 CT control + 6 CT osteoporosis + 8 MRI osteoporosis + 7 MRI control patients) and 228 corresponding images (57 for each of the control and osteoporosis groups) were extracted to represent different age samples from the dataset. The patient numbers varied because of the number of extracted slices of each patient. The unimodal and multimodal models were trained using the rest of the dataset independently to analyze the efficacy of the models for patient-based data.

The proposed model was compared in three stages to the traditional CNN model and six benchmark and recent pre-trained networks (EfficientNet B0,²⁴ InceptionV3,²⁵ ResNet50,²⁶ InceptionResNetV2,²⁷ EfficientNetV2S,²⁸ and ConvNeXt Tiny²⁹) to demonstrate the efficiency of the proposed model.

The architecture of the traditional CNN model was determined after performing several experiments. The experiments were performed by adding and removing convolutional layers and pooling operations and by increasing and decreasing filter sizes and

strides systematically and iteratively using MRI data. The architecture that produced the best results was considered in the comparisons. The final architecture of the traditional CNN included two convolutional layers (64 and 32 filters, respectively) and two fully connected layers (128 and 64 neurons, respectively). The abovementioned pre-trained networks were trained by adding a fully connected layer with 128 neurons for each and by using ImageNet weights. Therefore, the transfer-learning approach was used to transfer the acquired knowledge of the models to the diagnosis of osteoporosis.

All experiments were performed using 5-fold cross-validation to obtain consistent results. Cross-validation allowed the models to consider all images both in the training and testing phases. The models were trained five times, where the 4 of the folds were used for training, and the rest fold was used for testing. Therefore, the data dependency of the models was minimized in the evaluation. The data selection in the folds was performed randomly, and the final evaluation of the results was performed using the mean or sum of the correctly predicted samples ob-

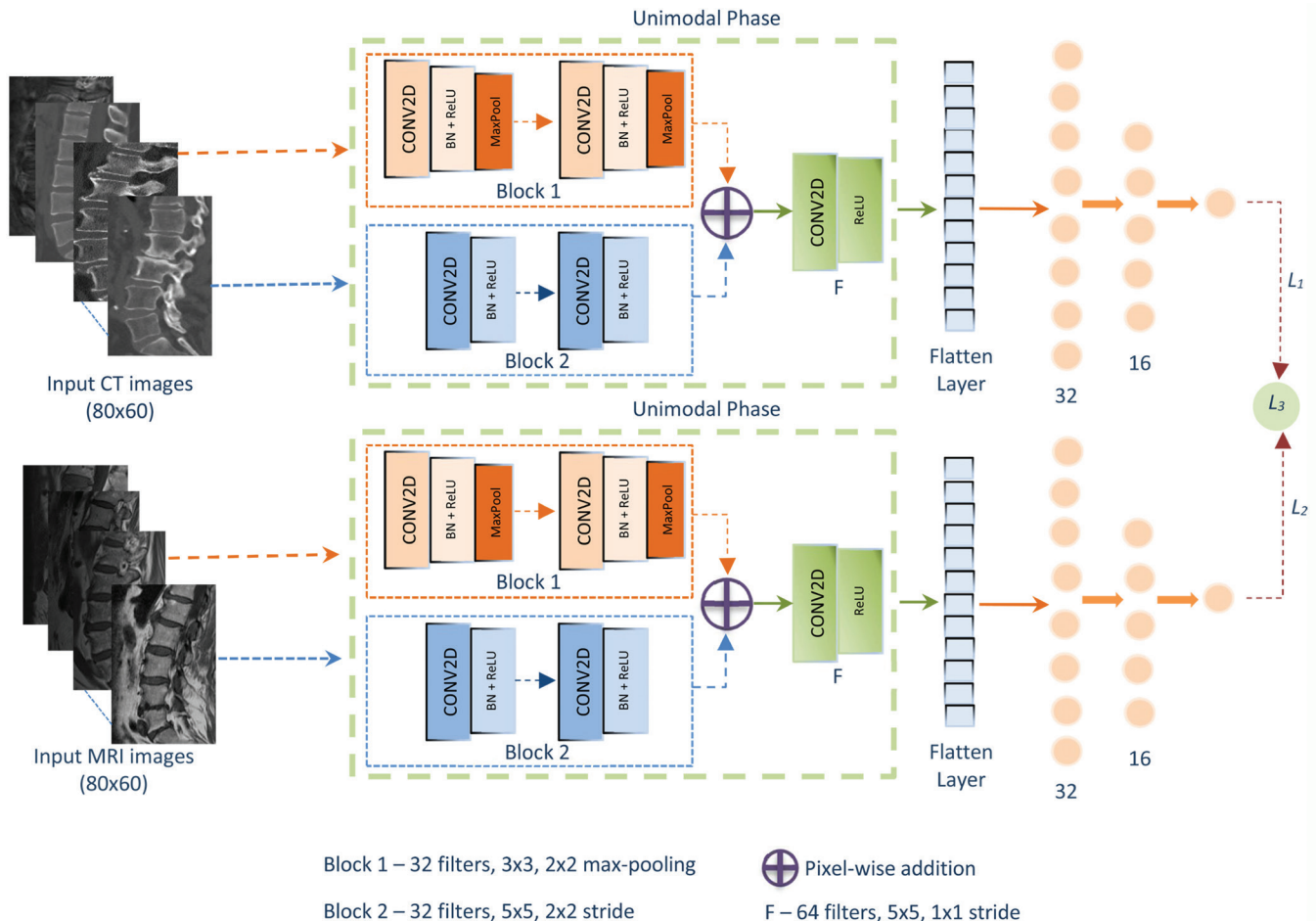


Figure 3. The multimodal architecture of the proposed convolutional neural network model for osteoporosis prediction.

tained in each fold. Data augmentation was not applied in the experiments.

Even though the datasets were balanced in this study, in which AI algorithms converged effectively,³⁰ we considered five different evaluation metrics—specificity, sensitivity, accuracy, ROC AUC score, and balanced accuracy for robust model evaluation.³¹ Additionally, 95% confidence intervals (CIs) were also provided for accuracy, sensitivity, and specificity. Accuracy was the primary evaluation metric of the classification tasks and provided a reliable measurement for balanced datasets. Sensitivity and specificity were used to measure the models' abilities to predict a dataset's positive and negative samples. Additionally, balanced accuracy was considered to measure the minor variations caused by the minimal number of output differences in the datasets; it measures the general classification ability of the model by calculating the average of sensitivity and specificity metrics and eliminates the effect of different-sized datasets. The formula for balanced accuracy is shown in equation (3):

$$\text{Balanced Accuracy} = \frac{\text{Sensitivity} + \text{Specificity}}{2}, \quad (3)$$

where

$$\text{Sensitivity} = \frac{TP}{TP + FN}, \quad (4)$$

and

$$\text{Specificity} = \frac{TN}{TN + FP} \quad (5)$$

The terms *TN*, *TP*, *FP*, and *FN* denote the true negative, true positive, false positive, and false negative samples predicted by the models. The ROC AUC score determines how the model distinguishes the positive and negative classes efficiently. The higher the score, the better the performance.

The abovementioned test set was used to test all models after training using all the data from the dataset. This allowed us to observe the diagnostic ability of all models and to check possible bias using the minimized age differences between the control and patient groups. Table 2 shows the details of the experimental stages.

Statistical analysis

The adaptive moment estimation optimizer was used in all models, and the proposed models were trained for 20 epochs using 16 batch sizes. The models were implemented on a Windows 11 PC with an Intel® Core™ i7-9750H CPU, 16 GB memory, 1,660 GTX GPU, and Python 3.8.16 using TensorFlow Keras 2.11.0.

Results

Results of stage-1 experiments

In the stage-1 experiments, all models were trained using MRI. The InceptionV3 and EfficientNetV2S models obtained the lowest results for all evaluation metrics considered in this study. The InceptionResNetV2 model produced more stable results than InceptionV3. ResNet50 achieved the highest specificity rate of the study, with 97.45% (95% CI for specificity: 96.1%–98.8%). However, it was observed that difficulties occurred in learning both classes, and the sensitivity rate of the model was measured as 88.84% (95% CI for sensitivity: 86.1%–91.6%). This caused a decrease in the general ability of the model. The ResNet50 model achieved 93.18% accuracy (95% CI: 91.6%–94.7%), a ROC AUC score of 0.932, and 93.15% balanced accuracy. The CNN model achieved more reliable and consistent results than the abovementioned models, with 94.62% sensitivity, 95.10% specificity, 0.948 ROC AUC score, and 94.86% balanced accuracy. The overall prediction ability of the CNN was measured as 94.86% (95% CI: 93.5%–96.2%) accuracy. Even though the EfficientNet B0 model obtained the highest results compared with the other pre-trained models within the transfer-learning experiments, it did not outperform the unimodal implementation of the proposed model. It achieved 94.22%, 96.86%, 95.55% (95% CI: 94.3%–96.8%), 0.955, and 95.54% for sensitivity, specificity, accuracy, ROC AUC score, and balanced accuracy, respectively, while the proposed model achieved the highest sensitivity (96.01%), ROC AUC score (0.965), and balanced accuracy (96.54%) results of this study. The overall prediction ability of the proposed method was 96.54% (95% CI: 95.4%–97.7%). The ConvNeXt Tiny model achieved the same and highest sensitivity rate as the proposed method; however, it did not show the same performance for the other metrics. Table 3 presents the results of stage-1 in detail.

Results of stage-2 experiments

In this stage, CT images were used for training. All models increased the ability of osteoporosis prediction using CT images compared with the stage-1 experiments. However, the ResNet50 model obtained the lowest specificity (93.60% with 95% CI: 91.6%–94.7%), ROC AUC score (0.942), and balanced accuracy rates (94.24%). Even though the InceptionV3 model obtained higher specificity and balanced accuracy than ResNet50, it obtained a minimum sensitivity of 94.69% (95% CI for sensitivity: 92.8%–96.6%). The proposed model achieved superior results and outperformed all the models considered in this study (98.48%, 99.20%, 0.988, and 98.84% for sensitivity, specificity, ROC AUC score, and balanced accuracy, respectively). The overall accuracy of the proposed method was 98.84% (95% CI for sensitivity: 92.8%–96.6%). In contrast to its performance using MRI, the EfficientNetV2S model achieved 99.20% specificity (95% CI for specificity: 98.4%–100%); however, it did not obtain sufficient results to outperform the proposed model and the InceptionV3 model in other metrics. Similarly, the ConvNeXt Tiny model obtained the same specificity as both the proposed method and EfficientNetV2S. The EfficientNetV2S and InceptionResNetV2 models followed the proposed model for all metrics. Table 4 presents the results of stage-2 in detail.

Results of stage-3 experiments

In this stage, CT and MRI were combined as input patterns in training without distinguishing the differences. The ResNet50, InceptionV3, and InceptionResNetV2 models did not produce reasonable results compared with the other models. The CNN model and EfficientNet B0 obtained similar and relatively higher balanced accuracies of 95.74% and 95.73% (95% CI: 94.9%–96.6%), respectively. However, the conventional CNN mod-

Table 2. Details of the experiments and stages

Stage no	Exp. name	Image set	Validation	# of images	# of trained models	Type
1	Exp. 1 (MRI)	MRI	5-fold CV	1,013	6	Unimodal
2	Exp. 2 (CT)	CT	5-fold CV	1,028	6	Unimodal
3	Exp. 3 (Com)	Combined	5-fold CV	2,041	6	Unimodal
4	Exp. 4 (MM)	MRI + CT	5-fold CV	2,004	1	Multimodal
5	Exp. 5	Hold-out test set	-	116	9	Both
6	Patient-based	MRI + CT	Hold-out	2,004		Both

Exp., experiment; MRI, magnetic resonance imaging; CT, computed tomography; Com, combined; MM, multimodal; CV: cross-validation.

el produced a higher specificity rate, while the EfficientNet B0 model obtained a more accurate sensitivity rate. Similar to the previous experiments, the proposed model outperformed all models and achieved 96.69%, 96.83%, and 0.968 for sensitivity, specificity, and ROC AUC score. It realized a balanced accuracy of 96.76% (95% CI: 96.0%–97.5%). The EfficientNetV2S and ConvNeXt Tiny models obtained 96.25% and 95.98% accuracy, with 95% CIs of 95.4%–97.1% and 95.0%–96.7%, respectively, and it followed the proposed model. Table 5 presents the results of stage-3 in detail.

Results of stage-4 multimodal experiments

The proposed model was implemented as a multimodal approach in the multimodal experiments, and CT and MRI were fed to the model in different modalities. The models' training was performed using a total of 2,004 CT and MRI in separate unimodal blocks and fused at the feature level after the feature extraction process of independent unimodal blocks. Fusing the different modalities of osteoporosis images allowed us to test the proposed system on 1,002 images in a 5-fold cross-validation. Even though the model's

training consisted of fewer samples than used in the combined datasets of stage-3, the multimodal approach achieved higher results in all metrics: 98.61%, 99.20%, 0.989, and 98.90% (95% CI: 98.4%–99.4%) for sensitivity, specificity, ROC AUC score, and balanced accuracy, respectively.

This experiment enabled us to observe the efficacy of feeding models with different image modalities instead of combining them into a single dataset. The obtained results showed that the multimodal image approach produced higher rates and was more effective in predicting osteoporosis. Table 6 presents the results obtained by the multimodal approach.

Figures 4 and 5 present the Grad-CAM++³² and saliency maps (using SmoothGrad³³) of the multimodal model for correctly predicted osteoporosis patients using MRI and CT scans, respectively. The figures show that the model focused on the lumbar vertebrae as expected to predict osteoporosis.

Results of stage-5 test-set experiments

All models, including the proposed multimodal and unimodal models (CT, MRI, and combined) and comparison models, were trained using the rest of the dataset and tested using the test set. In the CT experiments, the CT images of the test set were considered in the generalization phase, while in the MRI experiments, only the MRI were fed to the models. However, both modalities of the test sets were considered in the proposed combined unimodal and multimodal experiments. Table 7 presents the results obtained by all the models using the test set.

Additionally, the analysis of the prediction scores and DeLong statistical tests³⁴ were performed to evaluate the models' decision-making strengths and prediction capabilities and to compare the models' AUC scores statistically. As the same training and testing data were included for all models, a hold-out test was used for these analyses. The scores of correctly classified samples were considered, and the mean scores and SD were calculated for the unimodal and multimodal models. Even though all the models achieved reasonable scores, the results suggest that using a multimodal model increased the prediction scores and provided a more effective prediction of osteoporosis. Table 8 presents the mean and SD results obtained for each model using the hold-out test set.

Table 3. Results of stage-1 magnetic resonance imaging experiments

Model	Accuracy* (%)	Sensitivity* (%)	Specificity* (%)	Balanced accuracy (%)	ROC AUC score
Proposed model	96.54 (95.4–97.7)	96.01 (94.3–97.7)	97.06 (95.6–98.5)	96.54	0.965
CNN model	94.86 (93.5–96.2)	94.62 (81.5–87.8)	95.10 (93.2–97.0)	94.86	0.948
EfficientNet B0	95.55 (94.3–96.8)	94.22 (92.2–96.3)	96.86 (95.4–98.4)	95.54	0.955
ResNet50	93.18 (91.6–94.7)	88.84 (86.1–91.6)	97.45 (96.1–98.8)	93.15	0.932
InceptionV3	84.20 (82.0–86.5)	76.29 (72.6–80.0)	91.97 (89.6–94.3)	84.13	0.842
InceptionResNetV2	92.69 (91.1–94.3)	90.43 (87.9–93.0)	94.91 (93.0–96.8)	92.67	0.928
EfficientNetV2S	84.22 (82.1–86.6)	73.22 (69.5–76.93)	95.16 (93.3–97.1)	84.19	0.842
ConvNeXt Tiny	95.31 (94.1–96.6)	96.01 (94.3–97.7)	94.62 (92.7–96.5)	95.31	95.32

*Values in parentheses indicate a 95% confidence interval; CNN, convolutional neural network; ROC, receiver operating characteristics; AUC, area under the curve.

Table 4. Results of stage-2 computed tomography experiments

Model	Accuracy* (%)	Sensitivity* (%)	Specificity* (%)	Balanced accuracy (%)	ROC AUC score
Proposed model	98.83 (98.2–99.5)	98.48 (97.4–99.5)	99.20 (98.4–100)	98.84	0.988
CNN model	98.15 (97.3–99.0)	97.53 (96.2–98.9)	98.80 (97.8–99.8)	98.16	0.981
EfficientNet B0	97.85 (97.0–98.7)	97.15 (95.7–98.6)	98.61 (97.6–99.6)	97.87	0.978
ResNet50	94.26 (92.8–95.7)	94.88 (93.0–96.8)	93.65 (91.5–95.7)	94.24	0.942
InceptionV3	94.55 (93.2–95.9)	94.69 (92.8–96.6)	94.44 (92.4–96.4)	94.54	0.945
InceptionResNetV2	98.63 (97.9–99.3)	98.29 (97.2–99.4)	99.00 (98.1–99.9)	98.64	0.986
EfficientNetV2S	98.50 (97.8–99.4)	97.80 (96.4–99.2)	99.20 (98.4–100)	98.50	0.985
ConvNeXt Tiny	96.68 (95.6–97.6)	94.18 (92.4–96.2)	99.20 (98.4–100)	96.69	0.967

*Values in parentheses indicate a 95% confidence interval; CNN, convolutional neural network; ROC, receiver operating characteristics; AUC, area under the curve.

Table 5. Results of stage-3 combined experiments

Model	Accuracy* (%)	Sensitivity* (%)	Specificity* (%)	Balanced accuracy (%)	ROC AUC score
Proposed model	96.76 (96.0–97.5)	96.69 (95.6–97.8)	96.83 (95.8–97.9)	96.76	0.968
CNN model	95.73 (94.9–96.6)	95.33 (94.0–96.6)	96.14 (95.0–97.3)	95.74	0.957
EfficientNet B0	95.73 (94.9–96.6)	95.82 (94.6–97.0)	95.65 (94.4–96.9)	95.73	0.957
ResNet50	89.75 (88.4–91.1)	95.52 (94.3–96.8)	83.89 (81.6–86.2)	89.71	0.897
InceptionV3	89.75 (88.4–91.1)	88.04 (86.1–90.0)	91.50 (89.8–93.2)	89.77	0.899
InceptionResNetV2	92.65 (91.5–93.8)	88.62 (86.7–90.6)	96.73 (95.6–97.8)	92.68	0.926
EfficientNetV2S	96.25 (95.4–97.1)	96.20 (95.2–97.5)	96.28 (95.2–97.3)	96.24	0.962
ConvNeXt Tiny	95.98 (95.0–96.7)	95.94 (94.7–97.2)	96.03 (95.0–97.1)	95.99	0.960

*Values in parentheses indicate a 95% confidence interval; CNN, convolutional neural network; ROC, receiver operating characteristics; AUC, area under the curve.

Table 6. Results of the proposed model in the multimodal experiment

Model	Accuracy* (%)	Sensitivity* (%)	Specificity* (%)	Balanced accuracy (%)	ROC AUC score
Proposed model	98.90 (98.4–99.4)	98.61 (97.9–99.3)	99.20 (98.6–99.8)	98.90	0.989

*Values in parentheses indicate a 95% confidence interval; ROC, receiver operating characteristics; AUC, area under the curve.

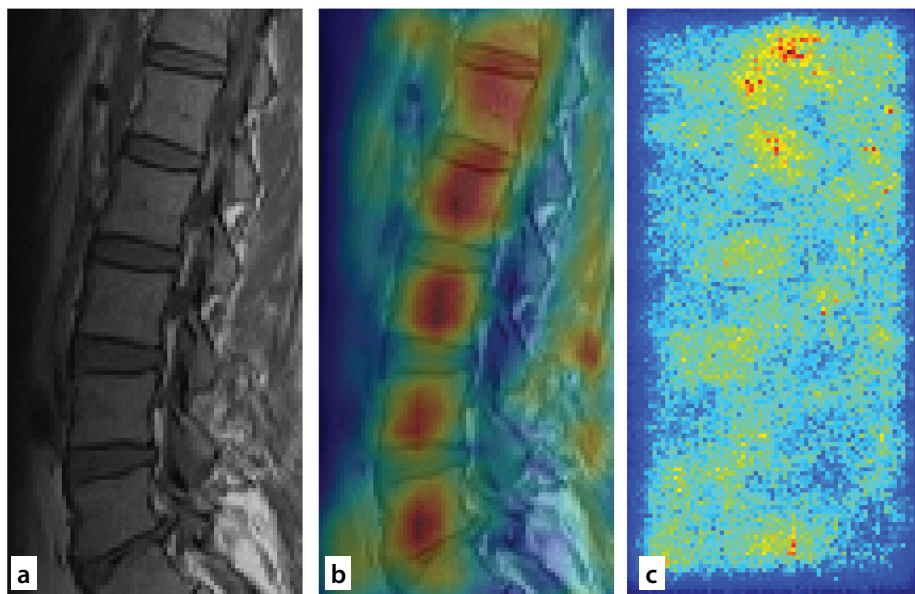


Figure 4. Grad-Cam++ and saliency visualization of the multimodal model for the magnetic resonance image (MRI) of correctly predicted osteoporosis: (a) original MRI, (b) Grad-CAM++, and (c) saliency map using SmoothGrad.

The *P* values obtained by performing the DeLong statistical test showed no significant differences; however, the multimodal model was slightly superior to the unimodal models. Table 9 presents the DeLong statistical test results.

Results of patient-based experiments

The proposed models were tested using representative patients. The unimodal model for CT scans achieved 100% specificity by predicting the control group correctly and

97.73% (95% CI: 88.9%–100%) sensitivity. The predictions of five patients were obtained accurately (100%); however, 70% (95% CI: 41.6%–98.4%) accuracy was obtained for a single patient.

The results of the unimodal model for patient-based MRI scans achieved slightly lower accuracy than CT scans, with 85.96% (95% CI: 76.9%–95.00%) sensitivity and 91.22% (95% CI: 83.9%–98.6%) specificity. Three of seven patients were accurately (100%) predicted for osteoporosis, and the remaining patients were predicted at between 66.67% (95% CI: 28.9%–100%) and 85.71% (95% CI: 59.8%–100%) accuracy.

The multimodal model obtained higher scores for MRI data and the same for CT data. The results for MRI data were 89.47% sensitivity (95% CI: 81.5%–97.4%) and 96.49% (95% CI: 91.7%–100%) specificity. The results obtained by the multimodal model for MRI and CT images were 92.98% (95% CI: 88.3%–97.7%) sensitivity and 98.24% (95% CI: 95.8%–100%) specificity. The accuracy was 95.61% (95% CI: 93.0%–98.3%). Table 10 shows the obtained patient-based results in detail.

Sample images, demo codes, and notebook implementations are available at: https://github.com/BoranSekeroglu/OSTEO_MODELS

Discussion

The obtained results are discussed in different sections to analyze the effect of different imaging modalities and multimodal approaches in predicting osteoporosis.

All the deep-learning models predicted osteoporosis at different rates. However, the proposed 5 × 5 convolutions in block 2 were used to predict more connected features at the vertebral bone boundaries. Adding the obtained features from both blocks and the consideration as new features enabled the proposed unimodal model to produce superior results compared with the other considered models. In addition, the multimodal approach of the proposed model resulted in superior prediction rates.

Although the pre-trained CNN models obtained fluctuating results in different experiments, it was observed that the ConvNeXt, EfficientNetV2S, EfficientNet B0, and InceptionResNetV2 models produced consistent and stable results, even though they did not outperform the proposed model. The fluctuations were considered to determine the consistency and stability of the models.

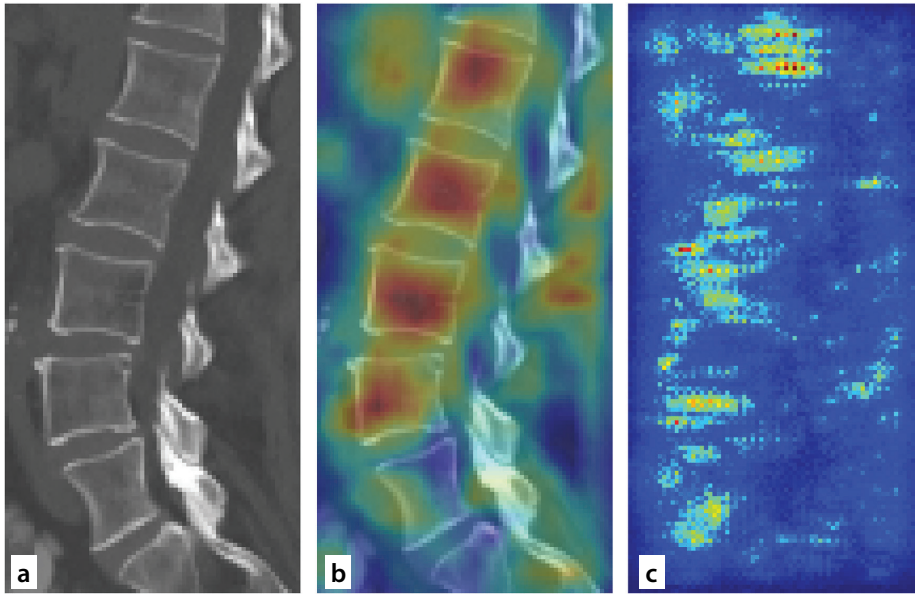


Figure 5. Grad-Cam++ and saliency visualization of the multimodal model for the computed tomography image of correctly predicted osteoporosis: (a) original computed tomography image, (b) Grad-CAM++, and (c) saliency map using SmoothGrad.

Table 7. Results of stage-5 test-set experiments					
Model	Accuracy* (%)	Sensitivity* (%)	Specificity* (%)	Balanced accuracy (%)	ROC AUC score
CNN MRI	83.33 (72.8–93.9)	79.16 (62.9–95.4)	87.50 (74.3–100)	83.33	0.833
CNN CT	85.29 (76.9–93.7)	82.35 (69.5–95.2)	88.23 (77.4–99.1)	85.29	0.854
CNN combined	87.06 (81.0–93.2)	86.20 (77.3–95.1)	87.93 (79.5–96.3)	87.06	0.871
Efficient B0 MRI	93.75 (86.9–100)	91.66 (80.6–100)	95.83 (87.8–100)	93.75	0.978
Efficient B0 CT	92.64 (86.4–98.9)	91.17 (81.6–100)	94.11 (86.2–100)	92.64	0.927
Efficient B0 combined	92.24 (87.4–97.1)	91.37 (84.2–98.6)	93.10 (86.6–99.6)	92.24	0.924
ResNet50 MRI	77.08 (65.2–89.0)	79.16 (62.9–95.4)	75.00 (57.7–92.3)	77.08	0.771
ResNet50 CT	82.35 (73.3–91.4)	79.41 (65.8–93.0)	85.29 (73.4–97.2)	82.35	0.824
ResNet50 combined	83.05 (77.9–91.1)	81.03 (70.9–91.1)	85.00 (79.5–96.3)	83.01	0.840
InceptionV3 MRI	79.16 (67.7–90.7)	75.00 (57.7–92.3)	83.33 (68.4–98.2)	79.16	0.792
InceptionV3 CT	85.29 (76.9–93.7)	85.29 (73.4–97.2)	85.29 (73.4–97.2)	85.29	0.823
InceptionV3 combined	83.05 (77.9–91.1)	82.75 (73.0–92.5)	83.33 (77.3–95.1)	83.04	0.831
InceptionResNetV2 MRI	85.41 (75.4–95.4)	83.33 (68.4–98.2)	87.50 (74.3–100)	85.41	0.854
InceptionResNetV2 CT	94.11 (88.5–99.7)	94.11 (86.2–100)	94.11 (86.2–100)	94.11	0.942
InceptionResNetV2 combined	87.28 (83.1–94.5)	89.65 (81.8–97.5)	85.00 (79.5–96.3)	87.32	0.874
EfficientNetV2S MRI	93.75 (86.9–100)	88.26 (78.6–100)	96.91 (89.9–100)	93.75	0.978

The 5% change in specificity and sensitivity results assumed that the models were focused on a particular training data class during convergence, and their generalization ability was inconsistent on the test folds. The traditional CNN demonstrated that the correct determination of the architecture might cause higher classification rates than with the pre-trained models. However, determining the correct architecture is challenging and time-consuming, and it increases the computation cost of the studies.

The proposed model provided learning with few trainable parameters compared with other models and minimized the computational cost in terms of training time. Contrary to the high computational cost of the pre-trained models (i.e., 37 sec/epoch for EfficientNet B0 and 76 sec/epoch for ResNet50), the computation cost of the proposed unimodal, multimodal, and CNN models was an average of 1.2, 2.1, and 5.8 sec/epoch with the GPU, respectively.

Recent studies showed that obtaining above 74% for sensitivity, specificity, and accuracy in osteoporosis prediction is possible using AI and deep-learning models with different imaging modalities, such as CT, DEXA, and micro-CT.^{8,15–18,35–37}

The results obtained using MRI of our study (stage-1) showed that MRI could be used effectively to predict osteoporosis with 96.54% accuracy (95% CI: 95.4%–97.7%) and eliminate the side effects of radiation-emitting devices.

On the other hand, the use of CT images resulted in more accurate results (98.84%), as they captured detailed anatomical structures. Combining CT and MRI without distinguishing the feature extraction process provided a limited contribution to osteoporosis prediction (96.76%). Even though a slight improvement occurred in the results compared with the results of the MRI experiments, there was a 2% decrease in the results obtained using CT images. However, the significant ability of deep-learning models in the feature extraction process provided superior results (98.90%) than those obtained in all experiments separately or combined using a multimodal approach. The consideration of both CT and MRI in individual unimodal blocks and the use of the loss of separate unimodal blocks to train the multimodal model provide further prediction contributions.

One of the most important outcomes of the experiments is that the trained model predicted osteoporosis using MRI or CT

Table 7. Continued

EfficientNetV2S CT	92.60 (86.3–98.8)	92.67 (83.1–100)	95.92 (88.0–100)	92.58	0.925
EfficientNetV2S combined	93.40 (87.2–99.6)	93.20 (86.1–100)	93.60 (87.1–100)	93.40	0.934
ConvNeXt Tiny MRI	93.75 (86.9–100)	91.66 (80.6–100)	95.83 (87.8–100)	93.75	0.978
ConvNeXt Tiny CT	90.56 (83.3–98.4)	85.29 (73.4–97.2)	95.83 (87.8–100)	90.56	0.906
ConvNeXt Tiny combined	90.55 (85.7–95.4)	93.20 (86.1–100)	87.93 (79.5–96.3)	90.56	0.905
Proposed unimodal MRI	95.83 (90.2–100)	91.66 (80.6–100)	100.00 (100–100)	95.83	0.959
Proposed unimodal CT	97.05 (93.0–100)	97.05 (91.4–100)	97.05 (91.4–100)	97.05	0.971
Proposed unimodal combined	95.68 (92.0–99.4)	94.82 (89.1–100)	96.55 (91.9–100)	95.68	0.957
Proposed multimodal	97.91 (95.1–100)	97.91 (95.1–100)	97.91 (95.1–100)	97.91	0.979

*Values in parentheses indicate a 95% confidence interval; MRI, magnetic resonance image, CT, computed tomography, ROC, receiver operating characteristics; AUC, area under the curve.

Table 8. Mean and standard deviation results of the prediction scores of the hold-out test set

Model	Mean ROC AUC score	Standard deviation
Proposed unimodal MRI	0.921	0.084
Proposed unimodal CT	0.952	0.056
Proposed unimodal combined	0.926	0.071
Proposed multimodal	0.965	0.039

MRI, magnetic resonance imaging; CT, computed tomography; ROC, receiver operating characteristics; AUC, area under the curve.

Table 9. Model comparison using the DeLong test for two correlated receiver operating characteristics area under the curve scores of the stage-5 test-set experiments

	Multimodal MRI vs. unimodal MRI	Multimodal CT vs. unimodal CT
Z value	0.574	0.444
P value	0.566	0.657
Confidence intervals	–0.021–0.038	–0.029–0.047

MRI, magnetic resonance imaging; CT, computed tomography.

Table 10. Results of patient-based experiments

Metric*	Unimodal CT	Unimodal MRI	Multimodal
Total accuracy (image-based)	97.38% (95% CI: 94.4%–100%)	88.59% (95% CI: 82.8%–94.4%)	95.61% (95% CI: 93.0%–98.3%)
Total sensitivity (image-based)	97.73% (95% CI: 88.9%–100%)	85.96% (95% CI: 76.9%–95.00%)	92.98% (95% CI: 88.3%–97.7%)
Total specificity (image-based)	100%	91.22% (95% CI: 83.9%–98.6%)	98.24% (95% CI: 95.8%–100%)
Maximum accuracy (patient group)	100%	100%	100%
Maximum accuracy (control group)	100%	100%	100%
Minimum accuracy (patient group)	70% (95% CI: 41.6%–98.4%)	66.67% (95% CI: 28.9%–100%)	87.5% (95% CI: 64.6%–100%)
Minimum accuracy (control group)	100%	77.78% (95% CI: 50.6%–100%)	88.88% (95% CI: 68.4%–100%)

*Total accuracy, total sensitivity, and total specificity indicate the image-based results of patients and the control group. The maximum and minimum scores indicate the highest and lowest scores from independent patient and control group analyses. MRI, magnetic resonance imaging; CT, computed tomography; CI, confidence interval.

images in a multimodal model, as the MRI and CT images used in this study were not obtained from the same patients. This will protect patients from being exposed to radiation from different imaging techniques. We believe that our study and its results demonstrate the efficiency of using deep-learning models, particularly the proposed unimodal and multimodal CNN models, in predicting osteoporosis more accurately.

Furthermore, using the hold-out test set with minimized age differences between the control and patient groups as well as patient-based experiments allowed us to observe the main prediction capabilities of the models and avoid any bias in the test data. As a result, all the proposed models outperformed the other models considered, and the unimodal models achieved 95.83% (95% CI: 90.2%–100%) and 97.05% (95% CI: 93.0%–100%) balanced accuracy on the hold-out test set for MRI and CT, respectively. Even though a slight decrease was observed in the combined unimodal model (95.68%), it also achieved higher scores than the other models. However, the multimodal model obtained superior results by obtaining 97.91% (95% CI: 95.1%–100%) balanced accuracy.

The patient-based analysis showed that the proposed models accurately predicted osteoporosis with superior specificity, particularly with CT images. However, the multimodal model provided better prediction ability with MRI. This proved once again that the combined use of different imaging modalities and the independent extraction of features during training improved the prediction capability of CNNs and might provide more accurate support for radiologists.

Even though the best prediction of osteoporosis was obtained using CT images in the unimodal experiments, considering MRI in unimodal and multimodal models could prevent patients from being exposed to radiation and assist radiologists in diagnosing osteoporosis.

This study has limitations. Patients with T scores higher than -1 and BMD levels within normal limits were excluded. This patient group could not be used as a control group because of the small number of patients. To protect non-indicated patients from DEXA-induced X-ray exposure, the DEXA data of the control group were not obtained. We are aware that the ideal scenario would have been to obtain the DEXA data of the control group, but we felt it would have been unethical. The control group was selected among pre-menopausal female patients and male patients under 50 years of age, and

patients with diseases and/or drug use that may cause secondary osteoporosis were excluded from the study. To demonstrate that the dataset was not biased, a hold-out test set was extracted from the dataset. However, the developed system was not tested with an external dataset, and the use of the proposed models in clinical practice requires further investigation.

Eliminating the abovementioned limitations might lead to more robust findings in further studies.

In conclusion, we considered two primary datasets that included MRI and CT images and proposed specifically designed CNN models for osteoporosis prediction. Several experiments were performed, and the obtained results were compared with those of the traditional CNN and six benchmark pre-trained models using the transfer-learning approach. The proposed unimodal CNN model outperformed the other considered models in predicting osteoporosis using MRI and CT images separately and obtained 96.54% and 98.84% balanced accuracy, respectively. Superior results were obtained using the proposed multimodal CNN model, and 98.90% balanced accuracy was achieved. Furthermore, a hold-out test and patient-based experiments were used to test the models, and the proposed models achieved superior results.

The obtained results showed that the developed deep-learning models could produce accurate results in osteoporosis prediction using different imaging techniques. However, considering MRI images, even in unimodal and multimodal models, could minimize DEXA and CT use and prevent patients from being exposed to radiation. Our future work will include risk assessment using MRI scans, and further studies might focus on increasing the accuracy obtained in this study using more patient data.

Conflict of interest disclosure

The authors declared no conflicts of interest.

References

- Lungdahl BL. Overview of treatment approaches to osteoporosis. *Br J Pharmacol*. 2021;178(9):1891-1906. [\[CrossRef\]](#)
- Burden AM, Tanaka Y, Ha XC, et al. Osteoporosis case ascertainment strategies in European and Asian Countries: a comparative review. *Osteoporos Int*. 2021;32(5):817-829. [\[CrossRef\]](#)
- US Preventive Services Task Force; Curry SJ, Krist AH, et al. Screening for Osteoporosis to Prevent Fractures: US Preventive Services Task Force Recommendation Statement. *JAMA*. 2018;319(24):2521-2531. [\[CrossRef\]](#)
- Tuzun S, Eskiyurt N, Akarirmak U, et al. Incidence of hip fracture and prevalence of osteoporosis in Turkey: the FRACTURK study. *Osteoporos Int*. 2012;23(3):949-955. [\[CrossRef\]](#)
- Dimai HP. Use of dual-energy X-ray absorptiometry (DXA) for diagnosis and fracture risk assessment; WHO-criteria, T- and Z-score, and reference databases. *Bone*. 2017;104:39-43. [\[CrossRef\]](#)
- Balasubramanya R, Selvarajan SK. Lumbar spine imaging. In: StatPearls [Internet]. Treasure Island (FL): StatPearls Publishing; 2023. 2021. Accessed 26 Nov 2021. [\[CrossRef\]](#)
- Li Y, Zhao J, Lv Z, Pan Z. Multimodal medical supervised image fusion method by CNN. *Front Neurosci*. 2021;15:638976. [\[CrossRef\]](#)
- Lim HK, Ha HI, Park SY, Han J. Prediction of femoral osteoporosis using machine-learning analysis with radiomics features and abdomen-pelvic CT: A retrospective single center preliminary study. *PLoS One*. 2021;4:16(3):e0247330. [\[CrossRef\]](#)
- Kocak B, Yardimci AH, Yuzkan S, et al. Transparency in artificial intelligence research: a systematic review of availability items related to open science in radiology and nuclear medicine. *Acad Radiol*. 2022. [\[CrossRef\]](#)
- Mongan J, Moy L, Kahn CE Jr. Checklist for artificial intelligence in medical imaging (CLAIM): a guide for authors and reviewers. *Radiol Artif Intell*. 2020;2(2):e200029. [\[CrossRef\]](#)
- Adali T, Sekeroglu B. Analysis of microRNAs by neural network for early detection of cancer. *Procedia Technology*. 2012;1:449-452. [\[CrossRef\]](#)
- Hamamoto R. Application of artificial intelligence for medical research. *Biomolecules*. 2021;11(1):90. [\[CrossRef\]](#)
- Kavur AE, Gezer NS, Baris M, et al. Comparison of semi-automatic and deep learning-based automatic methods for liver segmentation in living liver transplant donors. *Diagn Interv Radiol*. 2020;26(1):11-21. [\[CrossRef\]](#)
- Smets J, Shevroja E, Hügler T, Leslie WD, Hans D. Machine learning solutions for osteoporosis—a review. *J Bone Miner Res*. 2021;36(5):833-851. [\[CrossRef\]](#)
- Guglielmi G, Muscarella S, Bazzocchi A. Integrated imaging approach to osteoporosis: state-of-the-art review and update. *Radiographics*. 2011;31(5):1343-1364. [\[CrossRef\]](#)
- Xu Y, Li D, Chen Q, Fan Y. Full supervised learning for osteoporosis diagnosis using micro-CT images. *Microsc Res Tech*. 2013;76(4):333-341. [\[CrossRef\]](#)
- Yamamoto N, Sukegawa S, Kitamura A, et al. Deep learning for osteoporosis classification using hip radiographs and patient clinical covariates. *Biomolecules*. 2020;10(11):1534. [\[CrossRef\]](#)
- Jang R, Choi JH, Kim N, Chang JS, Yoon PW, Kim CH. Prediction of osteoporosis from simple hip radiography using deep learning algorithm. *Sci Rep*. 2021;11(1):19997. [\[CrossRef\]](#)
- Liu L, Si M, Ma H, et al. A hierarchical opportunistic screening model for osteoporosis using machine learning applied to clinical data and CT images. *BMC Bioinformatics*. 2022;23(1):63. [\[CrossRef\]](#)
- Miller SJ, Howard J, Adams P, Schwan M, Slater R. Multimodal classification using images and text. *SMU Data Science Review*. 2020;3:6. [\[CrossRef\]](#)
- Wisely CE, Wang D, Henao R, et al. Convolutional neural network to identify symptomatic Alzheimer's disease using multimodal retinal imaging. *Br J Ophthalmol*. 2022;106:388-395. [\[CrossRef\]](#)
- Li Y, Zhao J, Lv Z, Li J. Medical image fusion method by deep learning. *International Journal of Cognitive Computing in Engineering*. 2021;2:21-29. [\[CrossRef\]](#)
- Guo Z, Li X, Huang H, Guo N, Li Q. Medical image segmentation based on multi-modal convolutional neural network: Study on image fusion schemes. *ISBI*. 2018:903-907. [\[CrossRef\]](#)
- Tan M, Quoc Le. EfficientNet: Rethinking model scaling for convolutional neural networks, ICML 2019 Conference: 36th International Conference on Machine Learning, Long Beach, California; 2019:6105-6114. [\[CrossRef\]](#)
- Szegedy C, Vanhoucke V, Ioffe S, Shlens J, Wojna Z. Rethinking the inception architecture for computer vision. 2016 CVPR Conference: 2016 IEEE Conference on Computer Vision and Pattern Recognition. 2016:2818-2826. [\[CrossRef\]](#)
- He K, Zhang X, Ren S, Sun J. Deep residual learning for image recognition. 2016 IEEE Conference on Computer Vision and Pattern Recognition. 2016:770-778. [\[CrossRef\]](#)
- Szegedy C, Ioffe S, Vanhoucke V, Alemi AA. Inception-v4, Inception-ResNet and the Impact of Residual Connections on Learning, AAAI-2017 Conference: Thirty-First AAAI Conference on Artificial Intelligence. 2017:4278-4284. [\[CrossRef\]](#)
- Tan M, Quoc V. Le. EfficientNetV2: smaller models and faster training. Proceedings of the 38th International Conference on Machine Learning, PMLR 139, 2021 International Conference of Machine Learning. [\[CrossRef\]](#)

29. Liu Z, Mao H, Wu CY, Feichtenhofer C, Darrell T, Xie S. AConvNet for the 2020s, 2022 IEEE Conference on Computer Vision and Pattern Recognition (pp. 11976-11986). [\[CrossRef\]](#)
30. Kocak B. Key concepts, common pitfalls, and best practices in artificial intelligence and machine learning: focus on radiomics. *Diagn Interv Radiol.* 2022;28(5):450-462. [\[CrossRef\]](#)
31. Maier-Hein L, Reinke A, Christodoulou E, et al. Metrics reloaded: pitfalls and recommendations for image analysis validation. 2022. [\[CrossRef\]](#)
32. Chattopadhyay A, Sarkar A, Howlader P, Balasubramanian VN. Grad-CAM++: generalized gradient-based visual explanations for Deep Convolutional Networks, 2018 IEEE winter conference on applications of computer vision (WACV). [\[CrossRef\]](#)
33. Smilkov D, Thorat N, Kim B, Viégas F, Wattenberg M. Smoothgrad: removing noise by adding noise, workshop on visualization for deep learning, ICML 2017. [\[CrossRef\]](#)
34. DeLong ER, DeLong DM, Clarke-Pearson DL. Comparing the areas under two or more correlated receiver operating characteristic curves: a nonparametric approach. *Biometrics.* 1988;44(3):837-845. [\[CrossRef\]](#)
35. Zhang B, Yu K, Ning Z, et al. Deep learning of lumbar spine X-ray for osteopenia and osteoporosis screening: a multicenter retrospective cohort study. *Bone.* 2020;140:115561. [\[CrossRef\]](#)
36. Hsieh CI, Zheng K, Lin C, et al. Automated bone mineral density prediction and fracture risk assessment using plain radiographs via deep learning. *Nat Commun.* 2021;12(1):5472. [\[CrossRef\]](#)
37. Lee KS, Jung SK, Ryu JJ, Shin SW, Choi J. Evaluation of transfer learning with deep convolutional neural networks for screening osteoporosis in dental panoramic radiographs. *J Clin Med.* 2020;9(2):392. [\[CrossRef\]](#)



Coronary artery calcium score percentiles: data from a single center in Turkey

Gülsüm Kılıçkap
 Halil Tekdemir
 Kübra Bahadır
 Numan İlteriş Çevik
 Betül Akdal Dölek
 Murat Vural

Ankara Bilkent City Hospital, Clinic of Radiology,
Ankara, Turkey

The preliminary results of this study were presented (oral presentation) in the National Radiology Congress on November 3, 2022, Antalya, Turkey.

Corresponding author: Gülsüm Kılıçkap

E-mail: gklickap@yahoo.com.tr

Received 16 March 2023; revision requested 13 April 2023; accepted 18 May 2023.



Epub: 15.06.2023

Publication date: 08.01.2023

DOI: 10.4274/dir.2023.232196

PURPOSE

The coronary artery calcium (CAC) score is used in decision-making for preventive medications in patients with borderline clinical risk scores. Both absolute and percentile CAC scores can be used; however, a percentile CAC score is especially useful in young patients and women. The aim of this study is to present CAC score percentiles across age categories in women and men using a large database.

METHODS

Bilkent City Hospital database was screened for patients who underwent CAC score measurements between January 2021 and March 2022. Of the 4,487 patients, 546 were excluded due to 1) a history of coronary stent implantation or bypass surgery or 2) missing information regarding a history of revascularization or calcium scores. Therefore, the final study population included 3,941 participants. The percentiles for age categories within each sex were tabulated, and percentile plots were created for each sex using locally weighted scatterplot smoothing regression.

RESULTS

The proportion of men included in the study was higher compared with that of women (57.09% vs. 42.91%). The mean age was 52.20 ± 11.11 years, and it was higher in women than in men (54.07 ± 10.47 vs. 50.80 ± 11.37 , respectively; $P < 0.001$). A zero CAC score was observed in 2,381 (60.42%) patients; the percentage was higher in women than in men (68.60% vs. 54.27%; $P < 0.001$). When the cut-off value for the high-risk category was taken as the 75th percentile, a non-zero CAC score directly assigned a patient into the high-risk category in women aged <55 years and men aged <45 years. Percentile plots were also provided for each sex.

CONCLUSION

In this large-scale study, including patients referred for CAC scoring and/or coronary computed tomography angiography, CAC score percentiles were provided for women and men across the selected age categories which may be in therapeutic decision-making. As an approximate rule of thumb, a non-zero CAC score corresponds to the high-risk category in women aged <55 years and in men aged <45 years.

KEYWORDS

Coronary artery, calcium score, computed tomography, percentiles, cardiovascular risk scores

Cardiovascular (CV) diseases, particularly coronary artery disease, are the leading causes of death worldwide.^{1,2} Detection of high-risk individuals is of prime importance for the application of appropriate preventive measures. For this reason, guidelines recommend using clinical risk scores, such as the Framingham risk score or the pooled cohort estimates score for the American population³ and the SCORE-2 tool for the European population.⁴ Despite using these scores, some people may still experience CV events; therefore, other potential risk markers have been evaluated to make a better classification. The coronary artery calcium (CAC) score is independently associated with future risk of coronary events^{5,6} and is recommended for use as a risk modifier in patients with a borderline risk category based

on clinical risk scores. A CAC score can be used in risk estimation as an absolute value or percentile for sex and age categories. The use of absolute scores seems to be a better method than percentiles in risk classification for future CV events.⁷ However, percentile scores may especially be useful in young people and women, as the absolute score may be too low to predict future events.⁸⁻¹¹ The American guidelines recommend the cut-off value of the 75th percentile as the risk modifier in patients with a borderline risk score based on the conventional risk score calculation.³

CAC score percentiles vary not only among age and sex categories but also among populations.^{12,13} These findings suggest the necessity of calculating CAC scores and percentiles for each population. According to the authors' knowledge, there is no high-volume study evaluating the CAC score percentiles in Turkey; hence, it is possible that data from the Multi-ethnic Study of Atherosclerosis (MESA) for the white/Caucasian population are used for this purpose. In this study, the authors aimed to calculate the CAC percentiles for each sex and age categories and to evaluate the absolute values that correspond to the high-risk (75th) percentile. The authors also planned to provide percentile plots of CAC scores for each sex.

Methods

The present study was approved by the Ankara Bilkent City Hospital Institutional Review Board (20.04.2022/E1-22-2563) and was performed according to the Declaration of Helsinki principles. Informed consent was waived, as the study was conducted retrospectively with use of the hospital database.

Main points

- More than half of the study population (60.42%) had zero coronary artery calcium (CAC) scores; the percentage was significantly higher in women than in men (68.60% vs. 54.27%; $P < 0.001$).
- The prevalence of non-zero CAC scores increased with age; the increase was more prominent in men than in women. Of note, a non-zero CAC score developed approximately 10 years earlier in men than in women.
- As an approximate rule of thumb, a non-zero CAC score corresponded to the high-risk category (75th percentile) in women aged <55 years and in men aged <45 years.
- The CAC score percentiles were provided for each sex across the selected age categories.

Study population

The authors of the present study screened for patients who underwent coronary computed tomography (CT) angiography (CTA) and CAC score calculation between January 01, 2021, and March 01, 2022, in the radiology department of Ankara Bilkent City Hospital, Ankara, Turkey. The exclusion criteria were 1) patients with a coronary stent or bypass graft and 2) patients with missing information regarding history of revascularization or calcium scores. Of the 4,487 patients, 546 (12.2%) were excluded; finally, the study population included 3,941 participants. The flowchart for creating the present study population is presented in Figure 1. Among the study population ($n = 3,941$), 3,910 had received both CAC scoring and CTA, and only 31 patients had received CAC scoring alone.

Risk factors for coronary artery disease were obtained from the hospital database. The study population was divided into age categories: 1) patients aged <40 years; 2) patients with 5-year intervals aged 40–80 years; and 3) patients aged ≥80 years. Next, analyses were conducted for women and men separately.

Coronary computed tomography angiography and coronary artery calcium score calculation

Coronary CTAs and CAC score calculations were performed on a 512-detector CT scanner with dual-energy (General Electric, Revolution CT, GE Healthcare, Wisconsin, USA). A beta-blocker (metoprolol 50–100 mg) was given to patients with a heart rate of >65 bpm at least one hour before coronary CTA according to a cardiologist's recommendation, and an additional dose (up to the total dose of 200 mg) was given if necessary. CT was electrocardiographically triggered at 60%–80% of the R-R interval. Retrospective electrocardiogram (ECG) gating was per-

formed in patients with high heart rates for CTA, and prospective ECG-triggered CT acquisition was used for CAC scoring. Before contrast material injection, non-enhanced images for CAC scoring were obtained. Intravenous iodinated contrast material was injected at a rate of 4–6 mL/sec, followed by saline infusion. The CTA and CAC scan parameters were as follows: 1) 16 cm detector; 2) 100–120 Kv (120 kV for individuals with body mass index of >29, 100 kV for others); 3) 300–720 mA; 4) section thickness of 0.625 mm for CTA and 2.5 mm for CAC score scanning; 5) field of view of 25 cm; 6) rotation time of 0.28 secs; 7) 512 × 512 pixel matrix; and 8) window/level: 550/100.

The CAC was defined as a plaque of at least three contiguous pixels with an attenuation of ≥130 Hounsfield units (Figure 2). The SmartScore 4.0 (General Electric, Revolution CT, GE Healthcare, Wisconsin, US) software system was used for CT image postprocessing, and the CAC score was calculated using the Agatston method.¹⁴

Statistical analysis

Categorical variables were presented as frequency and percentages, and continuous variables were presented as mean ± standard deviation (SD) or median and interquartile range (IQR), depending on whether or not they have a normal distribution (with the exception of the CAC score). The CAC score had a skewed distribution but was presented as mean ± SD and median (IQR).

Categorical variables were compared using the chi-squared test. The trend of non-zero CAC scores across the age categories was assessed in women and men separately using the Cochran-Armitage test. Continuous variables were compared using the t-test if they conformed to the normal distribution and using the Mann-Whitney U test if they did not

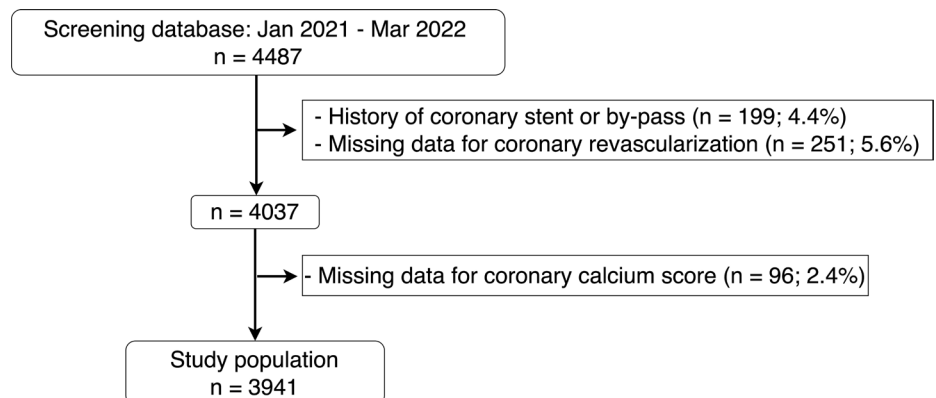


Figure 1. Flowchart for the study population.

conform to the normal distribution. The level of significance (alpha) was set at 0.05.

Percentiles were tabulated across the sex and age strata. Most of the patients had zero CAC scores. In the MESA, investigators proposed a flexible non-parametric model enabling the calculation of CAC percentiles for a particular age (rather than for age categories), while taking the inflated zero values into consideration.¹³ In order to be flexible and comparable to the MESA, the authors of the present study followed a similar method. Briefly, locally weighted scatterplot smoothing (LOWESS) regression with a bandwidth of 0.8 was applied to the log-transformed non-zero CAC score values for women and men, separately. The residuals were obtained by subtraction of the predicted value from each log-transformed observation; the residuals were then ranked, and percentiles from 1st to 99th were calculated. Adding these values to the fitted value for each age and sex provided the estimated percentile for the log-transformed non-zero CAC score values. Taking the exponential of the estimated percentiles yielded the kth percentile of non-zero

CAC distribution. For the zero CAC proportions (p), which is also calculated with LOWESS regression, the kth percentile was calculated according to the following formula: $100 * (p + [(1-p) * k] / 100)$. Using this method, the authors of the present study plotted the 25th, 50th, 75th, and 90th percentiles for women and men. The non-parametric method used a smoothing approach and estimated the percentiles from the shape of the observed CAC score distribution over the whole age range; it also had the advantage of requiring no assumption.^{13,15} Analyses were made using Stata, v. 17 (StataCorp, TX, USA).

Results

The proportion of men was higher than that of women (57.09% vs. 42.91%). The mean age was 52.20 ± 11.11 years; the mean age was higher in women than in men (54.07 ± 10.47 vs. 50.80 ± 11.37 , respectively; $P < 0.001$). While the proportions of diabetes mellitus and hypertension were significantly higher in women than in men, the smoking rate was lower. Statin use was similar in women and in men (Table 1).

The median value of the total CAC score was zero for women and men, but the values were higher in men than in women (Table 1).

A zero CAC score was observed in 2,381 (60.42%) patients, and the percentage was higher in women than in men (68.60% vs. 54.27%; $P < 0.001$). The distributions of CAC score categories over the age categories for each sex are presented in Figure 3. There was a significant decrease in patients with a zero CAC score across the age categories ($P < 0.001$), and the trend was more prominent in men than in women (the results of the chi-squared test and the P values for the non-linear were 26.7 and $P < 0.001$, respectively, in men; and 17.8 and $P = 0.013$, respectively, in women, Figure 3).

The percentiles of CAC scores over the age categories are presented in Table 2. The median CAC score (50th percentile) was zero for the age categories of <65 years in women and <55 years in men (Table 2); this suggests that at least half of women aged <65 years and men aged <55 years have a zero CAC score. This finding also indicates that a

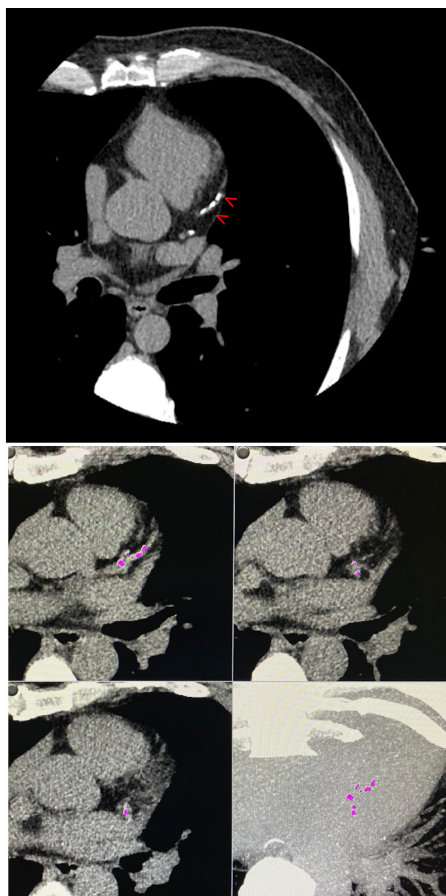
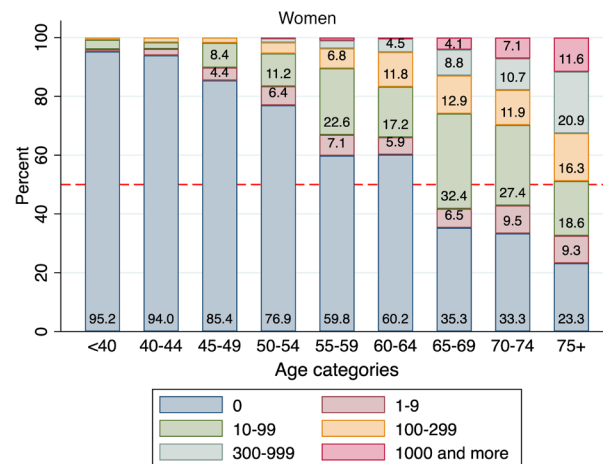
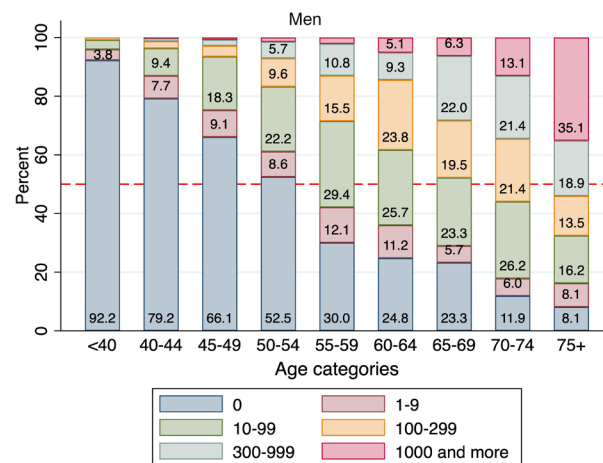


Figure 2. Calcified plaques in the coronary artery territory (arrows in the upper panel) and the postprocess of CAC score calculation with SmartScore (lower panels). CAC, coronary artery calcium.



a



b

Figure 3. (a, b) Coronary artery calcium score categories across the age categories in women (upper panel) and in men (lower panel). Some of the percentages with <4% were not shown for clarity of the figures.

10-year gap exists between women and men for the median CAC score to remain at zero.

In women aged <40 years, the 95th percentile of the CAC score was zero, meaning that a zero CAC score is expected in at least 95% of the women in this age group (Table 2). A non-zero CAC score puts a woman into the 95th percentile in the age category of 40–44 years and higher than the 75th percentile in the age categories of 45–49 and 50–54 years (Table 2). Therefore, when the cut-off value for the high-risk category is taken as the 75th percentile,³ a non-zero CAC score directly puts a woman into the high-risk category under the age categories of <55 years. On the other hand, in men, a non-zero CAC score corresponds to a >90th percentile for the age category of <40 years, and a >75th percentile for the age category of 40–44 years. Therefore, for the cut-off value of the ≥75th percentile, a non-zero CAC score directly puts a man into the high-risk category if he is in the age category of <45 years. This finding also indicates that a 10-year difference exists between women and men in terms of being in the high-risk group.

For each age, rather than the age categories, the 25th, 50th, 75th, and 90th percentiles of CAC scores are plotted in Figure 4.

Discussion

This study demonstrated that more than half of the included women and men had zero CAC scores. Also, the increase in the percentage of non-zero CAC scores with age is more prominent in the earlier ages (approximately 10 years earlier) in men than in women; furthermore, non-zero calcium approximately corresponds to the high risk [75th percentile according to the American College of Cardiology (ACC) and the American Heart Association (AHA) guidelines] group in women aged <55 years and in men aged <45 years.

Coronary artery disease is one of the leading causes of mortality and morbidity in developing countries. Preventive strategies regarding starting or intensifying preventive medications, particularly statins, are based on the individual risk of future CV events, which is usually calculated with clinical risk scores, such as Framingham, pooled cohort estimates, or SCORE-2 tools.^{3,10} To make a better risk stratification, non-traditional risk modifiers, such as a CAC score and carotid ultrasonography, have been recommended in patients with low to moderate risk for whom the decision for treatment is uncertain or at the threshold level.^{3,10,16}

Table 1. Characteristics of the study population

	Women	Men	Total	P value
n (%)	1691 (42.91)	2250 (57.09)	3941 (100.00)	
Age, mean ± SD	54.07 ± 10.47	50.80 ± 11.37	52.20 ± 11.11	<0.001
Diabetes mellitus, n (%)*	399 (23.81)	346 (15.57)	745 (19.11)	<0.001
Hypertension, n (%)*	701 (41.83)	652 (29.37)	1353 (34.73)	<0.001
Smoking, n (%)*	293 (19.42)	651 (32.80)	944 (27.02)	<0.001
Statin use, n (%)*	210 (12.57)	282 (12.69)	492 (12.64)	0.908
CAC score, mean ± SD	59.31 ± 254.16	106.79 ± 372.26	86.4 ± 327.66	<0.001
CAC score, median (IQR)	0.00 (0.00; 11.00)	0.00 (0.00; 50.00)	0.00 (0.00; 32.00)	<0.001
CAC score categories				
Zero	1160 (68.60)	1221 (54.27)	2381 (60.42)	<0.001
1-9	93 (5.50)	186 (8.27)	279 (7.08)	
10-99	255 (15.08)	414 (18.40)	669 (16.98)	
100-299	105 (6.21)	218 (9.69)	323 (8.20)	
300-999	55 (3.25)	149 (6.62)	204 (5.18)	
1000 or more	23 (1.36)	62 (2.76)	85 (2.16)	

*The denominator is slightly different due to some missing values; CAC, coronary artery calcium; IQR, interquartile range (Q1-Q3); SD, standard deviation.

Table 2. Coronary artery calcium score percentiles across the age categories in women (A) and in men (B)

A. Women								
Age	Percentiles							n
	5 th	10 th	25 th	50 th	75 th	90 th	95 th	
<40	0	0	0	0	0	0	0	126
40-44	0	0	0	0	0	0	1	182
45-49	0	0	0	0	0	11	25	274
50-54	0	0	0	0	0	43	119	295
55-59	0	0	0	0	27.5	109	170	296
60-64	0	0	0	0	42	180	281	221
65-69	0	0	0	28	104	361	578	170
70-74	0	0	0	22	148	700	1405	84
75-79	0	0	0	70	439.5	813	1330	36
80+	6	6	50	853	1628	2742	2742	7
B. Men								
Age	Percentiles							n
	5 th	10 th	25 th	50 th	75 th	90 th	95 th	
<40	0	0	0	0	0	0	9	346
40-44	0	0	0	0	0	28	88	298
45-49	0	0	0	0	9	56	127	383
50-54	0	0	0	0	50	200	385	406
55-59	0	0	0	20	130	400	600	323
60-64	0	0	1	34	179	432	1095	214
65-69	0	0	1	81	313	701	1080	159
70-74	0	0	14.5	114.5	443	1187	2218	84
75-79	0	5	38	215	1176	1795	4002	31
80+	153	153	422	643.5	1308	2656	2656	6

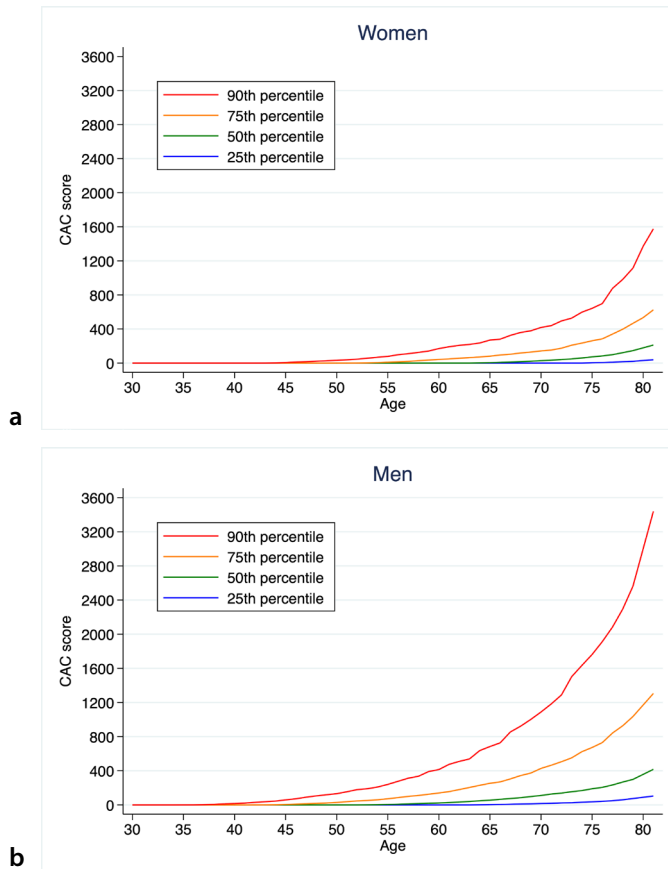


Figure 4. (a, b) Percentile plots for CAC scores in women and men. CAC, coronary artery calcium.

A CAC score is usually used either as an absolute or percentile value. In the MESA, the absolute score was found to be more predictive than the percentile score in predicting CV outcomes.⁷ However, percentile scores are preferable in young patients and women, as the absolute CAC score has low specificity in the risk reclassification in these patients due to the low probability of calcium in the atherosclerotic plaques.⁹⁻¹¹ The ESC prevention guidelines recommend comparing the CAC score with the values expected for a patient of the same age and sex.¹⁰ The ACC/AHA prevention guidelines use the cut-off value of ≥ 100 Agatston units or the 75th percentile to determine the high-risk group among patients with moderate risk or selected borderline risk according to the clinical risk scores.³

The authors of the present study found that 68.6% of women and 54.3% of men had zero CAC scores. The proportion of zero CAC scores differs between studies. For example, the proportion is 49% in the CAC consortium,¹¹ 36% in women and 17% in men in the ELSA-Brasil study,¹² and 62% in women and 40% in men in the MESA.¹³ These differences may be explained by the differences between the population characteristics, ethnicity, and age. The authors of the present study also observed that the mean CAC scores were lower

than the values for the white population in the MESA (59 vs. 96 for women and 106 vs. 298 for men).¹⁷ The major factor for these differences is that the white population in the MESA is, on average, 11 years older than that in the present study population. However, its effect on the interpretation of the results is probably negligible, as both studies present age-category-specific percentile values and plot the percentiles across ages rather than giving overall mean values alone. As expected, both studies showed that an increase in the CAC score with age is more prominent in men than in women.

Men usually develop CV diseases approximately 9–10 years earlier than women.¹⁸ The CAC consortium study showed that a 75% prevalence of a non-zero CAC score was observed nine years earlier in men than in women.¹¹ As expected, the present study shows that the percentage of patients with zero CAC score decreases significantly with age and that the decrease is more noticeable in men than in women. Moreover, when the cut-off value of percentiles for the definition of the high-risk group is taken as the 75th percentile, a non-zero CAC score corresponds to the high-risk group for the age categories of <55 years in women and <45 years in men. This finding simplifies the categorization of

patients, especially for busy clinicians, when using a treatment decision for a given patient with a borderline risk group based on the conventional risk scores. Similarly to the present findings, in the white ethnicity subset of the MESA, the CAC score for the 75th percentile was zero for the age categories of women aged <55 years.¹³ The MESA included participants between the ages of 45 and 84; therefore, no information for men aged <45 years was provided. Thus, no comparison could be made with the present results. In another analysis of the MESA, non-zero CAC was found to be a >75th percentile marker in women aged <60 years and in men aged <50 years in the overall population.¹⁹ Although the age limits are slightly different, the results are consistent with the present findings as well as with previous studies regarding a ~10-year gap of protection between women and men.^{11,18} It should be noted that these simplifications are based on age categories rather than on a particular age. More reliable risk estimation for each age can be obtained using the percentile plots for a certain age.

An overexpression of zero CAC values in the dataset may affect choosing statistical approaches. The traditional approach in calculating percentiles is to calculate the percentiles across each age category (Table 2).²⁰ On the other hand, the MESA investigators used a different approach that has several advantages to the conventional method, such as the flexibility of calculating percentiles for a particular age rather than age categories, considering the overexpression of zero values, and requiring no statistical assumption.^{13,15} In the present study, the percentiles were plotted by applying the method used in the MESA, letting the authors take advantage of this method and ensuring that the results would be comparable with other studies.

The percentiles may vary depending on the population. To the authors' current knowledge, centers providing CAC score percentiles in their reports in Turkey are probably using the data from the MESA for the white/Caucasian population due to a lack of data obtained from Turkey. The present study provides local data that may be used in treatment decisions for preventive measures, particularly statin treatment, in patients in the borderline risk category (according to the guidelines' recommendation).

A considerable number of patients undergoing coronary CTA have non-significant atherosclerotic plaques. The Scottish CT of the HEART study demonstrated that lesion

severity, CV risk score, CAC score, and plaque characteristics were all important factors for future CV events in univariable analyses.²¹ However, in the multivariable analysis, only the CAC score was found to be an independent risk factor for CV events. These findings suggest that the risk is dominated by CAC; this is probably due to being a surrogate marker of an atherosclerotic plaque burden. Therefore, the present data might also be useful in decision-making for statin treatment in patients with non-significant coronary plaques on coronary CTA, as it provides overall information for atherosclerotic plaque burdens.

The present study has both its strengths and its limitations. First, the data comes from a single center; hence, it cannot be said that the data is truly representative of the Turkish population. However, Bilkent City Hospital is one of the biggest hospitals in Turkey and admits patients from a diverse geographical population; this may, at least partially, reduce the negative impact on result generalizability. Second, CAC score calculation is appropriate and useful for patients without “known” significant coronary artery stenosis at the baseline. As the data was obtained from the hospital records, the history of coronary artery disease at the baseline could not be obtained in all patients. However, patients with a stent or bypass graft were excluded from the study. On the other hand, the study authors do not consider this an issue of major concern, as most patients with severe coronary artery disease undergo stenting or coronary bypass surgery, and patients with typical symptoms suggesting severe coronary artery disease are appropriately referred to conventional angiography rather than coronary CTA. Third, due to the retrospective nature of the study, there is no reliable information available on the symptom status. The present study’s population includes a referral population that underwent mostly CAC scoring and coronary CTA, making it more suitable for application of the study results. Considering the cost and difficulty of conducting a large prospective study, the present study provides acceptable results until such a prospective study is conducted and published. Fourth, the present data were obtained retrospectively from the hospital CT reports; therefore, the intra-observer and interobserver agreement of CAC score measurements was not assessed. However, the study authors think that this might not be a major issue, as CAC scoring is well-standardized, and the imag-

es are interpreted by dedicated and experienced radiologists at the Bilkent City Hospital. Fifth, this study provides cross-sectional data for CAC score percentiles in women and men across age groups. As in similar studies, the patient’s lifestyle, medications, and environmental factors were not taken into consideration for percentile calculation. As these factors are important potential confounding factors, they should be included in studies that evaluate (or create) a prediction model for future events. The present study provides only snapshot information for the study population but does not provide a prediction model. On the other hand, it provides information for a non-zero CAC score that corresponds to the guidelines-recommended cut-off value for the high-risk category (75th percentiles).

In conclusion, this study provides CAC score percentiles for sex and age categories from 3,941 participants referred for CAC scoring and/or coronary CTA; it also demonstrates that more than half of the study population have zero CAC scores. Also, a non-zero CAC score develops approximately 10 years earlier in men than in women, and a non-zero CAC score is assigned to the high-risk category (75th percentile) in women aged <55 years and in men aged <45 years.

Conflict of interest disclosure

The authors declared no conflicts of interest.

References

- Vaduganathan M, Mensah GA, Turco JV, Fuster V, Roth GA. The global burden of cardiovascular diseases and risk: a compass for future health. *J Am Coll Cardiol.* 2022;80(25):2361-2371. [\[CrossRef\]](#)
- Nowbar AN, Gitto M, Howard JP, Francis DP, Al-Lamee R. Mortality from ischemic heart disease. *Circ Cardiovasc Qual Outcomes.* 2019;12(6):e005375. [\[CrossRef\]](#)
- Arnett DK, Blumenthal RS, Albert MA, et al. 2019 ACC/AHA guideline on the primary prevention of cardiovascular disease: a report of the American College of Cardiology/American Heart Association Task Force on Clinical Practice Guidelines. *J Am Coll Cardiol.* 2019;74(10):e177-e232. Erratum in: *J Am Coll Cardiol.* 2019;74(10):1429-1430. Erratum in: *J Am Coll Cardiol.* 2020;75(7):840. [\[CrossRef\]](#)
- SCORE2 working group and ESC Cardiovascular risk collaboration. SCORE2 risk prediction algorithms: new models to estimate 10-year risk of cardiovascular disease

in Europe. *Eur Heart J.* 2021;42(25):2439-2454. [\[CrossRef\]](#)

- Erbel R, Möhlenkamp S, Moebus S, et al. Coronary risk stratification, discrimination, and reclassification improvement based on quantification of subclinical coronary atherosclerosis: the Heinz Nixdorf Recall study. *J Am Coll Cardiol.* 2010;56(17):1397-1406. [\[CrossRef\]](#)
- Detrano R, Guerci AD, Carr JJ, et al. Coronary calcium as a predictor of coronary events in four racial or ethnic groups. *N Engl J Med.* 2008;358(13):1336-1345. [\[CrossRef\]](#)
- Budoff MJ, Nasir K, McClelland RL, et al. Coronary calcium predicts events better with absolute calcium scores than age-sex-race/ethnicity percentiles: MESA (Multi-Ethnic Study of Atherosclerosis). *J Am Coll Cardiol.* 2009;53(4):345-352. Erratum in: *J Am Coll Cardiol.* 2009;53(16):1474. [\[CrossRef\]](#)
- de Ronde MWJ, Khoshiwal A, Planken RN, et al. A pooled-analysis of age and sex based coronary artery calcium scores percentiles. *J Cardiovasc Comput Tomogr.* 2020;14(5):414-420. [\[CrossRef\]](#)
- Javaid A, Dardari ZA, Mitchell JD, et al. Distribution of coronary artery calcium by age, sex, and race among patients 30-45 years old. *J Am Coll Cardiol.* 2022;79(19):1873-1886. [\[CrossRef\]](#)
- Visseren FLJ, Mach F, Smulders YM, et al. 2021 ESC Guidelines on cardiovascular disease prevention in clinical practice. *Eur Heart J.* 2021;42(34):3227-3337. [\[CrossRef\]](#)
- Wang F, Rozanski A, Dey D, et al. Age- and gender-adjusted percentiles for number of calcified plaques in coronary artery calcium scanning. *J Cardiovasc Comput Tomogr.* 2019;13(6):319-324. [\[CrossRef\]](#)
- Pereira AC, Gomez LM, Bittencourt MS, et al. Age, gender, and race-based coronary artery calcium score percentiles in the Brazilian Longitudinal Study of Adult Health (ELSA-Brasil). *Clin Cardiol.* 2016;39(6):352-359. [\[CrossRef\]](#)
- McClelland RL, Chung H, Detrano R, Post W, Kronmal RA. Distribution of coronary artery calcium by race, gender, and age: results from the Multi-Ethnic Study of Atherosclerosis (MESA). *Circulation.* 2006;113(1):30-37. [\[CrossRef\]](#)
- Agatston AS, Janowitz WR, Hildner FJ, Zusmer NR, Viamonte M Jr, Detrano R. Quantification of coronary artery calcium using ultrafast computed tomography. *J Am Coll Cardiol.* 1990;15(4):827-832. [\[CrossRef\]](#)
- Gerke O, McClelland RL. Nonparametric percentile curve estimation for a nonnegative marker with excessive zeros. *MethodsX.* 2022;9:101757. [\[CrossRef\]](#)
- Durhan G, Hazirolan T, Sunman H, et al. Does coronary calcium scoring with a SCORE better

- predict significant coronary artery stenosis than without? Correlation with computed tomography coronary angiography. *Eur Radiol.* 2015;25(3):776-784. [\[CrossRef\]](#)
17. Bild DE, Detrano R, Peterson D, et al. Ethnic differences in coronary calcification: the Multi-ethnic Study of Atherosclerosis (MESA). *Circulation.* 2005;111(10):1313-1320. [\[CrossRef\]](#)
 18. Anand SS, Islam S, Rosengren A, et al. Risk factors for myocardial infarction in women and men: insights from the INTERHEART study. *Eur Heart J.* 2008;29(7):932-940. [\[CrossRef\]](#)
 19. Osei AD, Mirbolouk M, Dardari Z, et al. A simple approach to the identification of guideline-based coronary artery calcium score percentiles (From the Multi-Ethnic Study of Atherosclerosis). *Am J Cardiol.* 2022;179:18-21. [\[CrossRef\]](#)
 20. Schmermund A, Möhlenkamp S, Berenbein S, et al. Population-based assessment of subclinical coronary atherosclerosis using electron-beam computed tomography. *Atherosclerosis.* 2006;185(1):177-182. [\[CrossRef\]](#)
 21. Williams MC, Moss AJ, Dweck M, et al. Coronary artery plaque characteristics associated with adverse outcomes in the SCOT-HEART study. *J Am Coll Cardiol.* 2019;73(3):291-301. [\[CrossRef\]](#)



Centrilobular ground-glass nodule pattern in acute myeloid leukemia patients receiving cytosine arabinoside chemotherapy: an important form of drug-induced lung disease

Ömer Önder¹
 Selin Ardalı Düzgün²
 Gamze Durhan²
 Orhan Macit Arıyürek²

¹Iğdır Dr. Nevruz Erez State Hospital, Clinic of Radiology, Iğdır, Turkey

²Hacettepe University Faculty of Medicine, Department of Radiology, Ankara, Turkey

Dear Editor,

We read with great interest the pictorial essay titled “Drug-induced lung disease: a brief update for radiologists” by Ufuk et al.¹ in the January 2023 of *Diagnostic and Interventional Radiology* issue. In this article, the authors comprehensively covered the imaging patterns and differential diagnoses of drug-induced lung disease (DILD) with demonstrative case examples.¹ We would like to mention a few points that may contribute to this article, which focuses on this complex issue, a popular topic in radiology.

First, according to the literature, a pulmonary hemorrhage can be classified as a radiological finding of DILD. A pulmonary hemorrhage can be seen as ground-glass opacities (GGO) or consolidations and is known to be associated with drugs such as penicillamine, rituximab, and cocaine.²

Second, Sridhar et al.³ proposed an alternative imaging-based classification system for DILDs consisting of six computed tomography patterns. Although this classification system overlaps with the patterns stated in the article, some differences draw attention.¹ “Organizing pneumonia” and “sarcoid-like” patterns show significant overlap. However, “fibrotic”, “diffuse GGO”, and “centrilobular ground-glass nodule (GGN)” patterns are suggested instead of “non-specific interstitial pneumonia”, “diffuse alveolar damage”, and “hypersensitivity pneumonitis” patterns, respectively.^{1,3} Last, the “linear-septal” pattern indicates the findings of interstitial pulmonary edema.³

As an oncological lung imaging center, we have seen the centrilobular GGN pattern in several acute myeloid leukemia (AML) cases receiving intermediate/high dose cytosine arabinoside (Ara-C) chemotherapy, and it causes a differential diagnosis problem. Therefore, we want to share our experience on this matter through two cases. Although Ara-C pulmonary toxicity mainly presents with non-cardiogenic pulmonary edema, in 2009, Chagnon et al.⁴ described a new pattern characterized by bilateral diffuse/upper lobe-predominant centrilobular nodules in six febrile neutropenic AML patients who had recently received Ara-C (Figure 1).

We believe that awareness of this pattern can assist radiologists in shaping patient management. However, opportunistic infections, especially miliary tuberculosis, should always be considered in febrile neutropenia. Although miliary tuberculosis is generally characterized by randomly distributed uniform micronodules with sharper contours, relying solely on radiological findings might have devastating consequences. Therefore, as emphasized by Ufuk et al.¹, multidisciplinary meetings are vital, especially to establish a diagnosis and determine the best management plan for patients with suspected DILD. Nevertheless, even with a multidisciplinary approach, it is not always possible to make a definitive diagnosis due to various confounders, including radiological mimickers, empirical treatments, limitations of microbiological/serological examinations, comorbidities, and variability in the drug-effect temporal relationship (Figure 2). Thus, it is important to keep in mind that proper patient management is far more crucial than the definitive diagnosis.

KEYWORDS

CT, chemotherapy, lung, pneumonitis, pulmonary toxicity

Corresponding author: Gamze Durhan

E-mail: gamzedurhan@gmail.com

Received 27 March 2023; revision requested 02 April 2023; last revision received 06 April 2023; accepted 08 April 2023.



Epub: 03.05.2023

Publication date: 08.01.2023

DOI: 10.4274/dir.2023.232217

You may cite this article as: Önder Ö, Ardalı Düzgün S, Durhan G, Arıyürek OM. Centrilobular ground-glass nodule pattern in acute myeloid leukemia patients receiving cytosine arabinoside chemotherapy: an important form of drug-induced lung disease. *Diagn Interv Radiol.* 2024;30(1):28-29.

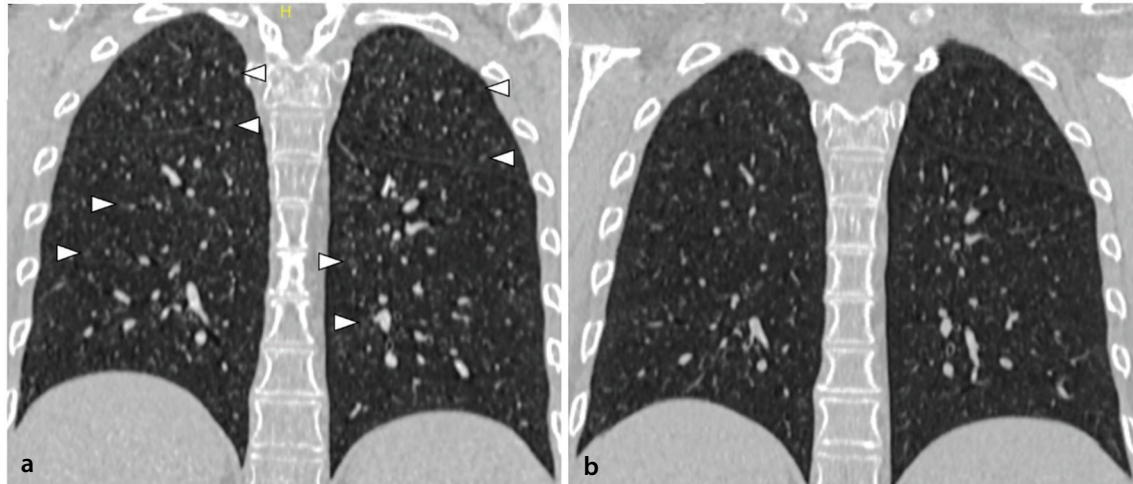


Figure 1. A 31-year-old female patient with acute myeloid leukemia. One week after receiving cytosine arabinoside (Ara-C) chemotherapy, a non-enhanced chest computed tomography (CT) was performed with complaints of low-grade fever and mild dyspnea. (a) Coronal plane chest CT shows bilateral upper lobe predominant centrilobular ground-glass nodules (arrowheads). The case was discussed in a multidisciplinary meeting due to the suspicion of miliary tuberculosis. Since all microbiological examinations were negative and clinical presentation was mild, the findings were primarily attributed to the Ara-C effect. After stopping chemotherapy, her symptoms regressed. (b) Follow-up chest CT 1 month later reveals almost complete resolution of radiological findings.

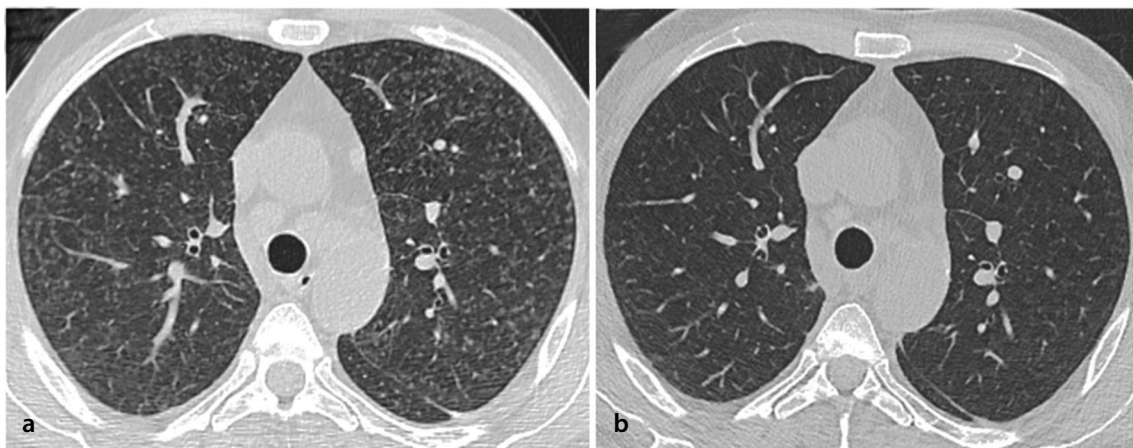


Figure 2. A 53-year-old febrile neutropenic male patient with acute myeloid leukemia. Five days after cytosine arabinoside (Ara-C) chemotherapy, a non-enhanced chest computed tomography (CT) was performed due to new-onset dyspnea and mild hypoxia. (a) Axial plane chest CT shows bilateral diffuse centrilobular ground-glass nodules. The case was discussed in a multidisciplinary meeting due to the suspicion of miliary tuberculosis. Radiologically, it was stated that the Ara-C effect might have caused this pattern. However, despite all negative microbiological examinations, miliary tuberculosis could not be excluded due to severe clinical presentation and previous history of contact with tuberculosis. Therefore, the patient was considered to have miliary tuberculosis. After stopping chemotherapy, an empirical antituberculosis regimen was started in addition to broad-spectrum antibiotics. (b) Follow-up chest CT 2 months later reveals complete resolution of centrilobular nodules. Retrospectively, the radiological findings were thought to be due to drug-induced lung disease, although it was not possible to make a definitive diagnosis in this case due to empirical antituberculosis treatment initiated simultaneously with chemotherapy discontinuation.

Conflict of interest disclosure

The authors declared no conflicts of interest.

References

1. Ufuk F, Bayraktaroğlu S, Rüksan Ütebey A. Drug-induced lung disease: a brief update for radiologists. *Diagn Interv Radiol.* 2023;29(1):80-90. [\[CrossRef\]](#)
2. Distefano G, Fanzone L, Palermo M, et al. HRCT Patterns of drug-induced interstitial lung diseases: a review. *Diagnostics (Basel).* 2020;10(4):244. [\[CrossRef\]](#)
3. Sridhar S, Kanne JP, Henry TS, Revels JW, Gotway MB, Ketani LH. Medication-induced pulmonary injury: a scenario- and pattern-based approach to a perplexing problem. *Radiographics.* 2022;42(1):38-55. [\[CrossRef\]](#)
4. Chagnon K, Boissel N, Raffoux E, Dombret H, Tazi A, Bergeron A. A new pattern of cytosine-arabioside-induced lung toxicity. *Br J Haematol.* 2009;147(5):771-774. [\[CrossRef\]](#)



Earthquakes from a radiological perspective: what is demanded from the radiologists, and what can we do? A pictorial review

Sonay Aydin¹
 Omer Kazci²
 Bunyamin Ece³
 Mecit Kantarci¹

¹Erzincan Binali Yıldırım University Faculty of Medicine, Department of Radiology, Erzincan, Turkey

²Ankara Training and Research Hospital, Clinic of Radiology, Ankara, Turkey

³Kastamonu University Faculty of Medicine, Department of Radiology, Kastamonu, Turkey

ABSTRACT

Earthquakes are among the most destructive and unpredictable natural disasters. Various diseases and ailments, such as bone fractures, organ and soft-tissue injuries, cardiovascular diseases, lung diseases, and infectious diseases, can develop in the aftermath of severe earthquakes. Digital radiography, ultrasound, computed tomography, and magnetic resonance imaging are significant imaging modalities utilized for the quick and reliable assessment of earthquake-related ailments to facilitate the planning of suitable therapy. This article examines the usual radiological imaging characteristics observed in individuals from quake-damaged regions and summarizes the strengths and functionality of imaging modalities. In such circumstances, where quick decision-making processes are life-saving and essential, we hope this review will be a practical reference for readers.

KEYWORDS

Earthquakes, disasters, embolism, emergencies, crush injuries, compartment syndromes, multiple trauma, radiology information systems

Earthquakes are among the most destructive and unpredictable natural disasters.¹ A magnitude 7.7 foreshock occurred in the epicenter of the Kahramanmaraş earthquake at 04:17:35 (UTC +03:00) on February 6, 2023. Then, at 13:24:49 (UTC+03:00), another earthquake of magnitude 7.6 occurred with its epicenter in Kahramanmaraş-Elbistan (Figure 1).^{2,3} The natural calamity devastated 10 cities, and thousands of injured individuals were taken to hospitals throughout Turkey. In the first month after the earthquake, it was reported that 46,104 people had perished and over 100,000 were injured as a result of the quakes centered in Kahramanmaraş.⁴

Various diseases and ailments, such as bone fractures, organ and soft-tissue injuries, cardiovascular diseases, lung diseases, and infectious diseases, can develop in the aftermath of severe earthquakes. Digital radiography (DR), ultrasound (US), computed tomography (CT), and magnetic resonance imaging (MRI) are significant imaging modalities utilized for the quick and reliable assessment of earthquake-related ailments to facilitate the planning of suitable therapy.⁵

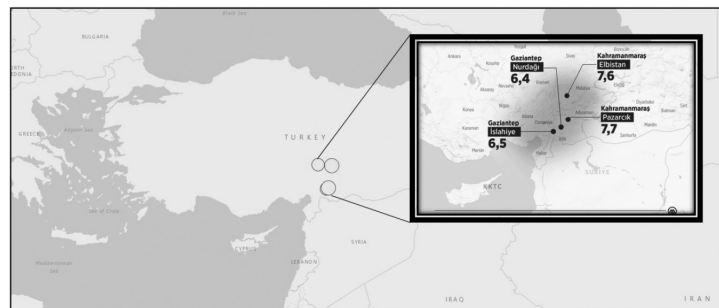


Figure 1. Epicenters and magnitudes of the recent earthquakes occurring in the south of Turkey.

Corresponding author: Omer Kazci

E-mail: omerkazci1990@gmail.com

Received 17 February 2023; revision requested 06 March 2023, accepted 03 April 2023.



Epub: 24.04.2023

Publication date: 08.01.2023

DOI: 10.4274/dir.2023.232157

You may cite this article as: Aydin S, Kazci O, Ece B, Kantarci M. Earthquakes from a radiological perspective: what is demanded from the radiologists, and what can we do? A pictorial review. *Diagn Interv Radiol.* 2024;30(1):30-41.

Based on previously published experiences after major earthquakes, this article examines the typical radiological imaging characteristics observed in individuals from quake-damaged regions and summarizes the strengths and functionality of imaging modalities. In this way, it aims to provide a practical source of information to radiologists during fieldwork in large-scale disasters where rapid diagnosis is of great importance.

Imaging method availability and utility

Ultrasound: US is the most useful and accessible method, both at the time of the disaster and in the following six-hour period. The main reason for this is the energy requirement of imaging methods. As the sole method of cross-sectional imaging accessible while CT was unavailable, US was widely utilized (it is easy to get to, can be used on the go, and helps doctors figure out which injuries are superficial and which are internal). US proved invaluable in the initial phases following the disaster, especially in the absence of CT, and should be incorporated into local disaster or mass-casualty strategies.⁶ Larger devices are less useful than portable ones. Even in the absence of biochemical laboratory tests, portable ultrasonography instruments can aid in narrowing the differential diagnosis or ruling out more serious illnesses. It is portable, simple, and painless, and in many instances, it has provided rapid results.⁷

Focused Assessment with Sonography for Trauma (FAST) is the main sonographic method for earthquake-related ailments (Figure 2). After Hurricane Katrina, 9/11 in New York, the Lebanon War in 2006, and the Iran earthquake in 2010, FAST was found to be successful in assessing and triaging patients during

periods of high patient volume. In the acute post-disaster phase, it can be utilized to check for hemothorax/pneumothorax, solid organ injury, fractures, pregnancy and vascular investigations, pediatric head scans, and intravenous access help.⁸ A clinician can perform FAST with the same sensitivity but less specificity compared to a radiology assistant. In addition, FAST can reduce the number of needless CT scans. In a study conducted after an earthquake in Christchurch, New Zealand, it was seen that the imaging method most frequently used and most accessible by physicians providing post-disaster health care was US (especially FAST).^{7,8}

Computed tomography: Power cuts and damage to health centers at the time of disasters seriously restrict the use of CT. It has been shown that the first use of CT in the delivery of health care to earthquake victims may extend to the fifth hour after the earthquake.⁶ Pan-CT examinations, if available, can guide emergency surgeries; nevertheless, in situations with a high patient volume, it is impossible and impractical to perform pan-CT on every patient. Therefore, FAST-guided CT examinations provide better and more effective results,⁸ and contrast-enhanced CT examinations should be approached with extreme caution. In circumstances that impede kidney function, such as crush syndrome caused by earthquakes, the use of contrast material may induce severe complications. Again, if contrast agent extravasation occurs in cases with compartment syndrome induced by earthquake-related traumas, the situation may worsen. However, in some special cases, such as suspected major vascular injury, dissection, or pulmonary embolism in a clinical examination, intravenous contrast agents can be administered without waiting for the results of the patient's kidney function tests.⁹

Digital radiography: The use of DR is also limited, for the same reasons as CT; however, DR can be commissioned more quickly because its energy requirement is less than CT. The fact that mobile DR devices allow bedside examinations provides great convenience, especially in cases with limited mobility. Versatile DR applications performed at the bedside are an important alternative in cases where CT cannot be reached. However, the fact that the batteries of these devices are sufficient for a finite time limits their use if there is a charging problem.⁶

Magnetic resonance imaging: Due to the possibility of quenching (quenching is the quick release of the liquid cryogen that keeps the MRI magnet in a superconducting state. If gas leaks into a room instead of leaving the building after an earthquake or other disaster, there is a chance of suffocation and freezing) MRI should not be utilized immediately following an earthquake.^{6,8}

Reporting alternatives

Serious difficulties have been experienced in accessing radiological images during disasters. For this reason, the ideal reporting method is verbal reporting if there is an opportunity to work closely with the clinician. In cases where there is no opportunity to work in close contact, written reports that provide short and concise information and that can be created quickly come to the forefront.⁶ After the recent earthquake disaster, it is satisfying that a system that allows remote, fast, and effective reporting was established very quickly (Figure 3).

Earthquake-related injuries

Traumatic injuries

Annually, earthquakes are the most lethal of all natural disasters. Between 2007 and 2017, 350,000 people died and over one

Main points

- Earthquake-induced power outages may limit the use of computed tomography and digital radiography and the risk of quenching may limit the use of magnetic resonance imaging.
- Ultrasonography, especially Focused Assessment with Sonography for Trauma, stands out as the most accessible and functional imaging method in disaster situations such as earthquakes.
- Contrast medium should be used with extreme caution due to the risk of rhabdomyolysis-related nephropathy.
- Knowing the typical features and distribution of earthquake-related injuries is important for rapid diagnosis and the detection of accompanying pathologies.

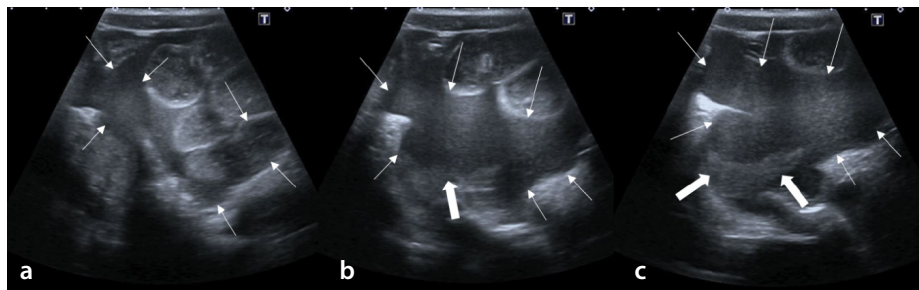


Figure 2. Intra-abdominal hemorrhage. The patient was trapped for 12 hours by earthquake debris. Eight-year-old boy, Focused Assessment with Sonography for Trauma ultrasonography images. (a) Axial view of the lower abdominal quadrant, diffuse free fluid with multiple internal echogenicities is seen between the inframezocolic bowel loops (thin arrows); (b, c) in more inferior sections, free fluid (thin arrows) with multiple internal echogenicities in the lower abdomen/pelvic region. Fluid–fluid leveling within the hemorrhage (thick arrows).

million were injured. Earthquakes appear to have a death-to-injury ratio of approximately 1:3–4,¹⁰ though this is variable depending on the severity of the injury.

In studies conducted both in our country and globally, it has been shown that the most common injuries after earthquakes are traumatic injuries, and the most needed interventions are orthopedic procedures. Debridement was the most common operation, followed by open reduction internal fixation and then closed reduction-casting.^{11–13}

Earthquake-related traumatic injuries are most common in the extremities, particularly the lower extremities. In order of frequency, extremities are followed by the thorax (Figures 4, 5), spinal injuries (Figures 6, 7), pelvic fractures, cranial and maxillofacial injuries, and abdominal traumatic findings (Figure 8).¹⁴ The femur is the most often injured bone in the extremities, followed by the tibial shaft and the ankle (Figures 9, 10). The humerus is the most often injured bone in the upper limb (Figure 11).¹⁵ It has been shown that earthquake-related lower extremity fractures, unlike other traumas, have a high rate of being multiple and comminuted (Figure 12).^{16,17} The characteristics of earthquake-related fractures seen in children are similar to adults; fractures are most commonly seen in the lower extremities, and external fixation is usually required.¹⁸

Pelvic fractures are generally seen as multiple and bilateral (Figure 13). In a study conducted in China, the most common pelvic fracture subtype was reported as type C, followed by type B3 and type B2.¹⁹ In a study conducted in Turkey, type C2 fractures were found most frequently, similar to the Chinese data (Table 1).^{20,21}



Figure 3. Workload management after the earthquake.

When the distribution of maxillofacial traumas is examined, it is seen that mandibular fractures are the most common, followed by the zygomatic complex and maxilla. Similar to lower extremity fractures, multiple and comminuted fractures are common. Cranial injuries and lower extremity fractures are the most common types of injuries to accompany maxillofacial fractures (Figure

14).^{22,23} Some studies report that nasal bone, ethmoid bone, and orbital fractures are also common. Maxillofacial fractures are injuries that require a multidisciplinary approach due to the complex anatomy of the region and the frequent occurrence of accompanying cranial traumas.²³

Additionally, one of the disorders associated with earthquakes is aggressive rhab-

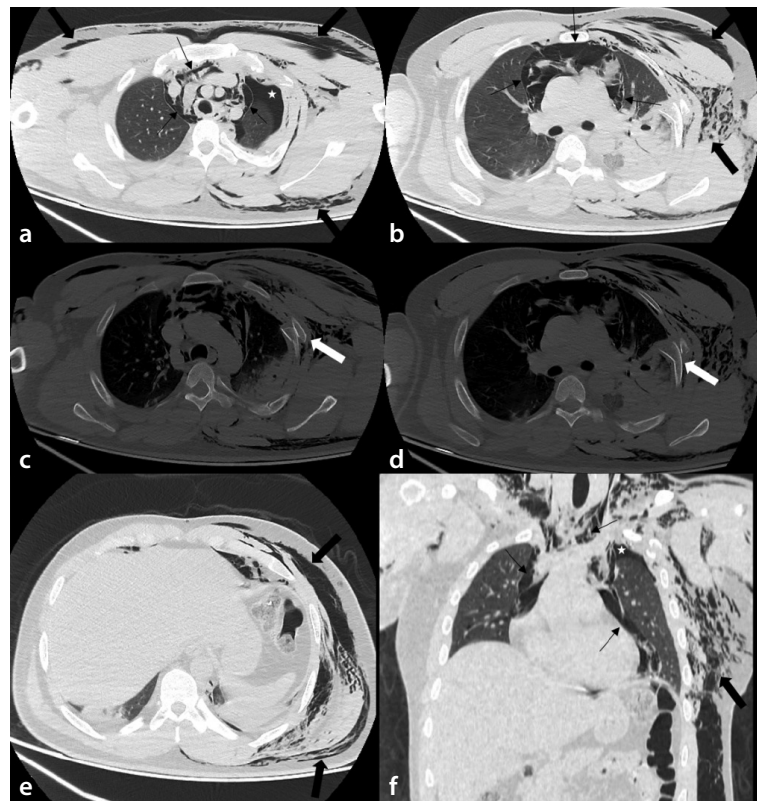


Figure 4. Traumatic pneumothorax, pneumomediastinum the patient was trapped for 19 hours by earthquake debris. Forty-three-year-old male. (a) On the axial images passing through the upper thoracic region, multiple air densities in the mediastinum (thin black arrows, pneumomediastinum), air densities near the left lung upper lobe (asterisk, pneumothorax), and diffuse subcutaneous emphysema more dominantly in the left hemithorax are seen (thick black arrows). (b) Pneumomediastinum (thin black arrows) and diffuse subcutaneous emphysema (thick black arrows) are seen in the axial sections passing through the middle part of the thorax. (c, d) Displaced rib fracture and extension of bone fragment into lung parenchyma on bone window axial section images are seen (thick white arrows). (e) Diffuse subcutaneous emphysema (thick black arrows) is seen in the axial sections passing through the inferior part of the thorax. (f) Pneumomediastinum (thin black arrows), pneumothorax (asterisk) and diffuse subcutaneous emphysema (thick black arrows) are seen in the coronal images.

Table 1. Tile classification of pelvic fractures

Type A (the pelvic ring is stable both rotationally and vertically)	A1: The fracture is observed, but the pelvic ring is not affected A2: A pelvic ring fracture is noticed, but the pelvic ring is stable
Type B (the pelvic ring is vertically stable but rotationally unstable)	B1: The appearance is likened to an open book B2: Detecting ipsilateral lateral compression B3: The contralateral or bucket handle injury pattern is examined for lateral compression.
Type C (both rotationally and vertically, the pelvic ring is unstable)	C1: Unilateral C2: Bilateral C3: Associated with acetabular fracture

domyolysis, which appears heterogeneously hypodense on CT. On post-contrast images, there may be rim enhancement. Rhabdomyolysis exhibits more diverse findings on MRI. It is also possible to detect the status of myonecrosis with MRI findings; in mild to moderate cases, damaged muscles exhibit edema, with signal intensity matching the severity of the injury. If severe myonecrosis

occurs, two different patterns can be seen: (a) homogeneously iso/hyperintense on T1 weighted images (WI), homogeneously hyperintense on T2WI/short tau inversion recovery homogeneously enhancing on postcontrast T1WI, and (b) homogeneously/heterogeneously hyperintense on T1WI, heterogeneously hyperintense on T2WI, rim-like enhancement on postcontrast T1WI

(Figure 15).²⁴ Based on data from an experimental animal study, contrast-enhanced ultrasonography (CEUS) is effective in the prehospital or bedside diagnosis of rhabdomyolysis. The study revealed that, compared with uninjured muscles, injured muscles showed early and high enhancement in CEUS images.²⁵

Acute compartment syndrome is a surgical emergency that poses limb- and life-threatening risks. It is a painful condition brought on by increased intracompartmental pressure, which compromises perfusion and causes muscle and nerve damage inside the affected compartment. The diagnosis of acute compartment syndrome is based on clinical symptoms and measurements of compartmental pressures. Utilization of imaging techniques is often restricted, and in some instances, imaging can delay diagnosis and surgical therapy. In addition to the aforementioned signs of rhabdomyolysis, MRI reveals herniation of muscle through a tear in the surrounding fascia. In addition, CT angiography and color Doppler US can be utilized to detect vascular luminal constriction due to elevated intracompartmental pressure (Figure 16).^{26,27}

Non-traumatic injuries

Cerebrovascular diseases: The increase in blood pressure and heart rate caused by the activation of the sympathetic nervous system in those impacted by a natural disaster is known as "disaster hypertension".²⁸ Hypertension is connected with an increased risk of stroke (Figure 17) and heart attack and is one of the primary causes of cardiovascular disease. In addition, various challenges connected with evacuee life (such as poor diet and water, difficulty obtaining regular medicine, and mental stress) may have a negative impact on disaster hypertension, resulting in cerebrovascular strokes and cardiovascular disorders. It was known that several of the patients in the evacuation facilities had suffered cerebrovascular attacks.²⁹ One month after an earthquake, spinal subdural and epidural hematomas that were not caused by trauma were also observed. It has been claimed that irregular use of antiplatelet medications and/or an uncomfortable posture resulting from spending nights in certain vehicles are potential risk factors for these types of hematomas.⁵

Cardiovascular diseases: Heart failure (HF), lower-extremity deep vein thrombosis (DVT), and pulmonary thromboembolism (PTE) are among the leading non-traumatic

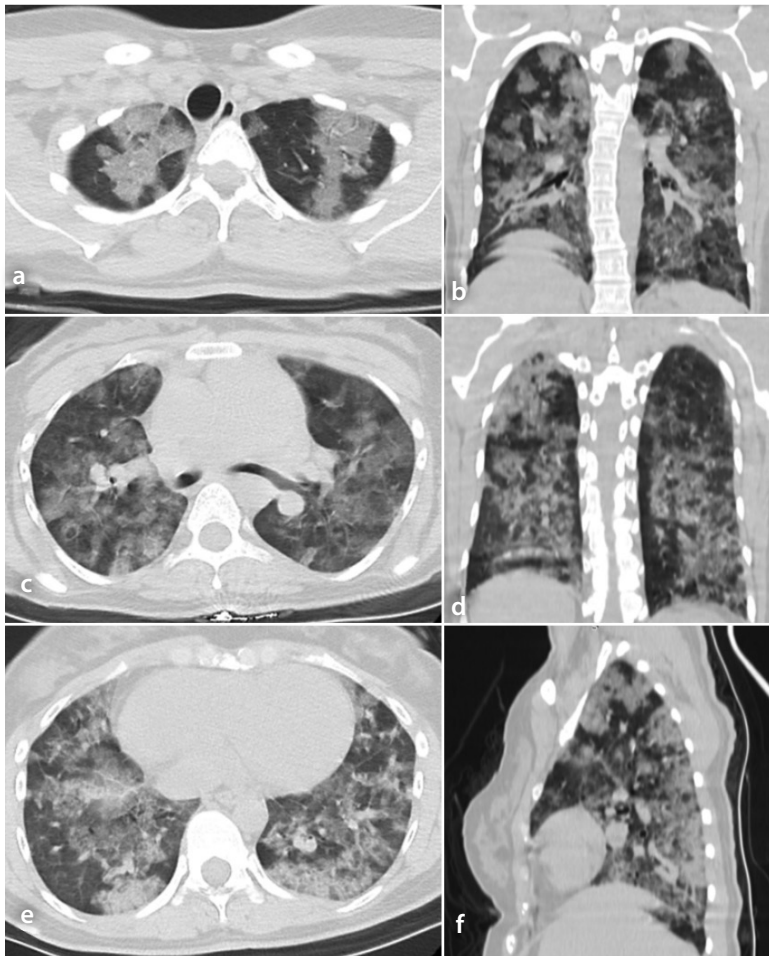


Figure 5. Diffuse alveolar hemorrhage. The patient was trapped for 22 hours by earthquake debris. Forty-three-year-old male. Diffuse widespread ground glass opacities and consolidations. (a, c, e) Axial images from different levels; (b, d) coronal images from different levels; (f) sagittal.

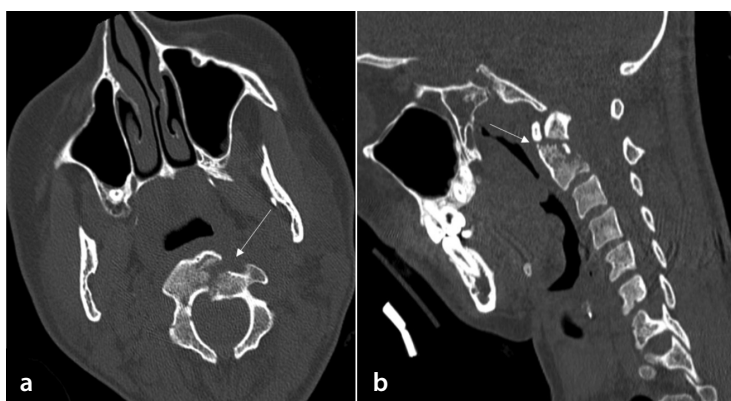


Figure 6. Type 2 odontoid fracture. The patient was trapped for 9 hours by earthquake debris. Thirty-nine-year-old male. A fragmented and displaced fracture of the odontoid process (arrows) is seen on axial (a) and coronal (b) computed tomography images.

diseases associated with earthquakes (Figures 18, 19).^{30,31} While HF increases occur over long periods, such as into the seventh week

after the earthquake, PTE and DVT cases increase closer to the occurrence of the earthquake. In addition, DVT and PTE more com-

monly affect women; it is thought that the primary reason for this is the combination of oral contraceptives with prolonged sitting or inadequate living conditions.^{30,31}

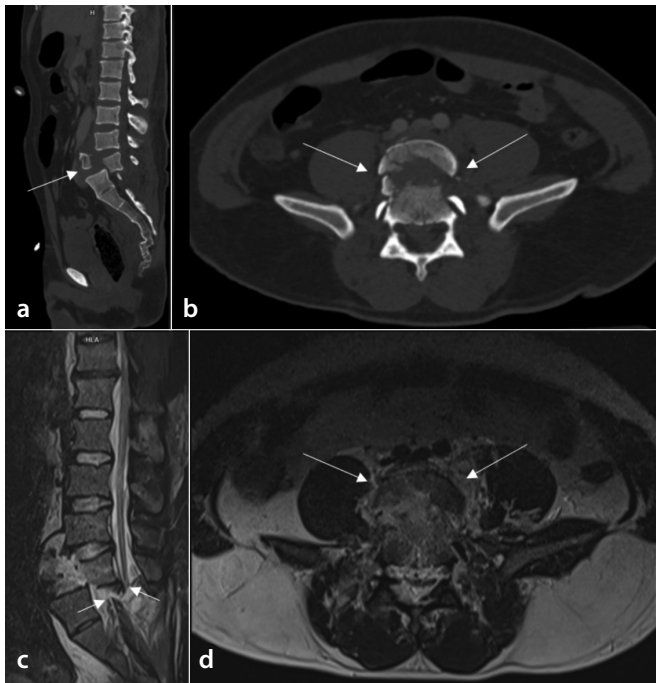


Figure 7. Traumatic listhesis and spinal cord injury. The patient was trapped for 31 hours by earthquake debris. Forty-one-year-old male. Retrolisthesis due to burst fracture of the L5 vertebrae (arrows) on the L5-S1 level. Spinal cord transection is seen on coronal Short tau inversion recovery (STIR) (c, arrows point to the two dissected edges of the spinal cord) (a) coronal computed tomography (CT) image, (b) axial CT image, (c) coronal STIR, (d) axial T2 weighted image.

Infections: Problems in clean water supply and sewage systems and poor housing conditions in evacuation centers are the main causes of post-disaster infections. Respiratory and gastrointestinal infections constitute the most common group, and increased cases of meningoencephalitis have also been reported after disasters (Figure 20).^{32,33} It has been shown that common orthopedic injuries are accompanied by wound infections in approximately 20% of cases.³³

Interventional radiologic procedures: In disaster situations such as earthquakes, where access to CT and fluoroscopy devices is limited, interventional radiological procedures cannot be widely performed. However, it is seen that the procedures performed under US guidance are practical and life-saving. Tube thoracotomies, pleural hemorrhage drainage, and central venous catheter procedures are the main life-saving interventional radiology applications in disaster areas.³⁴

Injuries with high mortality risk and forensic medicine–radiology cooperation

Immediate deaths are those that result from catastrophic injuries sustained during the earthquake. Severe trauma to the brain or spinal cord is a common cause of such injuries, and in most cases, these patients cannot be saved. Other earthquake victims die rapidly within the first few hours following the catastrophe, and historical experience indicates that mortality could be drastically decreased if treatment is administered promptly. These people suffer subdural hematomas, lacerations to the liver or spleen, and pelvic fractures. The third peak of mortality, which comes days to weeks following the earthquake, is caused by sepsis, multi-system organ failure, and disseminated intravascular coagulation. These individuals have the highest possibility of being saved since they succumb to injury complications more slowly.³⁵

Unfortunately, one of the post-disaster medical efforts is to determine the identities of those who lost their lives. At this point, forensic medicine physicians can also apply imaging methods. Considering the possibilities that the disaster environment can offer, it has been determined that the most frequently used method is dental radiographs. It is known that MRI and CT are highly functional in determining and clarifying the



Figure 8. Different patterns of traumatic abdominal injury. The patient was trapped for 35 hours by earthquake debris. Forty-seven-year-old male (a) American Association for the Surgery of Trauma (AAST) grade III injury in the right lobe-segment VII. (b) Left surrenal hematoma (circle), large perisplenic hematoma (arrows), splenic arterial injury, and corresponding contrast medium extravasation (thick arrow) (AAST grade V injury). (c) Large perisplenic hematoma (arrows), splenic arterial injury, and corresponding contrast medium extravasation (thick arrow). Sudden luminal narrowing in the left renal artery (circle) observed secondarily to blunt trauma. (d) Renal parenchymal infarct (arrows) due to the arterial narrowing shown in d (AAST grade V injury).

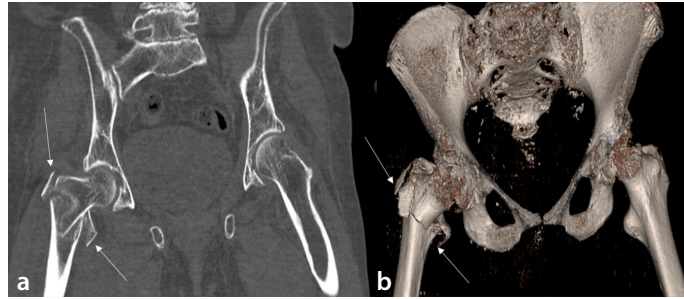


Figure 9. Intertrochanteric femur fracture. It was not possible to determine how long the patient was trapped by earthquake debris. Thirty-eight-year-old male. Displaced and comminuted fracture (arrows) in the right femoral intertrochanteric region on the coronal (a) and three-dimensional reconstruction (b) computed tomography images.

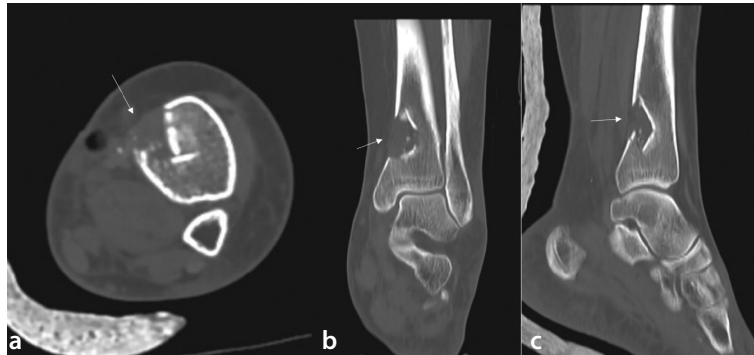


Figure 10. Distal tibial fracture. It was not possible to determine how long the patient was trapped by earthquake debris. Thirty-year-old male. (a) Medial cortical depression and internal displaced fracture (arrow) are seen in the distal metaphyseal–diaphyseal part of the tibia on axial (a), coronal (b), and sagittal (c) computed tomography images.

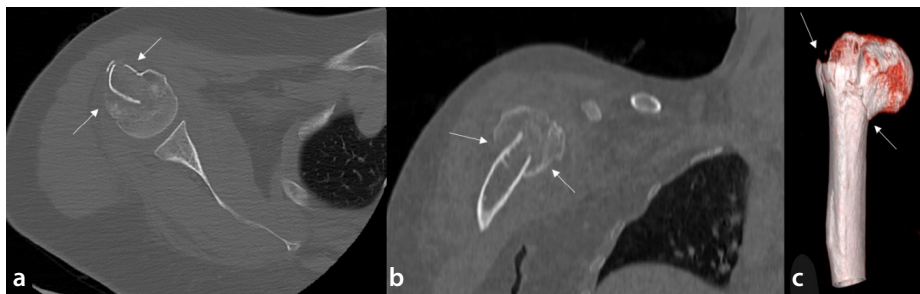


Figure 11. Proximal humeral fracture. It was not possible to determine how long the patient was trapped by earthquake debris. Sixty-year-old female. Fracture is seen in the surgical neck of humerus fracture (arrows) (a: axial view, b: coronal view, c: three-dimensional image).



Figure 12. Multiple lower extremity fractures. The patient was trapped for 23 hours by earthquake debris. Thirty-three-year-old male. Minimally displaced fractures are present in the medial malleolus of the tibia and distal metaphysis of the fibula on X-ray (a), coronal computed tomography (b), and three-dimensional reconstruction (c) images.

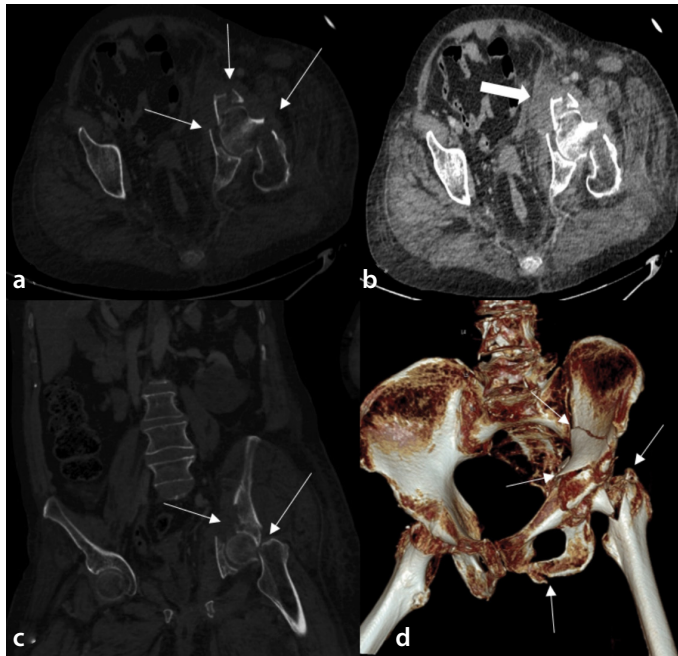


Figure 13. Pelvic and humeral fractures. The patient was trapped for 29 hours by earthquake debris. Seventy-six-year-old male. Displaced and comminuted fractures are seen in the left acetabulum and femoral neck (thin arrows) on axial (a) and coronal (c) computed tomography (CT) images. Large intramuscular hematoma due to the fractures is present on axial CT image (b, thick arrow). The fractures extend towards the iliac wing and inferior pubic ramus on the three-dimensional reconstruction image (d, arrow, Tile type A2 fracture).

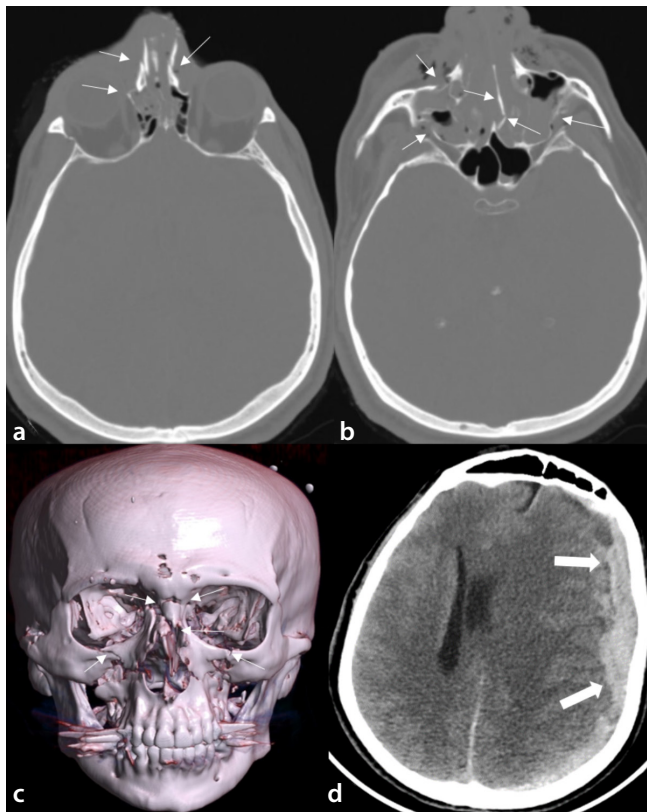


Figure 14. Multiple maxillofacial fractures and accompanying cranial hemorrhage. The patient was trapped for 17 hours by earthquake debris. Forty-four-year-old male. Multiple displaced fractures (thin arrows) are seen in maxillofacial bones in axial (a, b) and 3D reconstruction (c) computed tomography images. Extensive subdural hemorrhage causing a shift in midline structures accompanies the fractures (d, thick arrows).

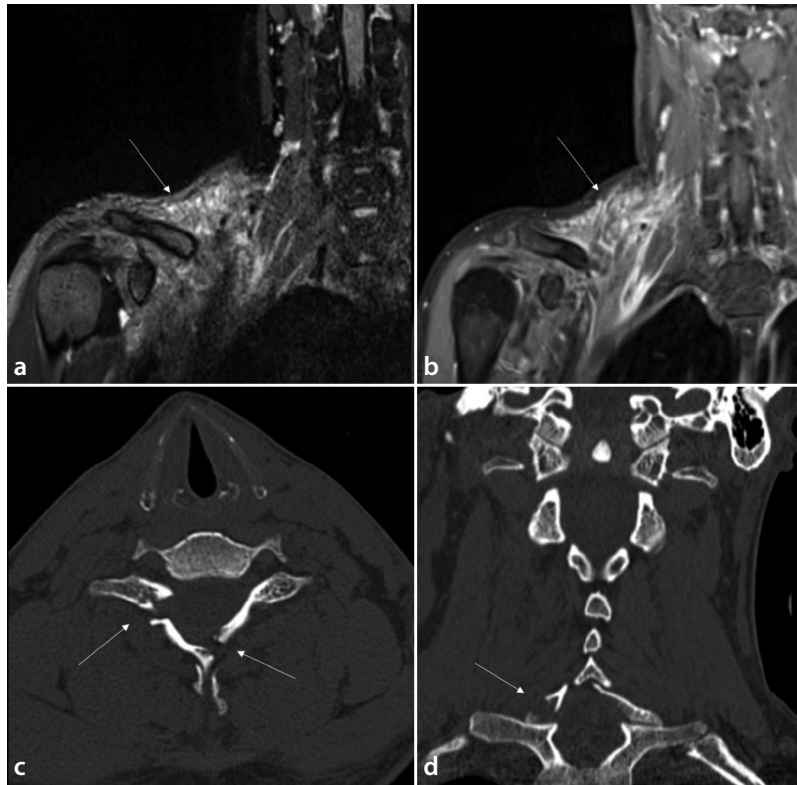


Figure 15. Rhabdomyolysis. The patient was trapped for 39 hours by earthquake debris. Twenty-year-old male. Rhabdomyolysis due to brachial plexus damage secondary to cervical fracture. Rhabdomyolysis (arrows) is seen as hyperintense on short tau inversion recovery (a) and it enhances on post-contrast T1 weighted image (b). The displaced fracture in the bilateral arch of the C7 vertebrae (arrows) is seen in axial (c) and coronal (d) sections on computed tomography.

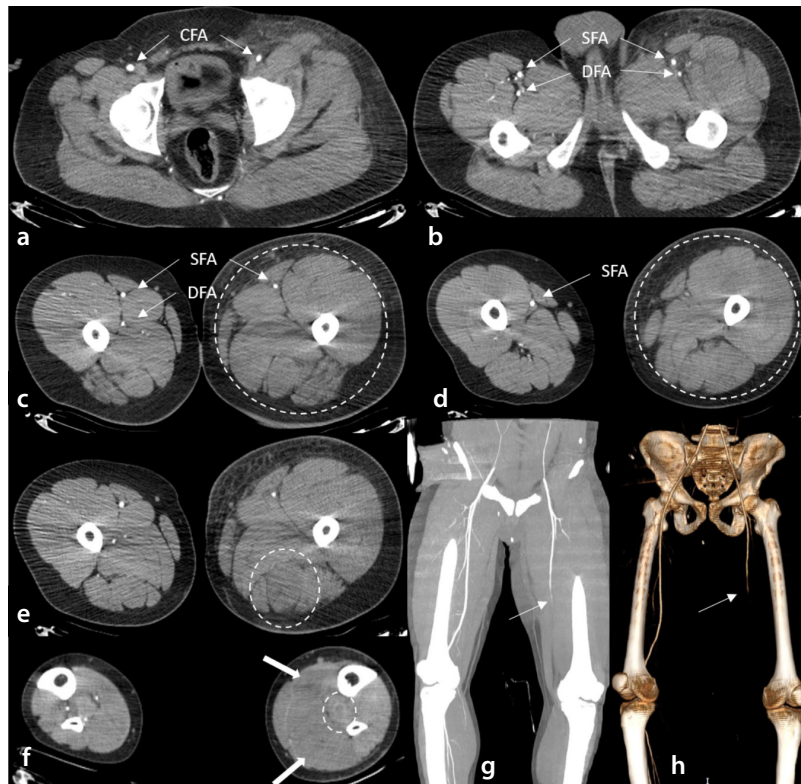


Figure 16. Compartment syndrome and rhabdomyolysis. The patient was trapped for 51 hours by earthquake debris. Thirty-four-year-old male. Left lower extremity is larger and subcutaneous edema is present (a-e). Common femoral artery, superficial femoral artery (SFA), and deep femoral artery are normal in the proximal segments of the left lower extremity (a-c). Due to increased intracompartmental pressure, left SFA narrows suddenly (d, g, h, arrows). Semitendinosus (e, circle) and gastrocnemius (f, arrows) muscles are hypodense; there is a ring-enhancing lesion in the popliteus muscle (f, circle) due to rhabdomyolysis.

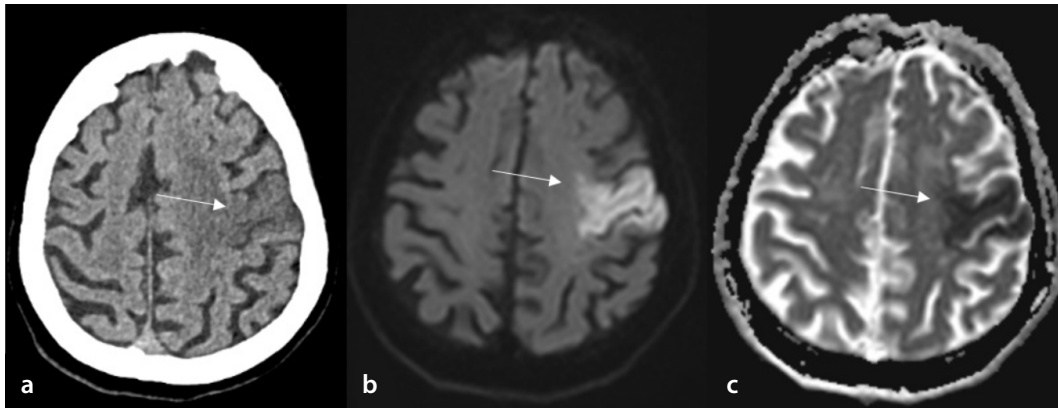


Figure 17. Acute cerebral infarction. Forty-four-year-old male, diagnosed 50 hours after being rescued from rubble. Ischemic brain parenchyma is seen as a hypodense area on computed tomography (a); corresponding diffusion restriction can be seen on diffusion-weighted imaging (b) and apparent diffusion coefficient map (c).

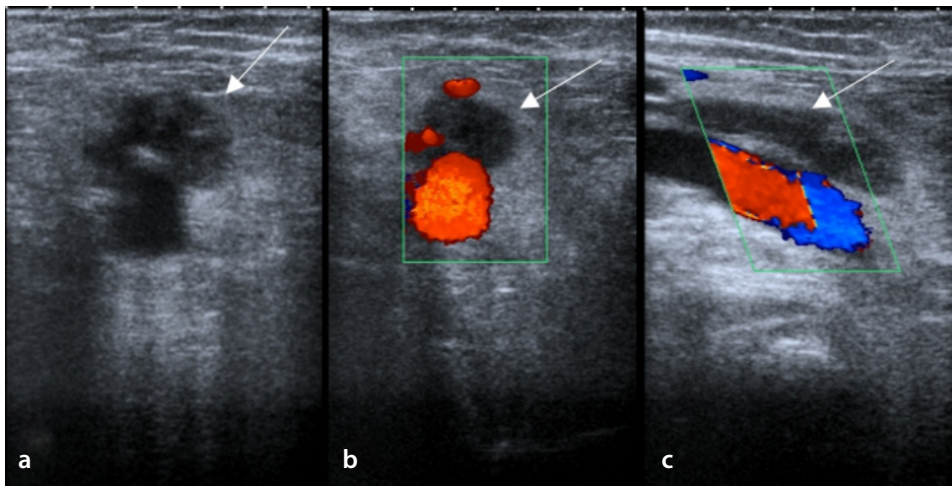


Figure 18. Deep vein thrombosis. Fifty-three-year-old female, diagnosed after rescue after 13 hours in the rubble. Thrombosis is seen in the superficial femoral vein (arrows) on grayscale ultrasound (a), axial (b), and longitudinal color Doppler ultrasonography images (c).

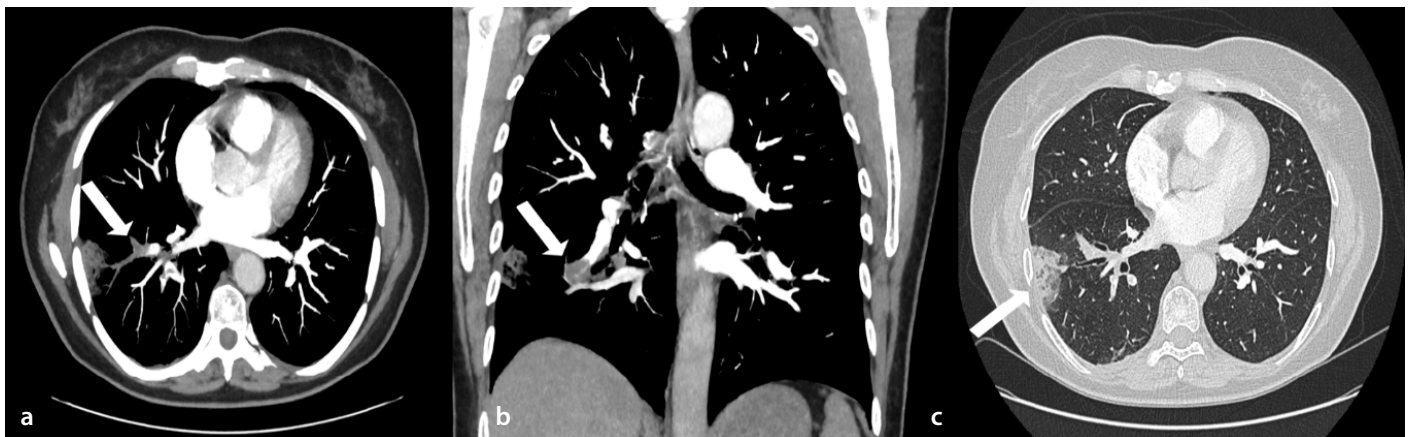


Figure 19. Pulmonary thromboembolism (PTE). The patient was trapped for 41 hours by earthquake debris. Forty-seven-year-old female. Filling defect corresponding to PTE, detected after 72 hours from the rescue from a rubble, is seen on axial (a, arrow) and coronal (b, arrow) images. A peripheral lung necrosis due to PTE is seen on the axial image with parenchymal windowing (c, arrow).

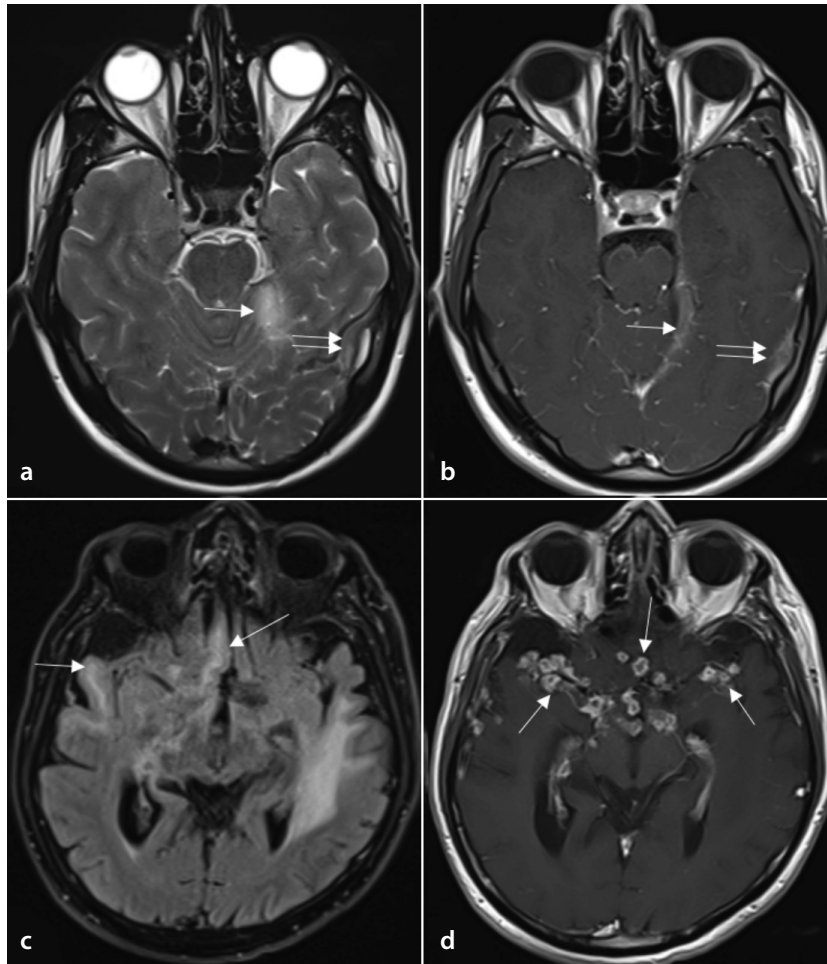


Figure 20. Viral meningitis (**a, b**) and tuberculous meningitis (**c, d**). Forty-three-year-old female and 73-year-old male, respectively. The images were obtained after 53 and 83 hours in the rubble, respectively.

Viral meningitis: left tentorium cerebelli is seen thickened and hyperintense on T2 weighted image (WI) (**a**, arrow), left temporal lobe and neighboring dura is hyperintense on T2WI (**a**, double arrow) (**a**), increased contrast enhancement is present in both corresponding areas (**b**).

Tuberculous meningitis: faint hyperintensities are present in the bilateral basal areas of the temporal lobes on fluid attenuated inversion recovery (**c**, arrows); increased contrast enhancement and ring-enhancing lesions can be seen in both corresponding areas (**d**, arrows).

cause of death, but, unfortunately, the use of both methods is limited. The main reasons for this are the great need for life-saving interventions for these imaging methods and the large number of bodies that need to be examined in an environment where there is mass loss of life. In addition, it has been observed that many radiologists do not have enough experience in forensic imaging.^{36,37}

In conclusion, in earthquakes and similar disaster situations, the need for imaging methods increases, and imaging plays an important role in saving lives. Due to the constraints in energy supply and easy accessibility, US examinations—especially FAST—have become the most useful method. Knowing the most common injuries, typical imaging findings of these injuries and their accompanying pathologies will help save more lives. Reporting procedures in close contact with the clinician, verbally or in the form of short notes, seems to be the most useful method. It should not be forgotten that the establishment of remote reporting systems is a practical and effective solution in cases where there is excessive demand.

Conflict of interest disclosure

Sonay Aydın, MD, is Section Editor in Diagnostic and Interventional Radiology. He had no involvement in the peer-review of this article and had no access to information regarding its peer-review. Other authors have nothing to disclose.

References

- Ishihara O, Yoshimura Y. Damages at Japanese assisted reproductive technology clinics by the Great Eastern Japan Earthquake of 2011. *Fertil Steril*. 2011;95(8):2568-2570. [\[CrossRef\]](#)
- United States Geological Survey (USGS), Earthquakes maps, Accessed February 15, 2023. [\[CrossRef\]](#)
- Anadolu Agency Infographics, Accessed February 15, 2023. [\[CrossRef\]](#)
- Earthquake news, Accessed March 8, 2023. [\[CrossRef\]](#)
- Iyama A, Utsunomiya D, Uetani H, et al. Emergency radiology after a massive earthquake: clinical perspective. *Jpn J Radiol*. 2018;36(11):641-648. [\[CrossRef\]](#)
- Gregan J, Balasingam A, Butler A. Radiology in the Christchurch earthquake of 22 February 2011: challenges, interim processes and clinical priorities. *J Med Imaging Radiat Oncol*. 2016;60(2):172-181. [\[CrossRef\]](#)
- Raja FS. Portable sonography in Haiti after the earthquake. *Can Assoc Radiol J*. 2011;62(3):222. [\[CrossRef\]](#)
- Kakaei F, Zarrintan S, Rikhtegar R, Yaghoobi AR. Iranian 2012 earthquake: the importance of Focused Assessment with Sonography for Trauma (FAST) in assessing a huge mass of injured people. *Emerg Radiol*. 2013;20(4):307-308. [\[CrossRef\]](#)
- Stavarakakis IM, Daskalakis II, Detsis EPS, Karagianni CA, Papantonaki SN, Katsafarou MS. Hand compartment syndrome as a result of intravenous contrast extravasation. *Oxf Med Case Reports*. 2018;2018(12):omy098. [\[CrossRef\]](#)
- Bartholdson S, von Schreeb J. Natural disasters and injuries: what does a surgeon need to know? *Curr Trauma Rep*. 2018;4(2):103-108. [\[CrossRef\]](#)
- Dursun R, Görmeli CA, Görmeli G. Evaluation of the patients in Van Training and Research Hospital following the 2011 Van earthquake in Turkey. *Ulus Travma Acil Cerrahi Derg*. 2012;18(3):260-264. [\[CrossRef\]](#)
- Guner S, Guner SI, Isik Y, et al. Review of Van earthquakes from an orthopaedic perspective: a multicentre retrospective study. *Int Orthop*. 2013;37(1):119-124. [\[CrossRef\]](#)
- MacKenzie JS, Banskota B, Sirisreerux N, Shafiq B, Hasenboehler EA. A review of the epidemiology and treatment of orthopaedic injuries after earthquakes in developing countries. *World J Emerg Surg*. 2017;12:9. [\[CrossRef\]](#)
- Dong ZH, Yang ZG, Chu ZG, et al. Earthquake-related injuries: evaluation with multidetector computed tomography and digital radiography of 1491 patients. *J Crit Care*. 2012;27(1):103.e1-103.e6. [\[CrossRef\]](#)
- Blumberg N, Lebel E, Merin O, Levy G, Bar-On E. Skeletal injuries sustained during the Haiti earthquake of 2010: a radiographic analysis of the casualties admitted to the Israel Defense Forces field hospital. *Eur J Trauma Emerg Surg*. 2013;39(2):117-122. [\[CrossRef\]](#)
- Chen TW, Yang ZG, Dong ZH, et al. Earthquake-related crush fractures and non-earthquake-related fractures of the extremities: a comparative radiological study. *Emerg Med Australas*. 2012;24(6):663-669. [\[CrossRef\]](#)
- Chen TW, Yang ZG, Wang QL, et al. Crush extremity fractures associated with the 2008 Sichuan earthquake: anatomic sites, numbers and statuses evaluated with digital radiography and multidetector computed tomography. *Skeletal Radiol*. 2009;38(11):1089-1097. [\[CrossRef\]](#)
- Morelli I, Sabbadini MG, Bortolin M. Orthopedic injuries and their treatment in children during earthquakes: a systematic review. *Prehosp Disaster Med*. 2015;30(5):478-485. [\[CrossRef\]](#)
- Chen TW, Yang ZG, Dong ZH, Chu ZG, Yao J, Wang QL. Pelvic crush fractures in survivors of the Sichuan earthquake evaluated by digital radiography and multidetector computed tomography. *Skeletal Radiol*. 2010;39(11):1117-1122. [\[CrossRef\]](#)
- Görmeli CA, Görmeli G, Güner S, et al. Evaluation of pelvic fractures by radiographical and multi-detector computed tomography following the 2011 Van earthquake in Turkey. *Eastern Journal of Medicine*. 2014;19(1):8-12. [\[CrossRef\]](#)
- Zingg T, Uldry E, Omoumi P, et al. Interobserver reliability of the Tile classification system for pelvic fractures among radiologists and surgeons. *Eur Radiol*. 2021;31(3):1517-1525. [\[CrossRef\]](#)
- Tang YL, Zhu GQ, Zhou H, et al. Analysis of 46 maxillofacial fracture victims in the 2008 Wenchuan, China earthquake. *Oral Surg Oral Med Oral Pathol Oral Radiol Endod*. 2009;108(5):673-678. [\[CrossRef\]](#)
- Chu ZG, Yang ZG, Dong ZH, et al. Features of cranio-maxillofacial trauma in the massive Sichuan earthquake: analysis of 221 cases with multi-detector row CT. *J Craniomaxillofac Surg*. 2011;39(7):503-508. [\[CrossRef\]](#)
- Lu CH, Tsang YM, Yu CW, Wu MZ, Hsu CY, Shih TT. Rhabdomyolysis: magnetic resonance imaging and computed tomography findings. *J Comput Assist Tomogr*. 2007;31(3):368-374. [\[CrossRef\]](#)
- Zhang CD, Lv FQ, Li QY, et al. Application of contrast-enhanced ultrasonography in the diagnosis of skeletal muscle crush injury in rabbits. *Br J Radiol*. 2014;87(1041):20140421. [\[CrossRef\]](#)
- Mahmoud OA, Mahmoud MZ. Spectral Doppler findings in a rare case of acute compartment syndrome following leg burn. *Radiol Case Rep*. 2018;13(2):352-355. [\[CrossRef\]](#)
- Nico MAC, Carneiro BC, Zorzenoni FO, Ormond Filho AG, Guimarães JB. The role of magnetic resonance in the diagnosis of chronic exertional compartment syndrome. *Rev Bras Ortop (Sao Paulo)*. 2020;55(6):673-680. [\[CrossRef\]](#)
- Kario K. Disaster hypertension—its characteristics, mechanism, and management. *Circ J*. 2012;76(3):553-562. [\[CrossRef\]](#)
- Omama S, Yoshida Y, Ogasawara K, et al. Influence of the great East Japan earthquake and tsunami 2011 on occurrence of cerebrovascular diseases in Iwate, Japan. *Stroke*. 2013;44(6):1518-1524. [\[CrossRef\]](#)
- Aoki T, Takahashi J, Fukumoto Y, et al. Effect of the Great East Japan earthquake on cardiovascular diseases—report from the 10 hospitals in the disaster area. *Circ J*. 2013;77(2):490-493. [\[CrossRef\]](#)
- Sueta D, Akahoshi R, Okamura Y, et al. Venous Thromboembolism due to oral contraceptive intake and spending nights in a vehicle—a case from the 2016 Kumamoto Earthquakes. *Intern Med*. 2017;56(4):409-412. [\[CrossRef\]](#)
- Kouadio IK, Aljunied S, Kamigaki T, Hammad K, Oshitani H. Infectious diseases following

- natural disasters: prevention and control measures. *Expert Rev Anti Infect Ther.* 2012;10(1):95-104. [\[CrossRef\]](#)
33. Phalkey R, Reinhardt JD, Marx M. Injury epidemiology after the 2001 Gujarat earthquake in India: a retrospective analysis of injuries treated at a rural hospital in the Kutch district immediately after the disaster. *Glob Health Action.* 2011;4:7196. [\[CrossRef\]](#)
34. Ferrara S. Radiology afloat: The impact of diagnostic and interventional radiology during the 2005 tsunami relief effort aboard the USNS Mercy. *J Vasc Interv Radiol.* 2009;20(3):289-302. [\[CrossRef\]](#)
35. Bartels SA, VanRooyen MJ. Medical complications associated with earthquakes. *Lancet.* 2012;379(9817):748-757. Erratum in: *Lancet.* 2012;379(9817):712. [\[CrossRef\]](#)
36. Guglielmi G, Sica G, Palumbo L, et al. Lethal injuries following building collapse: comparison between autopsy and radiographic findings. *Radiol Med.* 2011;116(6):969-981. [\[CrossRef\]](#)
37. Lino M, Aoki Y. The use of radiology in the Japanese tsunami DVI process. *Journal of Forensic Radiology and Imaging.* 2016;4:20-26. [\[CrossRef\]](#)



Techniques for portal vein targeting during a transjugular intrahepatic portosystemic shunt

Dan Laney
 Hector Ferral
 Alexandra Fairchild
 Bahri Üstünsöz

Louisiana State University Health Sciences Center,
Department of Radiology, Division of Interventional
Radiology, Los Angeles, USA

ABSTRACT

A transjugular intrahepatic portosystemic shunt (TIPS) is one of the most challenging procedures in interventional radiology. Hepatic and portal venous anatomy can be highly variable, and access to the portal vein, which can be quite difficult even for experienced surgeons, is the most critical step in a TIPS. Although there are multiple techniques to achieve a portal venous puncture, each access technique carries a unique set of risks and benefits. Thus, knowledge of these assistive techniques will add to the resources available to the surgeon when planning and subsequently performing a TIPS and, ultimately, increase the likelihood of a safe and successful procedure.

KEYWORDS

Hepatic vein, interventional, portal hypertension, portal vein, TIPS

A transjugular intrahepatic portosystemic shunt (TIPS) is one of the most challenging procedures in interventional radiology. It entails the creation of a shunt between the portal and hepatic venous systems, and access into the portal venous system is the critical step in a TIPS creation. Multiple techniques have been described concerning portal venous access, and each one carries a unique set of risks and benefits. The purpose of this article is to investigate the different techniques that have been described for portal venous access during a TIPS procedure.

Access techniques in patients with a patent portal vein

Direct and indirect portograms

The direct portogram technique was one of the first described techniques for guiding portal vein access during a TIPS procedure. This technique requires the placement of a catheter into a patent portal vein branch. The catheter is advanced into the main portal vein, and contrast is injected to demonstrate the portal venous anatomy. Direct access to the portal vein can be obtained by using an ultrasound-guided transhepatic approach or by ultrasound-guided access into a patent paraumbilical vein (Figure 1). An indirect portogram is another of the first described TIPS guiding techniques. A high-quality portal venogram is obtained by imaging the venous phase of a selective power injection of contrast into the superior mesenteric artery. Figure 2 illustrates the indirect portogram technique.

Iodinated contrast wedge portogram

With this technique, a contrast wedge portogram is obtained by injecting iodinated contrast through an end-hole catheter placed in a wedged position in the distal hepatic vein (Figure 3). Some of the iodinated contrast will pass through the sinusoids resulting in opacification of the portal venous system. Using this technique, the main portal vein is seldom opacified because of the viscous nature of the iodinated contrast. Krajina et al.¹ found that a wedged contrast portogram resulted in the visualization of the bifurcation of the portal vein

Corresponding author: Dan Laney

E-mail: dlane1@lsuhsc.edu

Received 06 Aug; revision requested 19 Sept; accepted
14 Nov 2022.



Epub: 21.12.2022

Publication date: 08.01.2023

DOI: 10.4274/dir.2022.221539

You may cite this article as: Laney D, Ferral H, Fairchild A, Üstünsöz B. Techniques for portal vein targeting during a transjugular intrahepatic portosystemic shunt. *Diagn Interv Radiol.* 2024;30(1):42-47.

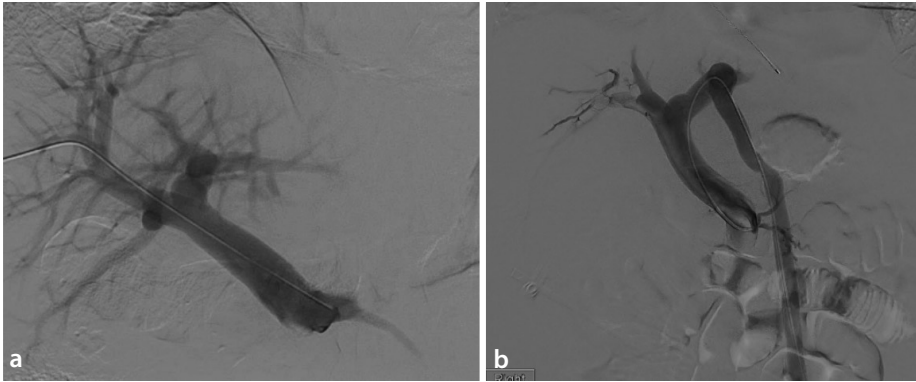


Figure 1. Direct portography techniques: the catheter is inserted directly into the portal vein via a transhepatic approach (a) or a via a patent umbilical vein (white arrow) (b).

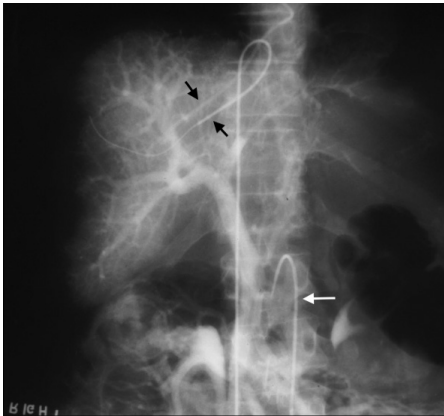


Figure 2. Indirect portogram: the radiograph shows a selected image obtained during the venous phase of a superior mesenteric artery (SMA) arteriogram. There are two catheters in the hepatic veins for reference (black arrows). An arterial catheter was placed in the SMA (white arrow), and an SMA portogram was performed (40 mL at 5 mL/sec). The image shows the relationship between the portal veins and the hepatic veins.

in 25% of patients, while only part of the portal vein was visualized in 36% of patients, and there was no portal vein opacification in 39% of patients. The major drawback of this technique is that the injected iodinated contrast can dissect into the liver parenchyma, resulting in permanent staining and obscuring visualization of the relevant vascular anatomy later in the procedure. This technique also carries the risk of liver laceration with capsular perforation.

Main points

- Multiple techniques exist to assist in portal venous puncture during a transjugular intrahepatic portosystemic shunt.
- Each portal vein access technique carries a unique set of risks, benefits, advantages, and disadvantages.
- Knowledge of these techniques increases the likelihood of a safe and successful procedure.

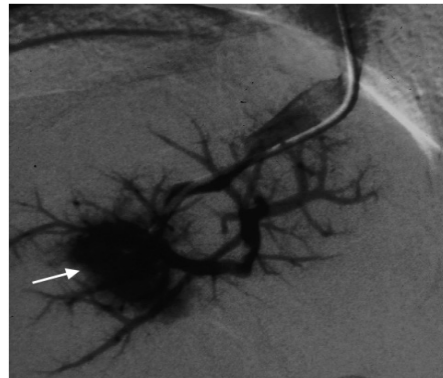


Figure 3. Contrast wedge injection: a catheter was wedged distally within the right hepatic vein to perform a portogram with iodinated contrast, resulting in opacification of the portal vein and an area of parenchymal staining (white arrow).

CO₂ wedge portogram and direct parenchymal CO₂ injection

A CO₂ wedge portogram is a very effective technique to map the position of the portal vein. The CO₂ wedge portogram is obtained by placing either an end-hole catheter or an occlusion balloon in the wedged position in the distal hepatic vein and gently injecting 10–15 mL of CO₂ (Figure 4). The two techniques are comparable, although it has been proposed that the occlusion balloon technique could be safer. Multiple studies have shown CO₂ to be a useful contrast agent for opacification of the portal venous system during a TIPS. Krajina et al.¹ demonstrated that the use of CO₂ leads to superior visualization of the portal vein compared to iodinated contrast during wedged hepatic venography due to the less viscous nature of CO₂. Using CO₂ as the contrast medium for wedged hepatic venography, opacification of the portal vein bifurcation was seen in 87% of patients, and there was no visualization of the portal venous system in 7% of patients, compared with 25% and 39%, respectively, when an iodinated contrast medium was used. Ad-

ditionally, the CO₂ does not stain the liver parenchyma, but, as with the previous technique, liver laceration with capsular rupture is a risk of this procedure.

Direct parenchymal injection of CO₂ can be used as an alternative to a CO₂-wedged hepatic venogram. This technique is useful when the portal vein is not visible after a CO₂-wedged venogram during a TIPS procedure (Figure 5) and involves advancing the transhepatic needle into the liver parenchyma. This is followed by a gentle injection of 10–15 mL of CO₂ directly into the parenchyma. Forceful injection of CO₂ should be avoided due to the risk of capsular rupture. An alternative technique is to perform a direct ultrasound-guided transhepatic puncture with a 21-gauge Chiba needle directly into the liver parenchyma and gently inject 10–15 mL of CO₂.

Percutaneous portal venous access

Percutaneous portal venous access is a localization technique that is useful in instances where an adequate contrast portogram cannot be achieved. A peripheral branch of the portal vein is punctured under ultrasound guidance. This is followed by the placement of a snare or a wire that can be used as a target for puncture. Alternatively, a snare or wire can be placed into the portal vein by first percutaneously accessing the splenic vein or a patent umbilical vein (Figure 6). A balloon occlusion catheter can be used as a target as well, instead of a snare or wire. The authors have not used this technique. In a 2021 study, Cam et al.² examined the effect of different techniques of portal vein cannulation during a TIPS placement on procedure efficiency. The study demonstrated that percutaneous portal vein guidewire placement for fluoroscopic targeting during a TIPS was associated with shorter procedure times, shorter fluoroscopic times, and potentially decreased complications when compared to more traditional fluoroscopically-guided wedged hepatic portography.

Intravascular sonographic imaging

The use of an intravascular ultrasound (IVUS) probe to obtain intravenous ultrasound images is a newer technique that involves using a catheter with a miniature ultrasound probe at the tip to assist in locating and puncturing the portal vein (Figure 7). The advantages of this technique include the ability to adjust the trajectory of the puncture and visualize the needle puncturing the portal vein based on real-time visualization with



Figure 4. CO₂ Wedge injection: (a) A catheter was wedged distally within the right hepatic vein to perform a CO₂ portogram with excellent opacification of the portal vein, (b) An iodinated contrast portogram was obtained in the anteroposterior projection view following a successful portal vein puncture, (c) A final transjugular intrahepatic portosystemic shunt (TIPS) completion venogram with iodinated contrast demonstrates portal vein opacification and opacification of the successfully created TIPS.

a level of spatial and anatomic detail that is not possible when utilizing fluoroscopy alone. In a 2016 study, Pillai et al.³ compared the safety and effectiveness of IVUS-guided portal vein access during a TIPS with conventional TIPS techniques. The study showed that IVUS-guided portal vein access during a TIPS procedure is associated with shorter portal vein access times, decreased needle pass-related capsular perforations, and reduced radiation dose when compared to conventional TIPS techniques. Recently, the intracardiac echocardiography (ICE) catheter has become the preferred tool for performing sonographic imaging guidance during a TIPS. With either jugular or femoral access, the ICE catheter can be advanced to the level of the intrahepatic inferior vena cava, allowing puncture of the portal vein under live ultrasound imaging.⁴ The use of the ICE allows the surgeon to increase the safety and technical success of the procedure by maximizing the accuracy of the portal vein puncture while also decreasing the radiation time and contrast dose.⁴

Overlay technique

The overlay technique involves superimposing cross-sectional imaging [magnetic resonance imaging, computed tomography (CT), or cone beam CT] on fluoroscopic imaging to help guide portal vein puncture. A study by Meine et al.⁵ assessed the technical

feasibility, success rate, puncture complications, and procedural characteristics of a TIPS using a three-dimensional vascular map overlay based on image registration of pre-procedural contrast-enhanced multidetector CT for portal vein puncture guidance. The study found that a TIPS using registra-

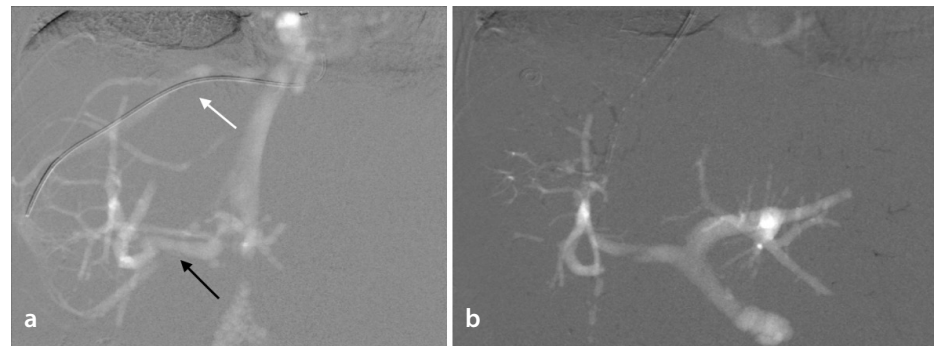


Figure 5. Direct intraparenchymal CO₂ injection: (a) the wedge portogram demonstrates a long distance between the right hepatic vein (white arrow) and the portal vein target (black arrow). The opacification of an accessory hepatic vein and the inferior vena cava is clear. The main trunk of the portal vein is not shown, (b) This shows direct intraparenchymal injection of CO₂ through the access needle to target the portal vein. The main portal and the right and left main portal branches are opacified.

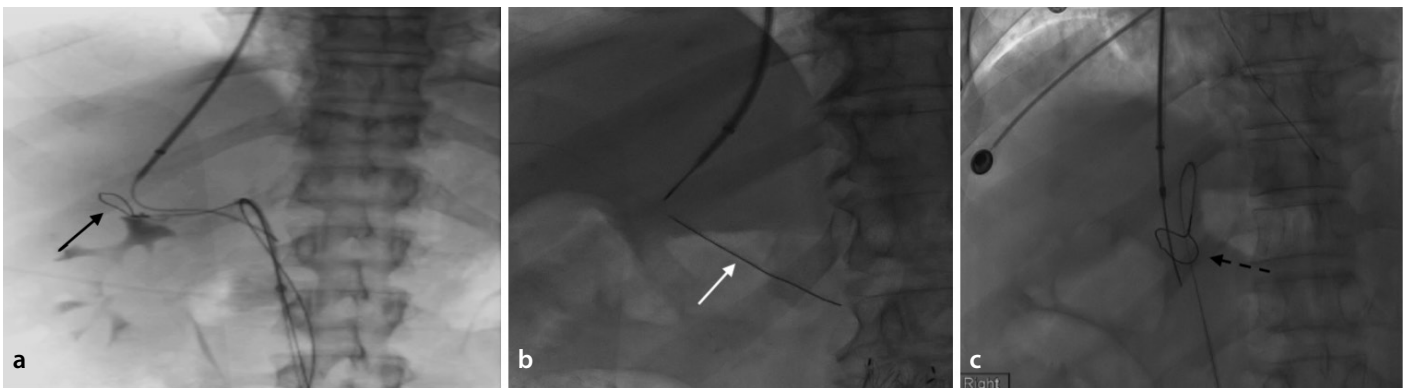


Figure 6. Snare technique: (a) a percutaneously inserted snare via the umbilical vein (black arrow) was used as a target for successful access into the portal vein from the right hepatic vein, (b) A percutaneously inserted wire (white arrow) can also be used for the same purpose. Please note that only the wire tip is radiopaque, (c) A snare (dashed arrow) was used as a target for portal vein access and placed into the portal system by first percutaneously accessing a patent umbilical vein.

tion-based contrast-enhanced multidetector CT vessel information for puncture guidance is feasible and safe. Additionally, this overlay technique was found to have the potential to improve hepatic vein catheterization, increase the ease of portal vein puncture, and decrease radiation exposure for the patient and surgeon.⁵ The example in Figure 8 utilizes cone beam CT performed in the angiography suite at the time of the procedure to create a plot of the locations of the right hepatic and portal veins, which is then used to direct the needle puncture under fluoroscopy. A drawback of this technique is that patient respiration and/or movement cannot be accounted for, leading to imprecise portal vein targeting.

Additional techniques

Additional techniques have been used to guide portal venous puncture during a TIPS procedure. Blind transparenchymal puncture involves inserting a transparenchymal needle into the hepatic veins in the direction of the anticipated anatomic location of the portal venous system under fluoroscopy without specific additional imaging guidance. However, this technique is not recommended, as it carries an elevated risk of technical failure, multiple unsuccessful puncture attempts, and a higher risk of complications. Additionally, surgically-assisted direct access to the superior mesenteric vein has been described. In this technique, femoral access is used to gain access to the hepatic vein, and a mini-laparotomy is performed to allow for transmesenteric access into the portal venous system.⁶ While this technique does allow for technical success, the involvement of a surgical team to perform a laparotomy is a logistical challenge. Neither of the aforementioned techniques has been used by the authors in their practice.

Access techniques in patients with a portal vein thrombosis

Transsplenic access to the portal venous system

Transsplenic access is a technique that allows for portal vein access in patients with both acute and chronic portal vein occlusion. A needle is inserted through the spleen into the splenic venous system. Once splenic vein access is established, the occluded portal vein can be recanalized to allow for the subsequent TIPS (Figure 9).⁷ Transsplenic access is a safe technique. As with transhepatic access, the main complication of concern is bleeding from the access tract leading to a

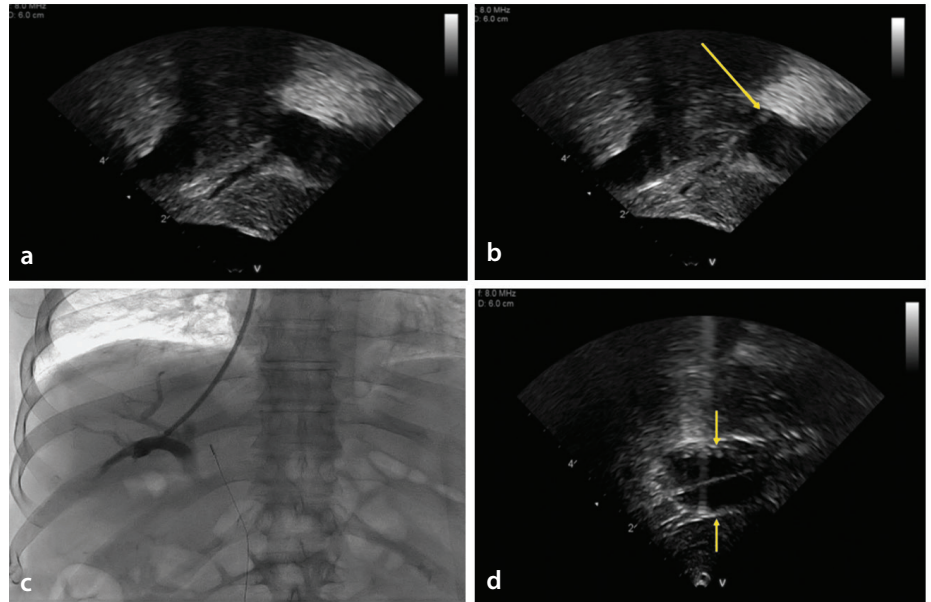


Figure 7. Intracardiac echocardiography-assisted puncture: images were obtained using an intracardiac echocardiography (ICE) catheter that demonstrate how the catheter advanced to the portal vein (a) and the needle (yellow arrow) within the portal vein (b). Fluoroscopic confirmation of successful access into the portal vein from the right hepatic vein can be seen here (c). The successful deployment of the stent (yellow arrows) from the hepatic vein to the portal veins is demonstrated in these ICE images (d).

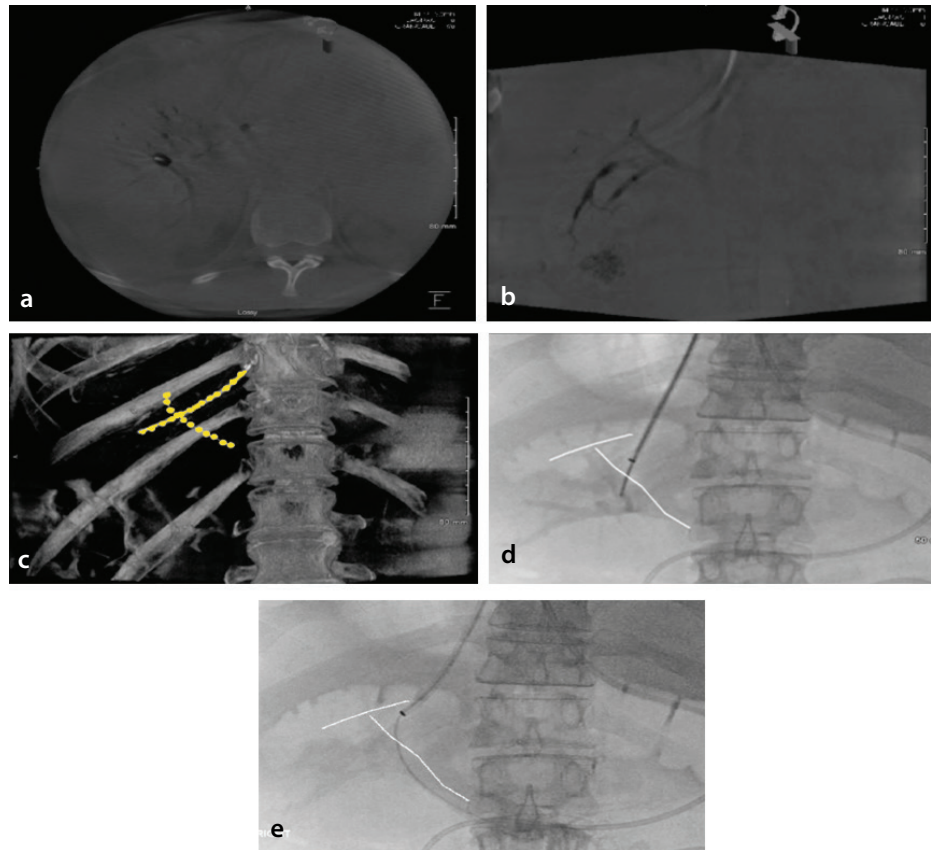


Figure 8. Imaging overlay technique: axial (a) and coronal (b) images from a wedged hepatic venogram during a 5-second cone beam computed tomography (CT) scan, which was performed at the time of the procedure. The images show a balloon occlusion catheter within the right hepatic vein and CO₂ opacifying the distal right hepatic vein and portal vein. A volume-rendered CT image (c) demonstrates the plotting of the right hepatic and portal veins (yellow dots). This plot is then translated to live fluoroscopy as lines on the monitor that mark the portal vein location with the movement of the detector. Two intra-procedure fluoroscopic images (d, e) demonstrate the marked portal vein appearing as white lines on the screen.

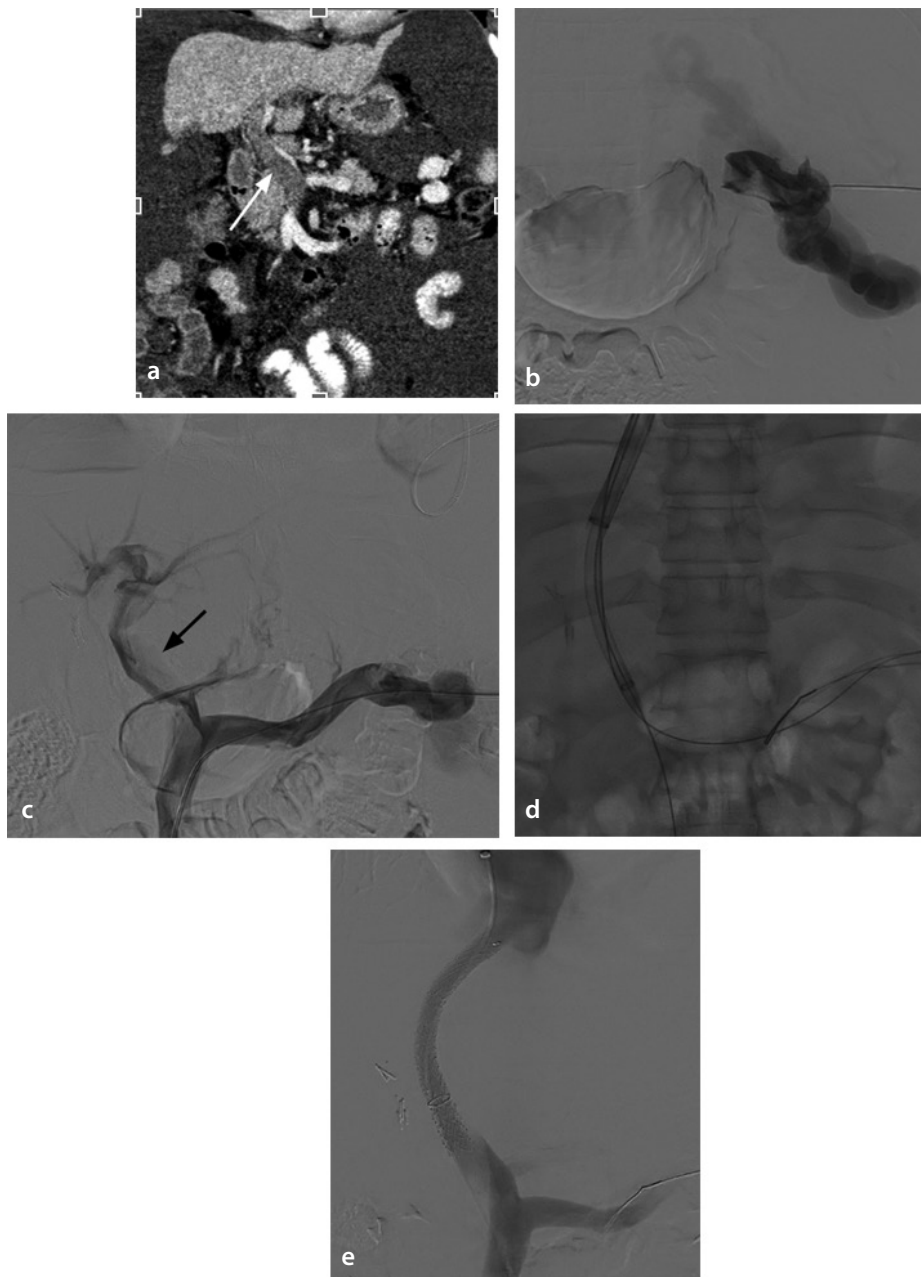


Figure 9. Transsplenic access to the thrombosed portal vein: (a) this coronal computed tomography image shows a thrombus within the main portal vein (white arrow), (b) This is a digital subtraction angiography (DSA) image of the splenic vein following transsplenic access, (c) This is a DSA image of the portal venous system demonstrating a large filling defect (black arrow) within the main portal vein representing a thrombus, (d) This shows an aspiration thrombectomy of the portal vein being performed using a 20 French FlowTrievers device (Inari Medical), (e) This is an angiography image following a successful transjugular intrahepatic portosystemic shunt.

hematoma formation, which can be mitigated by a coil or plug embolizing the transsplenic tract.⁷

Transabdominal ultrasound guidance

A TIPS under fluoroscopic guidance with additional transabdominal ultrasound guidance is another technique that is particularly useful when patients have acute portal vein thrombosis or when the hepatic venous sys-

tem is not patent.⁸ While the technical success rate utilizing this technique is high and the complication rate is low, the use of this technique is limited in obese patients and when ascites is present.⁸

Complications

Liver laceration with capsular injury is a complication that can occur during hepatic vein wedge or intraparenchymal contrast

injection. Carbon dioxide is preferred over iodinated contrast because of the higher rate of main portal vein visualization and its associated lower risk of capsular perforation. Previous research has found that extravasation of contrast occurs at a rate of 1.8% when using CO₂ and 7.5% when using iodinated contrast.⁹ The use of an occlusion balloon catheter for contrast injection may also decrease the risk of this complication by redirecting the flow of the contrast agent over a larger surface area of the liver. Lastly, and perhaps most importantly, the surgeon should always remember that forceful injection of contrast increases the risk of this complication, so the injection of the contrast material should be slow and gentle to decrease the risk of traumatic injury to the liver (Figure 10). If capsular perforation is detected, the surgeon should be prepared to proceed with further intervention to manage the complication.

Puncture of the biliary system, including the gallbladder, is not uncommon during TIPS procedures (Figure 11) and is typically well tolerated. However, there is a 5% chance of creating a fistula between the biliary and vascular systems after an accidental puncture of the biliary system.⁹ A fistula between the biliary and vascular systems can result in hemobilia, cholangitis, sepsis, and stent infection. In such cases, further intervention, including a biliary diversion via stenting or drainage, may be necessary.⁹

Accidental arterial puncture (Figure 12) occurs in approximately 6% of TIPS procedures. However, clinically significant arterial puncture only occurs in approximately 2% of cases. Complications associated with arterial puncture include hemorrhage, pseudoaneurysm, dissection or occlusion of the artery, and fistula formation.⁹ If such complications arise, angiography is the next best step in evaluation, with subsequent embolization if warranted. The surgeon should be careful to avoid dilating a tract between the hepatic vein and hepatic artery as this can result in patient death secondary to a sudden increase in right atrial pressure after arterial to venous shunt creation.¹⁰

A possible complication of direct transhepatic or transsplenic access to the portal venous system is bleeding through the puncture tract with subsequent perihepatic or perisplenic hematoma. Embolization of the portal vein access tract, with coils or plugs, has proven very effective in preventing this complication.²



Figure 10. Capsular perforation after CO₂ injection: forceful injection of CO₂ resulted in capsular perforation. Note the jet of extracapsular CO₂ extravasation (black arrow).



Figure 11. Biliary system puncture: this shows an accidental puncture of the biliary system with the transjugular intrahepatic portosystemic shunt access system, resulting in opacification of the bile ducts (black arrow) and the gallbladder (white arrow) with contrast. Dilatation of this tract should be avoided to prevent major biliary injury.



Figure 12. Arterial injury during a TIPS: this digital subtraction angiography image shows an arterial injection during a transjugular intrahepatic portosystemic shunt (TIPS) procedure. There is a complete hepatic artery (black arrow) replacement from the superior mesenteric artery trunk (white arrow). It is important to identify this complication and halt the TIPS in such a case as it could result in the patient's immediate death.

Conclusion

There are multiple reported techniques to assist in portal venous access during a TIPS procedure, all of which are aimed at obtaining access into the portal vein with the least number of attempts in the least amount of time. The correct use of these techniques increases the chance of technical success and decreases the chances of complications.

Conflict of interest disclosure

Bahri Üstünsöz, MD, is Section Editor in Diagnostic and Interventional Radiology. He had no involvement in the peer-review of this article and had no access to information regarding its peer-review. Other authors have nothing to disclose.

References

1. Krajina A, Lojik M, Chovanec V, Raupach J, Hulek P. Wedged hepatic venography for targeting the portal vein during TIPS: comparison of carbon dioxide and iodinated contrast agents. *Cardiovasc Intervent Radiol.* 2002;25(3):171-175. [\[Crossref\]](#)
2. Cam I, Gencturk M, Shrestha P, et al. Ultrasound-Guided portal vein access and percutaneous wire placement in the portal vein are associated with shorter procedure times and lower radiation doses during TIPS placement. *AJR Am J Roentgenol.* 2021;216(5):1291-1299. [\[Crossref\]](#)
3. Pillai AK, Andring B, Faulconer N, et al. Utility of intravascular US-guided portal vein access during transjugular intrahepatic portosystemic shunt creation: retrospective comparison with conventional technique

in 109 patients. *J Vasc Interv Radiol.* 2016;27(8):1154-1159. [\[Crossref\]](#)

4. Grimsbo MC, Brown MA, Lindquist JD, et al. Intracardiac echocardiography-guided TIPS: a primer for new operators. *Semin Intervent Radiol.* 2020;37(4):405-413. [\[Crossref\]](#)
5. Meine TC, Dewald CLA, Becker LS, et al. Transjugular intrahepatic portosystemic shunt placement: portal vein puncture guided by 3D/2D image registration of contrast-enhanced multi-detector computed tomography and fluoroscopy. *Abdom Radiol (NY).* 2020;45(11):3934-3943. Erratum in: *Abdom Radiol (NY).* 2020. [\[Crossref\]](#)
6. Rozenblit G, DelGuercio LR, Savino JA, et al. Transmesenteric-transfemoral method of intrahepatic portosystemic shunt placement with minilaparotomy. *J Vasc Interv Radiol.* 1996;7(4):499-506.
7. Ahmed O, Salaskar AL, Zangan S, Pillai A, Baker T. Transsplenic portal vein recanalization and direct intrahepatic portosystemic shunt placement to optimize liver transplantation. *CVIR Endovasc.* 2020;3(1):5. [\[Crossref\]](#)
8. Keshava SN, Moses V, Sharma A, et al. Technical and medium-term clinical outcomes of transjugular intrahepatic portosystemic shunt with fluoroscopy and additional trans-abdominal ultrasound guidance. *Indian J Radiol Imaging.* 2021;31(4):858-866. [\[Crossref\]](#)
9. Gaba RC, Khatani VL, Knuttinen MG, et al. Comprehensive review of TIPS technical complications and how to avoid them. *AJR Am J Roentgenol.* 2011;196(3):675-685. [\[Crossref\]](#)
10. Pattynama PM, van Hoek B, Kool LJ. Inadvertent arteriovenous stenting during transjugular intrahepatic portosystemic shunt procedure and the importance of hepatic artery perfusion. *Cardiovasc Intervent Radiol.* 1995;18(3):192-195. [\[Crossref\]](#)



Magnetic resonance imaging-guided radiofrequency ablation of breast cancer: a current state of the art review

Chuan Zhang^{1*}

Jing Shi^{2*}

Bing Li¹

Xiaoxuan Yu¹

Xu Feng¹

Hanfeng Yang¹

¹Affiliated Hospital of North Sichuan Medical College, Department of Radiology, Nanchong, China

²North Sichuan Medical College, School of Medical Imaging, Sichuan Province Nanchong, China

ABSTRACT

With a gradual increase in breast cancer incidence and mortality rates and an urgent need to improve patient prognosis and cosmetology, magnetic resonance imaging (MRI)-guided radiofrequency ablation (RFA) therapy has attracted wide attention as a new treatment method for breast cancer. MRI-RFA results in a higher complete ablation rate and extremely low recurrence and complication rates. Thus, it may be used as an independent treatment for breast cancer or adjuvant to breast-conserving surgery to reduce the extent of breast resection. Furthermore, with MRI guidance, accurate control of RFA can be achieved, and breast cancer treatment can enter a new stage of minimally invasive, safe, and comprehensive therapy. With progress in MR thermometry technology, the applications of MRI are expected to broaden.

KEYWORDS

MRI-guided, breast cancer, radiofrequency ablation, interventional therapy, MR thermometry

According to Global Cancer Statistics 2020, breast cancer has replaced lung cancer as the most common cancer diagnosed in women globally.¹ It is estimated that, within 10 years, new cases of breast cancer will rise worldwide to 2,300,000, and deaths due to breast cancer will rise to 684,996, increases of 35.3% and 30.7%, respectively.² Changes in reproductive patterns that are associated with an increased breast cancer risk, such as delays in childbearing and fewer births, may have contributed to this historic increase.³ The proportion of younger patients (<49 years old) has likewise increased over the years. As economies grow and beauty standards change, patients with breast cancer who seek treatment will have higher standards for their quality of life, aesthetics, and social and psychological recovery that surgery may fail to meet due to its proclivity for more extensive damage to the appearance of the breast and troublesome complications.

Accordingly, minimally invasive and non-invasive operations, such as radiofrequency ablation (RFA), microwave ablation (MWA), laser ablation (LA), high-intensity focused ultrasound (HIFU), and cryoablation, have been increasingly favored as treatments for breast cancer.⁴ Among these methods, magnetic resonance imaging-guided RFA (MRI-RFA) has become one of the major modalities used in minimally invasive breast cancer treatment,⁵ as it optimizes cosmetic results with shorter operative times and fewer complications. However, there is currently no review article regarding MRI-RFA. This article describes the current applications and development of this therapy to provide a reference for the clinical treatment and research of breast cancer.

1. Current status and progress of MRI in the clinical diagnosis and treatment of breast cancer

MRI has been used as a supplementary diagnostic tool for the general survey of breast cancer over the last 100 years, especially in those who fail to receive precise diagnoses by X-ray or ultrasound (US), those who are staging or planning breast-conserving surgery (BCS) before

*Joint first authors

Corresponding author: Hanfeng Yang

E-mail: yhfctjr@yahoo.com

Received 09 March 2022; revision requested 25 May 2022; last revision received 05 October 2022; accepted 22 November 2022.



Epub: 24.03.2023

Publication date: 08.01.2023

DOI: 10.4274/dir.2022.221429

You may cite this article as: Zhang C, Shi J, Li B, Yu X, Feng X, Yang H. Magnetic resonance imaging-guided radiofrequency ablation of breast cancer: a current state of the art review. *Diagn Interv Radiol.* 2024;30(1):48-54.

operation, those who require an evaluation of axillary lymph node metastasis, and those at high genetic risk.⁶ With advantages such as non-ionizing radiation, multiplane and multiparameter imaging, and high soft-tissue resolution, MRI has a level of examination efficiency that X-ray and computed tomography (CT) do not share and that leads to fewer missed diagnoses of malignant nodules in class 4 of the Breast Imaging Reporting and Data System.⁷

MRI performs exceptionally in the identification of occult breast cancers, carcinomas *in situ*, multifocal carcinomas, ductal infiltrating carcinomas, and intraductal papillomas. In a correlation study, Lee et al.⁸ found that, in 26% of 38 cases, the presumed sonographic correlate was not the true correlate, as a subsequent MRI-guided biopsy of the actual lesion revealed one malignancy among discordant cases. This is in line with the results of another meta-analysis suggesting that MRI has greater sensitivity than US in detecting nodal metastases.⁹

Besides its use in diagnosis, dynamic contrast-enhanced (DCE) MRI, the most sensitive modality of breast imaging, now plays a crucial role in interventional therapeutic regimens for breast cancer.¹⁰ It offers imaging guidance for tumor localization with the ability to evaluate and adjust probe placement during the operation. Moreover, it performs better than mammography, CT, and US in identifying information about tumor boundary and blood supply.¹¹ In the minimally invasive treatment of breast cancer under imaging guidance, it has been used frequently¹²⁻¹⁵ to monitor the presence of postoperative residual tumor, fibrous scarring, steatonecrosis, and tumor recurrence after radiotherapy¹⁶ and neoadjuvant surgery.¹⁷

Main points

- This review seeks to summarize the current therapeutic principles, adaptations, and procedures of magnetic resonance imaging-guided radiofrequency ablation (MRI-RFA) of breast cancer to encourage further exploration of this program.
- MRI-RFA's role in treating diseases such as breast cancer has been profound, and due to its imaging advantages, it excels in accurately targeting lesions. It is also useful for monitoring recurrence.
- MR thermometry allows practitioners to monitor temperature changes in real time to minimize injury to patients and evaluate the ablation process during the procedure.

2. Treatment principles and technical advantages of MRI-RFA

2.1. Principles of RFA for tumor treatment

Once the radiofrequency ablation needle penetration into the tumor through the skin under the guidance of an image is achieved, frequency waves are emitted through the needle tip. These frequency waves will lead to the movement of ions and particles in tissues causing collision and friction, leading to the generation of biological heat effect.¹⁸ During RFA treatment, the temperature of the probe needle tip reaches as high as 70°C–120°C. Due to poor heat dissipation of the tumor tissue, high temperature can cause degeneration, dissolution, coagulative necrosis and even carbonization of cancer cells. The blood within the tumor vessels also undergoes coagulation, so that the heat will not dissipate with the blood flow, thermal damage is limited to a precise range.¹⁹ Furthermore, the possibility for tumor metastasis with blood flow can be also declined.

In addition, RFA can coagulate the vascular tissue around the tumor and form a reaction zone about 0.5 ~ 1 cm thick, separating the tumor from the surrounding normal tissue, which can not only block the blood supply of malignant tumors, but also prevent distant metastasis to a certain extent.²⁰

2.2. Technical advantages of MRI-RFA: ablation method

With the popularization of minimally invasive treatments for tumors, the clinical value of ablation technologies, such as RFA, MWA, LA, HIFU, and cryoablation, has improved substantially. According to a meta-analysis of 1.608 cases by Peek et al.²¹, when comparing all ablative treatment options, RFA appears to perform optimally.^{22,23} In terms of its shorter treatment time (compared with HIFU), fewer short-term complications (compared with LA), and extremely low tumor recurrence rate among all methods, MRI-RFA presents certain advantages above other ablation methods.

Nonetheless, there exist some virtues of other ablation methods that RFA does not possess. Compared with RFA, HIFU leaves no scars. MRI-HIFU is now applied in uterine fibroids and bone metastasis-related pain management with a Comformité Européenne (CE) mark and United States Food and Drug Administration approval.^{14,15,24} Additionally, compared with RFA, the treatment procedure for cryoablation is less painful and more comfortable, though it carries the risk

of an incomplete ablation of perivascular lesions with a rich blood supply, as shown by Morin et al.²⁵ and Pusztaszeri et al.²⁶

In recent years, the use of MWA in clinical trials of early-stage breast cancer²⁷ has revealed that it can act as the trigger of an antitumor immune response in the Th1 variety of inducible T-cell co-stimulator (ICOS) pathways.²⁸ Thus, targeted agents based on MWA-induced systemic immune responses have aroused broad interest. Although it can accomplish a larger ablation volume within a short period, it is not clear if MWA offers more value than RFA,^{29,30} and operational difficulties and high costs related to equipment maintenance could also be a hindrance.

2.3. Technical advantages of MRI-RFA: imaging technique

On this basis of MRI-RFA technique, new treatment methods have been proposed and practiced. After confirming the presence of the malignant nodules of early micro- or occult lesions with MRI-guided biopsy, RFA can be employed as an accurate, minimally invasive, and efficient treatment. In addition, the complete ablation rate and boundary of tumor tissue that has been completely inactivated can be evaluated through the real-time measurement of physiological parameters during MRI³¹ [e.g., by proton resonance frequency (PRF), spin lattice relaxation time, and apparent dispersion coefficient (ADC)].

With the parameter and imaging advantages mentioned above, RFA can provide opportunities for reducing the degree of thermal damage to normal tissue under artificial control. The PRF shift (PRFS) has crystallized as the method of choice for temperature measurement due to its linear variability with temperature in most tissues, with the exception of fat, which contains relatively few hydrogen bonds and a small PRF thermal coefficient compared with water.

In recent years, there have been many efforts to confront the application restrictions of MR thermometry in areas with high fat content, such as the breasts and abdomen. Cheng et al.³² proposed a dual-step iterative temperature estimation of a fat-referenced PRFS method to improve both the accuracy and precision of temperature estimations in fat-containing tissues. T1- and T2-based³³ methods have been implemented recently to correct thermometry errors brought on by the non-local effects of heating in fatty tissues³⁴ or as an adjunct to PRFS thermometry in aqueous tissues (glandular, tumor, etc.).³⁵

In addition, multi-echo MR thermometry using iterative water-fat separation techniques³⁶ has been validated in simulations, phantom heating experiments, and *in vivo* breast and liver experiments. This method could help monitor ablative therapies in fatty tissues³⁴ such as the breast or liver. In contrast, US guidance cannot quantify the heat deposited in ablation target tissue.³⁷ Moreover, the shadow and strong echo generated by breast tissue when heated can affect the evaluation of any curative effect, making it more difficult to guarantee the completeness of any real-time monitoring of ablation by US.^{18,38,39}

3. Application of MRI-RFA in breast cancer therapy

MRI entered the clinical study of RFA for breast cancer for the first time when van den Bosch et al.⁴⁰ pioneered the use of 0.5T MRI for the RFA treatment of breast cancer, providing a new path for patients with advanced invasive breast cancer. Based on previous studies,^{32,41,42} the MRI-RFA procedure is summarized as follows: 1) patient lies in a prone position with the breast fixed on a biopsy frame with a breast coil; 2) appropriate puncture path is determined and puncture point is marked; 3) surgical drape is placed, surgical field is disinfected, and local anesthesia is administered; 4) the needle tip is verified to exceed the tumor edge by 0.5–1.0 cm; 5) RFA power is gradually adjusted to about 50 W to maintain a temperature of 100°C for 5–10 minutes, and a 0.9% NaCl aqueous solution at 0°–5°C is injected into the system in continuous circulation to maintain the uniform energy distribution of the needle tip; 6) ablation range changes, blood supply, and the ADC of the ablation area are monitored by MRI (the residual tumor will be monitored during timely supplementary treatment); and 7) regular follow-up after operation is required. The summarized procedure is depicted in Figure 1.

A personalized, comprehensive treatment approach for advanced breast cancer has been gradually gaining ground, and MRI-RFA has caught clinicians' and patients' eyes as a preferred treatment method. Here, the indications and contraindications of MRI-RFA for breast cancer are summarized, as shown in Table 1.

Neoadjuvant therapy makes it possible to downstage breast cancer and shrink tumors, giving access to BCS to patients who were initially ineligible.⁴³ Moreover, for those who are not candidates for surgery, MRI-RFA,

which is expected to completely eliminate local tumors, can be offered as an alternative.⁴⁴

Currently, axillary staging after neoadjuvant systemic therapy has contributed greatly to decreasing the incidence of axillary lymph node dissection (ALND) and its concomitant morbidities (especially lymphedema). While sentinel lymph node biopsy (SLNB) may be less valuable in MRI-RFA than in surgery as an independent treatment for local lesions, the value of SLNB after RFA warrants discussion to guide further systemic therapies, including endocrine, chemical, and targeted therapies.

Additionally, when there are positive sentinel node, radiotherapy has proved to have good curative effect of local lesion in axilla, which is comparable to that of ALND but with less morbidity and pain.⁴⁵ Notably, there

are concerns about whether SLNB should be offered to older people and those with underlying medical conditions. Although it is less invasive than ALND, a patient's condition should always be considered comprehensively.⁴⁶

3.1. Application of MRI-RFA in the treatment of small breast cancer

So far, MRI-RFA has only been put into clinical practice to treat small-diameter tumors in patients with moderately advanced breast cancer. In 2008, van den Bosch et al.⁴⁰ performed the first clinical study of MRI-RFA in patients with advanced invasive ductal carcinoma (1.2–2.3 cm in diameter). Three patients achieved 100%, 50%, and 33% tumor tissue ablation effects, respectively. In 2017, Yunian et al.⁴² administered RFA treatment to 11 patients with breast cancer with persistent residual tumors (1.5–3 cm) post-med-

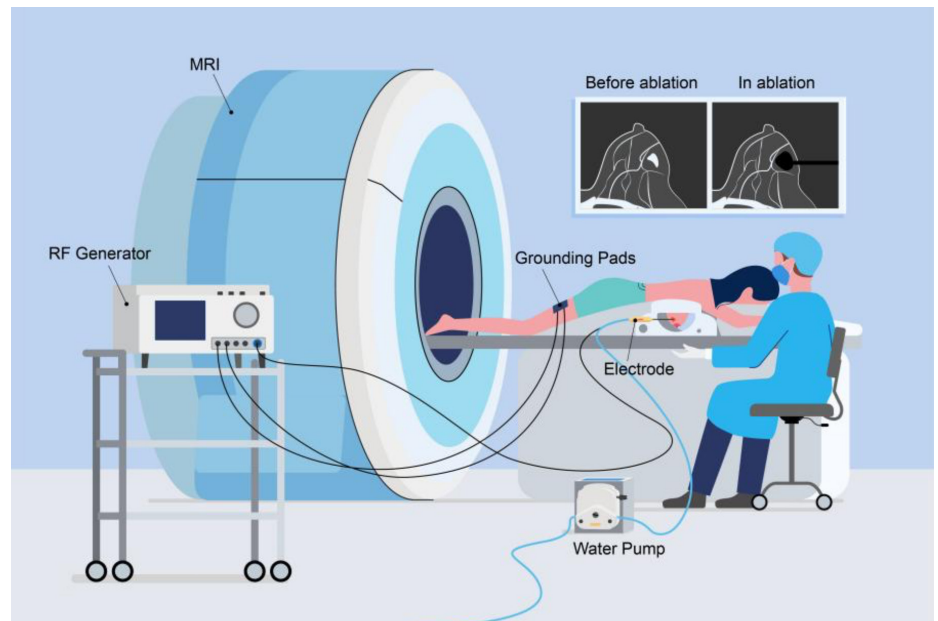


Figure 1. Procedure for magnetic resonance imaging radiofrequency ablation therapy for breast cancer. Patient lies prone with the breast placed on the biopsy frame with breast coil. The radiofrequency generator provides the necessary ablation energy which is applied through the needle into the tumor tissue. The water pump is utilized to adjust and maintain the temperature of the needle tip. MRI, magnetic resonance imaging.

Table 1. Indications and contraindications for MRI-RFA treatment of breast cancer

	Indications	Contraindications
Tumor characteristics	Tumor diameter <3 cm	Extensive or diffuse lesions
	Tumor margin >1 cm from the chest wall/skin	Malignant characteristic calcifications of diffuse distribution.
Combined factors	Severe underlying disease	Inflammatory breast cancer
	Tumor remains after non-surgical resection and multidisciplinary treatment	Severe coagulopathy, cardiovascular, and cerebrovascular diseases and those who cannot tolerate surgery
	Wishes of patients and their families	Pacemaker implantation and claustrophobia during MRI examination

MRI-RFA, magnetic resonance imaging-guided radiofrequency ablation.

ication therapy. Li et al.⁴¹ implemented MRI-RFA in 10 patients with moderately advanced breast cancer (tumors ≤ 3 cm in diameter). After at least one ablation, all cases achieved a radiographically complete response with a low complication rate and mild symptoms, and there were no recurrences or metastases at 2 years' follow-up. All of these studies confirm the safety and efficacy of MRI-RFA.

A comparison of these studies reveals that van den Bosch et al.⁴⁰ adopted a multi-needle RF system (in claw/umbrella shape) with an open 0.5T scanning imager in their study, while the others chose a cool-tip needle RF system with a 1.5T scanning imager. The multi-needle system used in the first study can better conform to more extensive lesions and simultaneously show the temperature distribution of the warming tissues via the FluorOptic fiber optic thermal sensor of its probe tip (Figure 2). At the same time, the MRI-compatible cryoprobes used in the other studies make it possible for circulated cooling of the RF needle tip. Furthermore, for corrections of susceptibility artefacts from MRI-compatible cryoprobes, van den Bosch et al.⁴⁰ recommend specific pulse sequences, such as view angle tilting, which helps mitigate distortion.

DCE-MRI was utilized for needle tip placement in all of the above studies to accurately identify the characteristics and boundaries of lesions. In addition, van den Bosch et al.⁴⁰ selected T1-fast spin echo (FSE) for imaging accurate probe placement and fewer artifacts, while PRFS thermometry (without reference) is used for the quantitative mapping of temperatures throughout the procedure. The other two studies also added the application of diffusion-weighted imaging (DWI) sequences into their procedures. There are increasing developments in the usage of ADC that add value to the diagnosis⁴⁷ and localization of breast cancer^{48,49} and breast DWI as an essential part of a multiparametric breast MRI is welcome by the European Society of Breast Radiology.⁵⁰ Dietzel et al.⁵¹ found that DWI can be used as a substitute for the delayed phase in DCE-MRI, shortening the scanning time without losing diagnostic information.

Tumor size also plays a role in the control of injury and treatment effect. Xia et al.⁵² found that, as far as achieving a complete response, RFA performs better in treating breast cancer tumors with a diameter of < 2 cm than those < 3 cm in diameter. Ohtani et al.⁵³ found that a single RFA treatment can eradicate breast cancer of less than 1.5 cm in diameter with-

out ductal invasion, while tumors larger than 1.5 cm in diameter may require two or more RFA treatments. Thus, to effectively exploit the advantages of MRI-RFA in the treatment of small breast tumors, further experiments are needed to determine the most suitable tumor diameter and biomorphological characteristics for this treatment.

3.2. Application of MRI-RFA in conservative surgery for breast cancer

Studies have shown that negative tumor margins can reduce the rate of tumor recurrence to some extent, be effective for local tumor control, and achieve better tumor-free margins compared to tumor resection.^{54,55} Moreover, MRI-RFA may be an effective procedure to avoid reoperation after tumor resection. However, excessive resection of breast tissue make its contour and aesthetic challenging to maintain. Reducing the residual lesion within the tumor bed through BCS is the key to reducing its recurrence. In some retrospective analyses, RFA treatment in neoadjuvant post-BCS led to a lower recurrence rate and higher cosmetic outcome satisfaction score than in neoadjuvant post-BCS alone. Zhang et al.⁵⁶ demonstrated the reliability and value of MRI-RFA's clinical application with an extremely low recurrence rate (0.87%) and low complication rate (3.48%).

The potential for the clinical implementation of RFA for treating breast cancer largely depends on the accuracy of the imaging techniques employed to assess tumor extent and guide ablation,^{21,57} and MRI has shown high accuracy in detecting residual disease after RFA in patients with invasive breast cancer. It is conceivable that inactivating viable residual tumor cells at tumor-resection margins with MRI-RFA makes it possible to effec-

tively reduce the extent of glandular tissue resection in BCS, which guarantees better preservation of the patient's breast contour. MRI-RFA treatment of free margins may lead breast-conserving therapy into a new stage. However, large sample multicenter studies, prospective clinical trials, and long-term follow-ups need to be implemented to support the validity of this study.

3.3. Evaluation of the efficacy of MRI-RFA in breast cancer treatment

It has been shown that MRI can significantly increase the detection rates of breast cancer remnants and recurrence depending on the shape of lesions, discrepancy of signal, enhancement characteristics, and dynamic time-signal curve. A tumor activity analysis of residual lesions on postoperative MRIs can be marked by distortion and alterations of signal intensity in the ablation zone. Mild enhancement can be detected at the margin of lesions, and MRI findings after ablation may be correlated with their histological results,^{57,58} which is beneficial to the prediction and monitoring of tumor metastasis in patients after operation.

As noted earlier, as a crucial part of multiparameter imaging based on DCE-MRI, DWI is applied not only in the diagnosis and localization of breast cancer but also in the evaluation of ablation efficacy. After the procedure, MRI showed that the structure of the ablation area was disordered, the edge of the lesion was slightly enhanced, or its periphery was scattered with irregular enhancement. Nodular or eccentric enhancement could be observed in follow-up. Burak et al.⁵⁹ observed that imaging manifestations of residual tumors were correlated with a discrepancy in contrast enhancement, a finding verified by

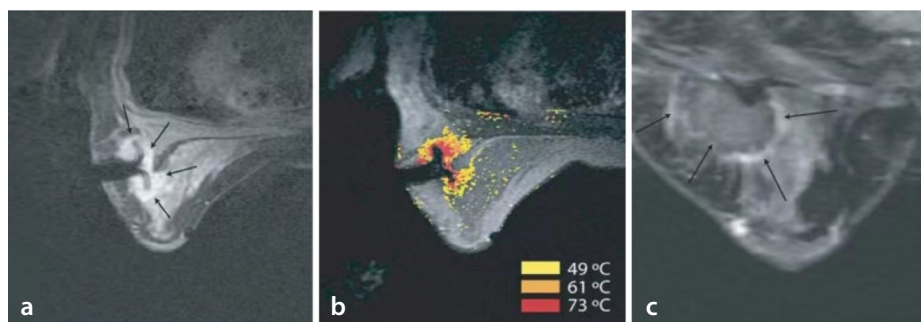


Figure 2. (a) Axial Comformité Européenne (CE) three-point Dixon gradient-echo images of the first patient in prone position showing the enhancing tumor mass (arrow) lateral in the right breast with the hypointense fully deployed LeVeen needle electrode centrally in the mass. (b) Axial CE three-point Dixon gradient-echo images of the same patient in prone position showing the magnetic resonance proton resonance frequency shift thermo map (yellow zone: 49°C, orange: 61°C, red: 73°C) around the hypointense deployed LeVeen needle electrode centrally in the mass (arrow). (c) Post-procedure CE water-selective, spectral-spatial axial FSE image of the right breast demonstrates a small enhancing rim representing the border of the ablation zone corresponding to fresh scar tissue (arrows) (van den Bosch et al.⁴⁰, 2008).

van den Bosch et al.⁴⁰, Li et al.⁴¹, and Yunian et al.⁴², who used maximum intensity projection (MIP) images to monitor tumors. They found that tumor blood supply disappeared in 100% of MIP images, and the ADC value of DWI was higher than before ablation, indicating complete ablation. In contrast, a lower ADC value after operation^{40,41} suggested that residual tumor remained, and supplementary RFA therapy should be considered.

Yamamoto et al.⁶⁰ performed a subsequent prospective MRI evaluation of small breast cancers treated with RFA prior to radiotherapy and chemotherapy and found that tumor margins could be determined to some extent. The probe placement during surgery and ablation completeness could also be predicted by MRI. The studies above indicate that MRI is necessary for evaluating post-ablation surgery, allowing prompt evaluation of possible tumor residuals, providing a basis for timely supplementary ablation, and demonstrating ablation's high safety and efficacy. However, this study is limited to a single center with a small number of cases. Further multicenter studies with large samples and prospective cohort studies are needed to offer a positive confirmation of MRI's clinical value.

3.4. Complications of MRI-RFA in breast cancer treatment

Due to patients' physical differences, complications after MRI-RFA treatment of breast cancer are diffuse and specific, but most can be predicted and controlled. The most common complication is burning of the skin, characterized by skin redness, elevated skin temperature at the body surface projection area of the lesion, and in severe cases, blisters. When the tumor is close to the chest wall, the skin is less than 1 cm thick, or multiple ablations are required to achieve satisfactory results, it is recommended to take specific protective measures, such as using a cool-tip needle for ablation during operation³⁹ or placing a sterile ice bag on the skin surface of the tumor. When skin temperature rises, cold saline gauze can be applied locally, and cold saline or 5% glucose solution can be injected subcutaneously to form a peritumoral isolation zone. Postoperative temperature measurement and care of the tumor area can involve the intermittent use of an ice compress⁶¹ to reduce potential skin damage. Burning pain in the operative area can often be relieved by local injection of lidocaine⁶² or by regional nerve block anesthesia before the operation begins.

Complications such as nipple discharge, burns, or retractions are rare. Yamamoto et al.⁶⁰ reported a rare case of chronic postoperative granulomatous mastitis in the surgical area, which they posited was related to an excessive autoimmune reaction induced by fat extravasation and production of this fluid after ablation. Therefore, comprehensive and predictable evaluations must be conducted prior to and after clinical treatment to develop an individualized therapeutic plan according to the size, location, and degree of enhancement of the patient's lesions. However, MRI can make a difference in reducing intraoperative pain in patients, preventing skin damage, and minimizing complications.

Conclusion

To conclude, MRI-RFA is a safe, feasible, minimally invasive, and less-painful interventional oncological procedure, rivalling surgical or other percutaneous techniques in its effectiveness as a partial treatment for early breast cancer. Due to its advantages in radiation, visualization, and real-time evaluation, MRI-RFA is being gradually accepted by clinicians and patients alike as a potentially valuable modality in treating breast cancer. To reduce the extent of extended resection and preserve breast integrity while ensuring negative margins, the introduction of MRI-RFA during BCS deserves more intensive investigation for patients with breast tumors of larger diameter. In addition, there is an urgent need to further explore the extraction of tumor characteristics related to the efficacy of MRI-RFA and to carry out more comparative efficacy evaluations and experimental studies focused on other means of ablation therapy to set reasonable and standardized indications and contraindications and thus maximize the benefit to patients. Further studies are also needed based on SLNB pro-RFA to guide management of the axilla. Toward this end, multicenter longitudinal studies and explorations of MRI-RFA in combination with systemic therapy require more attention.

Although technical issues, such as cost and MRI-RFA's compatibility with interventional equipment, impose constraints on its clinical application, MRI has assumed a supportive role in prompting medicine to evolve from precision diagnostics toward refined therapeutics. It is the key to improving the physiological and psychological prognoses of patients. With the development of technology and economic progression, the clinical application of MRI-RFA will gradually be generalized. Whether the effect of com-

prehensive treatment is similar to or better than that of traditional BCS requires further study. As such, collecting more empirical data to guide MRI-RFA's standardized application and help improve and innovate core technologies (e.g., ablation implementation and temperature monitoring) will offer a new treatment path for doctors and patients.

Conflict of interest disclosure

The authors declared no conflicts of interest.

References

1. Sung H, Ferlay J, Siegel RL, et al. Global Cancer Statistics 2020: GLOBOCAN estimates of incidence and mortality worldwide for 36 cancers in 185 countries. *CA Cancer J Clin.* 2021;71(3):209-249. [\[CrossRef\]](#)
2. Torre LA, Bray F, Siegel RL, et al. Global cancer statistics, 2012. *CA Cancer J Clin.* 2015;65(2):87-108. [\[CrossRef\]](#)
3. DeSantis CE, Ma J, Gaudet MM, et al. Breast cancer statistics, 2019. *CA Cancer J Clin.* 2019;69(6):438-451. [\[CrossRef\]](#)
4. Kang D, Choi EK, Kim IR, et al. Distress and body image due to altered appearance in posttreatment and active treatment of breast cancer patients and in general population controls. *Palliat Support Care.* 2018;16(2):137-145. [\[CrossRef\]](#)
5. Brem RF. Radiofrequency ablation of breast cancer: a step forward. *Radiology.* 2018;289(2):325-326. [\[CrossRef\]](#)
6. Podo F, Sardanelli F, Canese R, et al. The Italian multi-centre project on evaluation of MRI and other imaging modalities in early detection of breast cancer in subjects at high genetic risk. *J Exp Clin Cancer Res.* 2002;21(Suppl 3):115-124. [\[CrossRef\]](#)
7. Hrkac Pustahija A, Ivanac G, Brkljacic B. US and MRI in the evaluation of mammographic BI-RADS 4 and 5 microcalcifications. *Diagn Interv Radiol.* 2018;24(4):187-194. [\[CrossRef\]](#)
8. Lee AY, Nguyen VT, Arasu VA, et al. Sonographic-MRI correlation after percutaneous sampling of targeted breast ultrasound lesions: initial experiences with limited-sequence unenhanced MRI for postprocedural clip localization. *AJR Am J Roentgenol.* 2018;210(4):927-934. [\[CrossRef\]](#)
9. Liu CQ, Guo Y, Shi JY. Late morbidity associated with a tumour-negative sentinel lymph node biopsy in primary breast cancer patients: a systematic review. *Eur J Cancer.* 2009;45(9):1560-1568. [\[CrossRef\]](#)
10. Yu Y, Tan Y, Xie C et al. Development and validation of a preoperative magnetic resonance imaging radiomics-based signature to predict axillary lymph node metastasis and disease-free survival in patients with early-stage breast cancer. *JAMA Netw Open.* 2020;3(12):e2028086. [\[CrossRef\]](#)

11. Leithner D, Wengert GJ, Helbich TH, et al. Clinical role of breast MRI now and going forward. *Clin Radiol*. 2018;73(8):700-714. [\[CrossRef\]](#)
12. Schwartzberg B, Lewin J, Abdelatif O, et al. Phase 2 open-label trial investigating percutaneous laser ablation for treatment of early-stage breast cancer: MRI, pathology, and outcome correlations. *Ann Surg Oncol*. 2018;25(10):2958-2964. [\[CrossRef\]](#)
13. Merckel LG, Knuttel FM, Deckers R, et al. First clinical experience with a dedicated MRI-guided high-intensity focused ultrasound system for breast cancer ablation. *Eur Radiol*. 2016;26(11):4037-4046. [\[CrossRef\]](#)
14. Poplack SP, Levine GM, Henry L, et al. A pilot study of ultrasound-guided cryoablation of invasive ductal carcinomas up to 15 mm with MRI follow-up and subsequent surgical resection. *AJR Am J Roentgenol*. 2015;204(5):1100-1108. [\[CrossRef\]](#)
15. Simmons RM, Ballman KV, Cox C, et al. ACOSOG investigators. A phase II trial exploring the success of cryoablation therapy in the treatment of invasive breast carcinoma: results from ACOSOG (Alliance) Z1072. *Ann Surg Oncol*. 2016;23(8):2438-2445. [\[CrossRef\]](#)
16. Felipe VC, Bitencourt AGV, Souza JA, et al. MRI features after radiofrequency ablation in breast cancer. *Breast J*. 2020;26(3):541-542. [\[CrossRef\]](#)
17. Cao K, Liu H, Zhao B, Li Y, Qu Y, Sun Y. Texture features of pre-operative contrast enhanced MRI early phase images in predicting complete response for breast cancer after neoadjuvant chemotherapy. *Chinese J Radiol*. 2018;52(07):523-527. [\[CrossRef\]](#)
18. Gazelle GS, Goldberg SN, Solbiati L, Livraghi T. Tumor ablation with radio-frequency energy. *Radiology*. 2000;217(3):633-646. [\[CrossRef\]](#)
19. Paruch M. Mathematical modeling of breast tumor destruction using fast heating during radiofrequency ablation. *Materials (Basel)*. 2019;13(1):136. [\[CrossRef\]](#)
20. Yap S, Ooi EH, Foo JJ, Ooi ET. Bipolar radiofrequency ablation treatment of liver cancer employing monopolar needles: a comprehensive investigation on the efficacy of time-based switching. *Comput Biol Med*. 2021;131:104273. [\[CrossRef\]](#)
21. Peek MCL, Ahmed M, Napoli A, Usiskin S, Baker R, Douek M. Minimally invasive ablative techniques in the treatment of breast cancer: a systematic review and meta-analysis. *Int J Hyperthermia*. 2017;33(2):191-202. [\[CrossRef\]](#)
22. van de Voort EMF, Struik GM, Koppert LB, et al. Treatment of early-stage breast cancer with percutaneous thermal ablation, an open-label randomised phase 2 screening trial: rationale and design of the THERMAC trial. *BMJ Open*. 2021;11(9):e052992. [\[CrossRef\]](#)
23. van de Voort EMF, Struik GM, Birnie E, Moelker A, Verhoef C, Klem TMAL. Thermal ablation as an alternative for surgical resection of small (≤ 2 cm) breast cancers: a meta-analysis. *Clin Breast Cancer*. 2021;21(6):e715-e730. [\[CrossRef\]](#)
24. Pediconi F, Marzocca F, Cavallo Marincola B, Napoli A. MRI-guided treatment in the breast. *J Magn Reson Imaging*. 2018;48(6):1479-1488. [\[CrossRef\]](#)
25. Morin J, Traoré A, Dionne G, et al. Magnetic resonance-guided percutaneous cryosurgery of breast carcinoma: technique and early clinical results. *Can J Surg*. 2004;47(5):347-351. [\[CrossRef\]](#)
26. Pusztaszeri M, Vlastos G, Kinkel K, Pelte MF. Histopathological study of breast cancer and normal breast tissue after magnetic resonance-guided cryotherapy ablation. *Cryobiology*. 2007;55(1):44-51. [\[CrossRef\]](#)
27. Zhou W, Yu M, Pan H, et al. Microwave ablation induces Th1-type immune response with activation of ICOS pathway in early-stage breast cancer. *J Immunother Cancer*. 2021;9(4):e002343. [\[CrossRef\]](#)
28. Zhou W, Yu M, Mao X, et al. Landscape of the peripheral immune response induced by local microwave ablation in patients with breast cancer. *Adv Sci (Weinh)*. 2022;9(17):e2200033. [\[CrossRef\]](#)
29. Zhou W, Jiang Y, Chen L, et al. Image and pathological changes after microwave ablation of breast cancer: a pilot study. *Eur J Radiol*. 2014;83(10):1771-1777. [\[CrossRef\]](#)
30. Yu J, Han ZY, Li T, et al. Microwave ablation versus nipple sparing mastectomy for breast cancer ≤ 5 cm: a pilot cohort study. *Front Oncol*. 2020;10:546883. [\[CrossRef\]](#)
31. Nayak KS, Lim Y, Campbell-Washburn AE, Steeden J. Real-time magnetic resonance imaging. *J Magn Reson Imaging*. 2022;55(1):81-99. [\[CrossRef\]](#)
32. Cheng C, Zou C, Wan Q, et al. Dual-step iterative temperature estimation method for accurate and precise fat-referenced PRFS temperature imaging. *Magn Reson Med*. 2019;81(2):1322-1334. [\[CrossRef\]](#)
33. Baron P, Deckers R, Knuttel FM, Bartels LW. T1 and T2 temperature dependence of female human breast adipose tissue at 1.5 T: groundwork for monitoring thermal therapies in the breast. *NMR Biomed*. 2015;28(11):1463-1470. [\[CrossRef\]](#)
34. McLean M, Parker DL, Odéen H, Payne A. A T1-based correction method for proton resonance frequency shift thermometry in breast tissue. *Med Phys*. 2021;48(9):4719-4729. [\[CrossRef\]](#)
35. Poorman ME, Braškutė I, Bartels LW, Grissom WA. Multi-echo MR thermometry using iterative separation of baseline water and fat images. *Magn Reson Med*. 2019 Apr;81(4):2385-2398. [\[CrossRef\]](#)
36. Hue YK, Guimaraes AR, Cohen O, Nevo E, Roth A, Ackerman JL, et al. Magnetic resonance mediated radiofrequency ablation. *IEEE Trans Med Imaging*. 2018 Feb;37(2):417-427. [\[CrossRef\]](#)
37. Siedek F, Yeo SY, Heijman E, et al. Magnetic resonance-guided high-intensity focused ultrasound (MR-HIFU): technical background and overview of current clinical applications (part 1). *Rofo*. 2019;191(6):522-530. [\[CrossRef\]](#)
38. Nagashima T, Sakakibara M, Sangai T, et al. Surrounding rim formation and reduction in size after radiofrequency ablation for primary breast cancer. *Jpn J Radiol*. 2009;27(5):197-204. [\[CrossRef\]](#)
39. Fornage BD, Sneige N, Ross MI, et al. Small ($<$ or $= 2$ cm) breast cancer treated with US-guided radiofrequency ablation: feasibility study. *Radiology*. 2004;231:215-224. [\[CrossRef\]](#)
40. van den Bosch M, Daniel B, Rieke V, et al. MRI-guided radiofrequency ablation of breast cancer: preliminary clinical experience. *J Magn Reson Imaging*. 2008;27(1):204-208. [\[CrossRef\]](#)
41. Li J, Wang DD, Zhao YN, Zhou JW, Tang JH. Clinical assessment of magnetic resonance imaging-guided radiofrequency ablation for breast cancer. *Mol Clin Oncol*. 2019;11(4):411-415. [\[CrossRef\]](#)
42. Yunian Z, Qiao Y, Jianvey Q, et al. Clinical study of radiofrequency ablation guided by MRI in breast cancer. *Journal of Practical Medical Imaging*. 2017;18(6):461-465 (In Chinese). [\[CrossRef\]](#)
43. Hong R, Xu B. Breast cancer: an up-to-date review and future perspectives. *Cancer Commun (Lond)*. 2022;42(10):913-936. [\[CrossRef\]](#)
44. Palussièrre J, Henriques C, Mauriac L, et al. Radiofrequency ablation as a substitute for surgery in elderly patients with nonresected breast cancer: pilot study with long-term outcomes. *Radiology*. 2012;264(2):597-605. [\[CrossRef\]](#)
45. Donker M, van Tienhoven G, Straver ME, et al. Radiotherapy or surgery of the axilla after a positive sentinel node in breast cancer (EORTC 10981-22023 AMAROS): a randomised, multicentre, open-label, phase 3 non-inferiority trial. *Lancet Oncol*. 2014;15(12):1303-1310. [\[CrossRef\]](#)
46. Biganzoli L, Battisti NML, Wildiers H, et al. Updated recommendations regarding the management of older patients with breast cancer: a joint paper from the European Society of Breast Cancer Specialists (EUSOMA) and the International Society of Geriatric Oncology (SIOG). *Lancet Oncol*. 2021;22(7):e327-e340. [\[CrossRef\]](#)
47. Kurt N, Binboga Kurt B, Gulsaran U, et al. Diffusion tensor imaging and diffusion-weighted imaging on axillary lymph node status in breast cancer patients. *Diagn Interv Radiol*. 2022;28(4):329-336. [\[CrossRef\]](#)

48. Montemezzi S, Cardano G, Storer S, et al. MRI-guided breast biopsy based on diffusion-weighted imaging: a feasibility study. *Eur Radiol.* 2021;31(5):2645-2656. [\[CrossRef\]](#)
49. Pinker K, Moy L, Sutton EJ, et al. Diffusion-weighted imaging with apparent diffusion coefficient mapping for breast cancer detection as a stand-alone parameter: comparison with dynamic contrast-enhanced and multiparametric magnetic resonance imaging. *Invest Radiol.* 2018;53(10):587-595. [\[CrossRef\]](#)
50. Baltzer P, Mann RM, Lima M, et al. EUSOBI international breast diffusion-weighted imaging working group. Diffusion-weighted imaging of the breast—a consensus and mission statement from the EUSOBI International Breast Diffusion-Weighted Imaging Working Group. *Eur Radiol.* 2020;30(3):1436-1450. [\[CrossRef\]](#)
51. Dietzel M, Ellmann S, Schulz-Wendtland R, et al. Breast MRI in the era of diffusion weighted imaging: do we still need signal-intensity time curves? *Eur Radiol.* 2020;30(1):47-56. [\[CrossRef\]](#)
52. Xia LY, Hu QL, Xu WY. Efficacy and safety of radiofrequency ablation for breast cancer smaller than 2 cm: a systematic review and meta-analysis. *Front Oncol.* 2021;11:651646. [\[CrossRef\]](#)
53. Ohtani S, Kochi M, Ito M, et al. Radiofrequency ablation of early breast cancer followed by delayed surgical resection—a promising alternative to breast-conserving surgery. *Breast.* 2011;20(5):431-436. [\[CrossRef\]](#)
54. Jiménez Mazure C, Ribeiro González M, Soto Aguilar C, et al. Radiofrequency ablation of the surgical bed after lumpectomy in breast-conserving surgery. *Cir Esp (Engl Ed).* 2020;98(8):472-477. English, Spanish. [\[CrossRef\]](#)
55. García-Tejedor A, Guma A, Soler T, et al. Radiofrequency ablation followed by surgical excision versus lumpectomy for early stage breast cancer: a randomized phase II clinical trial. *Radiology.* 2018;289(2):317-324. [\[CrossRef\]](#)
56. Zhang D, Zhang H, Ge Z, et al. Clinical observation of radiofrequency ablation in breast-conserving surgery after neoadjuvant chemotherapy. *International Journal of Surgery.* 2020;12:31-35. [\[CrossRef\]](#)
57. Manenti G, Scarano AL, Pistolese CA, et al. Subclinical breast cancer: minimally invasive approaches. our experience with percutaneous radiofrequency ablation vs. cryotherapy. *Breast Care (Basel).* 2013;8(5):356-360. [\[CrossRef\]](#)
58. Lee HB, Han W, Kim SY, et al. Prediction of pathologic complete response using image-guided biopsy after neoadjuvant chemotherapy in breast cancer patients selected based on MRI findings: a prospective feasibility trial. *Breast Cancer Res Treat.* 2020;182(1):97-105. [\[CrossRef\]](#)
59. Burak WE Jr, Agnese DM, Povoski SP, et al. Radiofrequency ablation of invasive breast carcinoma followed by delayed surgical excision. *Cancer.* 2003;98(7):1369-1376. [\[CrossRef\]](#)
60. Yamamoto N, Fujimoto H, Nakamura R, et al. Pilot study of radiofrequency ablation therapy without surgical excision for T1 breast cancer: evaluation with MRI and vacuum-assisted core needle biopsy and safety management. *Breast Cancer.* 2011;18(1):3-9. [\[CrossRef\]](#)
61. Liu T, Chen K, Li L, Zhang S, Dong G. Primary study of radiofrequency ablation for early breast cancer with negative sentinel lymph node. *Chinese Journal of Ultrasonography.* 2021;30(3):236-242. [\[CrossRef\]](#)
62. Abdelrahman I, Steinvall I, Elmasry M, Sjöberg F. Lidocaine infusion has a 25% opioid-sparing effect on background pain after burns: a prospective, randomised, double-blind, controlled trial. *Burns.* 2020;46(2):465-471. [\[CrossRef\]](#)



Pre-emptive transjugular intrahepatic portosystemic shunt in pediatric cystic fibrosis-related liver disease and portal hypertension: prospective long-term results

Laurens Hermie¹
 Stephanie Van Biervliet²
 Anne Hoorens³
 Lien Van Cauwenberghe¹
 Eddy Robberecht²
 Luc Defreyne¹

¹Ghent University Hospital, Department of Vascular and Interventional Radiology, Gent, Belgium

²Ghent University Hospital, Department of Pediatrics, Gent, Belgium

³Ghent University Hospital, Department of Pathology, Gent, Belgium

PURPOSE

Portal hypertension (PHT) and its sequelae are the most clinically important manifestations in cystic fibrosis-related liver disease (CFLD). This paper aimed to evaluate the safety and efficacy of a pre-emptive transjugular intrahepatic portosystemic shunt (TIPS) to prevent PHT-related complications in pediatric patients with CFLD.

METHODS

This was a prospective single-arm study on pediatric patients with CFLD, signs of PHT, and preserved liver function who underwent a pre-emptive TIPS in a single tertiary CF center between 2007 and 2012. The long-term safety and clinical efficacy were assessed.

RESULTS

A pre-emptive TIPS was performed on seven patients with a mean age of 9.2 years (\pm standard deviation: 2.2). The procedure was technically successful in all patients, with an estimated median primary patency of 10.7 years [interquartile range (IQR) 0.5–10.7]. No variceal bleeding was observed during the median follow-up of 9 years (IQR 8.1–12.9). In two patients with advanced PHT and rapidly progressive liver disease, severe thrombocytopenia could not be stopped. Subsequent liver transplantation revealed biliary cirrhosis in both patients. In the remaining patients with early PHT and milder porto-sinusoidal vascular disease, symptomatic hypersplenism did not occur, and liver function remained stable until the end of the follow-up. Inclusion for pre-emptive TIPS was discontinued in 2013 following an episode of severe hepatic encephalopathy.

CONCLUSION

TIPS is a feasible treatment with encouraging long-term primary patency to avoid variceal bleeding in selected patients with CF and PHT. However, as the progression of liver fibrosis, thrombocytopenia, and splenomegaly is inevitable, the clinical benefits due to pre-emptive placement appear to be minor.

KEYWORDS

Cystic fibrosis, liver diseases, portal hypertension, children, transjugular intrahepatic portosystemic shunt, primary prophylaxis, variceal bleeding, hypersplenism

Corresponding author: Laurens Hermie

E-mail: Laurens.Hermie@uzgent.be

Received 22 August 2022; revision requested 26 September 2022; last revision received 16 November 2022; accepted 23 December 2022.



Epub: 20.03.2023

Publication date: 08.01.2023

DOI: 10.4274/dir.2022.221818

Cystic fibrosis (CF) is the most frequent autosomal recessive disorder in Caucasians and is caused by a mutation in the CF transmembrane conductance regulator gene.¹ Cystic fibrosis-associated liver disease (CFLD) is a well-known manifestation of CF and includes a wide range of hepatobiliary diseases.² Generally, CFLD remains subclinical, but 5% to 10% of patients will develop cirrhosis or portal hypertension (PHT).^{2,3} As liver failure is rather exceptional, the clinical outcome is determined mainly by PHT.⁴⁻⁷ Variceal bleeding is the most feared complication. While its prevalence is under debate, the physical and psychological im-

You may cite this article as: Hermie L, Van Biervliet S, Hoorens A, Van Cauwenberghe L, Robberecht E, Defreyne L. Pre-emptive transjugular intrahepatic portosystemic shunt in pediatric cystic fibrosis-related liver disease and portal hypertension: prospective long-term results. *Diagn Interv Radiol.* 2024;30(1):55-64.

pacts of a severe bleeding episode cannot be underestimated.³⁻⁷

The pathophysiological mechanism of CFLD and PHT remains poorly understood. Besides the main manifestation of focal biliary fibrosis leading to multilobular cirrhosis, an alternative vascular mechanism with obliterative portal venopathy (OPV) has been attributed to non-cirrhotic PHT (NCPH).⁸⁻¹² Therefore, since PHT can develop independently of cirrhosis, it should be evaluated carefully.¹² In NCPH, the hepatic venous pressure gradient does not represent the actual degree of PHT, and other non-invasive markers are required.^{8,12,13} An ultrasound (US) is a key examination for the predication and evaluation of PHT.¹²⁻¹⁸

Currently, treatment in CFLD focuses on screening and managing the complications of PHT and optimizing the nutritional status of the patient.¹⁹ In the absence of large prospective studies, there remains much ambiguity on the actual benefits, timing, and indications of different therapeutic interventions for PHT.²⁰ Endoscopic treatment is recommended for acute variceal bleeding but not for primary prevention in children.^{5,19,21,22} Nevertheless, primary prophylaxis by endoscopy is often pursued in children with a high risk of bleeding.^{2,23} However, the risks of repeated general anesthesia for the complete endoscopic eradication of varices should be considered in CF. In addition, it does not treat underlying PHT and other complications. Non-selective β -blockers are not endorsed because of poor tolerance and bronchoconstriction in CFLD.^{2,19} Liver transplantation (LT) is an effective therapeutic option in CFLD with end-stage liver failure and treatment-resistant and complicated PHT.^{5,20} However, because of the involvement of multiple organs

in CF, the decisions for transplant listing, graft selection, and timing are challenging.²⁰

A transjugular intrahepatic portosystemic shunt (TIPS) is a well-established procedure for portal vein decompression in adults.²⁴ In children with severe CFLD cirrhosis, TIPS has been proven as a feasible option in acute or refractory variceal bleeding or as a bridge to LT.^{6,25-27} However, as liver function may never deteriorate in CFLD with NCPH, portosystemic shunting to alleviate PHT might be preferable over LT.⁸ Currently, little data are available on the long-term outcome of interventional TIPS or surgical (distal spleno-renal or portocaval) shunts to mitigate PHT.¹⁹ The purpose of this prospective study was to evaluate early portal decompression with a TIPS as a safe and effective strategy to prevent PHT-related complications in the long term.

Methods

Study design and participants

This was a prospective single-arm study on pediatric patients with CFLD who underwent pre-emptive TIPS placement in a single CF center between January 2007 and December 2012. According to the trial protocol (Supplementary Figure 1) and following a multidisciplinary discussion, patients with CFLD with preserved liver function but early signs of PHT (thrombocytopenia, splenomegaly, US liver score, flow reduction/reversal in portal vein or portosystemic collaterals on US) were eligible for a pre-emptive TIPS.¹⁵ In these selected patients, it was assumed that fibrosis would progress, and the development of complications related to PHT would be highly probable. Inclusion was discontinued in 2013 due to some reluctance against pre-emptive TIPS after an episode of severe hepatic encephalopathy (HE) in one of the enrolled patients. Patient data were longitudinally evaluated from the time of the TIPS procedure to death, LT, or loss of follow-up. All data were censored on Dec 31, 2020. Written informed consent was obtained from each patient or representative. The trial protocol was reviewed and approved by Ghent University Hospital's Ethics Committee (EC UZG 2006/283, date: 03.15.2007). Prior to the enrolment of the first patient, the trial was registered with the National Trial Register (B67020071504).

TIPS procedure

All procedures were performed under general anesthesia by an experienced interventional radiologist (L.D.). Depending on

the patient's age and physiognomy, a TIPS was created following a conventional transjugular technique for adults or by a dedicated combined percutaneous transhepatic-transjugular approach for small children.²⁸ The principle of the latter technique is illustrated in Figure 1. Routinely, an expanded polytetrafluoroethylene (ePTFE)-covered endoprosthesis (Viatorr TIPS endoprosthesis, Gore) was used for shunt creation. If the sheath could not be negotiated into the main portal vein, a self-expandable non-covered stent (Wallstent, Boston Scientific) was placed. In all cases, stent dilatation was performed using an 8 mm angioplasty balloon. This was followed by direct portography and portosystemic pressure gradient (PPG) measurements. If the flow through the shunt was not sufficient, dilatation up to 10 mm was performed. We did not pursue a minimum gradient reduction. Prophylactic anticoagulant therapy after TIPS placement was not administered. Percutaneous "dual-pass" liver biopsy 18-Gauge Tru-Cut, throw length: 20 mm) was performed during the TIPS procedure. All patients were admitted to the pediatric intensive care unit following the TIPS procedure for overnight observation and then transferred to the pediatric floor. The follow-up data of these patients after discharge are shown in Supplementary Figure 1.

Outcome and definitions

The primary and secondary outcomes for efficacy were the prevention of variceal bleeding and the prevention of symptomatic hypersplenism (severe thrombocytopenia and/or splenomegaly requiring additional intervention/surgery), respectively, during the follow-up period. Thrombocytopenia was defined as a platelet count (PLT) of $<150.000/\mu\text{L}$, with a severe sub-definition of $<50.000/\mu\text{L}$. The spleen length for the age Z score was used to monitor the evolution of splenomegaly,²⁹ and the body-mass-index-for-age and height-for-age Z scores were used to monitor growth and nutritional status.³⁰

Safety was assessed according to immediate and late complications. Immediate complications were recorded in the 30-day post-procedural time frame.³¹ Late complications of TIPS placement, including the incidence of HE and the number of shunt revisions required, were monitored and recorded during the follow-up. Primary TIPS patency was defined as patency without shunt dysfunction requiring revision. Secondary patency was defined as restored full patency after shunt revision.

Main points

- A transjugular intrahepatic portosystemic shunt (TIPS) in pediatric cystic fibrosis-related liver disease (CFLD) is technically feasible, but there is an inherent risk of hepatic encephalopathy, especially alongside a high protein intake.
- In the long term, pre-emptive TIPS protects pediatric patients with CFLD from complications related to non-cirrhotic portal hypertension.
- Long-term TIPS patency in pediatric CFLD is encouraging and comparable with that in adult non-CF.
- Obliterative portal venopathy was the most prominent histological feature on biopsy and supports, at least partially, vascular disease in CFLD.

Following the new insights into NCPH, all liver biopsy samples were retrospectively re-analyzed by a hepatopathologist.³² For fibrosis scoring, the METAVIR scoring system was used (F0: no fibrosis, F4: cirrhosis).³³

Statistical analysis

The Shapiro–Wilk normality test was used to examine the normal distribution of variables. Data were expressed as the median with an interquartile range (IQR) if non-nor-

mally distributed and as the mean \pm standard deviation (SD) if normally distributed. A paired dot plot and the Wilcoxon signed-rank test were used to compare the paired pre-TIPS and end follow-up measurements.

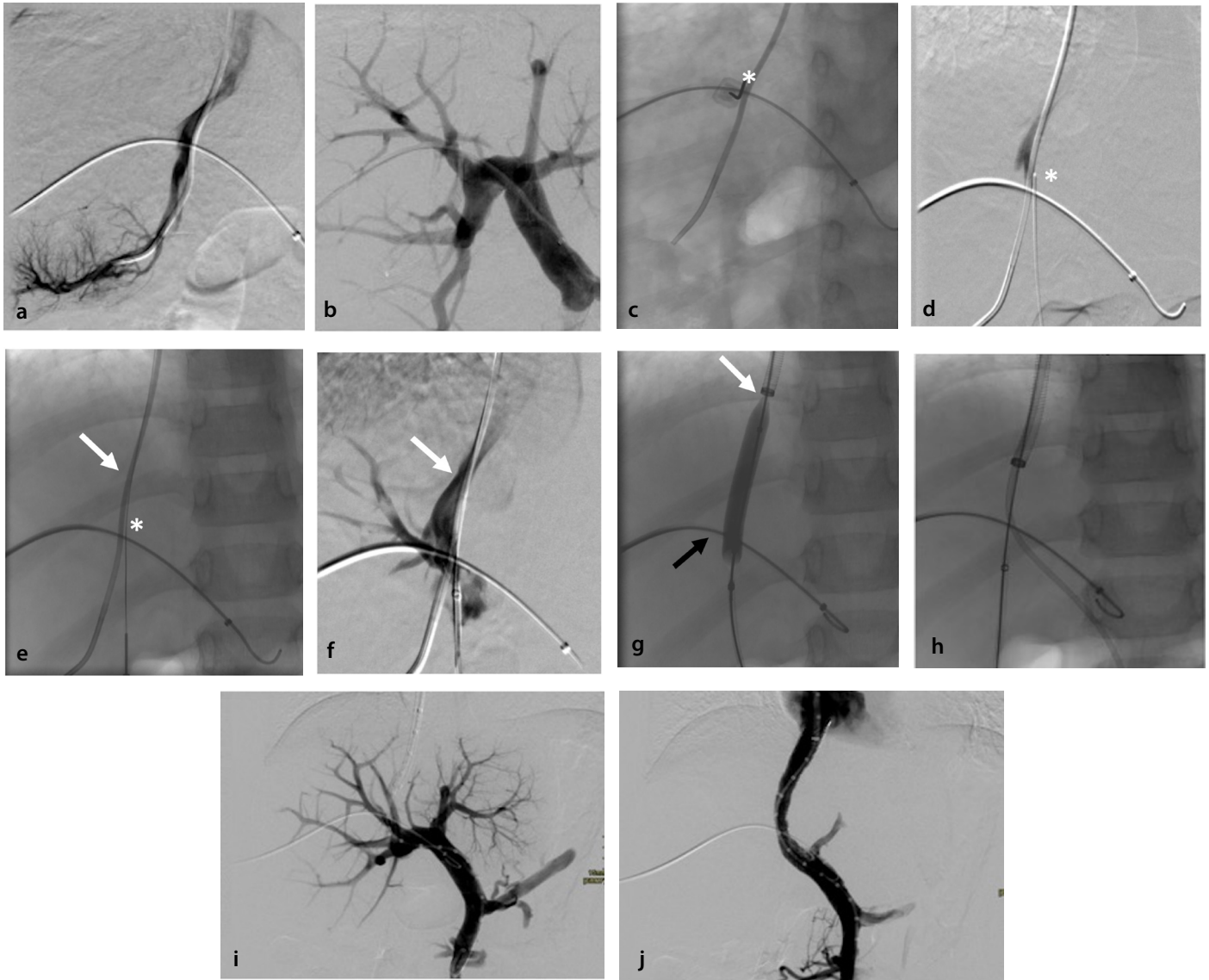


Figure 1. Modified percutaneous transhepatic–transjugular approach for small children. (a) Right transjugular vein access was used to advance a 10-F sheath (Flexor Check-flo II introducer set, Cook Medical) over a 5-F Headhunter-type catheter into the right hepatic vein. (b) Right-sided (midaxillary line) peripheral portal vein access was then obtained by percutaneous puncture, and a 5-F Cobra type was advanced through a 5-F introducer sheath into the main portal vein. (c) Subsequently, by inclining the X-ray tube, a favorable crossing of the catheters in the hepatic and portal vein was identified. From a ventral subcostal position, a third percutaneous puncture was performed using a long 21-gauge Chiba-type needle (white asterisk) directed perpendicular to the junction of the venous catheters, first perforating the portal vein and then entering the hepatic vein through the hepatic parenchyma. (d) The correct position of the needle (white asterisk) in the hepatic vein (white arrow) was confirmed by blood aspiration and a contrast medium injection performing digital subtraction angiography. (e) A 0.018 inch hydrophilic guidewire (Radifocus, Terumo) was introduced through the needle (white asterisk) into the right hepatic vein (white arrow). (f) The correct passing of the portal vein was confirmed by withdrawing the needle into the portal vein (black arrow) and through a contrast medium injection via a hemostatic valve (AccessPLUS hemostasis valve, Merit Medical). In this case, it also demonstrated the hepatic vein (white arrow). Over the 0.018 inch guidewire connecting the hepatic and portal veins, a 6-F coaxial access set (AccuStick II Introducer System, Boston Scientific) was advanced transhepatic into the hepatic vein. The small guidewire was then exchanged for a 300 cm long 0.035 inch stiff hydrophilic guidewire (Radiofocus Glidewire Advantage, Terumo), which was pushed upstream to the caval vein. (g) This guidewire was captured transjugular with a 25 mm snare (Amplatz GooseNeck Snare Kit, Covidien) (black asterisk) and used to guide the 6 mm balloon angioplasty of the parenchymal tract between the hepatic (white arrow) and portal vein (black arrow). (h) Subsequently, the transjugular sheath could be pushed towards the portal vein, and a 5-F Cobra-type catheter was introduced aside the safety guidewire into the portal vein. Through this catheter, a super-stiff guidewire (SupraCore, Abbott) was advanced in the splenic or mesenteric vein. (i) Direct portography was performed via a 5-F calibrated pigtail catheter to select the appropriate length for the endoprosthesis, followed by the measurement of the transhepatic portosystemic pressure gradient. Then, following the 8 mm balloon angioplasty of the parenchymal tract, the transjugular sheath was pushed into the main portal vein and the safety guidewire removed. From here, the procedure followed the same technique as for adults. (j) Final direct portography after transjugular intrahepatic portosystemic shunt placement. The percutaneous intrahepatic parenchymal tracts were closed using acrylic glue (Glubran2, GEM or Histoacryl, Braun) and diluted (1:2) with an oily contrast agent (Lipiodol UF, Guerbet).

A Kaplan–Meier plot was created to describe the primary and secondary TIPS patency. All analyses were performed using SPSS software version 27 and RStudio 4.0.2., with $P < 0.05$ considered significant.

Results

Patient selection

Seven children (five males and two females) with CFLD underwent a pre-emptive TIPS. The included patients had a mean age of 9.2 years (\pm SD 2.2) and a mean weight of 27.3 kg (\pm SD 6.9) (Table 1). They all exhibited signs of liver fibrosis on US, with a median US liver score of 7 (IQR 7–9).¹⁵ Clinical signs of PHT were hypersplenism (patients 1, 4, and 7) and splenomegaly without thrombocytopenia (patients 2 and 6). In patient 5, a progressive decline in PLT prompted a pre-emptive TIPS before reaching the threshold of thrombocytopenia. In patient 3, a pre-emptive TIPS

was performed due to hepatomegaly and early signs of PHT on US. None had a variceal bleeding episode before TIPS treatment.

During the TIPS, direct PPG measurements confirmed the presence of early PHT (PPG 6–10 mmHg) in five patients, with patients 1 and 4 unexpectedly having more severe PHT (17 mmHg). Some esophageal collaterals were seen (patients 1, 4, 6, and 7) during direct portal vein phlebography. Histopathological evidence of liver fibrosis was confirmed via biopsy in all patients, ranging from F1–F3 (Table 2). All had features suggestive of OPV, with different patterns, as illustrated in Supplementary Figure 2.

Technical and clinical outcomes (Table 3)

The pre-emptive TIPS procedure was technically successful in all patients, with no immediate post-procedural complications. An ePTFE-covered stent was placed in all pa-

tients except one. In patient 6, an uncovered stent was required because the 10-F sheath could not be passed into the main portal vein. All patients were discharged in a good condition after a hospitalization period of 2 to 5 days. Patient 1 suffered from intermittent hyperammonemia with doubtful neurological symptoms 19 days after the TIPS, which was treated medically without the recurrence of symptoms. Patient 6 was admitted because of rapid progressive HE, which evolved into a deep comatose state. This was related to a peptide-based drip-feed after receiving a gastrostomy because of poor nutritional intake 19 months after a TIPS. The patient was treated successfully with sodium benzoate. Then, lactulose and metronidazole were administered for 1 week per month, the drip feed was reduced and changed to a type with a lower protein load. Subsequently, the patient has been in a good condition for many years.

Table 1. Individual baseline characteristics at the time of the TIPS procedure

Patient no.	Patients with pre-emptive TIPS						
	1	2	3	4	5	6	7
Sex, age (years and months)	Male, 9 y 0 m	Male, 10 y 9 m	Female, 6 y 5 m	Female, 8 y 7 m	Male, 8 y 10 m	Male, 7 y 7 m	Male, 13 y 1 m
CFTR genotype	DF508/DF508	DF508/G542X	DF508/DF508	DF508/Y1092X	DF508/DF508	N1303K/2335delA	1717-1G>A/R553X
Weight (kg)/height (cm)	26/124	34/133	22/109	28/122	25/125	18/111	38/144
Pancreas insufficiency	Yes	Yes	Yes	Yes	Yes	Yes	Yes
BMI for age Z-score	0.2	0.9	1.0	0.5	0.6	-0.7	0
Length for age Z-score	-1.7	-1.6	-1.7	-1.4	-1.5	-2.7	-1.9
FEV1/FVC (%)	91/83	87/106	91/93	93/103	72/75	89/101	83/87
White blood cells ($\times 10^9/L$)	3.7	8.5	4.7	2.7	7.5	5.9	4.4
Platelets ($\times 10^9/L$)	62	264	242	55	154	247	142
AST (IU/L)	26	32	35	30	82	21	24
ALT (IU/L)	11	25	28	24	62	8	20
GGT (IU/L)	17	26	67	14	63	27	23
Albumin (g/dL)	3.3	4.5	4.3	4.2	4.2	4.0	5.0
Bilirubin (mg/dL)	0.4	0.4	0.2	0.6	0.2	0.3	0.4
INR	1.3	1.0	1.0	1.3	1.0	1.2	1.0
Serum creatinine (mg/dL)	0.3	0.7	0.6	0.3	0.4	0.5	0.7
APRI	1.0	0.3	0.4	1.4	1.3	0.2	0.4
MELD	9	6	6	9	6	8	6
Palpable liver (cm)	+ 3	+ 6	+ 9	+ 5	+ 3	+ 7	+ 1
Palpable spleen (cm)	+ 5	0	-	+ 7	0	-	-
Spleen size (cm)	16	11.5	7.5	18.5	11.0	11.0	13.8
Spleen for age Z-score	6.9	1.6	- 0.8	10.7	2.0	2.3	4.4
US liver score (Williams et al. ¹⁵)	7	7	7	9	9	7	8
US liver contour	Nodular	Nodular	Nodular	Nodular	Nodular	Nodular	Smooth

CFTR, cystic fibrosis transmembrane conductance regulator; TIPS, transjugular intrahepatic portosystemic shunt; BMI, body mass index; FEV1, forced expiratory volume; FVC, forced vital capacity; AST, aspartate aminotransferase; ALT, alanine aminotransferase; GGT, gamma-glutamyl transferase; INR, international normalised ratio; APRI, aspartate aminotransferase to platelet ratio index; MELD, model for end-stage liver disease; US, ultrasound.

During the median follow-up of 9 years (IQR 8.1–12.9) after the TIPS, none of the patients had an episode of variceal bleeding. In patients 1 and 4 with advanced PHT and marked hypersplenism at a young age, PLT continued to decrease even after TIPS treatment, ultimately resulting in severe throm-

bocytopenia with bleeding diathesis. Both underwent an LT because of progressive liver insufficiency, which was 2.8 years (LT in patient 1) and 8.1 years (LT in patient 4) following TIPS treatment. The histology of the explant showed a biliary pattern of cirrhosis. In the remaining patients, three (3, 5, and 7)

evolved to hypersplenism without the need for medical treatment. The PLT significantly decreased after TIPS, with an estimated median difference of 55.000/ μL ($P = 0.018$, Wilcoxon signed-rank test), whereas the spleen length for the age Z score did not increase (Figure 2). Patient 3 died after 12.9 years

Table 2. Histopathological features on liver biopsy during the TIPS procedure

Patient no.	Patients with pre-emptive TIPS						
	1	2	3	4	5	6	7
Number of portal tracts	8	10	5	2	1	6	1
Steatosis†	Mild, macro	Mild, macro	No	No	No	Severe, macro	No
METAVIR fibrosis score‡	F3	F2	F2-F3	F3	F3	F1-F2	F3
Classical features of CFLD§	No	No	Yes	No	Yes	No	Yes
Typical bile inspissation¶	No	No	No	No	Yes	No	Yes
Portal vascular changes#	PV absent	PV too small or absent	PV absent or thick wall	PV absent	PV absent	PV too small	PV absent
PHT features▲	Focal SD	No	Focal mild SD	No	No	SV	No
Cholate stasis♥	No	No	No	No	No	No	Focal
Conclusion	Advanced fibrosis, OPV	OPV	Advanced fibrosis, OPV	Advanced fibrosis, OPV	Advanced fibrosis, OPV	OPV	Advanced fibrosis, OPV

†Absent/mild <33%/moderate: 33%–66%/severe >66%, type: micro-/macrovesicular/mixed. ‡F0/F1: portal fibrosis with no septa/F2: few septa/F3: numerous septa without cirrhosis/F4: cirrhosis. §Focal biliary fibrosis with ductular reaction (>2 bile ducts in PT) and predominantly polymorphonuclear neutrophils infiltrate. ¶Periodic acid–Schiff positive. #Portal veins absent in $\geq 40\%$ of complete portal tract and/or portal vein too small (<2 \times size of accompanying artery or bile duct). ▲Paraportal shunt vessels and/or sinusoidal dilatation in >50% of draining areas of central veins. ♥Periportal ductular metaplasia on CK7 staining and/or periportal copper deposition. OPV, obliterative portal venopathy; TIPS, transjugular intrahepatic portosystemic shunt; CFLD, cystic fibrosis-related liver disease; PHT, portal hypertension. No biopsy was performed on patient 10.

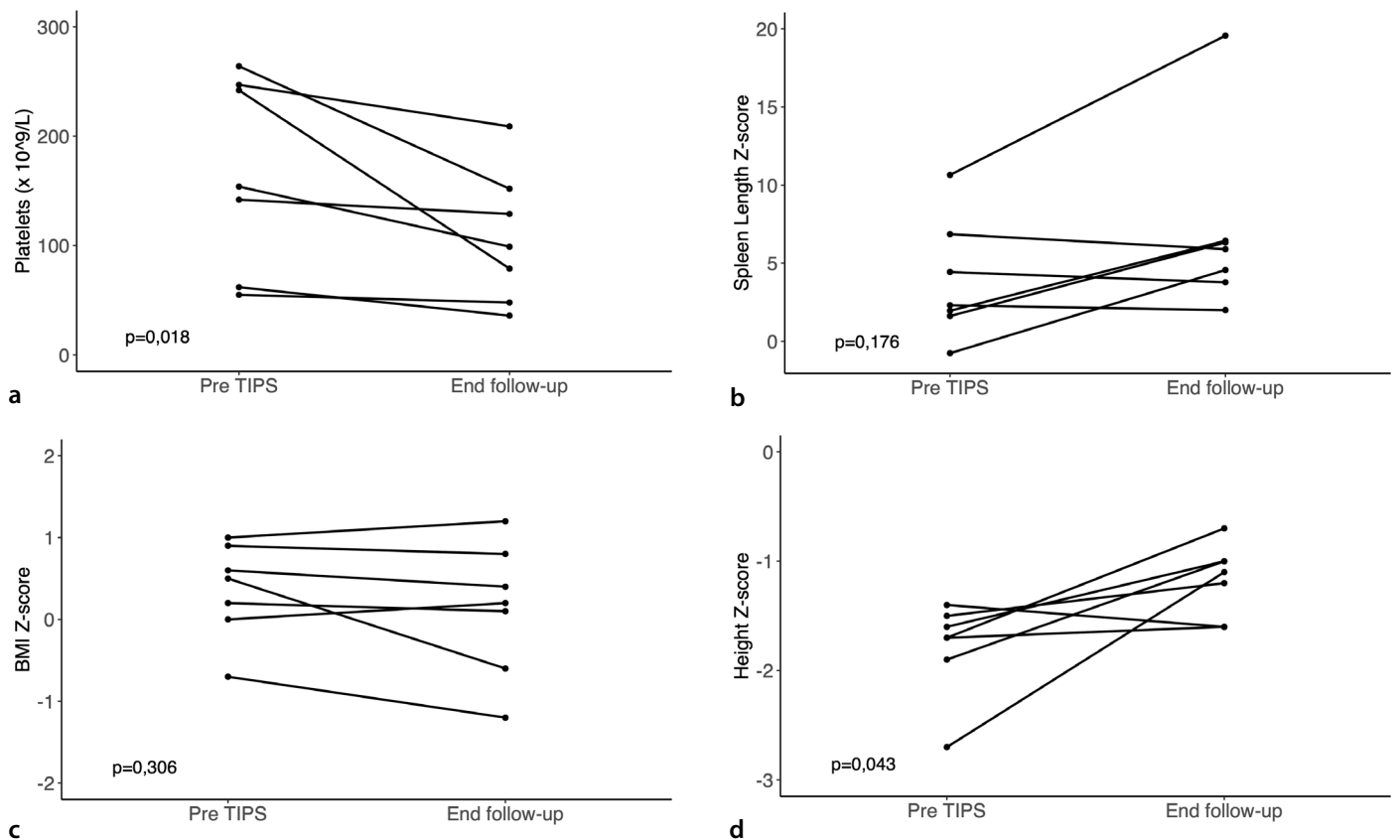


Figure 2. Individual evolution of hypersplenism, malnutrition, and growth. The paired dot plot and Wilcoxon signed-rank test for the paired results of (a) platelet count, (b) spleen length-for-age Z score, (c) body-mass-index (BMI)-for-age Z score, and (d) height-for-age Z score at the time of the transjugular intrahepatic portosystemic shunt (TIPS) procedure and at the end of the follow-up. A value of $P < 0.05$ was considered significant.

Table 3. Procedure details and outcome							
Patients with pre-emptive TIPS							
Patient no	1	2	3	4	5	6	7
TIPS procedure							
Technique	PIPS	PIPS	PIPS	PIPS	PIPS	PIPS	Transjugular
Stent type, diameter × length (mm)	Wallstent, 10 × 42	Viatorr, 8 × 50†	Viatorr, 8 × 60†	Wallstent, 10 × 42; Wallstent, 12 × 42; Viatorr, 10 × 60†	Viatorr, 8 × 40†	Viatorr, 10 × 60†	Viatorr, 10 × 50†
Stent position	Right–right	Right–right	Right–right	Right–left	Right–right	Right–right	Right–right
Final stent dilation	8	8	8	10	8	8	8
PPG before TIPS (mmHg)	17	8	7	17	6	8	6
PPG after TIPS (mmHg)	13	5	4	10	2	2	3
Time of procedure (min)	480	125	160	360	120	190	160
GOV							
TIPS patency							
Primary patency (y)	0.0	10.7	0.5	8.1, open	2.1	9.0, open	8.3, open
Secondary patency (y)	2.8, open	12.3	9.9	8.1, open	12.3, open	9.0, open	8.3, open
Follow-up time (y)	2.8, LT	13.3, alive	12.9, death	8.1, LLT	12.3, alive	9.0, alive	8.3, alive
Clinical outcome at the end follow-up							
Variceal hemorrhage	No	No	No	No	No	No	No
Liver transplantation	Yes	No	No	Yes	No	No	No
Spleen size (cm)	16	16.4	13.5	24	16.5	12.5	14.1
Spleen for age Z-score	5.90	6.33	4.57	19.57	6.44	2.00	3.78
Spleen length ratio	1.62	1.52	1.36	2.26	1.53	1.17	1.31
Platelets (× 10 ⁹ /L)	36	152	79	48	99	209	129
MELD score	14	10	33§	15	8	10	9
INR	1.9	1.1	4.6	1.6	1.1	1.2	1.1
Ammonia (µmol/L)	55	24	79	64	27	59	25
BMI for age Z-score	0.1	0.8	1.2	−0.6	0.4	−1.2	0.2
Length for age Z-score	−0.7	−1.0	−1.6	−1.6	−1.2	−1.1	−1.0

†Covered part, ‡last data before splenectomy, §related to hemophagocytic syndrome. TIPS, transjugular intrahepatic portosystemic shunt; PIPS, percutaneous intrahepatic portosystemic shunt; GOV, gastroesophageal varices; PPG, portosystemic pressure gradient; MELD, model for end-stage liver disease; LT, liver transplantation; LLT, lung/liver transplantation.

because of a sudden severe hemophagocytic syndrome with secondary multiple organ failure, which was not related to CFLD. On the last annual assessment, this patient had a stable liver function (model for end-stage liver disease 8). In the remaining patients with early PHT, liver function remained stable, and LT could be avoided until the end of the follow-up. No patients developed ascites. Regarding growth, the height for the age Z score significantly increased after the TIPS, with an estimated median difference of 0.6 ($P = 0.043$, Wilcoxon signed-rank test).

Four in seven patients required one or more revisions, resulting in an estimated median primary patency of 10.7 years (IQR 0.5–10.7) after TIPS treatment (Figure 3). The primary patency rates at 2, 4, and 6 years were

71.4%, 57.1%, and 57.1%, respectively. A total of 10 TIPS dysfunctions were detected by US, and the revisions revealed four stenoses and six occlusions. Patient 5 presented with progressive hypersplenism, despite no shunt deficiency on the duplex US. A subsequent 10 mm balloon angioplasty was performed with a PPG decrease from 5 to 4 mmHg. Except for patients 1 and 4, the PPG during the revision never exceeded the threshold of 10 mmHg. Patients 2 and 3 demonstrated a revision refractory occlusion of the TIPS after 12.3 and 9.9 years, respectively. In both patients, a new left–left TIPS was created to reduce the PPG (from 10 to 4 mmHg and from 9 to 5 mmHg, respectively). The first TIPS in five patients and the second TIPS in two patients were open at the end of the follow-up.

Discussion

The prospective selection of children for a pre-emptive TIPS was based on several non-invasive indicators. The intention was to include patients with early PHT, ideally before the onset of clinically significant PHT. However, two children with thrombocytopenia and marked splenomegaly showed post-hoc more severe PHT (PPG of 17 mmHg) on invasive pressure measurements during the TIPS procedure. In both, further deterioration of CFLD could not be prevented, and a hepatic decompensation developed, with a need for LT. A histopathological re-evaluation of the biopsy samples did not show any clear distinction between them and the other patients with early PHT. In all patients, OPV was the most prominent histopatho-

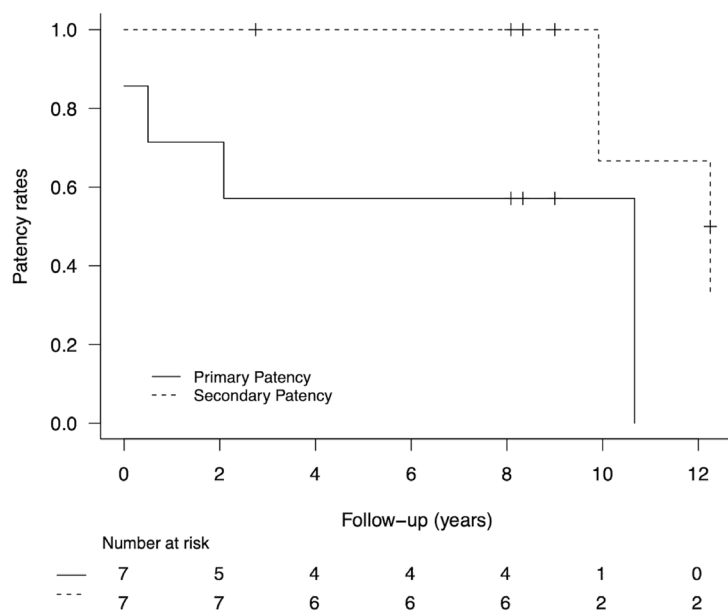


Figure 3. Primary and secondary patency of transjugular intrahepatic portosystemic shunt. Kaplan-Meier plot.

logical feature, supporting porto-sinusoidal vascular disease. Nevertheless, both patients with severe PHT showed advanced fibrosis (F3), which is indistinguishable from incomplete septal cirrhosis on a needle biopsy. Further, as CFLD is a highly heterogeneous disease, there is an inherent risk of a sampling error.^{13,26} Eventually, explant histology demonstrated a biliary pattern of cirrhosis in both patients. Consistent with previous assumptions, these patients likely suffered from an earlier and more severe phenotype of CFLD with extensive fibrosis (or cirrhosis), PHT, and liver failure, often requiring LT.¹¹ The remaining patients may have had a milder phenotype with a slowly progressive NCPH, as indicated by the moderately elevated PPG throughout the follow-up.

This study confirms that a TIPS, even in small children with CF, is feasible and can be performed safely without major adverse events in the immediate post-procedural period. Portal vein access from a conventional jugular approach can be problematic due to the wider anatomical variations and geometrical incompatibilities in a small child's liver. The use of a combined transjugular and transhepatic approach in the youngest children in our series enabled us to overcome this difficulty without complications related to the percutaneous technique. Nevertheless, although HE is of major concern after TIPS, it seems only to occur in patients with a high protein intake.⁵ Excessive shunting should be avoided by leaving a residual PPG of ≥ 3

mmHg. Furthermore, controlling the protein intake and monitoring ammonium levels are key points in the follow-up of patients with CFLD after shunt placement. Intermittent or chronic mild hyperammonemia could be observed in several patients after TIPS but without the manifestation of neurodegenerative complications or cognitive impairments in the long term.

Stent dysfunction in TIPS is a well-known long-term complication in adults. This study prospectively recorded 6-year primary and secondary patencies of 57% and 100%, respectively, which is in line with previous retrospective studies on pediatric PHT.^{26,34} Strict follow-ups with US are mandatory to detect early stent stenosis, allowing for an uncomplicated revision. Nevertheless, after almost 10 years, two patients eventually required a second TIPS because of stent occlusion, which was refractory to revision. Overall, the long-term permeability of a TIPS in children with CFLD appears comparable to the patency in adults.³⁵

This study achieved its objective in terms of efficacy, as pre-emptive TIPS placement avoided variceal bleeding in pediatric patients with CFLD and PHT in the long term. Except in one patient, portal decompression after primary or revisional TIPS resulted in a PPG below 12 mmHg, which is a critical threshold for bleeding protection in adults and is likely in the pediatric population.³⁶ Previous retrospective series indicated that a

TIPS could improve hypersplenism in pediatric PHT.^{37,38} In the present trial, we observed a significant decrease in PLT, with failure to avert severe thrombocytopenia in both patients with more advanced PHT at the time of the TIPS. It appears that hypersplenism progresses over time, despite a functional TIPS and a low PPG (5 mmHg), not even exceeding the classical threshold of PHT in adults. As portosystemic collaterals/varices were also identified in patients with a PPG below 10 mmHg, the upper limit of normal for the PPG might be lower in these pediatric patients.³⁹ Although liver fibrosis and the slow progression of PHT appeared inevitable in the present trial, a comparative case series indicated that a surgical distal splenorenal shunt (DSRS) could improve hypersplenism in CFLD.³⁸ This is presumably related to more effective decompression of the spleen. Moreover, while a pre-emptive TIPS prevented variceal bleeding during double the follow-up time, no episodes of HE occurred after DSRS.⁴⁰

The use of TIPS may be an interesting therapeutic strategy in a pre-emptive stage of NCPH, but it remains controversial, and there are some ongoing questions. First, this study was limited by its small sample size and the lack of a conservative control group. Furthermore, the incidence of CFLD is low, and subsequently, the number of patients with early-stage PHT is even lower. Therefore, randomization was never an option. Second, as shown in the present study, it remains challenging to correctly identify patients early who will progress to severe CFLD with cirrhosis or NCPH and are subsequently at risk of developing complications.^{12,41} Even revisiting the original histopathology could not find a way to distinguish the two phenotypes in CFLD. However, early clinical signs of PHT with progressive thrombocytopenia or an advanced PPG on invasive pressure measurements might be indicative of a more severe phenotype. Considering normal PLT with low PPG at the time of the TIPS in several patients, a selection bias toward a more favorable disease course may exist. Third, the implementation of primary prophylaxis is debatable, as the risk of variceal bleeding is currently estimated at 5%–10% within 10 years of diagnosis.^{3,18,42} Finally, a pre-emptive TIPS remains an invasive treatment for a fragile patient group without troublesome symptoms and with a limited tolerance for procedural complications.

In conclusion, this prospective study demonstrated TIPS as a feasible long-term treatment for selected CF patients with PHT to avert variceal bleeding. However, as the

progression of liver fibrosis, thrombocytopenia, and splenomegaly is inevitable, and the bleeding risk has previously been overestimated, the clinical benefits due to pre-emptive placement appear to be minor. Moreover, there is an inherent risk of HE, especially with excessive shunting or uncontrolled protein intake. Consistent with previous reports, a liver biopsy at the time of the TIPS showed histopathological features of porto-sinusoidal vascular disease and advanced fibrosis.

Acknowledgements

We thank Ellen Delanghe (Clinical Research Assistant, Department of Vascular and Interventional Radiology, Ghent University Hospital, Ghent, Belgium now working at Pfizer Pharmaceuticals, Puurs, Belgium) for her assistance with data collection and preparation, and Prof. Geoffrey Schouten (Gastroenterologist, Department of Gastroenterology and Hepatology, AZ Nikolaas, Sint-Niklaas, Belgium) for his expert opinion on the manuscript.

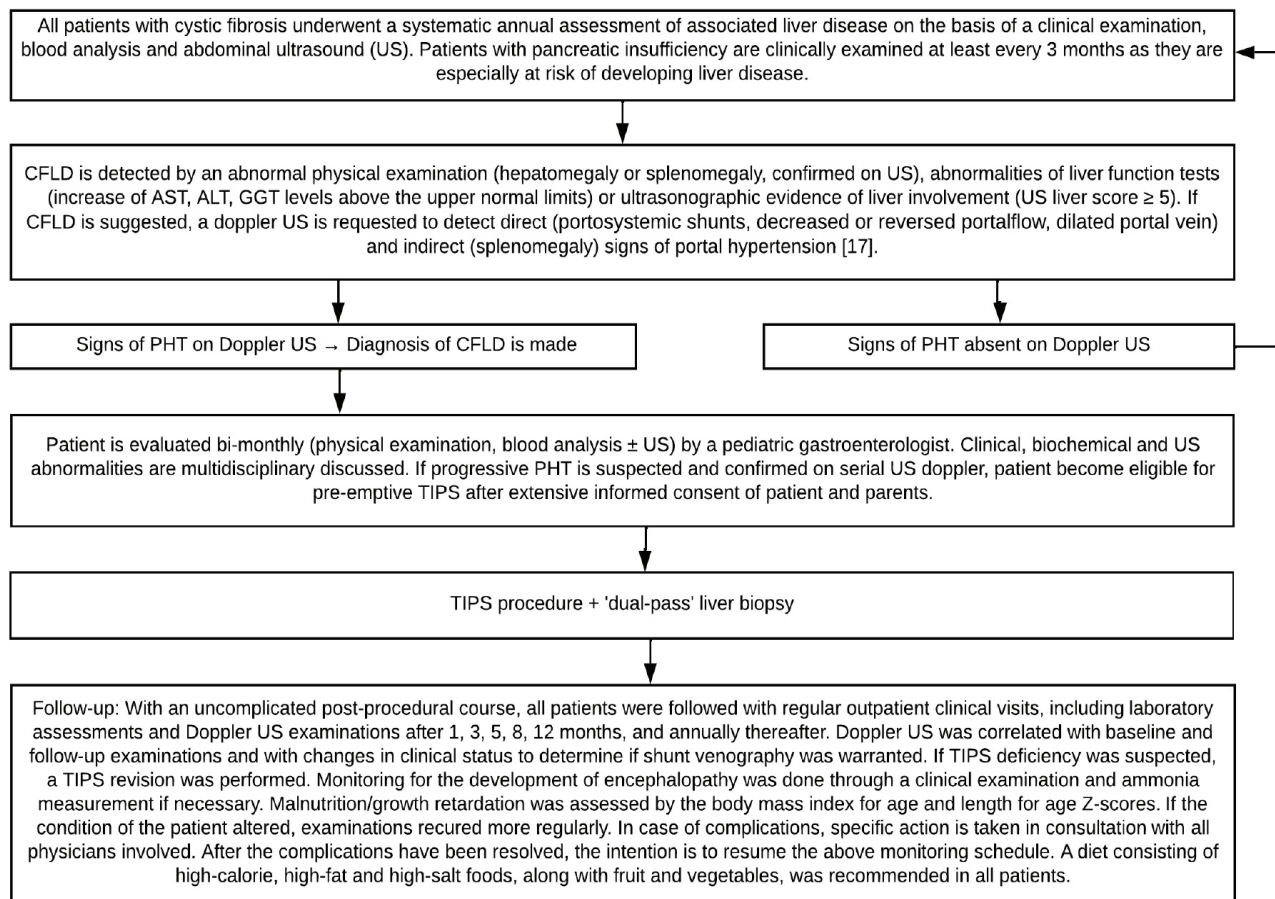
Conflict of interest disclosure

The authors declared no conflicts of interest.

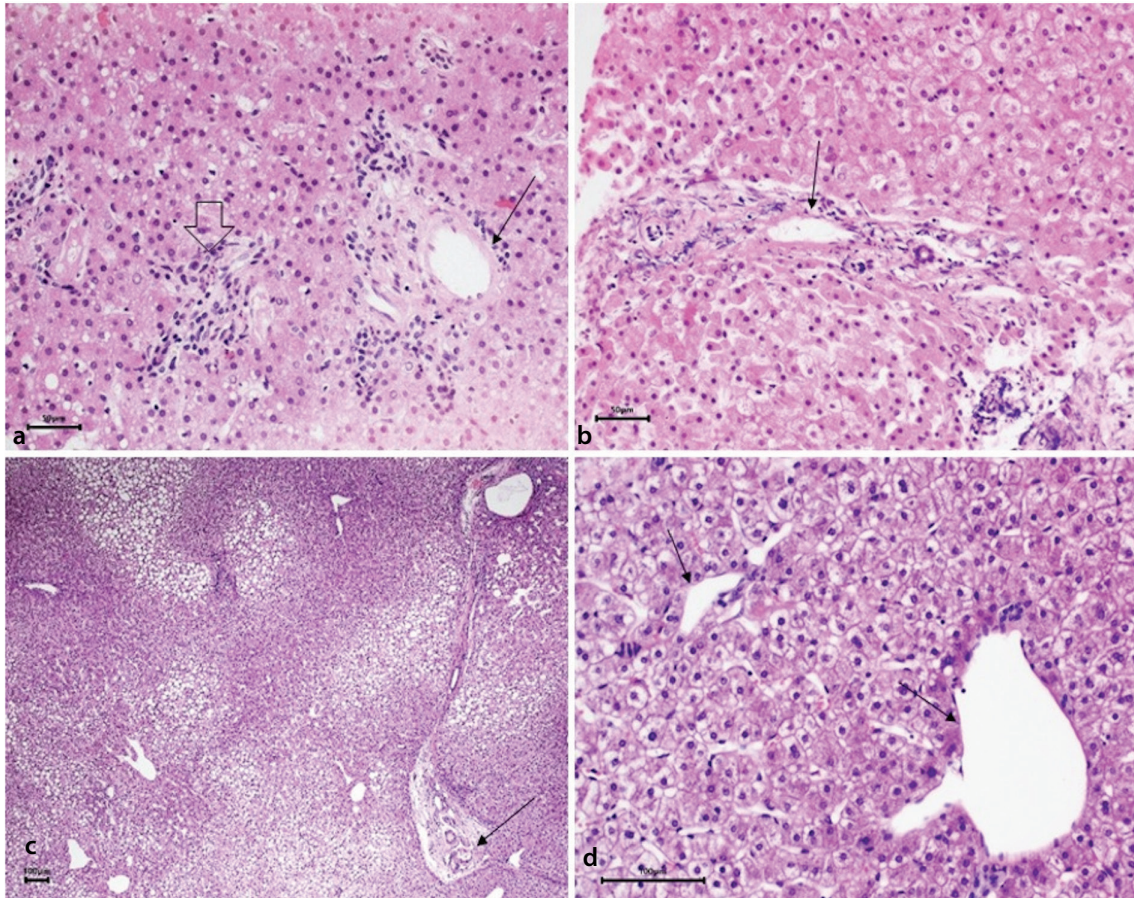
References

- O'Sullivan BP, Freedman SD. Cystic fibrosis. *Lancet*. 2009;373(9678):1891-1904. [\[CrossRef\]](#)
- Flass T, Narkewicz MR. Cirrhosis and other liver disease in cystic fibrosis. *J Cyst Fibros*. 2013;12(2):116-124. [\[CrossRef\]](#)
- Boëlle PY, Debray D, Guillot L, Clement A, Corvol H; French CF Modifier Gene Study Investigators. Cystic fibrosis liver disease: outcomes and risk factors in a large cohort of French patients. *Hepatology*. 2019;69(4):1648-1656. [\[CrossRef\]](#)
- Debray D, Lykavieris P, Gauthier F, et al. Outcome of cystic fibrosis-associated liver cirrhosis: management of portal hypertension. *J Hepatol*. 1999;31(1):77-83. [\[CrossRef\]](#)
- Leung DH, Narkewicz MR. Cystic Fibrosis-related cirrhosis. *J Cyst Fibros*. 2017;16 (Suppl 2):S50-S61. [\[CrossRef\]](#)
- Debray D, Kelly D, Houwen R, Strandvik B, Colombo C. Best practice guidance for the diagnosis and management of cystic fibrosis-associated liver disease. *J Cyst Fibros*. 2011;10 (Suppl 2):S29-S36. [\[CrossRef\]](#)
- Rowland M, Gallagher C, Gallagher CG, et al. Outcome in patients with cystic fibrosis liver disease. *J Cyst Fibros*. 2015;14(1):120-126. [\[CrossRef\]](#)
- Witters P, Libbrecht L, Roskams T, et al. Liver disease in cystic fibrosis presents as non-cirrhotic portal hypertension. *J Cyst Fibros*. 2017;16(5):e11-e13. [\[CrossRef\]](#)
- Wu H, Vu M, Dhingra S, et al. Obliterative portal venopathy without cirrhosis is prevalent in pediatric cystic fibrosis liver disease with portal hypertension. *Clin Gastroenterol Hepatol*. 2019;17(10):2134-2136. [\[CrossRef\]](#)
- Hillaire S, Cazals-Hatem D, Bruno O, et al. Liver transplantation in adult cystic fibrosis: clinical, imaging, and pathological evidence of obliterative portal venopathy. *Liver Transpl*. 2017;23(10):1342-1347. [\[CrossRef\]](#)
- Cipolli M, Fethney J, Waters D, et al. Occurrence, outcomes and predictors of portal hypertension in cystic fibrosis: a longitudinal prospective birth cohort study. *J Cyst Fibros*. 2020;19(3):455-459. [\[CrossRef\]](#)
- Dana J, Debray D, Beaufrère A, et al. Cystic fibrosis-related liver disease: clinical presentations, diagnostic and monitoring approaches in the era of CFTR modulator therapies. *J Hepatol*. 2022;76(2):420-434. [\[CrossRef\]](#)
- Da BL, Surana P, Kapuria D, et al. Portal pressure in noncirrhotic portal hypertension: to measure or not to measure. *Hepatology*. 2019;70(6):2228-2230. [\[CrossRef\]](#)
- Siegel MJ, Freeman AJ, Ye W, et al. Heterogeneous liver on research ultrasound identifies children with cystic fibrosis at high risk of advanced liver disease: interim results of a prospective observational case-controlled study. *J Pediatr*. 2020;219:62-69. [\[CrossRef\]](#)
- Williams SG, Evanson JE, Barrett N, Hodson ME, Boulton JE, Westaby D. An ultrasound scoring system for the diagnosis of liver disease in cystic fibrosis. *J Hepatol*. 1995;22(5):513-521. [\[CrossRef\]](#)
- Etzion O, Takyar V, Novack V, et al. Spleen and liver volumetrics as surrogate markers of hepatic venous pressure gradient in patients with noncirrhotic portal hypertension. *Hepatol Commun*. 2018;2(8):919-928. [\[CrossRef\]](#)
- Sutton H, Dhawan A, Grammatikopoulos T. Non-invasive markers of portal hypertension: appraisal of adult experience and potential utilisation in children. *J Pediatr Gastroenterol Nutr*. 2018;66(4):559-569. [\[CrossRef\]](#)
- Leung DH, Ye W, Schwarzenberg SJ, et al. Long-term follow-up and liver outcomes in children with cystic fibrosis and nodular liver on ultrasound in a multi-center study. *J Cyst Fibros*. 2022;S1569-1993(22)00635-X. [\[CrossRef\]](#)
- Palaniappan SK, Than NN, Thein AW, Moe S, van Mourik I. Interventions for preventing and managing advanced liver disease in cystic fibrosis. *Cochrane Database Syst Rev*. 2017;8(8):CD012056. [\[CrossRef\]](#)
- Freeman AJ, Sellers ZM, Mazariegos G, et al. A multidisciplinary approach to pretransplant and posttransplant management of cystic fibrosis-associated liver disease. *Liver Transpl*. 2019;25(4):640-657. [\[CrossRef\]](#)
- Debray D, Narkewicz MR, Bodewes FAJA, et al. Cystic fibrosis-related liver disease: research challenges and future perspectives. *J Pediatr Gastroenterol Nutr*. 2017;65(4):443-448. [\[CrossRef\]](#)
- Shneider BL, de Ville de Goyet J, Leung DH, et al. Primary prophylaxis of variceal bleeding in children and the role of MesoRex bypass: summary of the Baveno VI Pediatric Satellite Symposium. *Hepatology*. 2016;63(4):1368-1380. [\[CrossRef\]](#)
- Jeanniard-Malet O, Duché M, Fabre A. Survey on clinical practice of primary prophylaxis in portal hypertension in children. *J Pediatr Gastroenterol Nutr*. 2017;64(4):524-527. [\[CrossRef\]](#)
- Tripathi D, Stanley AJ, Hayes PC, et al. Transjugular intrahepatic portosystemic shunt-shunt in the management of portal hypertension. *Gut*. 2020;69(7):1173-1192. [\[CrossRef\]](#)
- Pozler O, Krajina A, Vanicek H, et al. Transjugular intrahepatic portosystemic shunt in five children with cystic fibrosis: long-term results. *Hepatogastroenterology*. 2003;50(52):1111-1114. [\[CrossRef\]](#)
- Johansen LC, McKiernan PJ, Sharif K, McQuirk SP. Transjugular intrahepatic portosystemic shunt insertion for the management of portal hypertension in children. *J Pediatr Gastroenterol Nutr*. 2018;67(2):173-179. [\[CrossRef\]](#)
- Bertino F, Hawkins CM, Shivaram G, et al. Technical feasibility and clinical effectiveness of transjugular intrahepatic portosystemic shunt creation in pediatric and adolescent patients. *J Vasc Interv Radiol*. 2019;30(2):178-186. [\[CrossRef\]](#)
- Hermie L, Dhondt E, Vanlangenhove P, Hoste E, Geerts A, Defreyne L. Model for end-stage liver disease score and hemodynamic instability as a predictor of poor outcome in early transjugular intrahepatic portosystemic shunt treatment for acute variceal hemorrhage. *Eur J Gastroenterol Hepatol*. 2018;30(12):1441-1446. [\[CrossRef\]](#)
- Megremis SD, Vlachonikolis IG, Tsilimigaki AM. Spleen length in childhood with US: normal values based on age, sex, and somatometric parameters. *Radiology*. 2004;231(1):129-134. [\[CrossRef\]](#)
- Roelants M, Hauspie R, Hoppenbrouwers K. References for growth and pubertal development from birth to 21 years in Flanders, Belgium. *Ann Hum Biol*. 2009;36(6):680-694. [\[CrossRef\]](#)
- Dariushnia SR, Haskal ZJ, Midia M, et al. Quality improvement guidelines for transjugular intrahepatic portosystemic shunts. *J Vasc Interv Radiol*. 2016;27(1):1-7. [\[CrossRef\]](#)

32. Witters P, Libbrecht L, Roskams T, et al. Noncirrhotic presinusoidal portal hypertension is common in cystic fibrosis-associated liver disease. *Hepatology*. 2011;53(3):1064-1065. [\[CrossRef\]](#)
33. Bedossa P, Poynard T. An algorithm for the grading of activity in chronic hepatitis C. The METAVIR Cooperative Study Group. *Hepatology*. 1996;24(2):289-293. [\[CrossRef\]](#)
34. Di Giorgio A, Nicastro E, Agazzi R, Colusso M, D'Antiga L. Long-term outcome of transjugular intrahepatic portosystemic shunt in children with portal hypertension. *J Pediatr Gastroenterol Nutr*. 2020;70(5):615-622. [\[CrossRef\]](#)
35. Perarnau JM, Le Gouge A, Nicolas C, et al. Covered vs. uncovered stents for transjugular intrahepatic portosystemic shunt: a randomized controlled trial. *J Hepatol*. 2014;60(5):962-968. [\[CrossRef\]](#)
36. Bosch J, Groszmann RJ, Shah VH. Evolution in the understanding of the pathophysiological basis of portal hypertension: How changes in paradigm are leading to successful new treatments. *J Hepatol*. 2015;62(Suppl 1):S121-S130. [\[CrossRef\]](#)
37. Verbeeck S, Mekhali D, Cassiman D, Maleux G, Witters P. Long-term outcome of transjugular intrahepatic portosystemic shunt for portal hypertension in autosomal recessive polycystic kidney disease. *Dig Liver Dis*. 2018;50(7):707-712. [\[CrossRef\]](#)
38. Liu J, Ma J, Yang C, et al. Impact of TIPS on splenic volume and thrombocytopenia. *AJR Am J Roentgenol*. 2021;216(3):698-703. [\[CrossRef\]](#)
39. Liu J, Ma J, Yang C, et al. Impact of TIPS on splenic volume and thrombocytopenia. *AJR Am J Roentgenol*. 2021;216(3):698-703. [\[CrossRef\]](#)
40. Lemoine C, Lokar J, McColley SA, Alonso EM, Superina R. Cystic fibrosis and portal hypertension: distal splenorenal shunt can prevent the need for future liver transplant. *J Pediatr Surg*. 2019;54(5):1076-1082. [\[CrossRef\]](#)
41. Koh C, Sakiani S, Surana P, et al. Adult-onset cystic fibrosis liver disease: diagnosis and characterization of an underappreciated entity. *Hepatology*. 2017;66(2):591-601. [\[CrossRef\]](#)
42. Ye W, Narkewicz MR, Leung DH, et al. Variceal hemorrhage and adverse liver outcomes in patients with cystic fibrosis cirrhosis. *J Pediatr Gastroenterol Nutr*. 2018;66(1):122-127. [\[CrossRef\]](#)



Supplementary Figure 1. Pre-emptive TIPS protocol. TIPS, transjugular intrahepatic portosystemic shunt; CFLD, cystic fibrosis liver disease; US, ultrasound; AST, aspartate aminotransferase; ALT, alanine aminotransferase; GGT, gamma-glutamyl transferase; PHT, portal hypertension; PPG, portosystemic pressure gradient.



Supplementary Figure 2. Obliterative portal venopathy. (a) Liver biopsy patient 4. Portal tract lacking a portal vein radicle (open arrow) next to a portal tract showing a portal vein radicle of reduced size (thin arrow). These two portal tracts are abnormally approximated to each other. (b) Liver biopsy patient 2. Portal tract showing a portal vein radicle of reduced size with a fibrous wall (arrow). (c) Liver biopsy patient 8. Thin fibrous septum connecting two portal tracts. The portal vein radicle shows a thick wall and a reduced size (arrow), while in other areas, the portal veins appear dilated. (d) Liver biopsy patient 8. Dilated portal veins herniating outside of the portal tracts in the periportal area indicating portal hypertension (arrows).



Short-term clinical outcomes of transarterial embolization for symptomatic hand osteoarthritis refractory to conservative treatment

Sieh-Yang Lee¹
 Wei-Xiong Lim¹
 Kuan-Ting Wu²
 Cheng-Ta Wu²
 Chung-Cheng Huang¹
 Ching-Di Chang¹

¹Kaohsiung Chang Gung Memorial Hospital and Chang Gung University College of Medicine, Department of Diagnostic Radiology, Kaohsiung, Taiwan

²Kaohsiung Chang Gung Memorial Hospital and Chang Gung University College of Medicine, Department of Orthopedic Surgery, Kaohsiung, Taiwan

PURPOSE

The present study aims to assess the short-term clinical outcomes and safety of transarterial embolization (TAE) for symptomatic hand osteoarthritis (OA) refractory to conservative treatment.

METHODS

The present retrospective cohort pilot study included nine patients who underwent TAE for symptomatic OA-associated hand pain in a single tertiary center between November 2022 and January 2023. The baseline and post-procedural OA-associated hand pain and function were assessed using the visual analog scale (VAS) and the Australian Canadian Hand Osteoarthritis Index (AUS-CAN). The use of conservative treatment and pain medications was also recorded. Post-procedural adverse events were evaluated according to the Society of Interventional Radiology classification.

RESULTS

Compared with the baseline, the overall VAS scores were significantly decreased at 1-week, 1-month, 3-months, and 6-months after TAE (76 ± 15 mm versus 34 ± 18 mm, $P < 0.001$; 32 ± 11 mm, $P < 0.001$; 21 ± 15 mm, $P < 0.001$; 18 ± 19 mm, $P = 0.002$). Similarly, improvement in the mean total AUSCAN scores (22.0 ± 10.0 versus 13.2 ± 6.6 , $P = 0.007$; 14.11 ± 7.3 , $P = 0.004$; 9.8 ± 6.8 , $P = 0.004$; 9.3 ± 7.4 , $P = 0.011$) were documented. The use of other conservative treatment methods also gradually decreased. There were no severe adverse events reported during the follow-up period.

CONCLUSION

TAE is a feasible and safe treatment method for symptomatic hand OA refractory to conservative treatment. This minimally invasive procedure effectively relieves debilitating OA-associated joint pain and restores hand function with a durable treatment effect.

KEYWORDS

Embolization, hand, musculoskeletal, osteoarthritis, pain control

Osteoarthritis (OA) is the most common musculoskeletal disorder among the elderly,¹ with the hands being the most frequently involved site of the disease.² In a population aged ≥ 70 years, 13.2% of men and 26.2% of women suffered from symptomatic hand OA.³ The debilitating symptoms of hand OA, such as pain, reduction of grip strength, and joint stiffness, have a negative impact on quality of life in the affected individuals.⁴⁻⁶

Despite the high prevalence of symptomatic hand OA, optimal treatment for the disease remains unestablished.⁷ Conservative management of symptomatic OA is mainly grouped into pharmacological (anti-inflammatory medications, analgesics, and intra-articular injection) and non-pharmacological [exercise, splint, assistive device, physical therapy (PT), etc.] categories. However, current conservative treatments usually provide limited and temporary therapeutic effects to the patients.⁸⁻¹⁰ Surgical intervention is reserved for patients with advanced OA and debilitating pain at the expense of motion range and other surgical complications.^{11,12}

Recently, transarterial embolization (TAE) has emerged as a safe and effective minimally invasive treatment for chronic musculoskeletal pain.¹³⁻¹⁶ Abnormal angiogenesis and ac-

Corresponding author: Ching-Di Chang

E-mail: haaman010@hotmail.com

Received 29 June 2023; revision requested 02 August 2023; last revision received 13 September 2023; accepted 27 September 2023.



Epub: 06.11.2023

Publication date: 08.01.2023

DOI: 10.4274/dir.2023.232350

You may cite this article as: Lee S-Y, Lim W-X, Wu K-T, Wu C-T, Huang C-C, Chang C-D. Short-term clinical outcomes of transarterial embolization for symptomatic hand osteoarthritis refractory to conservative treatment. *Diagn Interv Radiol.* 2024;30(1):65-71.

accompanying pain-related nerves have been demonstrated as a possible source of persistent inflammation and pain in OA.¹⁷⁻²⁰ Thus, eliminating abnormal neovessels by intra-arterially infusing an embolic agent into the target vessels might relieve pain and restore the joint motion in patients with symptomatic OA. Previous studies have described successful treatment of symptomatic hand OA with TAE, specifically focusing on the interphalangeal joint and trapeziometacarpal OA.^{10,21-23} However, data regarding the effectiveness and safety profile of TAE use for symptomatic hand OA with isolated or concurrent involvement of digit and wrist joints is still scarce.

This study aims to assess the short-term clinical outcomes and safety of TAE for symptomatic hand OA refractory to conservative treatment.

Methods

The present retrospective study was approved by the Chang Gung Medical Foundation Institutional Review Board Ethics Committee (protocol number: 202300669B0, date: 16.05.2023). Between November 2022 and January 2023, nine patients who underwent TAE for the treatment of symptomatic OA-associated hand pain in a single tertiary center were reviewed. All patients were referred from orthopedic clinics to the interventional radiology outpatient clinics. Hand OA was diagnosed by an orthopedist based on the American Rheumatology College Criteria,²⁴ and the hand radiography was confirmed by an experienced musculoskeletal radiologist.

The inclusion criteria of the procedure were as follows: (1) age ≥ 40 years; (2) hand OA with an involvement of single or multiple joints confirmed with plain radiography; (3)

visual analog scale (VAS) > 50 mm (the pain was rated on a 100 mm scale, with 0 representing no pain and 100 representing the worst pain imaginable); (4) OA-associated hand pain refractory to conservative treatment for ≥ 3 months, such as intra-articular injection, splint protection, PT, anti-inflammatory medications, or analgesics; and (5) radial artery type A/B/C based on the Barbeau test.

The exclusion criteria were as follows: (1) rheumatoid arthritis; (2) advanced atherosclerosis; (3) allergy to iodinated contrast material/antibiotics; and (4) local infection. After informed consent was obtained, the complete medical history of all patients was recorded, including the disease duration, medication, allergy history, prior conservative treatments, and affected hand joints. The location and severity of the hand OA was assessed via radiography using the Kellgren-Lawrence grading system.

Transarterial embolization procedure

The TAE procedures were performed by two experienced interventional radiologists. The treatment protocol was developed based on previous studies.^{10,21} All patients received a Barbeau test to assure adequate collateral circulation to the hand (type A to C). To reduce perioperative pain and discomfort, a non-steroidal anti-inflammatory drug (NSAIDs) (Parecoxib, 40 mg) was infused intravenously 10 min before the procedure. Then, under local anesthesia, a 24-gauge needle (BD Insyte Autoguard Becton Dickinson Infusion Therapy system) was inserted in an antegrade direction into the distal radial artery at the level of the wrist. The puncture process was performed under ultrasound guidance. Once brisk backflow of bright red blood was detected, the inner metallic needle was removed, with the outer plastic cannula remaining in the radial artery. Iodinated contrast material (Omnipaque GE healthcare) was injected manually to confirm the proper position of the cannula, and an angiogram

with optimal opacification of the deep palmar arch and digital arteries was performed under fluoroscopy. Abnormal neovessels were defined as tumor blush-type opacification during the arterial phase. The embolic agent was prepared by mixing 500 mg imipenem/cilastatin sodium (IPM/CS) powder (Kabi, Facta Farmaceutici S.p.A., Teramo, Italy) with 10 mL iodinated contrast material (Omnipaque). The embolic agent was gradually infused into the radial artery with a maximum dose limit of 5 mL. The endpoint of embolization was stasis of the antegrade blood flow within three heart beats or achievement of the maximal dose limit (Supplementary Video 1). After achieving the endpoint, the cannula was removed. The access site was compressed manually until hemostasis and covered with a band-aid. The patient was discharged after 20 min of observation. A two-session TAE was scheduled for each patient; the second procedure was arranged at 1-month after the first TAE. The maximal dose of the infused embolic agent was decreased to 3 mL for the second session. The pre-TAE and post-TAE angiographies for hand OA are presented in Figure 1.

Assessment of treatment effects and adverse events

The clinical severity of hand OA was assessed using the VAS and the Australian Canadian Hand Osteoarthritis Index (AUSCAN). The AUSCAN is a self-administered questionnaire that assesses pain, disability, and joint stiffness in hand OA with a total of 15 items.²⁵ Each item is rated on a scale of 0 (none) to 4 (extreme pain/stiffness/difficulty). The authors of the present study documented the following parameters: (1) VAS-night pain; (2) VAS-overall; (3) AUSCAN-pain; (4) AUSCAN-stiffness; and (5) AUSCAN-function at study entry and at 1-week, 1-month, 3-months, and 6-months after TAE. For patients with multiple-joint involvement, the affected joint with the worst pain was assessed. Compared with the baseline, the patient was classified as a responder

Main points

- Considering abnormal angiogenesis and accompanying sensory nerve growth as a possible source of persistent inflammation and pain in osteoarthritis (OA), angiogenesis might be a new therapeutic target for pain control.
- The percentage of responders ($\geq 50\%$ pain reduction) of hand transarterial embolization (TAE) at the 1-week, 1-month, 3-month, and 6-month follow-ups were 66.7%, 77.8%, 88.9%, and 88.9%, respectively.
- TAE effectively relieved joint pain and restored hand function without major adverse events in patients with symptomatic hand OA refractory to conservative treatment.



Figure 1. Transarterial embolization for symptomatic scaphotrapeziotrapezoid (STT) joint osteoarthritis. Angiography of (a) before, (b) during, and (c) after intra-arterial infusion of imipenem/cilastatin into the distal radial artery. Abnormal hypervascularity was present at the STT joint before embolization and disappeared after embolization. (d) During the second procedure, pre-infusion angiography showed abnormal neovessels in the affected joint; however, the occurrence was lower than in the initial procedure.

($\geq 50\%$ reduction) or a non-responder ($< 50\%$ reduction) based on changes in the overall pain VAS score at each time point. Pain recurrence was defined as a higher overall VAS score at 1-month (early recurrence), 3-months, and 6-months after TAE compared with previous recorded VAS scores or the baseline. The self-reported use of conservative treatment and pain medications in the last 3-months was also recorded at outpatient clinics before and after embolization.

Post-procedural adverse events were evaluated according to the Society of Interventional Radiology classification.²⁶ Possible complications, including tissue necrosis, peripheral paresthesia, and tendon rupture, were assessed during follow-up outpatient visits.

Statistical analysis

The statistical analyses of all data were conducted using the IBM SPSS software (version 22.0; IBM, Armonk, NY, USA). The baseline and outcome variables were compared using repeated-measures analysis of variance and post-hoc multiple comparisons to

determine changes in VAS scores, AUSCAN subscores, and AUSCAN total scores at each time point. All parameters were documented as the mean \pm standard deviation, and the *P* value for statistical significance was set at < 0.05 .

Results

A total of nine patients successfully underwent two-session TAE for the unilateral affected hand via the radial artery, with a mean procedural time of 15.7 min (range of 11–20 min; Table 1). Transient radial artery spasm occurred in 4 patients without any sequela. All patients experienced transient skin color changes of the infused hand; the skin turned pale initially and returned to its normal appearance approximately 30 min after infusion of embolic agents (Figure 2). No tissue necrosis, tendon rupture, muscle weakness, paresthesia, or other severe adverse events were reported during the follow-up period.

Compared with the baseline, the post-procedural mean nighttime VAS scores were significantly decreased at the 1-week, 1-month, 3-month, and 6-month follow-ups (58 ± 22

mm versus 22 ± 19 mm, $P < 0.001$; 20 ± 15 mm, $P < 0.001$; 10 ± 10 mm, $P < 0.001$; 8 ± 12 mm, $P = 0.004$; Figure 3). A significant improvement of the overall VAS score was also documented at 1-week, 1-month, 3-months, and 6-months after TAE (76 ± 15 mm versus 34 ± 18 mm, $P < 0.001$; 32 ± 11 mm, $P < 0.001$; 21 ± 15 mm, $P < 0.001$; 18 ± 19 mm, $P = 0.002$). The percentage of responders at the 1-week, 1-month, 3-month, and 6-month follow-ups were 66.7%, 77.8%, 88.9%, and 88.9%, respectively. The percentage of pain recurrence at the 1-month, 3-month, and 6-month follow-ups were 44.4% (early recurrence), 11.1%, and 11.1%, respectively (Supplementary Table 1).

Improvement was observed in the mean total AUSCAN scores (22.0 ± 10.0 versus 13.2 ± 6.6 , $P = 0.007$; 14.11 ± 7.3 , $P = 0.004$; 9.8 ± 6.8 , $P = 0.004$; 9.3 ± 7.4 , $P = 0.011$) and mean AUSCAN-pain subscores (10.0 ± 3.4 versus 5.7 ± 2.8 , $P = 0.004$; 5.6 ± 2.7 , $P = 0.001$; 3.7 ± 3.3 , $P < 0.001$; 3.0 ± 2.6 , $P = 0.001$) at every follow-up visit (Figures 4, 5). The mean AUSCAN-function subscores were significantly decreased at the post-procedural 1-week

Table 1. Clinical data and procedural details

Patient no.	Sex	Age (y)	Pain duration (mo)	Prior therapies	Main affected side	Main involved joint*	KL grading#	Embolic volume (mL) (1 st /2 nd)	Mean procedure time (min)
1	F	62	24	PT	Right	DIP, <u>PIP</u>	4	5 / 3	12
2	M	62	36	CSI	Right	CMC, <u>STT</u>	3	3 / 2	25
3	F	53	3	NSAIDs	Right	DIP	1	4 / 2	18
4	F	78	24	PT, NSAIDs, CSI	Right	DIP, <u>CMC</u> , STT	3	4 / 3	13
5	F	60	120	NSAIDs	Right	FIP, <u>DIP</u> , PIP	4	4 / 2	14
6	F	78	24	NSAIDs	Right	FIP, DIP, <u>PIP</u>	4	4 / 2.5	11
7	M	56	12	PT, CSI	Left	<u>CMC</u> , DIP	3	3.5 / 1.5	20
8	M	70	3	PT	Left	DIP	3	5 / 2.5	15
9	F	61	24	NSAIDs	Left	<u>FIP</u> , DIP	2	4 / 2	13

*The underlined joint indicated the involved joint with the worst pain. The KL grade was assigned to the involved joint with the worst pain. F, female; M, male; CSI, corticosteroid injection; KL: Kellgren–Lawrence system; NSAIDs, non-steroidal anti-inflammatory drugs; PT, physical therapy; DIP, distal interphalangeal joint; CMC, carpometacarpal joint; STT, scaphotrapezotrapezoid joint; FIP, first interphalangeal joint; PIP, proximal interphalangeal joint.



Figure 2. Skin color changes of the hand after intra-arterial infusion of imipenem/cilastatin sodium. The skin turned pale initially (5 min) and turned into hyperemia when reperfusion occurred (15 min). The skin color returned to normal appearance approx. 30 min after infusion of an embolic agent.

and 1-month follow-ups (11.1 ± 7.5 versus 6.8 ± 4.7 , $P < 0.05$; 7.8 ± 5.5 , $P < 0.05$); however, the differences were statistically insignificant at the 3-month and 6-month follow-ups (5.6 ± 5.1 , $P = 0.072$; 5.8 ± 5.6 , $P = 0.103$). There were also no differences in the mean AUSCAN-stiffness among all the timepoints (10.0 ± 3.4 versus 5.7 ± 2.8 , $P = 0.347$; 5.6 ± 2.7 , $P = 0.347$; 3.7 ± 3.3 , $P = 0.195$; 3.0 ± 2.6 , $P = 0.282$).

After initial embolization, the use of other conservative treatments gradually decreased (Table 2). Before TAE, 33% of the patients received corticosteroid injection (CSI), 44% of the patients received PT, and 55.6% of the patients took oral NSAIDs daily or almost daily. The rates of regular use of oral NSAIDs at the 1-week, 1-month, 3-month, and 6-month follow-ups were 33.3%, 22.2%, 11.1%, and 11.1%, respectively. No patients received PT or CSI after embolization.

Discussion

The present study demonstrated that TAE effectively relieved OA-associated joint pain and restored hand function with a durable treatment effect. After initial embolization, rapid reduction of nighttime and overall pain was documented (62% and 55% within 1-week, respectively), followed by gradual pain improvement up to the final 6-month follow-up. Similarly, the early improvement of hand function could also be observed within 1-week and 1-month after TAE, followed by a trend toward improved, albeit statistically insignificant, function scores. Moreover, most patients gradually decreased the use of other conservative treatments. There were no severe adverse events reported during the follow-up period.

Mounting evidence suggested that inflammation and hypervascularization played crucial roles in the pathogenesis of OA.^{17,18,20} During OA, cartilage degradation products initiate synovial inflammation, inducing the release of the pro-inflammatory mediators and recruitment of immune cells. The increased macrophage infiltration drives synovial angiogenesis and excessive production of proteolytic enzymes

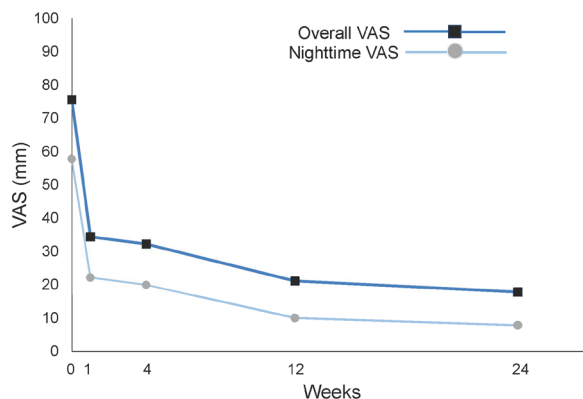


Figure 3. Reduction of the visual analog scale score after transarterial embolization (TAE). Both mean nighttime and overall pain decreased rapidly at 1-week after TAE, followed by gradual improvement at 4, 12, and 24-weeks after TAE (all $P < 0.01$). VAS, visual analog scale.

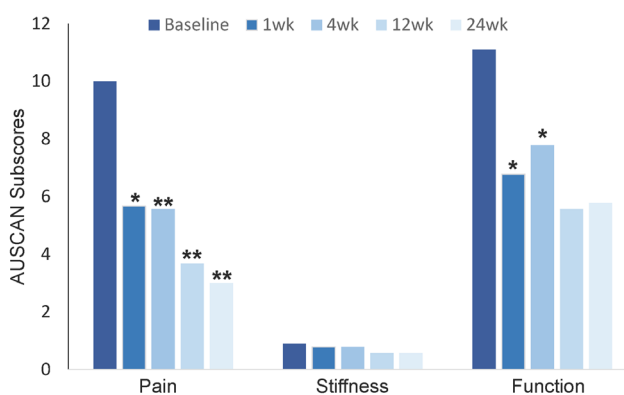


Figure 4. Changes in the Australian Canadian Hand Osteoarthritis Index pain, stiffness, and physical function subscores after embolization. A single asterisk indicates $P < 0.05$ and a double asterisk indicates $P < 0.01$.

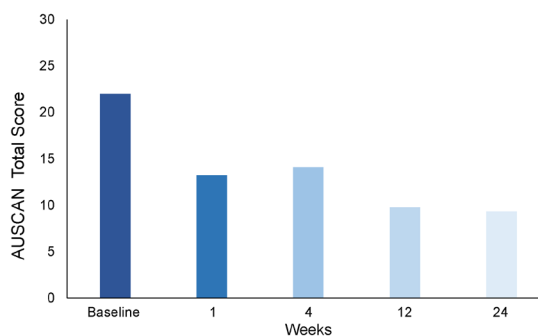


Figure 5. Changes in the total Australian Canadian Hand Osteoarthritis Index (AUSCAN) score after embolization. The AUSCAN score significantly decreased at the 1-week, 4-week, 12-week, and 24-week follow-ups compared with baseline (all $P < 0.05$).

Treatment options	Baseline	1-week	1-month	3-months	6-months
Physical therapy	4	0	0	0	0
Oral NSAIDs	5	3	2	1	1
Corticosteroid injection	3	0	0	0	0

NSAIDs, non-steroidal anti-inflammatory drugs.

responsible for aggravated osteochondral damage and further synovial inflammation, creating a positive feedback loop.²⁷ The sensory nerves grow along neovessels into the synovium, cartilage, osteophytes, and other joint tissues, contributing to the structural damage and pain in the OA joint.²⁰ Thus, as a key component in the pathogenesis of OA, angiogenesis might be a new therapeutic target for breaking the vicious cycle. Inui et al.²¹ and Liang et al.²³ demonstrated the treatment outcome of intra-arterial infusion of IPM/CS in refractory trapeziometacarpal and interphalangeal OA, respectively. However, hand OA usually involves multiple digits and wrist joints, including interphalangeal joints, carpometacarpal joints, and scaphotrapeziotrapezoid joints. Transarterial embolization is not limited to treating isolated joints, and multiple affected interphalangeal and wrist joints can be treated simultaneously by intra-arterial infusion of IPM/CS into the distal radial artery. The present study demonstrated that TAE is an efficient method for relieving OA-associated pain and improving hand function in patients with isolated or concurrent joint involvement.

With the use of TAE for chronic musculoskeletal joint pain, concerns regarding adverse events, especially ischemia and non-target embolization, might arise. IPM/CS sodium is slightly water soluble and has a short half-life of approx 1 h. When suspended in an iodinated contrast material, it forms a crystalline compound, with a particle size of 10–130 μm .²⁸ With a transient embolic effect and peripheral accessibility, IPM/CS has been used in the embolization of gastrointestinal bleeding and chronic musculoskeletal pain. In several studies,^{29–32} IPM/CS demonstrated its excellent safety profile, with no severe adverse event reported. In the present study, all patients experienced transient skin color changes of the infused hand; the skin turned pale initially and returned to its normal appearance approximately 30 min after infusion of embolic agents. There were no severe ischemic adverse events in the target and non-target areas of embolization. To avoid non-target embolization in the hand, several modified methods, such as manual compression and the use of a rubber band, might be useful for limiting the blood flow to the non-symptomatic joint. The decreased distribution of particles in the non-target areas might help improve post-procedural hand swelling and discomfort. However, further investigation on the effects of these methods is warranted.

In this study, early recurrence of joint pain was observed in 4 patients (44%) at the 1-month follow-up visit; however, the recurring pain was milder than before treatment. Previous literature reported early recurrence of local tenderness after successful initial TAE for chronic musculoskeletal pain.³¹ This phenomenon might be explained by partial recanalization of abnormal vessels or revascularization after initial TAE.³¹ The temporary embolic agent IPM/CS was used for TAE in this study due to its safety profile. During the second procedure, abnormal vessels were present in the affected joint; however, the occurrence was lower than in the initial procedure. These findings supported the present authors' hypothesis that the presence of partial recanalization or revascularization after the initial TAE procedure might lead to early recurrence of joint pain in some affected patients. Thus, a two-session procedure might be an appropriate regimen to maintain the effectiveness of the treatment.

Several limitations of this study should be addressed. First, the patients were allowed to receive conservative therapy after embolization, possibly confounding the treatment outcome of TAE. However, the use of conservative therapy was evidently decreased after TAE. This finding highlighted the effectiveness of TAE in the treatment of symptomatic hand OA. Secondly, the best endpoint of embolization has yet to be established. In this study, the endpoint of embolization was determined based on the achievement of the antegrade blood flow stasis within three heart beats or achievement of the maximal dose limit. Third, this small-scale study lacked a control group as a comparator arm, possibly leading to the occurrence of the placebo effect. Transarterial embolization is a novel treatment for symptomatic hand OA, and data regarding the treatment effectiveness and safety profile are currently limited. The present authors' initial experience might help introduce TAE as a potentially effective and safe treatment for symptomatic hand OA refractory to conservative treatment. Therefore, future sham-controlled randomized controlled studies are warranted to validate the preliminary results of this study.

In conclusion, TAE is a feasible and safe treatment for symptomatic hand OA refractory to conservative treatment. This minimally invasive procedure effectively relieves debilitating OA-associated joint pain and restores hand function with a durable treatment effect.

Conflict of interest disclosure

The authors declared no conflicts of interest.

References

1. Guccione AA, Felson DT, Anderson JJ, et al. The effects of specific medical conditions on the functional limitations of elders in the Framingham study. *Am J Public Health.* 1994;84(3):351–358. [\[CrossRef\]](#)
2. Kalichman L, Hernández-Molina G. Hand osteoarthritis: an epidemiological perspective. *Semin Arthritis Rehum.* 2010;39(6):465–476. [\[CrossRef\]](#)
3. Zhang Y, Niu J, Kelly-Hayes M, Chaisson CE, Aliabadi P, Felson DT. Prevalence of symptomatic hand osteoarthritis and its impact on functional status among the elderly: the Framingham study. *Am J Epidemiol.* 2002;156(11):1021–1027. [\[CrossRef\]](#)
4. Neogi T. The epidemiology and impact of pain in osteoarthritis. *Osteoarthritis and Cartilage.* 2013;21(9):1145–1153. [\[CrossRef\]](#)
5. Ye L, Kalichman L, Spittle A, Dobson F, Bennell K. Effects of rehabilitative interventions on pain, function and physical impairments in people with hand osteoarthritis: a systematic review. *Arthritis Res Ther.* 2011;13(1):28. [\[CrossRef\]](#)
6. Loef M, Damman W, de Mutsert R, Rosendaal FR, Kloppenburg M. Health-related Quality of life in patients with hand osteoarthritis from the general population and the outpatient clinic. *J Rheumatol.* 2020;47(9):1409–1415. [\[CrossRef\]](#)
7. Kroon FPB, Carmona L, Schoones JW, Kloppenburg M. Efficacy and safety of non-pharmacological, pharmacological and surgical treatment for hand osteoarthritis: a systematic literature review informing the 2018 update of the EULAR recommendations for the management of hand osteoarthritis. *RMD Open.* 2018;4(2):e000734. [\[CrossRef\]](#)
8. Kloppenburg M, Kroon FP, Blanco FJ, et al. 2018 update of the EULAR recommendations for the management of hand osteoarthritis. *Ann Rheum Dis.* 2019;78(1):16–24. [\[CrossRef\]](#)
9. Zhang W, Doherty M, Leeb BF, et al. EULAR evidence based recommendations for the management of hand osteoarthritis: report of a Task Force of the EULAR Standing Committee for International Clinical Studies Including Therapeutics (ESCSIT). *Ann Rheum Dis.* 2007;66(3):377–388. [\[CrossRef\]](#)
10. Kung SC, Chou MY, Yang KW, Hsu Y. Intra-arterial infusion of temporary embolic agent as a new treatment in a patient with osteoarthritis of the fingers. *Asia Pac J Pain.* 2022;32(1):10–15. [\[CrossRef\]](#)
11. Vitale MA, Fruth KM, Rizzo M, Moran SL, Kakar S. Prosthetic arthroplasty versus arthrodesis for osteoarthritis and posttraumatic arthritis

- of the index finger proximal interphalangeal joint. *J Hand Surg Am.* 2015;40(10):1937-1948. [\[CrossRef\]](#)
12. Rongièrès M. Surgical treatment of degenerative osteoarthritis of the fingers. *Chir Main.* 2013;32(4):193-198. [\[CrossRef\]](#)
 13. Wang B, Liang KW, Chen CH, Wang CK. Transcatheter arterial embolization for alleviating chronic musculoskeletal pain and improving physical function: a narrative review. *Diagnostics (Basel).* 2022;13(1):134. [\[CrossRef\]](#)
 14. Kim GH, Shin JH, Nam IC, Chu HH, Kim JH, Yoon HK. Transcatheter arterial embolization for benign chronic inflammatory joint pain: a systematic review and meta-analysis. *J Vasc Interv Radiol.* 2022;33(5):538-545. [\[CrossRef\]](#)
 15. Kishore S, Sheira D, Malin ML, Trost DW, Mandl LA. Transarterial embolization for the treatment of chronic musculoskeletal pain: a systematic review of indications, safety, and efficacy. *ACR Open Rheumatol.* 2022;4(3):209-217. [\[CrossRef\]](#)
 16. Beckmann NM, Villamaria EE. Interventional therapies for osteoarthritis: an update. *AJR Am J Roentgenol.* 2022;219(6):929-939. [\[CrossRef\]](#)
 17. Korchi AM, Cengarle-Samak A, Okuno Y, et al. Inflammation and hypervascularization in a large animal model of knee osteoarthritis: imaging with pathohistologic correlation. *J Vasc Interv Radiol.* 2019;30(7):1116-1127. [\[CrossRef\]](#)
 18. Berenbaum F. Osteoarthritis as an inflammatory disease (osteoarthritis is not osteoarthrosis!). *Osteoarthritis Cartilage.* 2013;21(1):16-21. [\[CrossRef\]](#)
 19. Ashraf S, Mapp PI, Walsh DA. Contributions of angiogenesis to inflammation, joint damage, and pain in a rat model of osteoarthritis. *Arthritis Rheum.* 2011;63(9):2700-2710. [\[CrossRef\]](#)
 20. Mapp PI, Walsh DA. Mechanisms and targets of angiogenesis and nerve growth in osteoarthritis. *Nat Rev Rheumatol.* 2012;8(7):390-398. [\[CrossRef\]](#)
 21. Inui S, Yoshizawa S, Shintaku T, Kaneko T, Ikegami H, Okuno Y. Intra-arterial infusion of imipenem/cilastatin sodium through a needle inserted into the radial artery as a new treatment for refractory trapeziometacarpal osteoarthritis. *J Vasc Interv Radiol.* 2021;32(9):1341-1347. [\[CrossRef\]](#)
 22. Kubo T, Miyazaki K, Shibuya M, Sugihara E, Nakata M, Okuno Y. Intra-arterial injection of temporary embolic material through a needle inserted into the radial or ulnar artery for distal and proximal interphalangeal joint osteoarthritis: a retrospective study of 92 patients. *Cardiovasc Intervent Radiol.* 2023;46(10):1375-1382. [\[CrossRef\]](#)
 23. Liang KW, Wang B, Huang HH, Tsao TF, Tyan YS, Wang PH. Effectiveness and safety of intra-arterial imipenem/cilastatin sodium infusion for patients with hand osteoarthritis-related interphalangeal joint pain. *J Vasc Interv Radiol.* 2023;34(9):1485-1492. [\[CrossRef\]](#)
 24. Altman R, Alarcón G, Appelrouth D, et al. The American College of Rheumatology criteria for the classification and reporting of osteoarthritis of the hand. *Arthritis Rheum.* 1990;33(11):1601-1610. [\[CrossRef\]](#)
 25. Bellamy N, Campbell J, Haraoui B, et al. Clinimetric properties of the AUSCAN Osteoarthritis Hand Index: an evaluation of reliability, validity and responsiveness. *Osteoarthritis Cartilage.* 2002;10(11):863-869. [\[CrossRef\]](#)
 26. Baerlocher MO, Nikolic B, Sze DY. Adverse event classification: clarification and validation of the Society of Interventional Radiology specialty-specific system. *J Vasc Interv Radiol.* 2023;34(1):1-3. [\[CrossRef\]](#)
 27. Mathiessen A, Conaghan PG. Synovitis in osteoarthritis: current understanding with therapeutic implications. *Arthritis Res Ther.* 2017;19(1):18. [\[CrossRef\]](#)
 28. Aihara T. A basic study of super-selective transcatheter arterial chemotherapy and chemoembolization (1)-establishment of an animal model for superselective transcatheter arterial chemotherapy and preparation for appropriate suspension of microembolization. *Kawasaki Igakkaishi.* 1999;25:47-54. [\[CrossRef\]](#)
 29. Woodhams R, Nishimaki H, Ogasawara G, et al. Imipenem/cilastatin sodium (IPM/CS) as an embolic agent for transcatheter arterial embolisation: a preliminary clinical study of gastrointestinal bleeding from neoplasms. *Springerplus.* 2013;2:344. [\[CrossRef\]](#)
 30. Okuno Y, Iwamoto W, Matsumura N, et al. Clinical outcomes of transcatheter arterial embolization for adhesive capsulitis resistant to conservative treatment. *J Vasc Interv Radiol.* 2017;28(2):161-167. [\[CrossRef\]](#)
 31. Iwamoto W, Okuno Y, Matsumura N, Kaneko T, Ikegami H. Transcatheter arterial embolization of abnormal vessels as a treatment for lateral epicondylitis refractory to conservative treatment: a pilot study with a 2-year follow-up. *J Shoulder Elbow Surg.* 2017;26(8):1335-1341. [\[CrossRef\]](#)
 32. Okuno Y, Korchi AM, Shinjo T, Kato S, Kaneko T. Midterm clinical outcomes and MR imaging changes after transcatheter arterial embolization as a treatment for mild to moderate radiographic knee osteoarthritis resistant to conservative treatment. *J Vasc Interv Radiol.* 2017;28(7):995-1002. [\[CrossRef\]](#)

Supplementary Table 1. Changes in overall VAS pain score and total AUSCAN scores after embolization

No.	VAS pain score					Total AUSCAN score				
	Baseline	1 w	1 m	3 m	6 m	Baseline	1 w	1 m	3 m	6 m
1	6	6	3	2	2	10	9	6	11	13
2	10	6	4	4	3	33	20	16	7	1
3	7	5	1	1	0	18	15	6	3	4
4	7	2	4	2	0	29	20	25	14	18
5	9	3	4	2	2	32	8	23	16	5
6	6	3	2	5	2	22	16	16	22	21
7	9	2	4	1	1	32	21	16	9	13
8	8	3	3	0	0	7	6	5	0	0
9	6	1	4	2	6	15	4	14	6	9

VAS, visual analog scale; AUSCAN, Australian Canadian Hand Osteoarthritis Index; PIP, proximal interphalangeal joints; CMC, carpometacarpal joint; DIP, distal interphalangeal joints; IP, interphalangeal joint.

Supplementary Video 1 link: <http://glns.co/m7w4u>

Supplementary Video 1. Angiography demonstrated the endpoint of embolization when stasis of the antegrade blood flow within three heart beats was achieved after intra-arterial infusion of imipenem/cilastatin sodium.



Unusual collaterals through interhemispheric connections in Moyamoya disease

Ömer Bağcılar¹
Bora Korkmazer²
Osman Kızılkılıç²
Civan Işlak²

¹University of Health Sciences Turkey, Şişli Hamidiye Etfal Training and Research Hospital, Clinic of Radiology, Istanbul, Turkey

²Istanbul University-Cerrahpaşa, Cerrahpaşa Faculty of Medicine, Department of Radiology, Division of Neuroradiology, Istanbul, Turkey

Dear Editor,

This paper aims to inform readers about some rare collateral structures of Moyamoya disease (MMD). Collateral circulation is crucial in preserving cerebral blood flow in patients with occlusion or reduced antegrade cerebral artery flow. In acute anterior or posterior circulation occlusions, the circle of Willis (including the anterior and posterior communicating arteries and, second, the extracranial-intracranial collaterals, mostly via the ipsilateral external carotid artery and ophthalmic artery) contributes to the maintenance of perfusion. In addition to these well-established anastomotic pathways, it is well known that pre-existing intraparenchymal and dural-pial anastomotic vascular structures are induced and become visible in chronic and gradual occlusion cases. These chronic collaterals are most typically seen in MMD. MMD describes a chronic progressive stenosis or occlusion of the supraclinoid internal carotid artery (ICA) and/or the proximal portions of the anterior (ACA) and middle cerebral arteries.¹ Collateral vessels at the base of the brain, called Moyamoya vessels, are mainly lenticulostriate, thalamoperforating, and choroidal arteries that are also intratrial, intrathalamic, transmedullary and transcallosal anastomotic structures, which have been described in many studies.^{2,3} Regarding submillimeter basal collateral vasculature, imaging with 7T time-of-flight magnetic resonance angiography was comparable to catheter angiography.⁴ Although these collateral structures have also been clearly demonstrated in some microsurgical studies, transhemispheric vascular anastomosis via the anterior commissure, interthalamic adhesion, or other interhemispheric connections has not yet been demonstrated radiologically according to this study's literature research.^{5,6} These anastomoses may contribute greatly to the preservation of contralateral hemispheric perfusion and may become radiologically visible. When ICA supraclinoid occlusion is accompanied by ipsilateral ACA A1 segment and posterior communicating artery occlusions, as in our illustrative images of a patient with MMD, these afore-

KEYWORDS

Anterior commissure, collateral vessels, internal carotid occlusion, interthalamic adhesion, Moyamoya disease

Corresponding author: Ömer Bağcılar

E-mail: dromerbagcilar@gmail.com

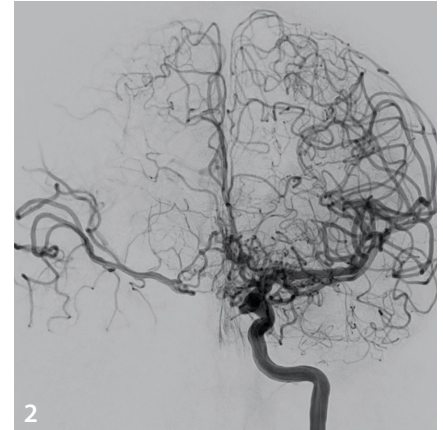
Received 13 February 2023; revision requested 06 March 2023; accepted 21 March 2023.



Epub: 05.04.2023

Publication date: 08.01.2023

DOI: 10.4274/dir.2023.232140



Figures 1, 2. Three-dimensional rotational angiography-magnetic resonance imaging fusion and left internal carotid angiogram images of a patient with Moyamoya disease showing right internal carotid artery (ICA) supraclinoid occlusion, right middle cerebral arteries reconstruction via anterior commissural, and interthalamic collaterals through the left ICA.

mentioned anastomotic vascular collaterals via interhemispheric white matter gain great importance. Recognition of the role of these collateral structures in the perfusion of the contralateral hemisphere is also important in treating aneurysms due to hemodynamic stress in these collaterals and may bring bypass surgery to the forefront rather than endovascular treatment (Figures 1, 2).

Conflict of interest disclosure

The authors declared no conflicts of interest.

References

1. Research Committee on the Pathology and Treatment of Spontaneous Occlusion of the Circle of Willis; Health Labour Sciences Research Grant for Research on Measures for Intractable Diseases. Guidelines for diagnosis and treatment of moyamoya disease (spontaneous occlusion of the circle of Willis). *Neurol Med Chir (Tokyo)*. 2012;52(5):245-266. [\[CrossRef\]](#)
2. Liu W, Xu G, Liu X. Neuroimaging diagnosis and the collateral circulation in moyamoya disease. *Interv Neurol*. 2013;1(2):77-86. [\[CrossRef\]](#)
3. Strother MK, Anderson MD, Singer RJ, et al. Cerebrovascular collaterals correlate with disease severity in adult North American patients with Moyamoya disease. *AJNR Am J Neuroradiol*. 2014;35(7):1318-1324. [\[CrossRef\]](#)
4. Matsushige T, Kraemer M, Sato T, et al. Visualization and classification of deeply seated collateral networks in Moyamoya angiopathy with 7T MRI. *AJNR Am J Neuroradiol*. 2018;39(7):1248-1254. [\[CrossRef\]](#)
5. Wollschlaeger G, Wollschlaeger PB. Arterial anastomoses of the human brain. A radiographic-anatomic study. *Acta Radiol Diagn (Stockh)*. 1966;5:604-614. [\[CrossRef\]](#)
6. Marinković SV, Milisavljević MM, Marinković ZD. Microanatomy and possible clinical significance of anastomoses among hypothalamic arteries. *Stroke*. 1989;20(10):1341-1352. [\[CrossRef\]](#)